Imperial College London
Department of Earth Science and Engineering

Finite element modeling of frictional contact and stress intensity factors in three-dimensional fractured media using unstructured tetrahedral meshes

Morteza Nejati

Submitted in part fulfilment of the requirements for the degree of Doctor of Philosophy

December 2015

Abstract

This thesis introduces a three-dimensional (3D) finite element (FE) formulation to model the linear elastic deformation of fractured media under tensile and compressive loadings. The FE model is based on unstructured meshes using quadratic tetrahedral elements, and includes several novel components: (i) The singular stress field near the crack front is modeled using quarter-point tetrahedral finite elements. (ii) The frictional contact between the crack faces is modeled using isoparametric contact discretization and a gap-based augmented Lagrangian method. (iii) Accurate stress intensity factors (SIFs) of 3D cracks computed using the two novel approaches of displacement correlation and disk-shaped domain integral. The main contributions in the FE modeling of 3D cracks are: (i) It is mathematically proven that quarter-point tetrahedral finite elements (QPTs) reproduce the square root strain singularity of crack problems. (ii) A displacement correlation (DC) scheme is proposed in combination with QPTs to compute SIFs from unstructured meshes. (iii) A novel domain integral approach is introduced for the accurate computation of the pointwise J-integral and the SIFs using tetrahedral elements. The main contributions in the contact algorithm are: (i) A square root singular variation of the penalty parameter near the crack front is proposed to accurately model the contact tractions near the crack front. (ii) A gap-based augmented Lagrangian algorithm is introduced for updating the contact forces obtained from the penalty method to more accurate estimates. The results of contact and stress intensity factors are validated for several numerical examples of cubes containing single and multiple cracks. Finally, two applications of this numerical methodology are discussed: (i) Understanding the hysteretic behavior in rock deformation; and (ii) Simulating 3D brittle crack growth. The results in this thesis provide significant evidence that tetrahedral elements are efficient, reliable and robust instruments for accurate linear elastic fracture mechanics calculations.

to my family

Acknowledgements

Undertaking this PhD has been a truly life-changing experience, which would not have been possible without the support and guidance from many people, to whom I wish to express my sincere appreciation.

First and foremost I would like to gratefully acknowledge the endless guidance, support and encouragement of my doctoral supervisors, Dr. Adriana Paluszny and Prof. Robert W. Zimmerman. Adriana has been a tremendous mentor for me, and always supported me with her patience and knowledge. She encouraged and motivated me throughout my PhD, and taught me many different technical and professional skills. One simply could not wish for a better and friendlier supervisor. Prof. Zimmerman has been a truly dedicated mentor, providing me with his great guidance, support, and deep insight. He gave me the freedom to do research in the area of my interest, yet at the same time continuing to contribute valuable feedback and advice with his immense knowledge. His guidance has been invaluable and motivational.

I would like to thank those who examined my PhD work. I am grateful to Dr. Nicolas Riesco, Dr. Raphael Blumenfeld and Dr. John-Paul Latham for their time and consideration, for examining the 3-month initial plan of study, 9-month early stage review and 21-month late stage review of my PhD. I would also like to express my sincere gratitude to my PhD viva examiners, Prof. Lidija Zdravkovic and Prof. Jon Trevelyan for their time and consideration.

My gratitude extends to The Rio Tinto Center for Advanced Mineral Recovery. This dissertation would not have been possible without funding from this center.

I take this opportunity to sincerely thank all my colleagues and friends in the ESE department. Their support and encouragements made this journey easier and more joyful for me.

Last but not the least, I owe my deepest gratitude to my loving and caring family for their love, support, and sacrifice. My parents have supported me throughout all stages of my life, and provided me with nothing but unconditional love, endless support, priceless care, and constant encouragement. My caring brothers Mohsen and Hossein, and my loving sisters Elaheh and Atefeh have always given me constant love and motivation.

I hereby declare that this thesis and the work reported herein was composed by and originated entirely from me. Information derived from the published and unpublished work of others has been acknowledged in the text and references are given in the list of sources.

Contents

List of Figures

Chapter 1

Introduction

Understanding the mechanical response of elastic fractured media subjected to different mechanical loads is of vital importance and great interest to a variety of scientific and engineering fields including material science [Kachanov, 1982a; Aleshin and Van Den Abeele, 2005], structural geology [Einstein and Dershowitz, 1990; Reeves et al., 2013], mining engineering [Jing, 2003; Wang and Tonon, 2011], oil and gas reservoir engineering [Yeo et al., 1998; Baghbanan and Jing, 2008], geothermal energy development [Jafari and Babadagli, 2011; De Dreuzy et al., 2012], mechanical engineering [Baietto et al., 2010; Pook et al., 2014] and structural and earthquake engineering [Segall and Pollard, 1983; Einstein and Dershowitz, 1990]. Both elastic and inelastic responses of fractured media to mechanical loads are significantly influenced by the presence of cracks, which indicates the great importance of the accurate modeling of cracks in elastic media [Walsh, 1965; Kachanov, 1982b; Aleshin and Van Den Abeele, 2007a]. When the material behavior is linear elastic, and the inelastic deformation is small compared to the size of the crack, the context of Linear Elastic Fracture Mechanics (LEFM) is used to investigate the mechanical response of fractured media [Anderson, 2005].

The size of cracks in elastic media varies significantly, ranging from micrometers to kilometers depending on the context. Examples of fractured media at the micro-scale are micro-structured materials such as rock and concrete. This class of materials contains a large number of embedded micro-cracks which significantly influence their deformation and strength behavior. Two key features of the deformation of these materials, nonlinearity and hysteresis, are generally attributed to the presence of micro-cracks and crack-like voids [Walsh, 1965; Lawn and Marshall, 1998; David et al., 2012]. Their inelastic processes such as yielding, failure, fracturing and fragmentation are also significantly controlled by these defects [Kachanov, 1982b; Aleshin and Van Den Abeele, 2007a]. Once micro-cracks are activated and propagated, larger cracks are generated via growth, coalescence and branching

mechanisms, conducing to fracturing and fragmentation of these materials [Shockey et al., 1974; Einstein and Dershowitz, 1990; Khanal et al., 2008].

Geological formations are examples of fractured media at larger scales, where rock joints have been shown to extend to lengths ranging from hundreds to thousands of meters [Bonnet et al., 2001]. Pre-existing natural fractures in rock masses act as local mechanical weaknesses and main flow pathways, and therefore determine not only the deformation and strength of the rock mass, but also its flow and transport properties [Segall and Pollard, 1983; Gudmundsson, 1987; Pyrak-Nolte and Morris, 2000; Nick et al., 2011]. Experimental and numerical investigations show that normal closure and shear dilation can significantly change fracture transmissivity [Yeo et al., 1998; Olsson and Barton, 2001]. Fluid flow in fractured rock masses is therefore strongly stress-dependent, both with regards to the magnitude and orientation of the principal permeabilities [Min et al., 2004; Baghbanan and Jing, 2008]. Accurate prediction of fluid pressure and solid deformation in fractured rocks, therefore, requires hydro-mechanically coupled models with the ability to resolve normal and shear components of contact tractions acting on the fractures [Barton et al., 1985].

An exact geometric representation of naturally fractured media in geological formations is challenging, for two main reasons. The first is related to the matter of scales and fracture size distribution. Observations suggest that fracture size is governed by power-law scaling models, spanning orders of magnitudes of length scales [Bonnet et al., 2001]. The second issue is fracture characterization, for which non-invasive methods to map fractures *in situ* are yet to be developed for more accurate fracture representations. Stochastic models are therefore required to investigate deformation/flow characteristics of fractured media. Stochastic models often use idealized fracture shapes [Dershowitz and Einstein, 1988; Huseby et al., 1999], based on a statistical description of parameters such as distributions of size and orientation [Huseby et al., 2000; Malinouskaya et al., 2014]. Models that opt for an explicit representation of fractures, as opposed to a continuum formulation, have been termed Discrete Fracture Network (DFN) models [Andersson and Dverstorp, 1987; Painter and Cvetkovic, 2005]. The concept of DFN was first introduced by Long et al. [1982] for homogenizing complex fracture networks, and has been extensively used for flow and transport applications [Min et al., 2004; Baghbanan and Jing, 2007; Leung and Zimmerman, 2012; De Dreuzy et al., 2012; Lang et al., 2014]. Nevertheless, despite great geometrical simplifications, this type of modeling approach is routinely applied to estimate effective values of engineering parameters relevant to fluid flow, e.g. permeability, [Reeves et al., 2013] as well as mechanical deformation of micro-structured materials, e.g. Young's modulus [Walsh, 1965; Lawn and Marshall, 1998; Aleshin and Van Den Abeele, 2007a; David et al., 2012].

Due to geometrical and physical complexities, numerical simulations are necessary in analyzing deformation in fractured media. The majority of numerical simulations of fracture networks have been conducted using discrete element method (DEM), while the use of the finite element method (FEM) has been limited to a few studies. DEM has also been very popular in simulating fracture growth and fragmentation of brittle solids, such as granular materials and rock and concrete [Kuna and Herrmann, 1996; Khanal et al., 2004; Carmona et al., 2008; Wang and Tonon, 2011]. DEM generally treats the fractured medium as an assemblage of discrete blocks formed by connected fractures, solves the equation of motion for the blocks, and updates the contact between the block as a consequence of the motion and deformation of the blocks [Jing, 2003]. The distinct element method introduced by Cundall [1988], as implemented in the commercial computer codes UDEC and 3DEC for two- and three-dimensional problems [UDEC, 1992; 3DEC, 1994], and the discontinuous deformation analysis (DDA) proposed by Shi [1988], have been the main approaches for analyzing the deformation and permeability of fractured rock masses [Zhang and Sanderson, 1998; Jing et al., 2001; Min et al., 2004; Baghbanan and Jing, 2007]. DDA uses standard FEM meshes over blocks and employs the penalty method for enforcing the contact constraint between blocks. A similar development to DDA is combined FEM/DEM introduced by Munjiza et al. [1995] which considers not only the block deformation but also fracturing and fragmentation of the blocks [Latham et al., 2013].

The application of DEM in modeling fracture growth and fragmentation entails the following difficulties: (1) Time-consuming and error-prone calibration of micro- to macro-properties must be performed for each material individually [Kuna and Herrmann, 1996]. Thus, elastic mechanical properties such as the Young's modulus and Poisson's ratio cannot be directly used to model elastic deformation. Moreover, resulting calibrated properties are scale and mesh size dependent [Lisjak and Grasselli, 2014]. (2) Fractures are not explicitly defined; in fact, they are modeled as the lack of cohesion between the particles in the material [Carmona et al., 2008; Wang and Tonon, 2011]. Therefore, the models do not capture stress singularities around the fractures. (3) For fragmentation purposes, materials often artificially behave as particulates or agglomerates [Khanal et al., 2004, 2008]. Therefore, 3D fragmentation simulations and qualitative pattern evaluation are scarce in relation to the maturity of DEM, possibly due to the lack of realism caused by the absence of a fracture mechanics-based crack growth models. Regarding the application of DEM in deformation and flow response of fractured networks, the following drawbacks are highlighted [Jing, 2003]: (1) Isolated fractures are ignored when using DEM in modeling the fracture networks, and fractures are only modeled as the boundaries of isolated blocks; (2) The deformation inside blocks and the contact forces between the block are roughly approximated, as explicit

methods are generally used to solve the balance equations. (3) The high stress gradients near the cracks cannot be captured accurately, and the variation of contact tractions over contact surfaces are estimated roughly. The deformation of fracture surfaces, which controls the aperture change within fractures, is also only roughly estimated. Overall, DEM tends to reproduce fracture patterns in a quantitative manner, but the qualitative prediction of strength is tied to the accurate calibration of the material properties.

In contrast, the finite element method is able to capture the high gradient stress state near the crack, and provides very accurate contact tractions based on implicit methods. Advantages of FEM for modeling fracture networks include: (1) Meso-scale definition of material properties such as elastic constants and material toughness are directly used in the method; (2) Fractures are explicitly modeled as local discontinuities in the continuum medium, where singular stress fields are modeled thorough adapting appropriate element size and type in the crack front region in a FE model, or appropriate enrichment functions in an XFEM formulation; (3) Fracture mechanics-based parameters such as the stress intensity factor and J-integral can be used to study the onset of fracture growth and fragmentation in fractured media; (4) Crack interactions are captured accurately. Despite so many advancements in the use of the finite element method in fracture mechanics, reliable and efficient finite element methodologies are still in great demand for modeling complex elastic fractured media.

Other numerical methods to solve crack problems and model crack propagation include boundary element method (BEM) [Mi and Aliabadi, 1992; Portela et al., 1993; Aliabadi, 1997; Simpson and Trevelyan, 2011], scaled boundary finite element method (SBFEM) [Yang, 2006; Ooi and Yang, 2011], peridynamics [Ha and Bobaru, 2010; Agwai et al., 2011] and the phase-field approach [Borden et al., 2012; Klinsmann et al., 2015]. BEM and SBFEM are advantageous in that they reduce the dimensionality of the problem, thereby only requiring discretization of lines and surfaces for 2D and 3D problems, respectively [Aliabadi, 1997]. BEM can also be enriched to enhance the accuracy of the numerical solution; this is also known as X-BEM [Peake et al., 2013]. The coupled BE-SBFEM combines the geometric flexibility of the BEM to model sections of a domain that may not be simple in nature, with the accuracy of the SBFEM to model the region around a crack tip [Chidgzey et al., 2008; Bird et al., 2010]. Peridynamics is a nonlocal integral formulation that includes damage as part of the material response. The main difference between the peridynamic theory and the finite element method is that the former is formulated using integral equations as opposed to derivatives of the displacement components [Agwai et al., 2011]. Peridynamics is able to correctly model and simulate dynamic fracture, in particular crack branching in brittle materials [Ha and Bobaru, 2010]. In phase-field models, discontinuities are not

introduced into the solid, but instead, the fracture surface is approximated by a smooth phase-field, which smears the domain and boundary of the crack over a small region [Borden et al., 2012]. Nevertheless, for solving complex crack problems in geological applications, the FE method is overall more efficient and appropriate due to its simplicity, accuracy, and reliability, and due to its ability to interface with solutions to flow, temperature, and chemical processes that may occur side-by-side with fracturing.

The use of the FE method to solve fracture mechanics problems attracted great attention in the early 1970s. However, conventional elements were unable to reproduce an accurate FE solution near the crack tip [Chan et al., 1970]. This was due to the fact that conventional finite elements employ polynomials to interpolate field variables in the domain, and therefore are not able to reproduce the singular crack tip fields. Significant development of the FE analysis of crack problems was made by Barsoum [1976] and Henshell and Shaw [1975] who showed that the singularity at the crack tip can be modeled by placing the mid-side node near the crack tip at the quarter-point position. This shift simply results in a nonlinear mapping between the natural and local coordinate systems in a way that a singular strain at the crack tip occurs, and an inverse square root singularity is modeled throughout the element. The following element types, collapsed quarter-point hexahedrals, quarter-point pentahedrals, and quarter-point bricks, have been widely employed in the last three decades for modeling 3D fractures [Kuna, 2013]. The use of these types of elements relies upon the generation of a fully structured mesh around the 3D crack front, which is a difficult and cumbersome task for complex crack configurations.

There have been three main finite element meshing schemes used for analyzing crack bodies and simulating fracture growth. The first employs pure hexahedral elements to discretize the entire domain. This methodology has been widely accepted and used for simple geometries [Abaqus, 2012]. Hexahedral elements are advantageous because: (i) collapsed quarter-point hexahedrals have proven to accurately reproduce the singular fields near the crack [Hussain et al., 1981; Walters et al., 2005], and (ii) straightforward algorithms such as domain integral methods are available to extract the J-integral and stress intensity factors from the FE solutions by hexahedrals [DeLorenzi, 1982; Bremberg and Faleskog, 2015]. These algorithms neatly represent tubular domains used for energy-based SIF computation. However, this approach requires a fully structured mesh, not only in the neighborhood of the crack front, but also in regions remote from cracks. It is known that meshing an arbitrary crack geometry with hexahedrals is very difficult and cumbersome, and for complex crack and body configurations it may not be feasible.

The second methodology employs a combination of hexahedral and tetrahedral elements. This hybrid methodology is developed to combine the good performance of col-

lapsed quarter-point hexahedral finite elements as well as the efficiency of the tetrahedral elements to mesh complicated geometries. One approach is to discretize the crack region using hexahedra, while tetrahedra are employed to generate an unstructured mesh in the remote regions [Bremberg and Dhondt, 2008, 2009; Bremberg and Faleskog, 2015]. The major drawback is that tie constraints must be used to satisfy the compatibility and equilibrium conditions at the surfaces where tetrahedrals connect to hexahedrals [Bremberg and Dhondt, 2009]. In the other approach, one analysis is performed to model the global structure by tetrahedrals, and then by mapping the FE-solution, a sub-model is generated to solve for the near crack fields using hexahedrals [Schöllmann et al., 2003; Rabold et al., 2013]. This approach is also computationally expensive, as it requires performing two FE analyses in addition to complications which may arise in sub-modeling procedures.

The third methodology is to use pure tetrahedrals in an unstructured mesh to model the entire domain. This methodology has been applied in modeling crack propagation and fragmentation [Paluszny and Zimmerman, 2011; Paluszny et al., 2013]. Meshing procedures using tetrahedra are much simpler, as these elements are best suited to mesh arbitrary domains and complicated geometries automatically. Additionally, adaptive meshing procedures can be applied to discretize the domain efficiently. However, until recently the applicability, efficiency, and accuracy of tetrahedral elements for modeling crack singular fields had not been well investigated in the literature. In addition, existing methods to extract J-integrals and the SIFs using tetrahedral elements are complex and suffer from oscillations [Červenka and Saouma, 1997; Rajaram et al., 2000; Paluszny and Zimmerman, 2011], while others require very fine meshes near the crack front, rely on complicated numerical procedures, and are applied on arbitrary domain shapes and sizes [Okada et al., 2008; Daimon and Okada, 2014].

One of the main applications of numerical modeling of cracks is the simulation of crack growth in solids. Three popular methodologies to simulate crack propagation in solids are erosion element, cohesive elements, and X-FEM. The erosion element algorithm is one of the simplest numerical methodologies to model crack propagation, and is simply based on the deletion of elements. In this method, once a certain damage criterion is met within an element, the stiffness of the element is reduced to model the damaged material [Fan and Fish, 2008; Rabczuk et al., 2010]. This method does not require modeling cracks explicitly, which is a great advantage in terms of computational cost. However, the numerical results from this method exhibit mesh-dependency unless an appropriate energy-based failure criterion is employed [Beissel et al., 1998]. In addition, this method is not able to model the strain singularity at the front of sharp cracks in elastic materials.

Cohesive elements are another attractive tool to model crack growth without modeling the crack singularity [Needleman, 1987; Ortiz, 1988; Ortiz and Pandolfi, 1999]. In this method, once a local failure criterion is met, the separation of finite element boundaries is allowed, and a crack path is generated due to the detachment of elements. One of the main weaknesses of this method is that a non-smooth crack growth path is obtained, since the crack propagation path must conform to the mesh structure. Therefore, the results are vulnerable to mesh-sensitivity, unless very fine meshes are employed [Camacho and Ortiz, 1996]. In fact, the mesh size independent results can be obtained only when the mesh adequately resolves the cohesive zone [Camacho and Ortiz, 1996]. Moreover, since the crack singular fields are not modeled, crack interactions may not be obtained accurately.

The extended finite element method (X-FEM) proposed by Moës et al. [1999] and Sukumar et al. [2000] has recently been a popular tool for modeling crack growth. X-FEM allows one to model the crack independent of mesh by using enrichment functions, which avoids the need for remeshing during crack propagation. The level set method proposed by Osher and Sethian [1988] is also used with X-FEM to simplify the selection of enriched nodes, and the definition of enriched functions. Due to the simplicity of modeling crack propagation by X-FEM, this method has become very popular. In order to maintain the convergence rate of X-FEM with mesh size, a fixed number of elements or elements inside a fixed radius must be supported by the enrichment functions. However, defining enrichment functions for very close cracks may be problematic, and difficulties may arise when cracks interact or intersect.

One of the main difficulties of FEM-based fracture models is the procedure to handle contact between crack faces. Previous work has been mainly limited to the XFEM formulation and two-dimensional cracks [Dolbow et al., 2001; Ribeaucourt et al., 2007; Elguedj et al., 2007; Khoei and Nikbakht, 2007; Liu and Borja, 2008; Béchet et al., 2009; Liu and Borja, 2010; Pierrès et al., 2010; Baietto et al., 2010; Trollé et al., 2012]. Both LATIN, LArge Time INcrement, [Dolbow et al., 2001; Ribeaucourt et al., 2007; Pierrès et al., 2010; Baietto et al., 2010; Trollé et al., 2012] and Newton-Raphson [Elguedj et al., 2007; Khoei and Nikbakht, 2007; Liu and Borja, 2010] iterative strategies have been employed in dealing with the nonlinearity of the contact problem. However, Liu and Borja [2008] demonstrated the superior convergence performance of Newton-Raphson method as compared to the LATIN strategy. These previous work mainly focus on XFEM modeling of two-dimensional cracks and interfaces which are initially closed, yielding a low contact precision model. Moreover, the accuracy of the contact tractions near the crack tip/front has not been investigated. This accuracy directly influences the computation of stress intensity factors when using an

energy-based method such as the interaction integral. The accuracy of the stress intensity factors of cracks under compression has not also been well evaluated in previous work.

This thesis introduces a new finite element framework based on unstructured tetrahedral meshes for simulating three-dimensional elastic fractured media subjected to tensile and compressive mechanical loadings. To this end, three main steps are taken to demonstrate efficiency, reliability and robustness of tetrahedral meshes in analyzing cracks: (i) The applicability and efficiency of quarter-point tetrahedrals in reproducing the strain singularity along the crack front is proven. (ii) Reliable and efficient methods for the computation of crack parameters such as the stress intensity factors and J-integral are introduced. (iii) A robust and efficient contact algorithm for enforcing frictional contact constraints over the crack surfaces is proposed. Numerous numerical examples of penny-shaped and elliptical cracks under extension and compression demonstrate the accuracy and efficiency of the methods developed in this thesis. Recommendations are made for the values of the parameters involved in the proposed numerical procedures. Applications of the proposed numerical methodology in modeling rock hysteresis and crack growth path are also presented.

The structure of this thesis is as follows: Chapter 2 investigates the behavior of quarter-point tetrahedral elements. It is mathematically proven that these elements reproduce the strain singularity along the crack front. The mapping procedures between natural and global coordinates using these elements are also described. Chapter 3 introduces a displacement correlation scheme for the fast and accurate estimation of stress intensity factors. In addition, the efficiency of quarter-point tetrahedrals in reproducing the singularity is demonstrated. Chapter 4 describes a new disk-shaped domain integral approach for computing the J-integral and stress intensity factors from tetrahedral meshes. It also reviews all previous domain integral methods, and compares the results of the disk-shaped domain against classical volumetric domain integral methods. Chapter 5 introduces an effective gap-based augmented Lagrangian method for enforcing the contact constraints between fracture surfaces. Together with an isoparametric discretization of the contact surfaces, the developed algorithm is able to apply contact constraints in high contact precision models such as high density fracture networks. Chapter 6 reports several applications of the numerical developments in this thesis, including the simulation results for crack growth and hysteretic behavior of fractured media. Chapter 7 gives a summary of conclusions, a discussion of contributions, and potential areas for future work. This thesis also includes one appendix in which the analytical formulas on the stress intensity factors of penny-shaped and elliptical cracks in infinite medium are obtained.

Chapter 2

Modeling the stress singularity using quarter-point tetrahedral elements

Contents

2.1 Abstract

This chapter discusses the reproduction of the square root singularity in quarter-point tetrahedral (QPT) finite elements. These elements are simply generated by moving the mid-side nodes near the crack front to the quarter-point position. This creates a nonlinear mapping by which an inverse square root singularity occurs along the crack front. The mappings between natural and global coordinate systems of QPTs are also given in detail. The use of QPTs makes it possible to accurately model the strain singularity in fully unstructured tetrahedral meshes while effectively exploiting the simplicity, and efficiency of meshing schemes by tetrahedra in discretizing complex three-dimensional crack configurations.

2.2 Introduction

Inherent flaws and cracks exist in many materials and structures; as a result, analyzing cracks in bodies has attracted much attention in a variety of fields, including material science, structural engineering, and oil and gas reservoir engineering. In the context of Linear Elastic Fracture Mechanics (LEFM), the accurate computation of stress intensity factors (SIFs) is the first step in analyzing cracked bodies. The SIFs fully characterize the stress state adjacent to the crack, and therefore are the key factors in the accurate estimation of the onset of crack propagation. The SIFs can be calculated analytically or experimentally only for a few simple crack configurations, and the use of numerical techniques such as the finite element (FE) method is unavoidable for more complicated crack problems. The use of the FE method to analyze crack problems, however, involves a major difficulty which lies in capturing the high stress gradient near the crack and accurately reproducing the crack tip singular stress field. This is the reason for conducting numerous investigations in the last four decades on the development of accurate and reliable FE methods to model crack problems.

The use of the FE method to solve crack problems gained great popularity in the early 1970s. Soon after the poor performance of conventional elements in capturing singular stress field adjacent to the crack was identified. This is because the field variables in conventional finite elements are interpolated by polynomials which are not able to reproduce the crack tip singular stress field. Significant contributions were made by Barsoum [1976] and Henshell and Shaw [1975] who independently showed that the singularity at the crack tip can be properly modeled by placing the mid-side node near the crack tip or front at the quarter-point position. Due to a nonlinear mapping, these so-called quarter-point/singular elements reproduce square root stress singularity. The following three types of elements have been studied and used for modeling 3D cracks: collapsed quarter-point hexahedra, quarter-point pentahedrals, and quarter-point bricks. Among these, collapsed quarter-point hexahedra have been very popular for modeling crack problems, for two main reasons: (i) these elements reproduce the singular stress field near the crack accurately. (ii) straightforward algorithms like displacement correlation and domain integral methods have been available for these elements to extract the SIFs from the FE solution. However, the use of these elements requires the generation of a fully structured mesh around the crack front. Generating such meshes in an arbitrary cracked geometry is very difficult and cumbersome, and for complex crack and body configurations it may not be feasible.

These meshing restrictions encouraged researchers to make use of tetrahedra in dealing with crack problems. One proposed methodology is based on the combination of hexahe-

dral and tetrahedral elements. This takes advantage of the good performance of collapsed quarter-point hexahedral elements at the crack front region, and the efficiency of tetrahedral elements for meshing complicated geometries. One approach is to discretize the neighborhood region of the crack by hexahedra, and remote region by tetrahedra [Bremberg and Dhondt, 2008, 2009; Bremberg and Faleskog, 2015]. The major drawback is that either tie constraints or transition pyramid elements are required at the interface region between hexahedral and tetrahedral elements. This is because the node structures of these two types of elements are incompatible at their interface. In another approach, one analysis is performed to model the global structure by tetrahedra, and then by mapping the FE-solution, a submodel is generated to solve for the near-crack fields using hexahedra [Schöllmann et al., 2003; Rabold et al., 2013; Rabold and Kuna, 2014]. This approach is computationally expensive, as it requires performing two FE model analyses, and complications may arise in sub-modeling procedures. All these complications have recently encouraged the use of pure tetrahedra in an unstructured and arbitrary mesh to model the entire cracked body domain. Unlike other types of elements, tetrahedra can be used in a fully unstructured and arbitrary mesh, such as are required to mesh dense three-dimensional fracture patterns. This methodology has been successfully applied in the context of crack propagation [Paluszny and Zimmerman, 2011] as well as fragmentation [Paluszny et al., 2013]. However, the applicability, efficiency, and accuracy of tetrahedral elements for modeling crack singular fields have not been well investigated in the literature.

In order to prove the applicability and reliability of tetrahedral elements in crack problems, two major steps are required. (i) The efficiency of quarter-point tetrahedral elements for reproducing square root stress singularity must be investigated. Unlike other types of quarter-point elements, which have been extensively addressed in the literature (see Section 2.3), no research has evaluated the applicability and efficiency of the quarter-point tetrahedra in reproducing crack front singular stress field. (ii) Accurate, efficient and reliable methods have to be introduced to extract the fracture parameters from the FE solution of tetrahedra. This chapter discusses the behavior of quarter-point tetrahedra in reproducing the square root stress singularity at the crack front. The accurate computation of SIFs from the FE solution of tetrahedra will be addressed in detail in Chapters 3 and 4.

2.3 A review on quarter-point finite elements

Conventional finite elements employ polynomials to interpolate field variables in the FE domain [Zienkiewicz and Taylor, 1989]. Hence, they are not able to reproduce the crack tip square root singular stress field. Without any special formulation for the elements attached to the crack tip, a very fine mesh is required in order to obtain accurate field

variables adjacent to the crack. Poor results of the FE solutions of crack problems by conventional elements were identified in the early 1970s, when many researchers suggested using special element formulations around the crack tip. These investigations mainly focused on the development of special crack tip elements (CTEs) in which the shape functions are able to reproduce the singular fields near the crack tip. These elements were used to discretize the immediate neighborhood of the crack tip, while the remainder of the domain is discretized with the conventional elements. The early development and use of CTEs for SIF computation can be found in [Byskov, 1970; Tracey, 1971, 1974; Benzley, 1974; Akin, 1976]. The following are the major drawbacks that prevented CTEs to be successful: (i) the shape functions of the CTEs and conventional elements are not often compatible, and transition elements must be used to connect CTEs at the crack tip region to the conventional elements at the remote region; (ii) CTE shape functions do not often permit constant strain and rigid body motion modes; (iii) implementation of CTEs in commercial FE codes involves algorithmic peculiarities.

Significant development in the FE analysis of crack problems was made by Barsoum [1976] and Henshell and Shaw [1975] who proposed the idea of quarter-point elements (QPEs). They independently demonstrated that the singularity at the crack tip is properly modeled when the mid-side node near the crack tip is placed at the quarter-point position. This shift simply results in a nonlinear mapping between the natural and global coordinates by which an inverse square root stress singularity is reproduced throughout the element. With the use of QPEs, there was no need to incorporate CTEs into commercial FE codes since the entire domain of the cracked body is modeled with the same element. QPEs are simple in terms of the algorithmic implementation, the continuity of the shape functions between elements is automatically satisfied, and the rigid body motion and constant strains are included in the shape functions. These characteristics caused the QPEs to be extensively studied and used over the past four decades. Generally, the following types of quarter-point elements have been employed for analyzing 2D and 3D crack problems:

(i) Quarter-point eight-noded quadrilateral element (Fig. 2.1a): This element is generated from an isoparametric eight-noded quadrilateral by shifting the mid-side nodes near the crack tip to the quarter-point position. Early investigators of the quarter-point quadrilateral elements showed some deficiencies, attributed to the incorrect assumptions that the rectangular element models the square root singularity only on the element boundaries [Barsoum, 1977], and that the strain energy of this element was incorrectly demonstrated to be unbounded [Hibbitt, 1977]. However, Banks-Sills and Bortman [1984] demonstrated that stresses are square root singular at all rays emanating from the crack tip in a small region adjacent to the crack tip, expanding to the entire element along the element sides.

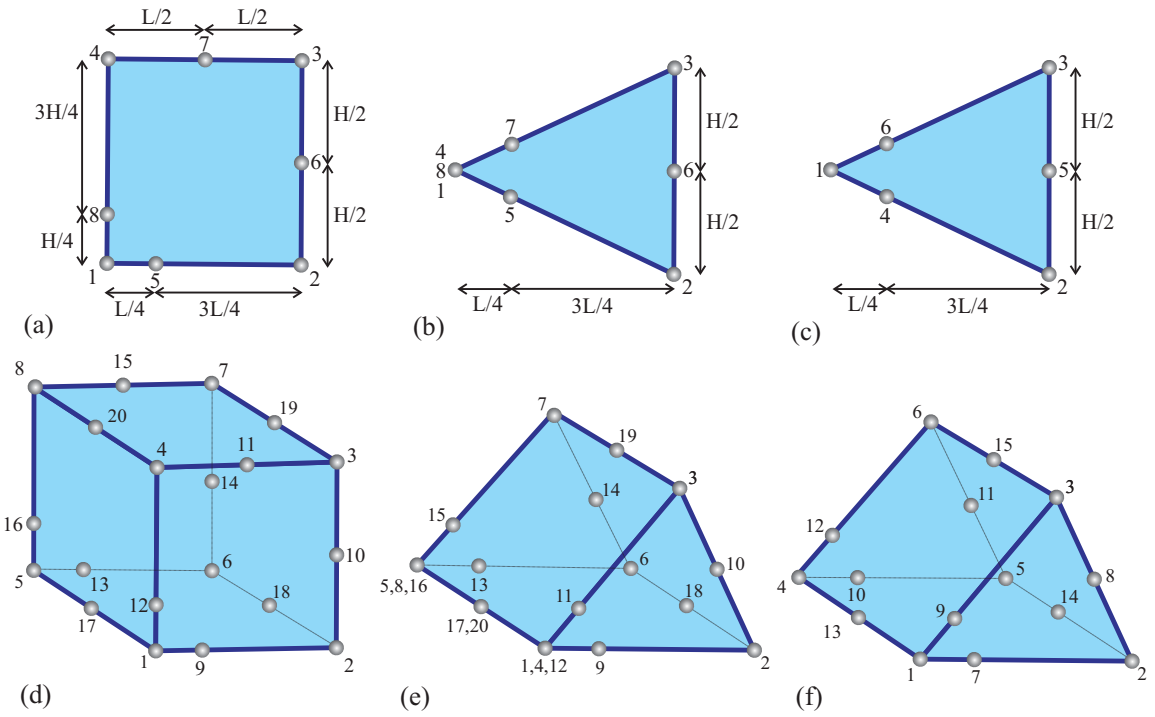

Figure 2.1: (a) Quarter-point eight-noded quadrilateral element, (b) Collapsed quarter-point eight-noded quadrilateral element, (c) Quarter-point six-noded triangular elements (d) Quarter-point twenty-noded brick element (e) Collapsed quarter-point twenty-noded brick element, (f) Quarter-point fifteen-noded pentahedral element.

It was also later proved that the strain energy and element stiffness is bounded in these elements [Banks-Sills and Bortman, 1984]. For accurate results, the distortion of these elements from a rectangle should be minimum [Banks-Sills, 1987]. Since these elements can poorly reproduce the angular distribution of stress due to the large element angle at the crack tip, they are used very rarely and they are discarded in favor of triangular elements (categories ii and iii).

(ii) Collapsed quarter-point eight-noded quadrilateral element (Fig. 2.1b): This element is degenerated by collapsing one side of a 8-noded isoparametric quadrilateral element to a point which is located at the crack tip, and moving the mid-side nodes near the crack tip to the quarter-point position. In LEFM application, the displacements of the nodes on the collapsed side are also coupled, to prevent blunting at the crack tip. This element models the required stress singularity at all rays emanating from the crack tip, and a group of these elements can be crafted in a fan-shape arrangement around the crack tip in order to accurately reproduce the angular variations of the crack tip fields. Any shape of this element may be used as long as the edges are straight lines [Freese and Tracey, 1976; Banks-Sills, 1987]. This element has been frequently used for crack simulations, and has

been implemented in several commercial FE tools [Kuna, 2013].

(iii) Quarter-point six-noded triangular elements (Fig. 2.1c): This element is developed by shifting the mid-side nodes near the crack tip of an isoparametric 6-noded triangular element to the quarter-point position. This QPE also reproduces square root stress singularity at all rays emanating from the crack tip. The shape makes it possible to lay many of these elements around the crack tip to represent the angular distribution of stress around the crack tip. Unlike collapsed quarter-point elements, the edge opposite to the crack tip can be curved in these elements [Freese and Tracey, 1976]. Quarter-point triangular and collapsed quarter-point quadrilateral elements have been shown to be quite similar both analytically and numerically [Freese and Tracey, 1976; Wait, 1978; Lim et al., 1993].

(iv) Quarter-point twenty-noded brick elements (Fig. 2.1d): This element is generated from an isoparametric twenty-noded hexahedral by shifting the mid-side nodes near the crack front to the quarter-point position. Inverse square root singular fields are developed at all rays emanating from of crack front that lie in any cross-sectional orthogonal plane to the crack front. The region in which this singular behavior occurs is a small neighborhood of the crack front for the rays far from the element sides, becoming larger and expanding to the entire element along the element sides [Banks-Sills, 1991]. In the case of curved crack fronts, the mid-side nodes on the surface opposing the crack front must be moved to define a parabolic-cylindrical surface [Banks-Sills, 1991]. Like quarter-point quadrilaterals, these elements are rarely used, because of the poor reproduction of angular distribution of stress due the large element angle at the crack front, and they are discarded in favour of the collapsed hexahedral and pentahedral elements (categories v and vi).

(v) Collapsed quarter-point twenty-noded brick elements (Fig. 2.1e): This element is generated by collapsing one face of 20-noded isoparametric brick element, which gives a wedge-shaped element, and moving the mid-side nodes near the crack to the quarter-point position. The displacements of the conformed nodes on the crack front are also constrained to model the crack sharpness in the LEFM applications [Barsoum, 1976; Koers, 1989]. It reproduces the inverse square root stress singularity along all rays emanating from the crack tip. An accurate angular distribution is reproduced when a group of these elements are arranged around the crack front. In the case of curved crack fronts, the mid-side nodes of the element face opposing the crack front must be moved in a way that a parabolic-cylindrical surface is defined [Hussain et al., 1981; Manu, 1983].

(vi) Quarter-point fifteen-noded pentahedral element (Fig. 2.1f): This element is generated by placing the mid-side nodes near the crack front of an isoparametric fifteen-noded pentahedral at the quarter-point position. This element also reproduces square root stress

singularity at all rays emanating from the crack front and lying in any cross-sectional orthogonal plane to the crack front [Kuna, 2013]. An accurate angular distribution is reproduced by arranging a group of these elements around the crack front in a fan-shaped arrangement. In the case of curved crack fronts the mid-side nodes of the element face opposing the crack must also be moved to define a parabolic-cylindrical surface [Peano and Pasini, 1982].

Transition elements with appropriately placed side-nodes have also been suggested to be used along with the QPEs for more accurate computation of SIFs [Lynn and Ingraffea, 1978]. These elements are placed between the QPEs and the remaining non-singular elements, resulting in more accurate stresses around the crack tip. However, the level of additional accuracy these elements offered was not high enough to make them popular. Various parameters, including the order of integration, element aspect ratio, number of elements surrounding the crack tip, use of transition elements, and the singular element length, may influence the accuracy of the FE results when using QPEs [Ingraffea and Manu, 1980; Saouma and Schwemmer, 1984; Murti and Valliappan, 1986; Jayaswal and Grosse, 1993]. Ease of implementation, computational efficiency and excellent performance are the main advantages of QPEs, which has resulted in their frequent use over the past four decades.

2.4 Finite element formulation of tetrahedral elements

The mapping of the geometry and displacement fields of a ten-noded isoparametric tetrahedral element from the global coordinate system xyz into the natural coordinate system $\xi\eta\zeta$ $(0 \leq \xi, \eta, \zeta \leq 1)$ is given by:

$$\begin{aligned} x(\xi,\eta,\zeta) &= \sum_{i=1}^{10} N_i x_i \ , \ y(\xi,\eta,\zeta) = \sum_{i=1}^{10} N_i y_i \ , \ z(\xi,\eta,\zeta) = \sum_{i=1}^{10} N_i z_i \\ u(\xi,\eta,\zeta) &= \sum_{i=1}^{10} N_i u_i \ , \ v(\xi,\eta,\zeta) = \sum_{i=1}^{10} N_i v_i \ , \ w(\xi,\eta,\zeta) = \sum_{i=1}^{10} N_i w_i \end{aligned} \tag{2.1}$$

in which N_i is the shape function corresponding to the node i with coordinates (x_i, y_i, z_i) in the local space, and (u_i, v_i, w_i) are the displacements of the node i in the x, y and z directions, respectively (Fig. 2.2). The shape functions of a ten-noded tetrahedral finite element are given by:

$$\begin{aligned} &N_1 = \lambda(2\lambda - 1) \ , \ N_2 = \xi(2\xi - 1) \ , \ N_3 = \eta(2\eta - 1) \ , \ N_4 = \zeta(2\zeta - 1) \\ &N_5 = 4\lambda\xi \ , \ N_6 = 4\xi\eta \ , \ N_7 = 4\lambda\eta \ , \ N_8 = 4\lambda\zeta \ , \ N_9 = 4\xi\zeta \ , \ N_{10} = 4\eta\zeta \end{aligned} \tag{2.2}$$

where $\lambda = 1 - \xi - \eta - \zeta$. Using the infinitesimal strain theory, the Cauchy strains are

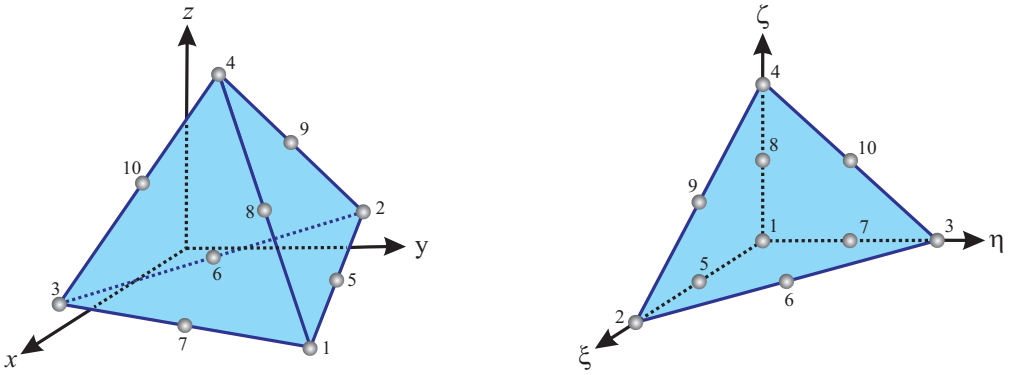

(a) (b)

Figure 2.2: Tetrahedral finite element in (a) local and (b) natural coordinate systems.

obtained from the displacement fields as:

$$\varepsilon = \begin{Bmatrix} \varepsilon_{xx} \\ \varepsilon_{yy} \\ \varepsilon_{zz} \\ \varepsilon_{xy} \\ \varepsilon_{yz} \\ \varepsilon_{xz} \end{Bmatrix} = \begin{Bmatrix} \dfrac{\partial u}{\partial x} \\ \dfrac{\partial v}{\partial y} \\ \dfrac{\partial w}{\partial z} \\ \dfrac{\partial u}{\partial y} + \dfrac{\partial v}{\partial x} \\ \dfrac{\partial w}{\partial y} + \dfrac{\partial v}{\partial z} \\ \dfrac{\partial u}{\partial z} + \dfrac{\partial w}{\partial x} \end{Bmatrix} = \begin{Bmatrix} \dfrac{\partial \mathrm{N}^{\mathrm{T}}}{\partial x}\mathrm{u} \\ \dfrac{\partial \mathrm{N}^{\mathrm{T}}}{\partial y}\mathrm{v} \\ \dfrac{\partial \mathrm{N}^{\mathrm{T}}}{\partial z}\mathrm{w} \\ \dfrac{\partial \mathrm{N}^{\mathrm{T}}}{\partial y}\mathrm{u} + \dfrac{\partial \mathrm{N}^{\mathrm{T}}}{\partial x}\mathrm{v} \\ \dfrac{\partial \mathrm{N}^{\mathrm{T}}}{\partial z}\mathrm{v} + \dfrac{\partial \mathrm{N}^{\mathrm{T}}}{\partial y}\mathrm{w} \\ \dfrac{\partial \mathrm{N}^{\mathrm{T}}}{\partial z}\mathrm{u} + \dfrac{\partial \mathrm{N}^{\mathrm{T}}}{\partial x}\mathrm{w} \end{Bmatrix} \tag{2.3}$$

where $\mathrm{N}^{\mathrm{T}} = \{N_1, ..., N_{10}\}$ is the vector of shape functions, and the vectors $\mathrm{u}^{\mathrm{T}} = \{u_1, ..., u_{10}\}$, $\mathrm{v}^{\mathrm{T}} = \{v_1, ..., v_{10}\}$ and $\mathrm{w}^{\mathrm{T}} = \{w_1, ..., w_{10}\}$ contain the nodal displacements in x, y, and z directions, respectively. The partial derivatives of the shape functions with respect to x, y and z are computed using the so-called Jacobian matrix inverse as follows:

$$\begin{Bmatrix} \dfrac{\partial N_i}{\partial x} \\ \dfrac{\partial N_i}{\partial y} \\ \dfrac{\partial N_i}{\partial z} \end{Bmatrix} = \mathbf{J}^{-1} \begin{Bmatrix} \dfrac{\partial N_i}{\partial \xi} \\ \dfrac{\partial N_i}{\partial \eta} \\ \dfrac{\partial N_i}{\partial \zeta} \end{Bmatrix} \quad , \quad \mathbf{J} = \begin{bmatrix} \dfrac{\partial x}{\partial \xi} & \dfrac{\partial y}{\partial \xi} & \dfrac{\partial z}{\partial \xi} \\ \dfrac{\partial x}{\partial \eta} & \dfrac{\partial y}{\partial \eta} & \dfrac{\partial z}{\partial \eta} \\ \dfrac{\partial x}{\partial \zeta} & \dfrac{\partial y}{\partial \zeta} & \dfrac{\partial z}{\partial \zeta} \end{bmatrix} \tag{2.4}$$

By combining Eqs. (2.3) and (2.4), the vector of strains is given by

$$\varepsilon = \hat{\mathbf{J}}\mathbf{C} \left\{ u_1 \; v_1 \; w_1 \; \ldots \; u_{10} \; v_{10} \; w_{10} \right\}^{\mathrm{T}} \tag{2.5}$$

in which

$$\hat{\mathbf{J}} = \begin{bmatrix} \mathbf{J}_{11}^{-1} & 0 & 0 & \mathbf{J}_{12}^{-1} & 0 & 0 & \mathbf{J}_{13}^{-1} & 0 & 0 \\ 0 & \mathbf{J}_{21}^{-1} & 0 & 0 & \mathbf{J}_{22}^{-1} & 0 & 0 & \mathbf{J}_{23}^{-1} & 0 \\ 0 & 0 & \mathbf{J}_{31}^{-1} & 0 & 0 & \mathbf{J}_{32}^{-1} & 0 & 0 & \mathbf{J}_{33}^{-1} \\ \mathbf{J}_{21}^{-1} & \mathbf{J}_{11}^{-1} & 0 & \mathbf{J}_{22}^{-1} & \mathbf{J}_{12}^{-1} & 0 & \mathbf{J}_{23}^{-1} & \mathbf{J}_{13}^{-1} & 0 \\ 0 & \mathbf{J}_{31}^{-1} & \mathbf{J}_{21}^{-1} & 0 & \mathbf{J}_{32}^{-1} & \mathbf{J}_{22}^{-1} & 0 & \mathbf{J}_{33}^{-1} & \mathbf{J}_{23}^{-1} \\ \mathbf{J}_{31}^{-1} & 0 & \mathbf{J}_{11}^{-1} & \mathbf{J}_{32}^{-1} & 0 & \mathbf{J}_{12}^{-1} & \mathbf{J}_{33}^{-1} & 0 & \mathbf{J}_{13}^{-1} \end{bmatrix}$$

$$\mathbf{C} = \begin{bmatrix} \frac{\partial N_1}{\partial \xi} & 0 & 0 & \cdots & \frac{\partial N_{10}}{\partial \xi} & 0 & 0 \\ 0 & \frac{\partial N_1}{\partial \xi} & 0 & \cdots & 0 & \frac{\partial N_{10}}{\partial \xi} & 0 \\ 0 & 0 & \frac{\partial N_1}{\partial \xi} & \cdots & 0 & 0 & \frac{\partial N_{10}}{\partial \xi} \\ \frac{\partial N_1}{\partial \eta} & 0 & 0 & \cdots & \frac{\partial N_{10}}{\partial \eta} & 0 & 0 \\ 0 & \frac{\partial N_1}{\partial \eta} & 0 & \cdots & 0 & \frac{\partial N_{10}}{\partial \eta} & 0 \\ 0 & 0 & \frac{\partial N_1}{\partial \eta} & \cdots & 0 & 0 & \frac{\partial N_{10}}{\partial \eta} \\ \frac{\partial N_1}{\partial \zeta} & 0 & 0 & \cdots & \frac{\partial N_{10}}{\partial \zeta} & 0 & 0 \\ 0 & \frac{\partial N_1}{\partial \zeta} & 0 & \cdots & 0 & \frac{\partial N_{10}}{\partial \zeta} & 0 \\ 0 & 0 & \frac{\partial N_1}{\partial \zeta} & \cdots & 0 & 0 & \frac{\partial N_{10}}{\partial \zeta} \end{bmatrix} \tag{2.6}$$

In this equation, the so-called $\mathbf{B}$ matrix is written as the multiplication of an extended version of the Jacobian matrix inverse, $\hat{\mathbf{J}}$, by $\mathbf{C}$ which contains the derivatives of shape functions with respect to the natural coordinates ($\mathbf{B} = \hat{\mathbf{J}}\mathbf{C}$). According to Eq. (2.2), the shape functions are in the form of polynomials, and therefore their derivatives with respect to the local coordinates are non-singular. Therefore, as long as the Jacobian matrix determinant is non-zero, the strains are non-singular. The singularity of strains, however, occurs when the determinant of the Jacobian matrix becomes zero. Considering linear elastic behavior, and in the absence of initial strain and initial residual stress, the stress components are determined by $\sigma = \mathbf{D}\varepsilon$, where $\mathbf{D}$ is the elasticity matrix containing the material properties. Using the principle of minimum potential energy or the principle of virtual work, the element stiffness matrix is developed by integration over the element domain V as

$$\mathbf{K}^{\mathrm{e}} = \int_V \mathbf{B}^{\mathrm{T}}\mathbf{D}\mathbf{B}\mathrm{d}V = \int_V \mathbf{C}^{\mathrm{T}}\hat{\mathbf{J}}^{\mathrm{T}}\mathbf{D}\hat{\mathbf{J}}\mathbf{C}\mathrm{d}V \tag{2.7}$$

As the strains near a linear elastic crack front are square root singular, enabling the elements adjacent to the crack front to reproduce a square root strain singularity results in a more accurate finite element solution. In a standard tetrahedral element with straight edges, the components of the Jacobian matrix inverse depend only on the coordinates of the corner nodes. Therefore, the strains and stresses can only vary linearly within these elements. However, a square root singular behavior can be achieved by moving the mid-side nodes near the crack front to the quarter-point position. This shift makes the integrand in

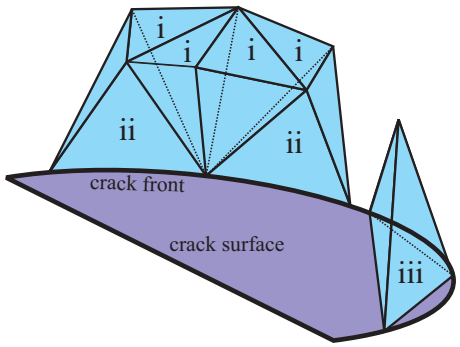

Figure 2.3: Three types of tetrahedral elements generated along the crack front.

the stiffness matrix in Eq. (2.7) a singular function of order 1, as the strain singularity is of order 1/2.

2.5 Quarter-point tetrahedral elements

A fully unstructured mesh of a 3D cracked body mainly generates two types of tetrahedral elements surrounding the crack front: (i) tetrahedra which share a corner node with the crack front; (ii) tetrahedra which share an edge with the crack front (see Fig. 2.3). Accordingly, shifting the mid-side nodes near the crack front to the quarter-point position also generates two types of quarter-point elements: (i) corner-based quarter-point tetrahedra (CQPT); and (ii) edge-based quarter-point tetrahedra (EQPT) as shown in Figs. 2.4a and 2.4b. It is noteworthy that in very coarse meshes and very curved crack fronts, some tetrahedra can share two edges with the crack front (see element iii in Fig. 2.3). Nevertheless, these elements are rarely generated in mesh resolutions which are fine enough to be suitable for the high stress gradients near the crack front. As these elements can barely capture properly the fields variations at the crack front, they must be degenerated into two tetrahedra in case they occur. None of these elements was observed in meshes used in Sections 3.4 and 4.8.

2.5.1 Corner-based quarter-point tetrahedral (CQPT)

Consider the CQPT shown in Fig. 2.4a in which nodes 5, 7 and 8 are moved to the quarter-point position from node 1. Considering a straight-sided tetrahedral, and assuming the corner node i is located at the position (x_i, y_i, z_i), the positions of mid-side and quarter-

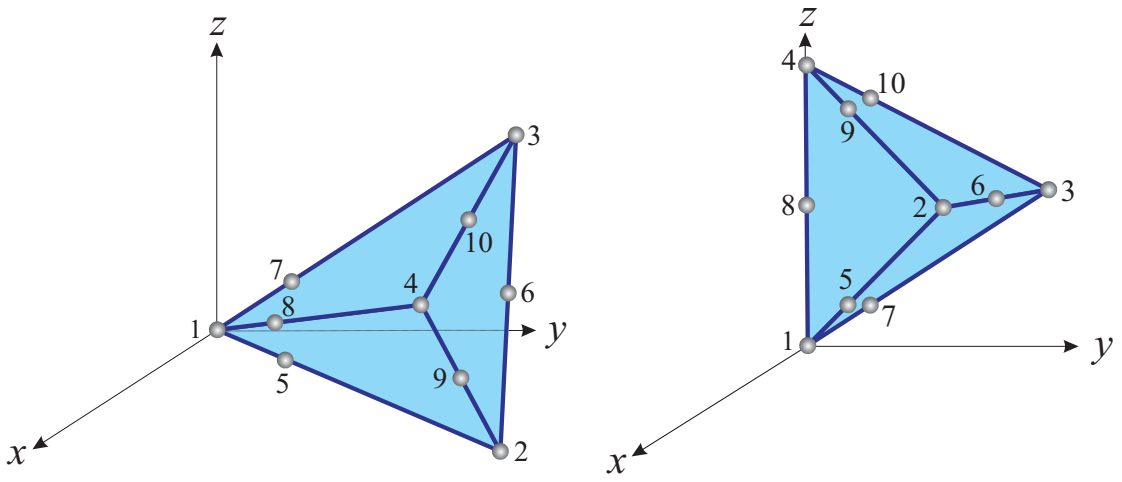

Figure 2.4: Different types of quarter-point tetrahedral finite elements: (a) Corner-based quarter-point tetrahedral (CQPT), (b) Edge-based quarter-point tetrahedral (EQPT).

point nodes are given in terms of the corner nodes coordinates as:

$$\begin{aligned}
&x_5 = (3x_1 + x_2)/4,\ y_5 = (3y_1 + y_2)/4,\ z_5 = (3z_1 + z_2)/4\\
&x_6 = (x_2 + x_3)/2,\quad y_6 = (y_2 + y_3)/2,\quad z_6 = (z_2 + z_3)/2\\
&x_7 = (3x_1 + x_3)/4,\ y_7 = (3y_1 + y_3)/4,\ z_7 = (3z_1 + z_3)/4\\
&x_8 = (3x_1 + x_4)/4,\ y_8 = (3y_1 + y_4)/4,\ z_8 = (3z_1 + z_4)/4\\
&x_9 = (x_2 + x_4)/2,\quad y_9 = (y_2 + y_4)/2,\quad z_9 = (z_2 + z_4/2\\
&x_{10} = (x_3 + x_4)/2,\ y_{10} = (y_3 + y_4)/2,\quad z_{10} = (z_3 + z_4)/2
\end{aligned} \tag{2.8}$$

Assume without loss of generality that the local Cartesian coordinate system xyz is located at node 1 as shown in Fig. 2.4a ($x_1 = y_1 = z_1 = 0$). The mapping between the natural coordinate $\xi\eta\zeta$ and the local coordinate xyz, and the polar distance from the z axis, r, are given as:

$$\begin{aligned}
x &= (\xi + \eta + \zeta)(\xi x_2 + \eta x_3 + \zeta x_4)\\
y &= (\xi + \eta + \zeta)(\xi y_2 + \eta y_3 + \zeta y_4)\\
z &= (\xi + \eta + \zeta)(\xi z_2 + \eta z_3 + \zeta z_4)\\
r &= (\xi + \eta + \zeta)\sqrt{(\xi x_2 + \eta x_3 + \zeta x_4)^2 + (\xi y_2 + \eta y_3 + \zeta y_4)^2}
\end{aligned} \tag{2.9}$$

A ray emanating from node 1 in the plane perpendicular to the crack front ($z = 0$, $y = \rho x$) is mapped into $\eta = \alpha_1 \xi$ and $\zeta = \alpha_2 \xi$ in natural coordinate system, where α_1 and α_2 are functions of nodal coordinates and ρ:

$$\begin{aligned}
\alpha_1 &= \frac{(\rho x_4 - y_4)z_2 + (y_2 - \rho x_2)z_4}{(y_4 - \rho x_4)z_3 + (\rho x_3 - y_3)z_4}\\
\alpha_2 &= \frac{(y_3 - \rho x_3)z_2 + (\rho x_2 - y_2)z_3}{(y_4 - \rho x_4)z_3 + (\rho x_3 - y_3)z_4}
\end{aligned} \tag{2.10}$$

By substituting these relations for η and ζ into Eq. (2.9), the distance from the z axis is given by $r = \gamma_1 \xi^2$, and the Jacobian matrix inverse is developed as:

$$\mathbf{J^{-1}} = \frac{\sqrt{\gamma_1}}{c_1\sqrt{r}} \begin{bmatrix} p_{11} & p_{12} & p_{13} \\ p_{21} & p_{22} & p_{23} \\ p_{31} & p_{32} & p_{33} \end{bmatrix} \tag{2.11}$$

where

$$\begin{aligned}
\gamma_1 &= \frac{|z_2[y_4 - y_3 - \rho(x_4 - x_3)] + z_3[y_2 - y_4 - \rho(x_2 - x_4)] + z_4[y_3 - y_2 - \rho(x_3 - x_2)]|}{[(\rho x_4 - y_4)z_3 + (y_3 - \rho x_3)z_4]^2} \\
&\qquad |x_2(y_3 z_4 - y_4 z_3) + x_3(y_4 z_2 - y_2 z_4) + x_4(y_2 z_3 - y_3 z_2)|\sqrt{1+\rho^2} \\
c_1 &= 2(1 + \alpha_1 + \alpha_2)^2[x_4(y_3 z_2 - y_2 z_3) + x_3(y_2 z_4 - y_4 z_2) + x_2(y_4 z_3 - y_3 z_4)] \\
p_{11} &= y_2(z_3 - z_4) + z_2(y_4 - y_3) + (1 + 2\alpha_1 + 2\alpha_2)(y_4 z_3 - y_3 z_4) \\
p_{21} &= x_2(z_4 - z_3) + z_2(x_3 - x_4) + (1 + 2\alpha_1 + 2\alpha_2)(x_3 z_4 - x_4 z_3) \\
p_{31} &= x_2(y_3 - y_4) + y_2(x_4 - x_3) + (1 + 2\alpha_1 + 2\alpha_2)(x_4 y_3 - x_3 y_4) \\
p_{12} &= \alpha_1 y_3(z_4 - z_2) + \alpha_1 z_3(y_2 - y_4) + (2 + \alpha_1 + 2\alpha_2)(y_2 z_4 - y_4 z_2) \\
p_{22} &= \alpha_1 x_3(z_2 - z_4) + \alpha_1 z_3(x_4 - x_2) + (2 + \alpha_1 + 2\alpha_2)(x_4 z_2 - x_2 z_4) \\
p_{32} &= \alpha_1 x_3(y_4 - y_2) + \alpha_1 y_3(x_2 - x_4) + (2 + \alpha_1 + 2\alpha_2)(x_2 y_4 - x_4 y_2) \\
p_{13} &= \alpha_2 y_4(z_2 - z_3) + \alpha_2 z_4(y_3 - y_2) + (2 + 2\alpha_1 + \alpha_2)(y_3 z_2 - y_2 z_3) \\
p_{23} &= \alpha_2 x_4(z_3 - z_2) + \alpha_2 z_4(x_2 - x_3) + (2 + 2\alpha_1 + \alpha_2)(x_2 z_3 - x_3 z_2) \\
p_{33} &= \alpha_2 x_4(y_2 - y_3) + \alpha_2 y_4(x_3 - x_2) + (2 + 2\alpha_1 + \alpha_2)(x_3 y_2 - x_2 y_3)
\end{aligned} \tag{2.12}$$

As it is seen, all the components of the Jacobian matrix inverse are square root singular. On the other hand, the components of $\mathbf{C}$ in Eq. (2.6) are linearly dependent on the natural coordinates. Along a ray emanating from node 1, these components have the form of either a square root function or a combination of constant and square root functions. As a result, from Eq. (2.5) any component of strain tensor appears as a combination of a singular square root term together with a constant term.

2.5.2 Edge-based quarter-point tetrahedral (EQPT)

This type of element has straight sides when used near straight crack fronts, However, the edge lying on the crack front becomes curved when this type of element is employed along a curved crack front.

EQPT along straight crack front

Consider a EQPT element shown in Fig. 2.4b where side 184 lies along the crack front and nodes 5, 7, 9 and 10 are moved to the quarter-point position. Assuming the corner node i is located at (x_i, y_i, z_i), the mid-side and quarter-point nodes positions are given in terms

of the corner nodes coordinates as:

$$\begin{array}{lll} x_5 = (3x_1 + x_2)/4, & y_5 = (3y_1 + y_2)/4, & z_5 = (3z_1 + z_2)/4 \\ x_6 = (x_2 + x_3)/2, & y_6 = (y_2 + y_3)/2, & z_6 = (z_2 + z_3)/2 \\ x_7 = (3x_1 + x_3)/4, & y_7 = (3y_1 + y_3)/4, & z_7 = (3z_1 + z_3)/4 \\ x_8 = (x_1 + x_4)/2, & y_8 = (y_1 + y_4)/2, & z_8 = (z_1 + z_4)/2 \\ x_9 = (3x_4 + x_2)/4, & y_9 = (3y_4 + y_2)/4, & z_9 = (3z_4 + z_2)/4 \\ x_{10} = (3x_4 + x_3)/4, & y_{10} = (3y_4 + y_3)/4, & z_{10} = (3z_4 + z_3)/4 \end{array} \tag{2.13}$$

Now consider the local Cartesian coordinate system xyz located at node 1 ($x_1 = y_1 = z_1 = 0$) in a way that the straight crack front lies along z axis ($x_4 = y_4 = 0$), as shown in Fig. 2.4b. The mapping between the natural coordinate $\xi\eta\zeta$ and the local coordinate xyz, and also the polar distance from the z axis, r, are given by:

$$\begin{array}{l} x = (\xi + \eta)(\xi x_2 + \eta x_3) \\ y = (\xi + \eta)(\xi y_2 + \eta y_3) \\ z = (\xi + \eta)(\xi z_2 + \eta z_3) + \zeta(1 + \xi + \eta) z_4 \\ r = (\xi + \eta)\sqrt{(\xi x_2 + \eta x_3)^2 + (\xi y_2 + \eta y_3)^2} \end{array} \tag{2.14}$$

Consider a ray emanating from the point $(x, y, z) = (0, 0, d)$ lying on the plane $z = d$ stretching in the direction of $y = \rho x$. This ray is mapped into $\eta = \beta_1 \xi$ and $\zeta = (d + \beta_2 \xi^2)/(z_2 + \beta_3 \xi)$, in which $\beta_1 = -(y_2 - \rho x_2)/(y_3 - \rho x_3)$, $\beta_2 = -(\beta_1 + 1) z_2 - \beta_1(\beta_1 + 1) z_3$ and $\beta_3 = (\beta_1 + 1) z_4$, in the natural coordinate system. By substituting these relations into Eq. (2.14), the polar distance from the z axis is given by $r = \gamma_2 \xi^2$, and the inverse of the Jacobian matrix is developed as:

$$\mathbf{J^{-1}} = \frac{\sqrt{\gamma_2}}{c_2 \sqrt{r}} \begin{bmatrix} q_{11} & q_{12} & \dfrac{f_1 + f_2\sqrt{r} + f_3 r}{h_1 + h_2\sqrt{r} + h_3 r} \\ q_{21} & q_{22} & \dfrac{g_1 + g_2\sqrt{r} + g_3 r}{h_1 + h_2\sqrt{r} + h_3 r} \\ 0 & 0 & \dfrac{c_2\sqrt{r}}{z_4[\gamma_2 + (1 + \beta_1)\sqrt{r}]} \end{bmatrix} \tag{2.15}$$

where γ_2, c_2, q_{ij}, f_i, g_i, and h_i are functions of the nodal coordinates and ρ:

$$
\begin{aligned}
\gamma_2 &= \frac{|(\rho x_2 - y_2 - \rho x_3 + y_3)(x_3 y_2 - x_2 y_3)|}{(\rho x_3 - y_3)^2}\sqrt{1+\rho^2} \\
c_2 &= 2(x_3 y_2 - x_2 y_3)(1+\beta_1)^2 \\
q_{11} &= -y_2 - y_3(1+2\beta_1) \\
q_{21} &= x_2 + x_3(1+2\beta_1) \\
q_{12} &= y_3\beta_1 + y_2(2+\beta_1) \\
q_{22} &= -x_3\beta_1 - x_2(2+\beta_1) \\
f_1 &= d\gamma_2 z_4(y_3 - y_2)(1+\beta_1) \\
f_2 &= 2\sqrt{\gamma_2} z_4(y_3 z_2 - y_2 z_3)(1+\beta_1)^2 \\
f_3 &= z_4(1+\beta_1)\beta_2(y_3 - y_2) + 2(y_3 z_2 - y_2 z_3)(1+\beta_1)^2\beta_3 \\
g_1 &= d\gamma_2 z_4(x_2 - x_3)(1+\beta_1) \\
g_2 &= -2\sqrt{\gamma_2} z_4(x_3 z_2 - x_2 z_3)(1+\beta_1)^2 \\
g_3 &= z_4\beta_2(1+\beta_1)(x_2 - x_3) - 2(x_3 z_2 - x_2 z_3)(1+\beta_1)^2\beta_3 \\
h_1 &= \gamma_2 z_4^2 \\
h_2 &= \sqrt{\gamma_2} z_4(z_4(1+\beta_1) + \beta_3) \\
h_3 &= z_4(1+\beta_1)\beta_3
\end{aligned}
\tag{2.16}
$$

At the region close to the edge 184 ($r \to 0$) the components of the first two rows of Jacobian matrix inverse are square root singular. In addition, the components of $\mathbf{C}$ in Eq. (2.6) are linearly dependent of the natural coordinates. Along a ray emanating from the point $(x, y, z) = (0, 0, d)$ and normal to the edge 184, it was shown that $\eta = \beta_1\xi$ and $\zeta = (d + \beta_2\xi^2)/(z_2 + \beta_3\xi)$. Considering a two term Taylor series for ζ about $\xi = 0$ at the region close to the edge 184, the components of $\mathbf{C}$ take the form of either a square root function or a combination of constant and square root functions. As a result, from Eq. (2.5) any component of strain tensor except ε_{zz} appears as a combination of the dominant terms of a singular square root and a constant. The normal strain along the crack front ε_{zz}, however, appears as a combination of a square root term together with a constant term. It is noteworthy that generally a plane strain condition prevails near the front of an embedded crack, and therefore the strain component ε_{zz} is non-singular.

EQPT along curved crack front

Most 3D embedded cracks have curved crack fronts, and therefore analyzing the performance of quarter-point tetrahedra along curved crack fronts is essential. For simplicity, consider a trirectangular tetrahedral element of the leg length of L, as shown in Fig. 2.5. When this element is used as an EQPT along the curved crack front, edge 184 becomes curved and nodes 5, 7, 9 and 10 are placed at the quarter-point position. The curvature of the crack front is controlled by the position of node 8 with respect to nodes 1 and 4. Let us assume that node 8 is located at $(x_8, y_8, z_8) = (\delta_1, \delta_2, L/2)$. The mapping between the natural

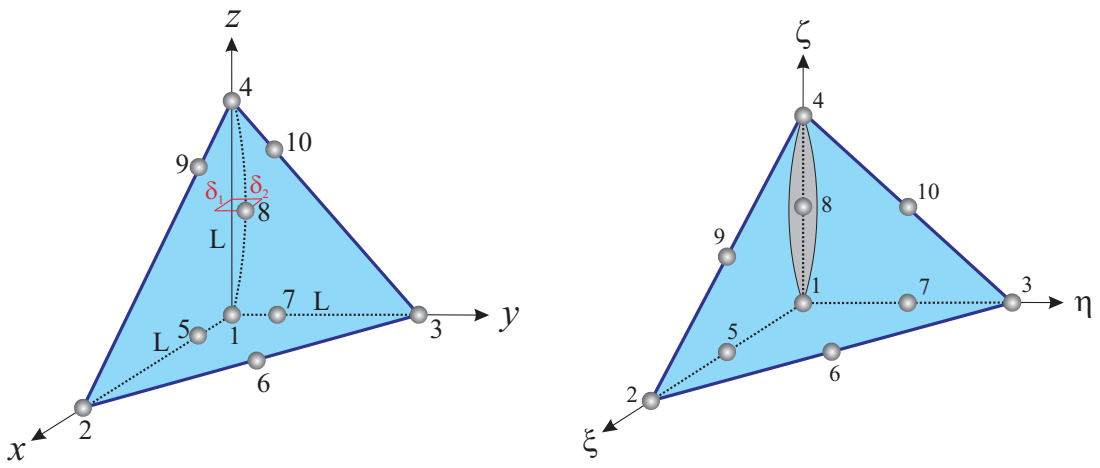

Figure 2.5: Trirectangular EQPT attached to a curved crack front in (a) local and (b) natural coordinate systems.

coordinates $\xi\eta\zeta$ and the local coordinates xyz is given by Eq. (2.17), which results in the formation of Jacobian matrix determinant, or simply called Jacobian, as in Eq. (2.18).

$$\begin{aligned} x &= L\xi(\xi+\eta) - 4\zeta\delta_1(\xi+\eta+\zeta-1) \\ y &= L\eta(\xi+\eta) - 4\zeta\delta_2(\xi+\eta+\zeta-1) \\ z &= L\zeta(1+\xi+\eta) \end{aligned} \tag{2.17}$$

$$|\mathbf{J}| = 2L^2(\xi+\eta)[L(\xi+\eta)(1+\xi+\eta) + 4\zeta(\zeta-1)(\delta_1+\delta_2)] \tag{2.18}$$

As it is seen in Eq. (2.18), the Jacobian vanishes both along the crack front ($\xi+\eta=0$) and on the parabolic cylinder of $\xi+\eta = -1/2+\sqrt{1/4-4\zeta(\zeta-1)(\delta_1+\delta_2)/L}$. The Jacobian also becomes negative in the region enclosed by the crack front and this parabolic cylinder (see Fig. 2.5). If the Jacobian is found to be negative, the mapping for the element is not bijective, indicating that the region of the parent element enclosed by the edge and the parabolic cylinder has been mapped outside the boundary of the real element. The volume of the overlapped region, and therefore the integration error in the element stiffness matrix, depends on the curvature of the element edge, the element size, and the element aspect ratio. As δ_1 and δ_2 approach zero, the parabolic cylinder becomes narrower, and the numerical error decreases. This parabolic-cylindrical region with negative Jacobian also occurs in the quarter-point twenty-noded brick element [Banks-Sills, 1991], collapsed quarter-point twenty-noded brick element [Manu, 1983], and quarter-point fifteen-noded pentahedral element [Peano and Pasini, 1982], if the surface opposing the crack front remains planar. However, moving the mid-side nodes of that face opposing the crack front defines a parabolic-cylindrical surface, which makes the overlapped region near the crack front

vanish. In the case of QPTs, however, there is no element face opposing the crack front elements, and therefore the overlapped region cannot be removed using such a technique. Here it is suggested that the mid-side nodes on the crack front are moved in order to make the EQPTs straight-sided.

2.5.3 Numerical integration in QPTs

Despite the singularity of strains at one node in CQPT and along an edge in EQPT, these elements still satisfy the necessary conditions for finite element convergence [Zienkiewicz and Taylor, 1989]. These conditions include: (1) Inter-element compatibility and continuity are satisfied as the elements are isoparametric. (2) Shape functions accommodate the rigid body motion of the element. (3) Element deformation accommodates a constant strain form. (4) Strain energy in these elements is finite. This implies that although strains are singular at a node or an edge, the components of stiffness matrix in Eq. (2.7) have finite values. However, in order for the FE convergence to occur, the required order of numerical integration in each element has to be met. In the case of standard quadratic tetrahedral, the lower bound for the number of Gauss points is four [Zienkiewicz and Taylor, 1989].

The lower bound for the number of Gauss points must integrate the volume of quarter-point tetrahedra exactly. This is because as the mesh is indefinitely refined, a constant strain and strain energy is approached throughout each element. In quarter-point tetrahedra, the Jacobian determinant is developed as $|\mathbf{J}| = 12V(\xi+\eta+\zeta)^3$ and $|\mathbf{J}| = 12V(\xi+\eta)^2(1+\xi+\eta)$ for CQPT and EQPT, respectively, where V is the element volume. It can be shown that a four-point Gauss rule computes the volume of CQPT with 0.43% error, while it determines the exact volume of EQPT. As the CQPTs exist only in a small region near the crack front, this very small error can be neglected. Moreover, although higher-order integrations compute a more accurate stiffness matrix, they add significantly to the computation cost, while the improvement in the accuracy of the finite element solution might be trivial. In fact, the error in the reduced integration scheme may compensate for the overestimation of the structural stiffness, and some of the more compicated displacement modes show less resistance to deformation. Therefore, a reduced integration by a four-point Gauss rule seems to be suitable for the quarter-point tetrahedra. It is noteworthy that a higher order integration may be required for quarter-point tetrahedra when interface/contact elements are used on the crack surface.

Discretizing the boundary of the domain yields a set of surface elements on external boundaries and crack surfaces. These elements make no stiffness contribution, and are only used to evaluate surface integrals by external or contact tractions. Employing quarter-point tetrahedra introduces quarter-point triangle elements over the crack surfaces (see Fig.

2.7). To compute the vector of nodal forces produced by surface traction, a numerical integration is required, for which the minimum order of integration has to be determined. The lower bound of the order of numerical integration must compute the area of quarter-point triangle elements exactly. Considering the Jacobian determinant for straight-sided quarter-point triangles, it can be shown that a three-point quadrature rule computes the area exactly. A higher order numerical integration improves the accuracy of the values of nodal forces produced by surface tractions. In fact, the numerical integration of order four, which requires six integration points, computes the exact values of nodal forces for a uniform surface traction. However, in this case the improvement in the accuracy of the crack tip fields and SIFs when increasing the order is trivial. Hence, a standard three-point Gauss rule, which is already recommended for standard quadratic triangular elements, is also suggested for quarter-point triangles. It is noteworthy that when a non-uniform surface traction is applied on the crack surfaces, or the quarter-point triangles perform as contact elements, a higher order integration may be necessary.

Although a strain singularity occurs at quarter-point tetrahedra, these elements seem to be less accurate than other types of quarter-point elements shown in Fig. 2.1. Element types collapsed quarter-point hexahedrals and quarter-point pentahedrals are crafted in a fan-shape arrangement around the crack front. Therefore, in addition to reproducing the required strain singularity in their entire domains, they accurately model the angular distributions of crack tip fields. This is not the case for the quarter-point tetrahedra, which are placed randomly around the crack front in arbitrary meshes, and their size and shape are not often controlled. This random arrangement leads to a considerable variation of the size of the QPTs along the crack front. Elements with large angles are also generated that poorly reproduce the angular distribution of the crack tip fields. Therefore, as is shown later in this chapter, although QPTs perform significantly better than the standard tetrahedra, there might still be inaccuracies very close to the crack front. Some strategies, which are presented later in this chapter, can be used to avoid these inaccuracies influencing the SIF results.

2.6 Mapping between natural and global coordinates

The computation of the SIFs from the displacement correlation and disk-shaped domain integral methods in Chapters 3, 4, and 5 requires the computation of the FE field values at a given point inside tetrahedra or triangles. In order to obtain the field values at the given point p, first the tetrahedral or triangular element containing it must be identified through a search algorithm. Then, the natural coordinates of that point inside the element must be determined. This requires explicit relations for the mapping between the natural

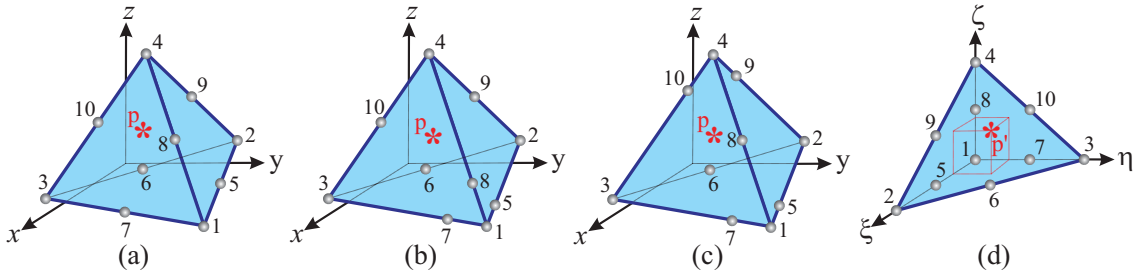

Figure 2.6: Mapping of the point p inside (a) standard quadratic tetrahedral, (b) corner-based quarter-point tetrahedra (CQPT), and (c) edge-based quarter-point tetrahedra (EQPT) from global coordinate system xyz to point p' inside (d) parent tetrahedral element in natural system $\xi\eta\zeta$.

and global coordinates in standard and quarter-point tetrahedra and triangles. Once the natural coordinates are computed from the mapping relations, the fields can then be readily obtained through the shape functions. This section describes in detail the mapping between natural and global coordinates in standard and quarter-point tetrahedra and triangles, and explains the procedure to obtain the field values at a given point in these elements.

2.6.1 Tetrahedral element

Consider a tetrahedral element of any type with straight edges as shown in Fig. 2.6a-c. The corner node i of these elements has the coordinates (x_i, y_i, z_i), and the point p is located at $(x_\mathrm{p}, y_\mathrm{p}, z_\mathrm{p})$ in the coordinate system xyz. The volume of the tetrahedral element V is computed by the determinant given in Eq. (2.19). The volumes of smaller internal tetrahedra which are generated with one face of the main tetrahedral and the point p are also computed from the determinants in Eq. (2.20). The point p is inside the tetrahedral element if all the determinants, or volumes, in Eq. (2.20) are non-negative ($V_i \geq 0$).

$$V = \frac{1}{6}\begin{vmatrix} x_2 & y_2 & z_2 & 1 \\ x_3 & y_3 & z_3 & 1 \\ x_4 & y_4 & z_4 & 1 \\ x_1 & y_1 & z_1 & 1 \end{vmatrix} \tag{2.19}$$

$$\begin{aligned} V_1 &= \frac{1}{6}\begin{vmatrix} x_2 & y_2 & z_2 & 1 \\ x_3 & y_3 & z_3 & 1 \\ x_4 & y_4 & z_4 & 1 \\ x_p & y_p & z_p & 1 \end{vmatrix}, \quad V_2 = \frac{1}{6}\begin{vmatrix} x_p & y_p & z_p & 1 \\ x_3 & y_3 & z_3 & 1 \\ x_4 & y_4 & z_4 & 1 \\ x_1 & y_1 & z_1 & 1 \end{vmatrix}, \\ V_3 &= \frac{1}{6}\begin{vmatrix} x_2 & y_2 & z_2 & 1 \\ x_p & y_p & z_p & 1 \\ x_4 & y_4 & z_4 & 1 \\ x_1 & y_1 & z_1 & 1 \end{vmatrix}, \quad V_4 = \frac{1}{6}\begin{vmatrix} x_2 & y_2 & z_2 & 1 \\ x_3 & y_3 & z_3 & 1 \\ x_p & y_p & z_p & 1 \\ x_1 & y_1 & z_1 & 1 \end{vmatrix} \end{aligned} \tag{2.20}$$

The point p inside any type of tetrahedral element in Fig. 2.6a-c is mapped to the point p' inside the parent tetrahedral element shown in Fig. 2.6d. In the case of standard tetrahedral element in Fig. 2.6a, the global coordinates are mapped linearly into the natural ones through Eq. (2.21). Solving these equations for the natural coordinates gives the coordinates of p' as volume fractions in Eq. (2.22):

$$\begin{aligned} x &= x_1 + (x_2 - x_1)\xi + (x_3 - x_1)\eta + (x_4 - x_1)\zeta \\ y &= y_1 + (y_2 - y_1)\xi + (y_3 - y_1)\eta + (y_4 - y_1)\zeta \\ z &= z_1 + (z_2 - z_1)\xi + (z_3 - z_1)\eta + (z_4 - z_1)\zeta \end{aligned} \tag{2.21}$$

$$\xi_{p'} = \frac{V_2}{V} \quad , \quad \eta_{p'} = \frac{V_3}{V} \quad , \quad \zeta_{p'} = \frac{V_4}{V} \tag{2.22}$$

In the case of quarter-point tetrahedra, however, careful attention is required, as the mapping is not linear, and the volume fractions in Eq. (2.22) are no longer valid for the computation of the natural coordinates. In addition, these types of elements have specific orientations, which need to be taken into account. Assume the orientations shown in Fig. 2.6b,c, which renders the midside nodes 5, 7, and 8 for the CQPT moved to the quarter-point position from node 1, and the nodes and 5, 7, 9, and 10 for the EQPT moved to the quarter-point position from nodes 1 and 4. The mapping functions are developed as Eqs. (2.23) and (2.24) for the CQPT and EQPT, respectively. Solving these equations for non-negative natural coordinates, and simplifying the resulting algebraic equations give the natural coordinates of p' for CQPT and EQPT through Eqs. (2.25) and (2.26), respectively.

$$\begin{aligned} x &= x_1 + (\xi + \eta + \zeta)\big[(x_2 - x_1)\xi + (x_3 - x_1)\eta + (x_4 - x_1)\zeta\big] \\ y &= y_1 + (\xi + \eta + \zeta)\big[(y_2 - y_1)\xi + (y_3 - y_1)\eta + (y_4 - y_1)\zeta\big] \\ z &= z_1 + (\xi + \eta + \zeta)\big[(z_2 - z_1)\xi + (z_3 - z_1)\eta + (z_4 - z_1)\zeta\big] \end{aligned} \tag{2.23}$$

$$\begin{aligned} x &= x_1 + (\xi + \eta)\big[(x_2 - x_1)\xi + (x_3 - x_1)\eta\big] + (x_4 - x_1)(1 + \xi + \eta)\zeta \\ y &= y_1 + (\xi + \eta)\big[(y_2 - y_1)\xi + (y_3 - y_1)\eta\big] + (y_4 - y_1)(1 + \xi + \eta)\zeta \\ z &= z_1 + (\xi + \eta)\big[(z_2 - z_1)\xi + (z_3 - z_1)\eta\big] + (z_4 - z_1)(1 + \xi + \eta)\zeta \end{aligned} \tag{2.24}$$

$$\xi_{p'} = \frac{V_2}{\sqrt{V(V - V_1)}} \quad , \quad \eta_{p'} = \frac{V_3}{\sqrt{V(V - V_1)}} \quad , \quad \zeta_{p'} = \frac{V_4}{\sqrt{V(V - V_1)}} \tag{2.25}$$

$$\xi_{p'} = \frac{V_2}{\sqrt{V(V_2 + V_3)}} \quad , \quad \eta_{p'} = \frac{V_3}{\sqrt{V(V_2 + V_3)}} \quad , \quad \zeta_{p'} = \frac{V_4}{V + \sqrt{V(V_2 + V_3)}} \tag{2.26}$$

Once the natural coordinates are known, the displacements of the point p are obtained by interpolating the values of nodal displacements. The displacement gradients and strains are also determined by substituting the natural coordinates in the so-called B matrix. The stress tensor is then computed from the strains using $\sigma = \mathbf{D}\varepsilon$, where $\mathbf{D}$ is the elasticity matrix containing the material properties.

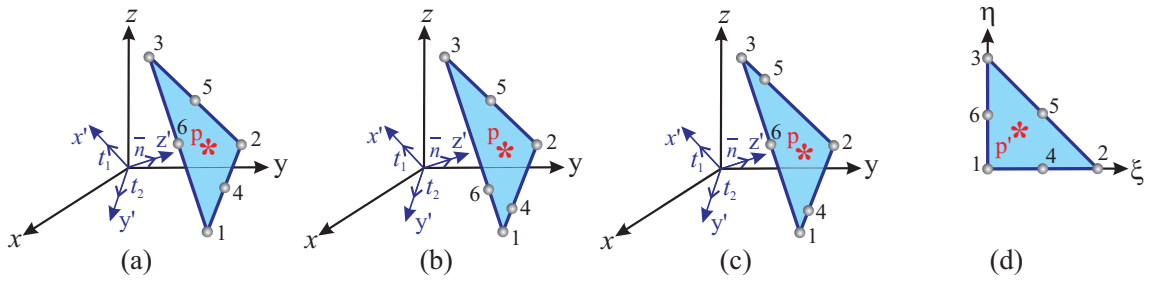

Figure 2.7: Mapping of point p inside (a) standard quadratic triangle, (b) corner-based quarter-point triangle (CQPTr), and (c) edge-based quarter-point triangle (EQPTr) from the global coordinate system xyz to a point p' inside the (d) parent triangle element in the natural coordinate system $\xi\eta$ ($\bar{n} = n/|n|$).

2.6.2 Triangular element

Due to moving of the mid-side nodes to the quarter-point position at the crack front region, two types of quarter-points triangles are also developed at the crack surfaces: corner-based quarter-point triangles (CQPTr) which share one node with the crack front, and edge-based quarter-point triangles (EQPTr) which share one edge with the crack front. Consider a planar triangular element of any type with straight edges on the crack surfaces as shown in Fig. 2.7a-c. The corner node i of these elements has the coordinates (x_i, y_i, z_i), and the point p lies on the crack surface, locating at (x_p, y_p, z_p) in the global coordinate system xyz. The normal vector to these elements ($n = (n_x, n_y, n_z)$) is computed from Eq. (2.27), and the area of the triangular element A is given by the determinant in Eq. (2.28). The area of smaller internal triangles which are generated with one edge of the main triangle and the point p are also computed from the determinants in Eq. (2.29). The point p is inside the triangle element if all determinants in Eq. (2.29) are non-negative ($A_i \geq 0$).

$$n_x = \begin{vmatrix} 1 & 0 & 0 & 0 \\ x_2 & y_2 & z_2 & 1 \\ x_3 & y_3 & z_3 & 1 \\ x_1 & y_1 & z_1 & 1 \end{vmatrix}, \quad n_y = \begin{vmatrix} 0 & 1 & 0 & 0 \\ x_2 & y_2 & z_2 & 1 \\ x_3 & y_3 & z_3 & 1 \\ x_1 & y_1 & z_1 & 1 \end{vmatrix}, \quad n_z = \begin{vmatrix} 0 & 0 & 1 & 0 \\ x_2 & y_2 & z_2 & 1 \\ x_3 & y_3 & z_3 & 1 \\ x_1 & y_1 & z_1 & 1 \end{vmatrix} \tag{2.27}$$

$$A = \frac{1}{2|n|} \begin{vmatrix} n_x & n_y & n_z & 0 \\ x_2 & y_2 & z_2 & 1 \\ x_3 & y_3 & z_3 & 1 \\ x_1 & y_1 & z_1 & 1 \end{vmatrix} \tag{2.28}$$

$$A_1 = \frac{1}{2|n|} \begin{vmatrix} n_x & n_y & n_z & 0 \\ x_2 & y_2 & z_2 & 1 \\ x_3 & y_3 & z_3 & 1 \\ x_p & y_p & z_p & 1 \end{vmatrix}, \quad A_2 = \frac{1}{2|n|} \begin{vmatrix} n_x & n_y & n_z & 0 \\ x_p & y_p & z_p & 1 \\ x_3 & y_3 & z_3 & 1 \\ x_1 & y_1 & z_1 & 1 \end{vmatrix}, \quad A_3 = \frac{1}{2|n|} \begin{vmatrix} n_x & n_y & n_z & 0 \\ x_2 & y_2 & z_2 & 1 \\ x_p & y_p & z_p & 1 \\ x_1 & y_1 & z_1 & 1 \end{vmatrix} \tag{2.29}$$

Using the shape functions of a quadratic triangular element in Eq. (2.30), the point p inside any type of triangular elements in Fig. 2.7a-c is mapped to the point p' inside the parent triangle element shown in Fig. 2.7d ($\lambda = 1 - \xi - \eta$). Consider two arbitrary unit vectors t_1 and t_2 which lie on the plane passing through element face in a way that three vector t_1, t_2, and n build a right-handed Cartesian coordinate system $x'y'z'$ ($n = t_1 \times t_2$). Also consider the vectors $r_p = (x_p, y_p, z_p)$, and $r_i = (x_i, y_i, z_i), i = 1, 2, 3$. The mapping function of a standard triangular element in Fig. 2.7a from $x'y'z'$ space to $\xi\eta$ space is therefore obtained as Eq. (2.31). Solving these equations for the natural coordinates and simplifying the resulting equations using $t_1 \times t_2 = n/|n|$ give the coordinates of p' as the area fractions in Eq. (2.32):

$$\begin{aligned} &N_1 = \lambda(2\lambda - 1)\ ,\ N_2 = \xi(2\xi - 1)\ ,\ N_3 = \eta(2\eta - 1) \\ &N_4 = 4\lambda\xi\ ,\ N_5 = 4\xi\eta\ ,\ N_6 = 4\lambda\eta \end{aligned} \tag{2.30}$$

$$\begin{aligned} x' &= t_1.r_p = t_1.r_1 + t_1.(r_2 - r_1)\xi + t_1.(r_3 - r_1)\eta \\ y' &= t_2.r_p = t_2.r_1 + t_2.(r_2 - r_1)\xi + t_2.(r_3 - r_1)\eta \\ z' &= n.r_p = n.r_1 \end{aligned} \tag{2.31}$$

$$\xi_p = \frac{A_2}{A}\ \ ,\ \ \eta_p = \frac{A_3}{A} \tag{2.32}$$

In the case of quarter-point triangles, special attention is required as the mapping is no longer linear and these elements have specific orientations. Assume the orientations shown in Fig. 2.7b and c, which renders the midside nodes 4 and 6 in the CQPTr are moved to the quarter-point position towards node 1, and nodes 4 and 5 for the EQPTr are moved to the quarter-point positions towards nodes 1 and 3, respectively. Using the shape functions in Eq. (2.30), the mapping functions are developed as Eqs. (2.33) and (2.34) for the CQPTr and EQPTr elements, respectively. Solving these equations for non-negative natural coordinates and simplifying the resulting algebraic equations give the natural coordinates of p' for CQPTr and EQPTr through Eqs. (2.35) and (2.36), respectively.

$$\begin{aligned} x' &= t_1.r_p = t_1.r_1 + \big[t_1.(r_2 - r_1)\xi + t_1.(r_3 - r_1)\eta\big](\xi + \eta) \\ y' &= t_2.r_p = t_2.r_1 + \big[t_2.(r_2 - r_1)\xi + t_2.(r_3 - r_1)\eta\big](\xi + \eta) \\ z' &= n.r_p = n.r_1 \end{aligned} \tag{2.33}$$

$$\begin{aligned} x' &= t_1.r_p = t_1.r_1 + t_1.(r_2 - r_1)\xi^2 + t_1.(r_3 - r_1)(\xi + 1)\eta \\ y' &= t_2.r_p = t_2.r_1 + t_2.(r_2 - r_1)\xi^2 + t_2.(r_3 - r_1)(\xi + 1)\eta \\ z' &= n.r_p = n.r_1 \end{aligned} \tag{2.34}$$

$$\xi_{p'} = \frac{A_2}{\sqrt{A(A_2 + A_3)}}\ \ ,\ \ \eta_{p'} = \frac{A_3}{\sqrt{A(A_2 + A_3)}} \tag{2.35}$$

$$\xi_{p'} = \sqrt{\frac{A_2}{A}}\ \ ,\ \ \eta_{p'} = \frac{A_3}{A + \sqrt{AA_2}} \tag{2.36}$$

Once natural coordinates are known, the displacements of point p are obtained by interpolating the values of nodal displacements using triangle shape functions in Eq. (2.30) and $u = \sum_{i=1}^{6} N_i u_i, v = \sum_{i=1}^{6} N_i v_i, w = \sum_{i=1}^{6} N_i w_i$. Surface tractions are also computed in the same way using the values of tractions at the nodes. The nodal tractions may be known through predefined boundary conditions, or the FE results of a contact treatment on the crack surfaces.

2.7 Conclusions

It is demonstrated that both types of quarter-point tetrahedral elements generated at the crack font can reproduce a square root stress singularity near the crack front. It is also shown that the Jacobian becomes negative in a small region near the curved side of the quarter-point tetrahedra attached to the curved crack fronts. It is therefore suggested to make curve sides straight when using the quarter-point tetrahedra along the curved crack fronts.

Chapter 3

A displacement correlation scheme for the computation of SIFs

Contents

3.1 Abstract

A displacement correlation (DC) scheme is proposed in combination with QPTs to compute stress intensity factors (SIFs) from unstructured meshes. This straightforward method is of computational low cost and easy to implement. The accuracy of the SIFs computed for through-the-thickness, penny, and elliptical crack configurations has been validated by using the available analytical formulations. The average error of the computed SIFs using relatively fine unstructured meshes varies from 1% for the through crack to about 4% for the elliptical crack configurations. The results of an extensive parametric study also suggest

the existence of an optimum mesh-dependent distance from the crack front at which the DC method computes the most accurate SIFs. Overall, numerical results in this chapter confirm that the stress singularity is modeled with good accuracy by using quarter-point tetrahedral finite elements in a fully unstructured tetrahedral mesh.

3.2 Introduction

Chapter 2 discusses how unstructured tetrahedral meshes are effective in analyzing complex three-dimensional cracked bodies due to the simplicity, efficiency and robustness of meshing schemes by tetrahedra. It also describes how quarter-point tetrahedra accurately reproduce the crack front strain singularity. This chapter addresses the second difficulty in using unstructured meshes in fracture mechanics: the accurate computation of SIFs from the FE solution of tetrahedral elements. It is well known that the SIFs fully characterize the stress state adjacent to the crack in the context of Linear Elastic Fracture Mechanics (LEFM), and therefore they are the key factors in the accurate estimation of the onset of brittle crack propagation. Existing methods to extract the SIFs using tetrahedral elements are complex, and often suffer from oscillations [Červenka and Saouma, 1997; Rajaram et al., 2000; Paluszny and Zimmerman, 2011], while others require very fine meshes near the crack front, rely on complicated numerical procedures, and are applied on arbitrary domain shapes and sizes [Okada et al., 2008; Daimon and Okada, 2014]. Therefore, accurate, efficient and reliable methods have yet to be introduced.

Techniques for the SIF computation from FE results generally fall into two categories: energy methods and direct approaches. Energy methods are based on the computation of energy released rate $\mathcal{G}$, and the use of the relationships between $\mathcal{G}$ and the SIFs to compute the SIFs indirectly [Irwin, 1956]. Three main methods have been proposed to compute $\mathcal{G}$ under LEFM assumption: (i) J-integral, which is equivalent to $\mathcal{G}$ for elastic materials, was originally developed as a contour integral around the crack tip [Rice, 1968], and was later transformed into an equivalent domain integral [DeLorenzi, 1982; Li et al., 1985]. (ii) Virtual crack extension (VCE) which was proposed by Parks [1974] and computes the rate of the change in total potential energy for a system for a small virtual extension of the crack. (iii) Virtual crack closure technique, which was originally proposed by Rybicki and Kanninen [1977] and uses Irwin's crack closure integral. Direct approaches, on the other hand, are based on the comparison of FE stress or displacement distribution adjacent to the crack with the stress or displacement field expressions. Stress/displacement extrapolation and correlation are the main approaches in this category.

The direct methods based on displacements have been of more interest due to the fact that the FE displacement fields are the most accurate fields obtained from a FE solution.

This methodology was first developed for a general FE solution of a crack problem without using any crack tip or quarter-point elements around the crack [Chan et al., 1970]. As the FE results for stresses at crack tip are bounded in these solutions, the FE results for displacements are not very accurate close to the crack tip. To avoid these numerical inaccuracies very close the crack tip, Chan et al. [1970] proposed a linear extrapolation scheme. In this approach, the SIFs obtained from displacements at nodes along a ray emanating from the crack tip are extrapolated to the crack tip. The most accurate results were obtained when the extrapolation procedure was based on the displacements on the crack faces. A major drawback of the extrapolation method is that it is based on a relatively arbitrary extrapolation process which can be a source of error in the SIF computation. By the introduction of QPEs, Barsoum [1976] suggested a correlation scheme in which displacements of the quarter-point nodes are fitted to the crack tip displacement expressions. This method, which shall be referred to as displacement correlation (DC), does not require arbitrary extrapolation and computes the SIFs using the displacements of the two quarter-point nodes only, one on the top crack face and the other on the bottom one. Shih et al. [1976] then modified this correlation scheme by correlating the displacement distribution over the entire quarter-point element. This scheme uses the displacements of four nodes of quarter-point elements lying on the crack faces. Ingraffea and Manu [1980] generalized this approach to compute the SIFs for 3D crack configurations using collapsed quarter-point twenty-noded brick elements. The DC method is computationally very cheap and is able to yield very good approximations of the SIFs [Kuna, 2013].

The concept of employing the displacement fields to extract the SIFs has also been widely used in experimental fracture mechanics. Experimental methods such as *moiré* and digital image correlation (DIC) provide the experimental displacement fields around the crack tip [Dally and Riley, 1991; McNeill et al., 1987]. In order to estimate crack parameters from these fields, correlation methods are generally used to fit the local displacement data points to the established crack tip expressions. Some techniques such as the over-deterministic approach, which was originally developed for the experimental estimation of the SIFs [Dally and Riley, 1991], have recently been applied to estimate the 2D crack and sharp notch parameters from the FE displacement solutions [Ayatollahi and Nejati, 2011a,b]. This methodology is called the finite element over-deterministic (FEOD) approach, and is based on a least-squares scheme to fit the displacements of a large number of points near the crack tip to the crack tip field expressions. This simple and straightforward method is able to compute very accurate results, not only for the SIFs, but also the higher-order parameters of the crack tip asymptotic fields. This literature provides evidence of the applicability and efficiency of the near-tip displacement fields for the accurate computation of the SIFs.

The DC approach is conceptually simple and straight-forward, its results can be interpreted easily, and unlike displacement extrapolation, it does not require any arbitrary extrapolation procedure. Unlike energy methods which usually require further integration, which can be a further source of error, the DC method directly use the FE nodal values to obtain the SIFs. Therefore, the level of the accuracy of the SIFs values obtained by this method directly indicates the level of the accuracy of the FE solution around the crack tip. However, the applicability and efficiency of the DC method on unstructured meshes has not previously been investigated. This chapter describes the application of this method on quarter-point tetrahedral elements in an unstructured mesh around the crack front. This is done in order to (i) develop a simple and straightforward method to provide computationally cheap approximations of the SIFs from the unstructured meshes, and (ii) evaluate the accuracy of the quarter-point tetrahedra in reproducing the square root stress singularity near the crack front. As the DC method directly uses the FE fields to estimate the SIFs, the accuracy of fields obtained by the quarter-point tetrahedra can be assessed by investigating the accuracy of SIFs obtained from the DC method. The results presented in this chapter provide evidence on the reliability, efficiency and accuracy of the unstructured meshes by tetrahedral elements for analyzing cracked bodies.

3.3 Displacement correlation method to extract SIFs

Generally, there is no analytical solution for the fields near the crack front of an arbitrary 3D crack configuration. However, it has been shown that asymptotically, as $r \to 0$, a plane strain condition prevails locally, so that the three-dimensional deformation fields approach the two-dimensional plane strain fields [Nakamura and Parks, 1988, 1989]. Therefore, the 2D plane strain fields can be employed to express the stress/displacement fields near any point along the crack front. The so-called Williams series expansions describe the linear elastic stress fields for a 2D cracked plate subjected to an arbitrary load [Williams, 1957]. In the region close to the crack tip, the first terms, which are singular terms, in these expansions are dominant, giving singular stress fields near the crack tip. The stress field near any point on the crack front of 3D embedded cracks is therefore considered to be in

the form of this singular field in the plane strain condition [Anderson, 2005]:

$$\begin{Bmatrix} \sigma_{xx} \\ \sigma_{yy} \\ \sigma_{xy} \\ \sigma_{zz} \end{Bmatrix} = \frac{K_I}{\sqrt{2\pi r}} \begin{Bmatrix} \cos\frac{\theta}{2}\left(1 - \sin\frac{\theta}{2}\sin\frac{3\theta}{2}\right) \\ \cos\frac{\theta}{2}\left(1 + \sin\frac{\theta}{2}\sin\frac{3\theta}{2}\right) \\ \cos\frac{\theta}{2}\sin\frac{\theta}{2}\cos\frac{3\theta}{2} \\ 2\nu\cos\frac{\theta}{2} \end{Bmatrix} + \frac{K_{II}}{\sqrt{2\pi r}} \begin{Bmatrix} \sin\frac{\theta}{2}\left(-2 - \cos\frac{\theta}{2}\cos\frac{3\theta}{2}\right) \\ \sin\frac{\theta}{2}\cos\frac{\theta}{2}\cos\frac{3\theta}{2} \\ \cos\frac{\theta}{2}\left(1 - \sin\frac{\theta}{2}\sin\frac{3\theta}{2}\right) \\ -2\nu\sin\frac{\theta}{2} \end{Bmatrix}$$

$$\begin{Bmatrix} \sigma_{xz} \\ \sigma_{yz} \end{Bmatrix} = \frac{K_{III}}{\sqrt{2\pi r}} \begin{Bmatrix} -\sin\frac{\theta}{2} \\ \cos\frac{\theta}{2} \end{Bmatrix} \tag{3.1}$$

where ν is Poisson's ratio, and r and θ are the polar coordinates in the local Cartesian coordinate system xyz which is perpendicular to the crack front, as shown in Fig. 3.1a. At the meeting point of the crack front and free surfaces, where a plane strain condition is no longer valid, the definition of the stress intensity factor loses its meaning, as the order of singularity at these corners is different from the order of singularity at cracks [Nakamura and Parks, 1988, 1989]. Therefore, the assumption of plane strain conditions is true anywhere on the crack front at which the definition of the SIFs exists. Using Eq. (3.1), the displacement fields adjacent to the crack tip are given as [Anderson, 2005]:

$$\begin{Bmatrix} u \\ v \end{Bmatrix} = \frac{K_I}{2\mu}\sqrt{\frac{r}{2\pi}} \begin{Bmatrix} \cos\frac{\theta}{2}\left(\kappa - 1 + 2\sin^2\frac{\theta}{2}\right) \\ \sin\frac{\theta}{2}\left((\kappa + 1 - 2\cos^2\frac{\theta}{2}\right) \end{Bmatrix} + \frac{K_{II}}{2\mu}\sqrt{\frac{r}{2\pi}} \begin{Bmatrix} \sin\frac{\theta}{2}\left(1 + \kappa + 2\cos^2\frac{\theta}{2}\right) \\ \cos\frac{\theta}{2}\left(1 - \kappa + 2\sin^2\frac{\theta}{2}\right) \end{Bmatrix}$$

$$w = \frac{2K_{III}}{\mu}\sqrt{\frac{r}{2\pi}}\sin\frac{\theta}{2} \tag{3.2}$$

where $\mu = E/2(1+\nu)$ is the shear modulus, E and ν are the Young's modulus and Poisson's ratio, and κ is the Kolosov parameter which is equal to $\kappa = 3 - 4\nu$ in the plane strain condition. Eq. (3.2) characterizes the distribution of the displacements in an orthogonal plane to the crack front ($z = 0$) as shown in Fig. 3.1a. Once the FE analysis is performed, the displacement field over the domain is available, and the displacements near crack front can be employed to compute the SIFs by fitting the local FE displacements to the expressions in Eq. (3.2). The original DC method involves the correlation of the relative FE nodal displacements on the crack faces/surfaces with the crack tip displacement field expressions [Barsoum, 1976; Shih et al., 1976; Ingraffea and Manu, 1980]. The displacements are recommended to be taken from the crack faces, because there: (i) The displacement fields

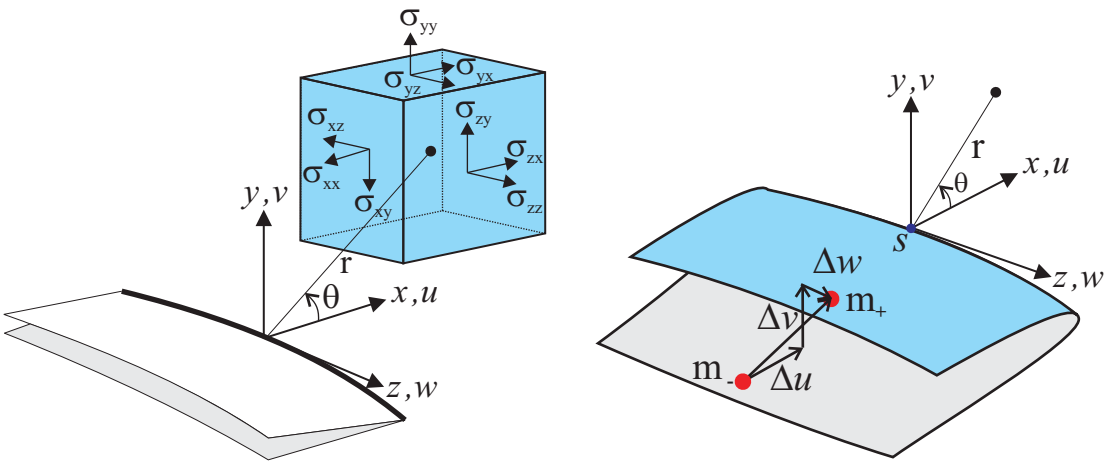

Figure 3.1: (a) Local Cartesian coordinate system at a point along a curved crack front and crack tip stresses, (b) The relative displacements of two matched points lie on top $m_+(r_m, \pi)$ and bottom $m_-(r_m, -\pi)$ surfaces.

corresponding to different crack modes are uncoupled; (ii) The displacement corresponding to each mode has a significant value on the crack surfaces compared to other rays emanating from the crack tip, and therefore the relative numerical error in the displacement value is less on the crack surfaces; (iii) Since the relative displacements of the matched nodes lying on the top and bottom crack surfaces are used, the rigid body translation and rotation of the crack cancels out [Ayatollahi and Nejati, 2011a]. Using Eq. (3.2), the distribution of relative displacements of the top surface ($\theta = \pi$) with respect to the bottom surface ($\theta = -\pi$) e.g. $\Delta u = u_{\theta=\pi} - u_{\theta=-\pi}$, are given by

$$\Delta u = K_{\mathrm{II}}\left(\frac{\kappa+1}{\mu}\right)\sqrt{\frac{r}{2\pi}}\ ,\ \Delta v = K_{\mathrm{I}}\left(\frac{\kappa+1}{\mu}\right)\sqrt{\frac{r}{2\pi}}\ ,\ \Delta w = K_{\mathrm{III}}\left(\frac{4}{\mu}\right)\sqrt{\frac{r}{2\pi}} \tag{3.3}$$

Once the FE solution of the crack problem is performed, the relative displacement of the points over the crack surfaces can be employed in Eq. (3.3) to compute the SIFs. The available displacement correlation schemes, which are based on the use of one of the three types of quarter-point elements described in Section 2.3, correlate the displacement distribution over the entire quarter-point elements in order to estimate the SIFs [Ingraffea and Manu, 1980; Kuna, 2013]. Section 3.3.1 extends this methodology to unstructured tetrahedral meshes, by developing relations to compute the SIFs from the displacement distribution over the entire CQPTs. However, the results from this approach, which are presented and discussed in Section 3.5.2, clearly reveal that the SIF accuracy is influenced significantly by the local mesh size and quality. This seems to be due to displacement inaccuracies resulted from the significant variation of the radial size of the quarter-point elements along the fracture front. Section 3.3.2 proposes a correlation scheme based on the

displacements of matched points at a fixed distance from the crack front (see Fig. 3.1b), which circumvents these numerical inaccuracies influencing the SIF computation. Finally, Section 3.5.2 shows that the SIF results from this correlation scheme are not dependent on the quality of the mesh near the crack front.

3.3.1 Displacement correlation over entire quarter-point tetrahedra

Quarter-point tetrahedral elements generate two types of triangular elements over the crack surfaces: (i) when a CQPT shares a face with the crack surface, a corner-based quarter-point triangular (CQPTr) element is generated which shares only one node with the crack front; (ii) when a EQPT shares a face with the crack surface, an edge-based quarter-point triangle (EQPTr) is developed, which shares three nodes with the crack front. Since the square root singularity occurs in the entire domain of the CQPTs, the displacement representation of these elements is employed here for the SIF computation. However, the same approach can be applied to approximate the SIFs from the displacement field in the EQPTs. Assume that the element face $\zeta = 0$ of a CQPT is one of the corner-based quarter-point triangles shown in Fig. 3.2. By using Eq. (2.1), the distribution of displacement component u, which is along the x axis in the local coordinate system xyz, is given by $u = N_1u_1 + N_2u_2 + N_3u_3 + N_5u_5 + N_6u_6 + N_7u_7$. Assume that the ray normal to the crack front, OP in Fig. 3.2, is defined by the natural coordinate $0 \leq \psi \leq 1$ in such a way that $\psi = 0$ and $\psi = 1$ represents points O and P, respectively. Along this line, the natural coordinates ξ and η are $\xi = \xi_p\psi$ and $\eta = \eta_p\psi$ where (ξ_p, η_p,0) represents the coordinate of the point P in the natural coordinate system $\xi\eta\zeta$. Using Eq. (2.2), the relative displacement along the ray OP with respect to crack tip displacement is written as:

$$u = \Big(\xi_p(4u_5 - u_2) + \eta_p(4u_7 - u_3)\Big)\psi + 2\Big(\xi_p(u_2 - 2u_5) + \eta_p(u_3 - 2u_7) + 2\xi_p\eta_p(u_6 - u_5 - u_7)\Big)\psi^2 \tag{3.4}$$

Employing Eqs. (2.1) and (2.2), the distance of any point lying on OP from the crack tip is obtained from $r = L_p\psi^2$, where $L_p = \sqrt{(\xi_p x_2 + \eta_p x_3)^2 + (\xi_p y_2 + \eta_p y_3)^2 + (\xi_p z_2 + \eta_p z_3)^2}$ is the length of the line OP. The displacement along the ray OP is therefore given by:

$$u = \Big(\xi_p(4u_5 - u_2) + \eta_p(4u_7 - u_3)\Big)\sqrt{\frac{r}{L_p}} + 2\Big(\xi_p(u_2 - 2u_5) + \eta_p(u_3 - 2u_7) + 2\xi_p\eta_p(u_6 - u_5 - u_7)\Big)\frac{r}{L_p} \tag{3.5}$$

In the special case when $\xi_p = 1$ or $\eta_p = 1$, one of the sides of triangle is normal to the crack front. The displacement is then given by $u = (4u_5 - u_2)\sqrt{r/L_2} + (2u_2 - 4u_5)r/L_2$ and $u = (4u_7 - u_3)\sqrt{r/L_3} + (2u_3 - 4u_7)r/L_3$ for $\xi_p = 1$ and $\eta_p = 1$, respectively. Here $L_2 = \sqrt{x_2^2 + y_2^2 + z_2^2}$ and $L_3 = \sqrt{x_3^2 + y_3^2 + z_3^2}$ are the lengths of the element sides on ξ and η axes, respectively. The equation for this special case is similar to the ones reported

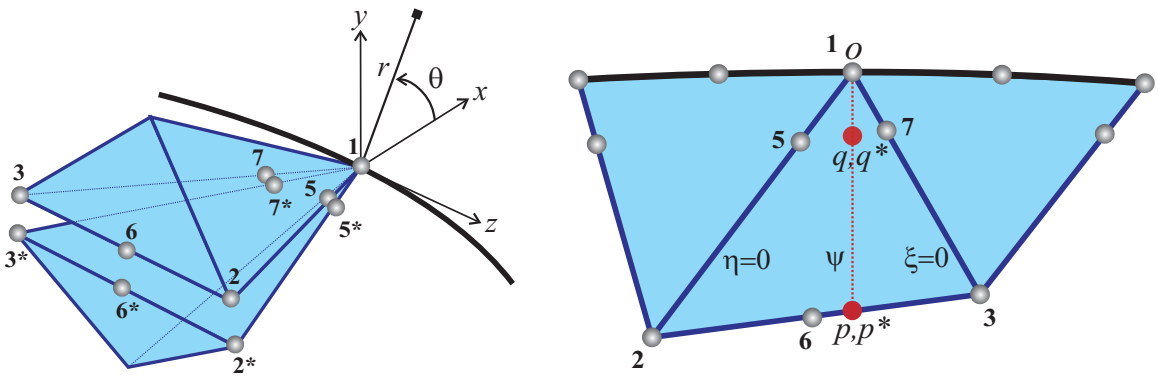

Figure 3.2: Matched triangular elements used to extract the SIFs from CQPTs.

in Shih et al. [1976]; Ingraffea and Manu [1980]. The first term in Eq. (3.5) reproduces the displacement field due to the singular stress field, while the second term represents the displacement due to the constant stress. To compute the coefficients of the singular stress terms, only the first term needs to be considered. One can now write these expressions in terms of the relative displacement of the top surface element with respect to the bottom surface element, and extend these equations to include the displacement variation in y and z directions (v and w) as Eq. (3.6). Equating Eqs. (3.6) and (3.3) gives the SIFs as Eq. (3.7):

$$\begin{aligned}
\Delta u &= \left[\xi_p\Big(4(u_5-u_{5^*})-(u_2-u_{2^*})\Big)+\eta_p\Big(4(u_7-u_{7^*})-(u_3-u_{3^*})\Big)\right]\sqrt{\frac{r}{L_p}}\\
\Delta v &= \left[\xi_p\Big(4(v_5-v_{5^*})-(v_2-v_{2^*})\Big)+\eta_p\Big(4(v_7-v_{7^*})-(v_3-v_{3^*})\Big)\right]\sqrt{\frac{r}{L_p}}\\
\Delta w &= \left[\xi_p\Big(4(w_5-w_{5^*})-(w_2-w_{2^*})\Big)+\eta_p\Big(4(w_7-w_{7^*})-(w_3-w_{3^*})\Big)\right]\sqrt{\frac{r}{L_p}}
\end{aligned} \tag{3.6}$$

$$\begin{aligned}
K_{\mathrm{I}} &= \sqrt{\frac{2\pi}{L}}\left(\frac{\mu}{\kappa+1}\right)\left[\xi_p\Big(4(v_5-v_{5^*})-(v_2-v_{2^*})\Big)+\eta_p\Big(4(v_7-v_{7^*})-(v_3-v_{3^*})\Big)\right]\\
K_{\mathrm{II}} &= \sqrt{\frac{2\pi}{L}}\left(\frac{\mu}{\kappa+1}\right)\left[\xi_p\Big(4(u_5-u_{5^*})-(u_2-u_{2^*})\Big)+\eta_p\Big(4(u_7-u_{7^*})-(u_3-u_{3^*})\Big)\right]\\
K_{\mathrm{III}} &= \sqrt{\frac{2\pi}{L}}\left(\frac{\mu}{4}\right)\left[\xi_p\Big(4(w_5-w_{5^*})-(w_2-w_{2^*})\Big)+\eta_p\Big(4(w_7-w_{7^*})-(w_3-w_{3^*})\Big)\right]
\end{aligned} \tag{3.7}$$

With the presence of symmetry in the geometry and symmetry/antisymmetry in the loading conditions, only one of the crack faces needs to be modeled. In this case $u_{\theta=-\pi} = -u_{\theta=\pi}$, $v_{\theta=-\pi} = -v_{\theta=\pi}$ and $w_{\theta=-\pi} = -w_{\theta=\pi}$, and therefore the SIFs are computed using the displacements of the nodes on the top crack surface as:

$$
\begin{aligned}
K_{\mathrm{I}} &= \sqrt{\frac{2\pi}{L}}\left(\frac{2\mu}{\kappa+1}\right)\Big(\xi_p(4v_5 - v_2) + \eta_p(4v_7 - v_3)\Big) \\
K_{\mathrm{II}} &= \sqrt{\frac{2\pi}{L}}\left(\frac{2\mu}{\kappa+1}\right)\Big(\xi_p(4u_5 - u_2) + \eta_p(4u_7 - u_3)\Big) \\
K_{\mathrm{III}} &= \sqrt{\frac{2\pi}{L}}\left(\frac{\mu}{2}\right)\Big(\xi_p(4w_5 - w_2) + \eta_p(4w_7 - w_3)\Big)
\end{aligned}
\tag{3.8}
$$

It will be demonstrated in Section 3.5.2 that the results from the relations provided in this section exhibit dependency on the quality of the mesh near the crack front. The reason for such behavior can be attributed to the significant variation of quarter-point tetrahedra along the crack front in a fully unstructured mesh. When a 3D cracked body is discretized using a structured mesh, one of the three types of quarter-point elements described in Section 2.3 is often used at the crack front. Due to the special arrangement of these elements, the radial and angular sizes of the elements are fully controlled. Two lateral sides of the quarter-point elements are also constrained to be perpendicular to the crack front [Ingraffea and Manu, 1980; Kuna, 2013]. In unstructured meshes, however, no constraint is imposed on the radial and angular sizes of quarter-point tetrahedra. Therefore, despite the reproduction of the singularity over the quarter-point tetrahedra, the displacement fields over these elements may not be as accurate as the fields obtained by the other three types of quarter-point elements. This is because the radial size of the quarter-point elements may vary significantly along the fracture front, and the angular dependence of the displacement fields can only be reproduced poorly due to their arbitrary, and often large, angles. The radial and angular distribution of crack tip fields may not therefore be captured very accurately, even though the stress singularity has been reproduced. This inaccuracy may not influence the SIF computation when energy methods such as the J-integral are employed. This is because these methods rely on an integration over a domain, which reduces the influence of local numerical inaccuracies on the SIF computation (see Chapter 4). However, the SIF values may be considerably influenced by local numerical inaccuracies when local displacements are used in a displacement correlation scheme. Therefore, it is expected that a correlation method based on the displacement distribution over the quarter-point tetrahedral elements would be dependent not only on the local mesh size, but also on the quality of mesh near the crack front.

3.3.2 Displacement correlation at a fixed distance

In this section we propose a correlation scheme where the crack tip displacement expressions are correlated with the relative displacements of two matched points located at a fixed distance from the crack front. Assume that two matched points m_+ and m_- located on

the top and bottom surfaces of the crack, and the line connecting these matched points to the point s on the crack front is orthogonal to the crack front. These points have the coordinates (r_m, π) and $(r_m, -\pi)$ in the local coordinate system xyz located at the point s (see Fig. 3.1b). Since these points are located at a fixed distance r_m from the point s, they do not necessarily belong to the quarter-point tetrahedral elements. A search algorithm can find the tetrahedral and triangular elements that contain these points (see Section 2.6). The natural coordinates of these points in their corresponding elements can also be determined by using the relations given in Section 2.6. Once the natural coordinates are obtained, the displacements are readily computed using the shape functions. The relative displacement in the local coordinate system xyz are then given by $\Delta u = u_{m_+} - u_{m_-}$, $\Delta v = v_{m_+} - v_{m_-}$, and $\Delta w = w_{m_+} - w_{m_-}$. Due to the presence of symmetry in the geometry and symmetry/antisymmetry in the loading conditions, only one of the crack faces needs to be modeled. In these cases the crack is deformed under only one of the deformation modes, and the following relations hold: $v_{m_+} = -v_{m_-}$ for pure mode I, $u_{m_+} = -u_{m_-}$ for pure mode II, and $w_{m_+} = -w_{m_-}$ for pure mode III. Therefore, the relative displacement for half-crack models can be obtained by $\Delta u = 2u_{m_+} = -2u_{m_-}$, $\Delta v = 2v_{m_+} = -2v_{m_-}$, and $\Delta w = 2w_{m_+} = -2w_{m_-}$. By correlating the numerical values of the relative displacements with the expressions in Eq. (3.3), the pointwise SIFs at the point s are then computed from:

$$K_{\mathrm{I}} = \sqrt{\frac{2\pi}{r_m}}\left(\frac{\mu}{\kappa+1}\right)\Delta v \;\;,\;\; K_{\mathrm{II}} = \sqrt{\frac{2\pi}{r_m}}\left(\frac{\mu}{\kappa+1}\right)\Delta u \;\;,\;\; K_{\mathrm{III}} = \sqrt{\frac{2\pi}{r_m}}\left(\frac{\mu}{4}\right)\Delta w \qquad (3.9)$$

Unlike the correlation scheme presented in Section 3.3.1, the correlation based on matched points at a fixed distance computes accurate values for the SIFs. This accuracy is not influenced by the mesh structure and quality at the crack front, as long as the point of correlation is far enough from the crack front. The next Section provides numerical results obtained from this correlation scheme, and Section 3.5 discusses the efficiency and accuracy of the method and evaluate the influence of various parameters including the distance of correlation point on the SIF computation accuracy.

3.4 Numerical examples

In order to demonstrate the efficiency and the accuracy of the proposed displacement correlation approach, the SIFs were computed for the following three crack configurations: (i) through-the-thickness crack in a large thin plate with lateral constraint (plane strain condition); (ii) penny-shaped crack embedded in a large cube; and (iii) elliptical crack embedded in a large cube (see Fig. 3.3).

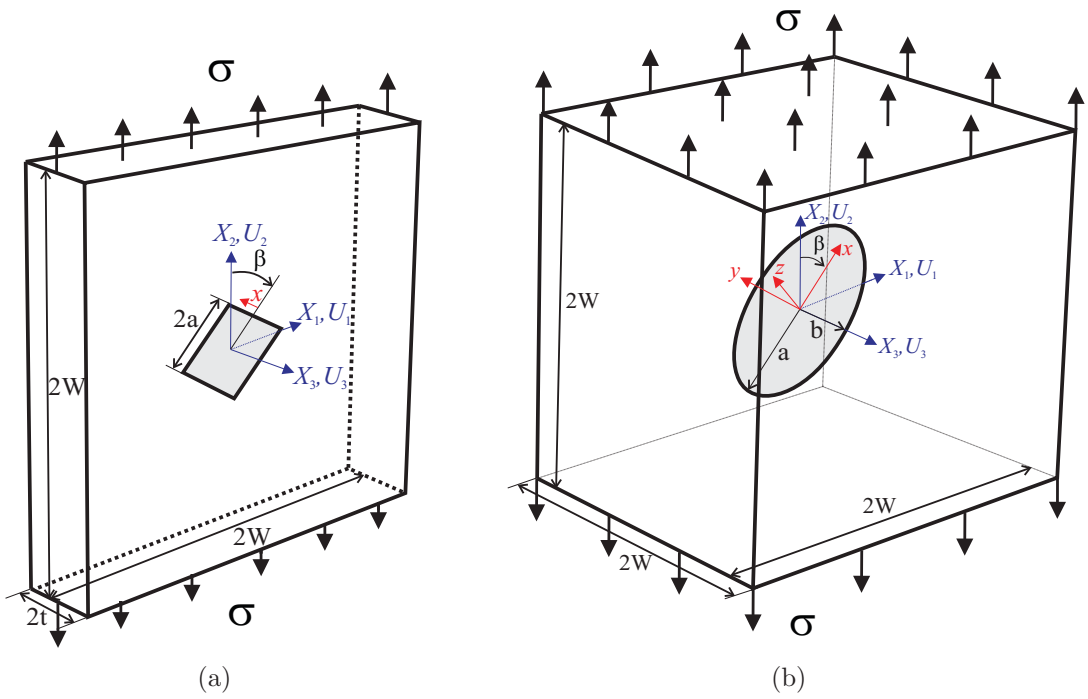

Figure 3.3: Schematics of (a) Through-the-thickness crack in a large thin plate under uniaxial tension; (b) Penny-shaped/elliptical crack embedded in a large cube under uniaxial tension.

3.4.1 Experimental setup

All the cracked bodies are subjected to a uniform uniaxial tension in the X_2 direction over the top and bottom surfaces. The cracks lie in the plane $X_2 = X_1 \cot \beta$ which makes an angle β with the direction of the applied load. A horizontal crack configuration ($\beta = 90°$) produces pure mode I crack deformation, while the inclined one ($0° < \beta < 90°$) creates a mixed-mode condition. In these configurations a denotes half of the crack length for the through crack, crack radius for the penny-shaped crack, and semi-major axis for the elliptical crack. The semi-minor axis b of the elliptical crack is perpendicular to the X_1X_2 plane. A crack length to body width ratio of $a/w = 0.1$ was considered for all the cracked bodies. Crack length to plate thickness ratio of $a/t = 1$ was also considered for the through-the-thickness crack configuration. As the fracture parameters of these crack configurations are independent of the value of Young's modulus, the arbitrary value of $E = 1\,\text{GPa}$ was used in all models. This is not the case for Poisson's ratio since the modes II and III SIFs of embedded cracks depend strongly on the value of this parameter (see analytical solutions in Appendix). A Poisson's ratio of $\nu = 0.3$ was used for all the crack simulations except the ones in Section 3.5.4. Note that the Young's modulus of $E = 0$ is considered for triangles in the model since they do not contribute to the stiffness matrix.

Boundary conditions

Due to the symmetry in geometry and loading conditions, only one-eighth ($X_1 > 0, X_2 > 0, X_3 < 0$) and one-half ($X_3 < 0$) of the cracked bodies were modeled for pure mode I ($\beta = 90°$) and mixed-mode ($\beta = 45°$) conditions, respectively. The following boundary conditions were applied for mode I models: $U_1 = 0$ over the plane $X_1 = 0$, $U_2 = 0$ over the plane $X_2 = 0$ except over the crack surface, $U_3 = 0$ over the plane $X_3 = 0$, and $\sigma = 1\,\text{MPa}$ over the plane $X_2 = W$. The applied boundary conditions for the mixed-mode models are also as follows: $U_1 = 0$ at the point $X_1 = X_2 = -W, X_3 = 0$, $U_2 = 0$ over the plane $X_2 = -W$, $U_3 = 0$ over the plane $X_3 = 0$, and $\sigma = 1\,\text{MPa}$ over the plane $X_2 = W$. For the through-the-thickness crack, the following additional boundary condition was also applied, to ensure zero lateral displacement: $U_3 = 0$ over the plane $X_3 = -t$. This boundary condition imposes a plane strain condition over the cracked plate, where the pointwise SIFs at any point on the crack front follows the solution of the equivalent 2D problem of an inclined central crack in a large plane. This solution gives the SIFs as follows: $K_\text{I} = \sigma\sqrt{\pi a}\sin^2\beta$, $K_\text{II} = \sigma\sqrt{\pi a}\sin\beta\cos\beta$, and $K_\text{III} = 0$. These formulas, along with the analytical solutions for the SIFs of embedded inclined penny-shaped and elliptical cracks in infinite solids given in Appendix, will be used to validate the numerical results.

Mesh

An octree-based mesh generation software was employed to generate arbitrary meshes for all specimens by using 10-noded isoparametric tetrahedral elements. For the elements attached to the crack front, the nodes near the front are moved from the mid-side point to the quarter-point position to produce quarter-point tetrahedral elements. The curved edges on the curved crack fronts were straightened by moving the mid-side nodes of the curved segments. This avoids the Jacobian becoming negative near the crack front (see Section 2.5.2). The refinement of the mesh near the crack front was controlled by assigning the number of segments along the crack front. Consider the crack front of length L_f is discretized by N_f segments. A parameter called the nominal length (size) of the elements in the crack front region can be defined as $L_n = L_f/N_f$. The nominal element length L_n represents the approximate length of the elements sides near the crack front, and therefore gives an approximation for the average size of the quarter-point elements in the crack front region. In all models, the degree of mesh refinement in the crack front region was controlled by keeping the nominal crack front element size about 0.03 of the crack length ($L_n \approx a/33$). Fig. 3.4 shows the finite element mesh of the mixed-mode penny-shaped crack problem together with the local mesh refinements near the crack front in different mixed-mode crack

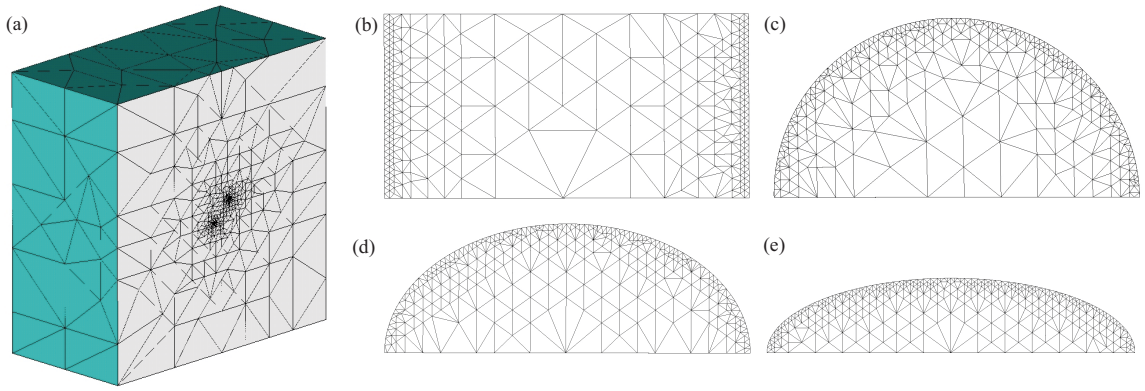

Figure 3.4: (a) Finite element mesh discretizing one-half of an embedded penny-shaped crack (Total number of nodes: 43141, Total number of elements: 32892). Details of mesh in crack-front region for (b) through-the thickness ($L_n/a \approx 0.032$), (c) penny-shaped ($L_n/a \approx 0.030$), (d) elliptical ($b/a = 0.7, L_n/a \approx 0.029$), (e) elliptical ($b/a = 0.4, L_n/a \approx 0.026$) cracks.

configurations. Four- and three-point Gaussian quadrature rules were employed for the numerical integration over tetrahedral and triangular elements, respectively.

3.4.2 Numerical results

The pointwise SIF values were computed at the location of existing crack front nodes using Eq. (3.9) when considering $r_m = 2L_n$. The reason for this choice is discussed in Section 3.5.3. The average numerical error of SIF computation for individual modes e_{i} ($\mathrm{i} = \mathrm{I}, \mathrm{II}, \mathrm{III}$) and average total error e_{t} were then evaluated by using Eq. (3.10). In these expressions K_{i}^A and K_{i}^N are the pointwise analytical and numerical mode i SIFs, respectively, and L_f is the crack front length. Wherever closed-form integration was not possible, the trapezoidal rule has been employed to evaluate the integrals numerically.

$$e_{\mathrm{i}} = \frac{\displaystyle\int_{L_f} |K_{\mathrm{i}}^A - K_{\mathrm{i}}^N| \mathrm{d}l}{\displaystyle\int_{L_f} |K_{\mathrm{i}}^A| \mathrm{d}l} \quad \mathrm{i} = \mathrm{I}, \mathrm{II}, \mathrm{III} \qquad e_{\mathrm{t}} = \frac{\displaystyle\sum_{\mathrm{i}=\mathrm{I}}^{\mathrm{III}} \int_{L_f} |K_{\mathrm{i}}^A - K_{\mathrm{i}}^N| \mathrm{d}l}{\displaystyle\sum_{\mathrm{i}=\mathrm{I}}^{\mathrm{III}} \int_{L_f} |K_{\mathrm{i}}^A| \mathrm{d}l} \tag{3.10}$$

Fig. 3.5 shows the variation of the pointwise mode I stress intensity factor along the crack front of different crack configurations when the cracks are subjected to pure mode I loading condition ($\beta = 90°$). Analytical solutions for a 2D plane strain central crack problem, and for 3D penny-shaped and elliptical cracks embedded in infinite solids (Appendix), are also plotted. The average error e_{I} for these four sets varies from $e_{\mathrm{I}} = 0.009$ in through-the-thickness crack to $e_{\mathrm{I}} = 0.037$ in the elliptical crack with $b/a = 0.4$. Fig. 3.6 also shows the variation of pointwise mixed-mode SIFs along the crack front of four different crack

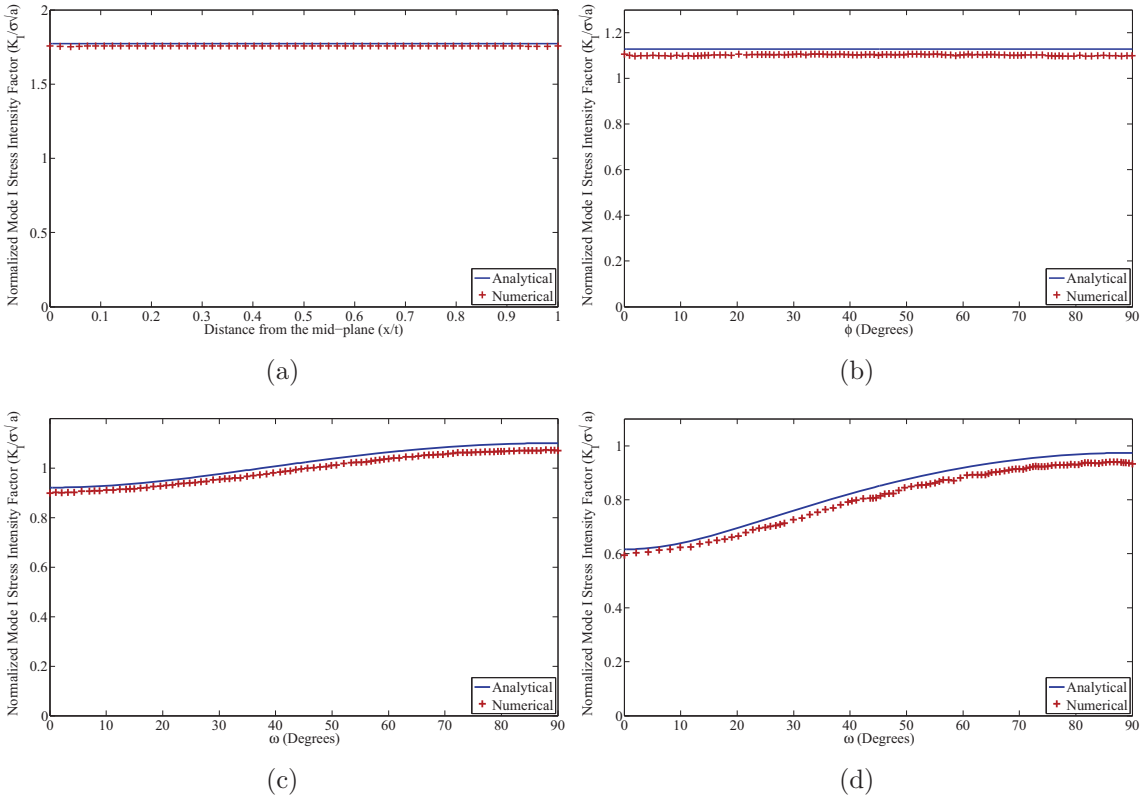

Figure 3.5: The variation of normalized mode I ($\beta = 90°$) analytical and numerical SIFs along the fronts of (a) through-the-thickness ($L_n/a \approx 0.032$), (b) penny-shaped ($L_n/a \approx 0.03$), (c) elliptical ($b/a = 0.7, L_n/a \approx 0.029$), (d) elliptical ($b/a = 0.4, L_n/a \approx 0.024$) cracks. For all cases $r_m = 2L_n$. The mode I average error is as follows: (a) $e_{\mathrm{I}} = 0.009$, (b) $e_{\mathrm{I}} = 0.023$, (c) $e_{\mathrm{I}} = 0.024$, (d) $e_{\mathrm{I}} = 0.037$.

configurations when $\beta = 45°$. The average total error e_{t} varies from $e_{\mathrm{t}} = 0.014$ in through-the-thickness crack to $e_{\mathrm{t}} = 0.039$ in the elliptical crack with $b/a = 0.4$. These results are obtained from the meshes shown in Fig. 3.4, and the use of finer meshes will result in the computation of more accurate SIFs. These results demonstrate the efficiency of the displacement correlation method for computing very good approximations of the SIFs from arbitrary meshes. Section 4.8 discusses the effects of different parameters involved in the DC method on these results.

3.5 Discussion

It was mathematically proven in Section 2.5 that a square root strain singularity is reproduced near the crack front in the quarter-point tetrahedral elements. A displacement correlation scheme was also suggested in Section 3.3.2 for the fast approximation of the SIFs from unstructured meshes. Several numerical tests were then performed using the quarter-point tetrahedra, and the SIFs were computed using the DC approach. This section aims

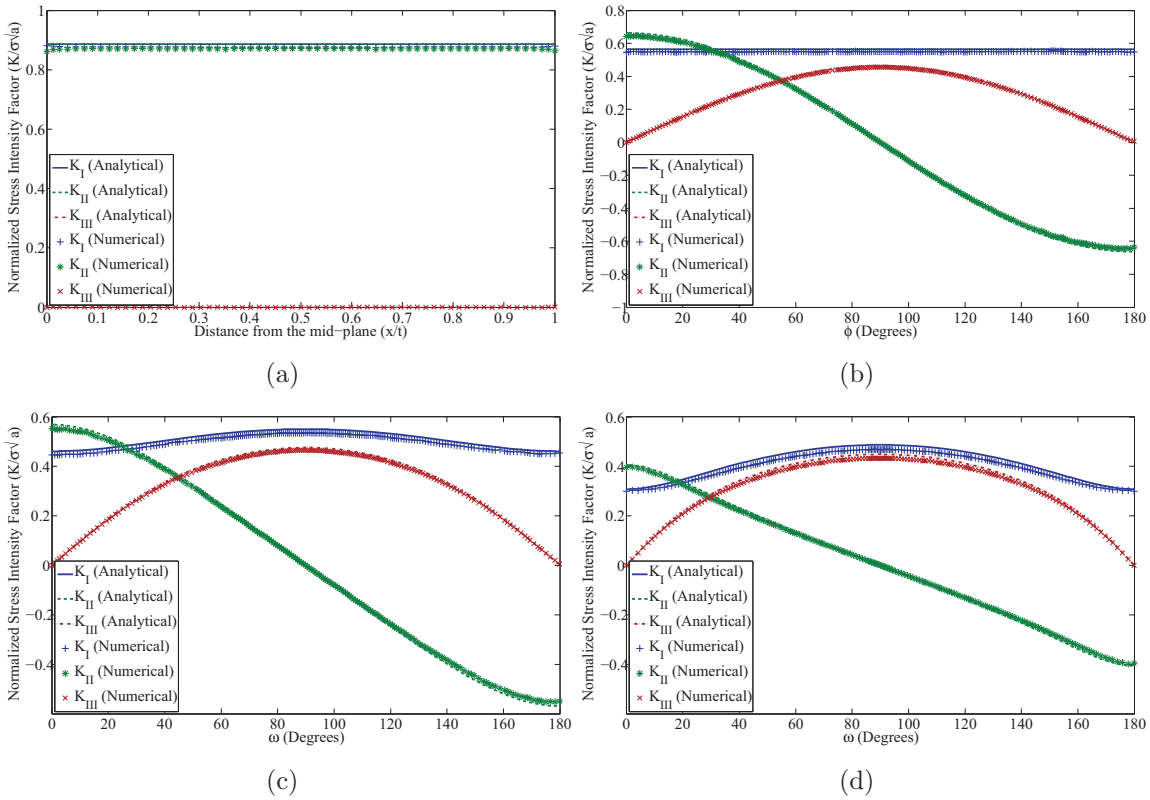

Figure 3.6: The variation of normalized mixed-mode ($\beta = 45°$) analytical and numerical SIFs along the fronts of (a) through-the-thickness, (b) penny-shaped, (c) elliptical ($b/a = 0.7$), (d) elliptical ($b/a = 0.4$) cracks. The meshes are shown in Fig. 3.4. For all cases $r_m = 2L_n$. The average total SIF computation error is as follows: (a) $e_{\mathrm{t}} = 0.014$, (b) $e_{\mathrm{t}} = 0.025$, (c) $e_{\mathrm{t}} = 0.028$, (d) $e_{\mathrm{t}} = 0.039$.

to discuss these numerical results. To this end, first the performance of the quarter-point tetrahedra in reproducing the square root singularity is addressed. Then, the reason for correlating the displacements at points located at a fixed distance from the crack front is explained. The influence of r_m as the main input parameter in the proposed DC method on the accuracy of the SIFs is discussed afterwards. Finally, the influence of Poisson's ratio on the accuracy of DC method and the applicability of the DC method to non-matched crack surface meshes are addressed.

3.5.1 The performance of quarter-point tetrahedra

This section evaluates the performance of quarter-point tetrahedra in reproducing singularity, and compares them with the standard tetrahedra. Consider the penny-shaped crack configuration shown in Fig. 3.3b in a mixed-mode loading condition ($\beta = 45°$), with a crack surface mesh structure shown in Fig. 3.7a. Two points on the crack front are selected, and the normal rays emanating from these points, which also lie on the crack surfaces, are shown in Fig. 3.7a. The relative displacements of the top surface with respect to the bottom sur-

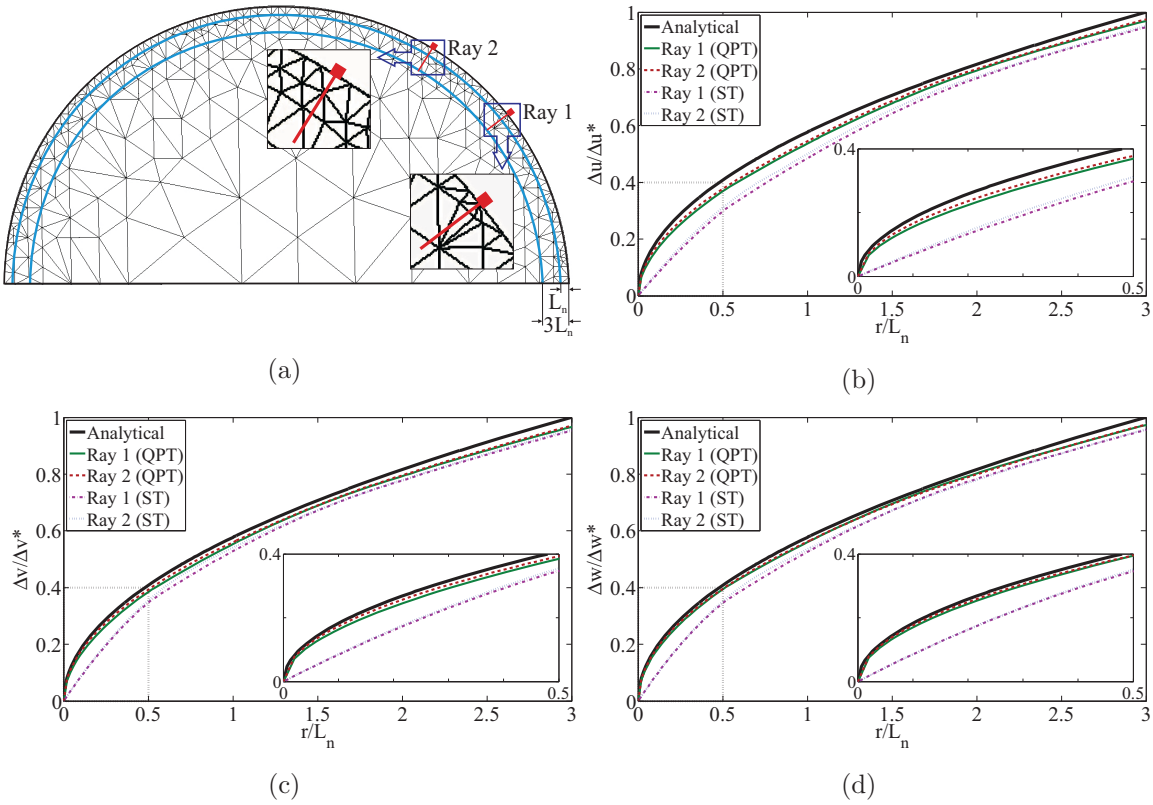

Figure 3.7: (a) The mesh structure on the crack surfaces of a penny-shaped crack under mixed-mode loading condition ($\beta = 45°$, $L_n/a \approx 0.030$). It also shows two normal rays to the crack front which lie on the crack surface and emanate from two arbitrary points. (b,c,d) The variation of normalized relative displacements of the crack surfaces along the two rays against the normalized distance from the crack front. The results are reported for two cases: (QPT) when quarter-point tetrahedra are used at the crack front; and (ST) when standard tetrahedra are employed at the crack front. $\Delta u^* = K_{\rm II}(\kappa+1)\sqrt{3L_n/2\pi}/\mu$, $\Delta v^* = K_{\rm I}(\kappa+1)\sqrt{3L_n/2\pi}/\mu$, $\Delta w^* = 4K_{\rm III}\sqrt{3L_n/2\pi}/\mu$ where $K_{\rm I}$, $K_{\rm II}$, and $K_{\rm III}$ are the analytical values of the SIFs at the corresponding points (see Appendix).

face, i.e. $\Delta u, \Delta v, \Delta w$ shown in Fig. 3.1b, are computed for the points along these rays. These values are then normalized using the analytical values of relative displacements at the points $r = 3L_n$ on each ray ($\Delta u^*, \Delta v^*$, and Δw^*). Figs. 3.7b-d compare the numerical values of these normalized relative displacements along the two rays with the analytical results obtained from Eq. (3.3). The numerical values are reported for two cases: (i) when quarter-point tetrahedra are used at the crack front, where ray 1 and ray 2 pass through a CQPT and an EQPT, respectively, and (ii) when standard tetrahedra are employed at the crack front.

The main features of these plots are as follows: (1) The quarter-point tetrahedra significantly improve the FE displacements near the crack front by reproducing the square root singularity at the crack front. The standard tetrahedra, however, capture poorly the high displacement gradients near the crack front, which results in considerable numerical

error near the crack front. These plots clearly depict the difference between a polynomial interpolation of displacement in standard tetrahedra and a square root one in quarter-point tetrahedra. (2) For either of these element types, the displacement variation near the crack front ($r/L_n < 1.5$) differs slightly from one ray to another. This suggests that the FE results are sensitive to the quality of the elements near the crack front. This mesh sensitivity, however, decays at further points from the crack front, and the displacement variations along all rays match very well. (3) For $r/L_n > 1.5$ an offset is observed between the relative displacements from quarter-point and standard tetrahedra, with the result from quarter-point tetrahedra being more accurate. This suggests that the use of the quarter-point tetrahedra improves not only the near-front fields, but also the displacements far from the crack front. (4) It is seen that the FE results, when using either of the quarter-point element types, start deviating from the analytical values at $r/L_n = 2$. The reason is that the analytical formula in Eq. (3.3) ignores the higher-order terms of the crack tip field expressions, and only considers the displacements generated by the singular stress terms. The FE results, however, capture the effects of higher order terms. Therefore, the points far from the crack front should not be used in a correlation scheme for the SIF computation. The displacement variation along any other ray follows the same behavior. Overall, quarter-point tetrahedra provide much more accurate results compared with standard tetrahedra, and thus, should generally be favoured.

3.5.2 The method of correlation

A similar correlation scheme to the one proposed for collapsed quarter-point hexahedra [Ingraffea and Manu, 1980] was developed for the quarter-point tetrahedra in Section 3.3.1. This scheme uses the displacement distribution over the entire corner-based quarter-point elements. From Eqs. (3.7) and (3.8), it is clear that the correlation is carried out using the displacements at two points: point p located at the intersection of the normal to the crack front and the element edge opposing the crack front, and point q located at the quarter-point position of point p. It is also seen that the displacement of the mid-side node on the edge opposing to the crack front, node 6, cancels out in this formulation. The penny-shaped crack under pure mode I condition ($\beta = 90°$) is now used to compare the SIF results from the two-point correlation scheme with the values obtained from the proposed method based on the correlation at a fixed distance. Fig. 3.8a shows the mesh over the crack surface, where the normals to the crack front at two nodes are drawn, and the points p, q and m on the normal line are marked. The points m are located at fixed distances from the crack front, with $r_m = L_n$ or $r_m = 2L_n$. Fig. 3.8b compares the normalized mode I analytical SIF with the numerical ones obtained from different correlation schemes. Two-point correlation

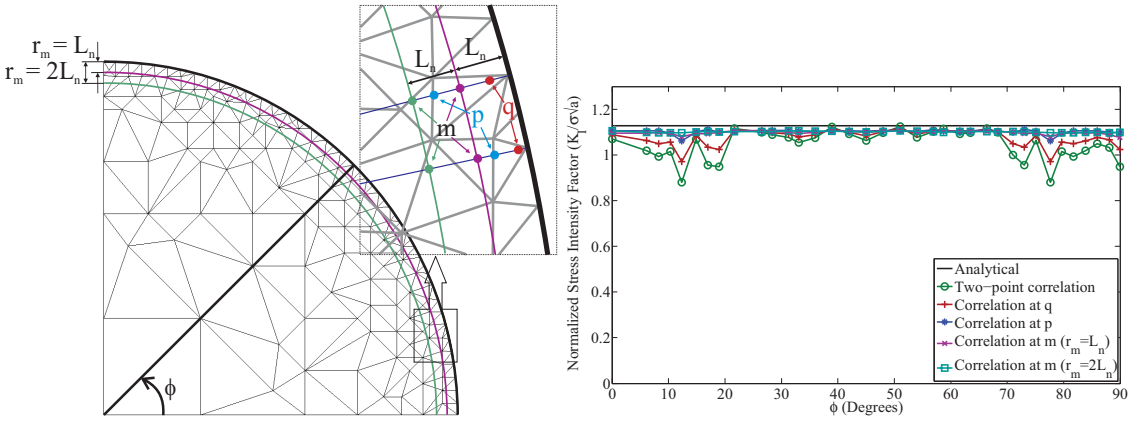

(a) (b)

Figure 3.8: (a) Mesh structure on the crack surfaces of the penny-shaped crack ($L_n/a \approx 0.03$), and the points used in the correlation method, (b) The variation of normalized mode I ($\beta = 90°$) analytical and numerical SIFs along the crack front when different correlation schemes are used.

scheme uses Eq. (3.8) in which the displacements at both points p and q are used in the correlation process. Correlations at p and q employ the displacements at those points, and correlation at m uses the displacements at fixed distances from the crack front.

The following features in this plot are highlighted: (i) The two-point correlation computes the least accurate and the most mesh-sensitive SIFs. Although this scheme gives accurate values at some points on the crack front, considerable fluctuations in the SIFs are seen, especially at the places where the radial size of the quarter-point elements varies significantly (see Fig. 3.8a). The main reason for these fluctuations seems to be the significant variation of the size of quarter-point elements, which influences the accuracy of the displacement fields over these elements. Moreover, the absence of the displacement at node 6 in the formulation of two-point correlation may also influence the accuracy of the results (see Fig. 3.2 and Eq. (3.8)). (ii) The results for the correlation at only one point p or q are more accurate than the two-point correlation scheme, with the results for point p being considerably more accurate than the ones for the point q. This is mainly because the relative numerical error is usually higher for the point closer to the crack front. However, slight fluctuations are still visible in the variation of the SIFs even when using correlation at the point p. (iii) The fluctuations decay considerably when correlating the displacement at point m ($r_m = L_n$), giving more accurate results for the SIFs throughout the entire crack front. When further points from the crack front are used ($r_m = 2L_n$), the fluctuations disappear completely, and the SIFs are no longer sensitive to mesh quality at the crack front elements. The same behavior is seen in other crack configurations and loading conditions. Overall, these results suggest that the two-point correlation scheme based the displacement distribution over the entire quarter-point tetrahedral element exhibits sensitivity to the

quality of mesh near crack front, whereas a simple one-point correlation at a fixed distance from the crack front is able to provide accurate SIFs, exhibiting no sensitivity to the quality of quarter-point tetrahedra as long as the correlation points are far enough from the crack front.

3.5.3 The distance of the point of correlation from the crack front (r_m)

The main parameter in the proposed DC method is the distance of the correlation point from the crack front (r_m). On the one hand, r_m must be small enough compared to the crack size so that the point of correlation remains in the singular dominant region, where a plane strain condition prevails. Moreover, higher-order terms influence the crack tip displacement fields significantly at the region far from the crack front, which is another reason why one should avoid using points at that region. On the other hand, r_m must be large enough to avoid high numerical errors and displacement inaccuracies in the region very close to the crack front due to the complex singular stress state there. The relative numerical error is also much higher as the displacements assign smaller magnitudes there. Therefore, the use of the points very close to the crack tip is also problematic. The accuracy of the near front FE fields depends considerably on the mesh refinement in that region. Therefore, for each mesh resolution, there must be an optimum value for the r_m at which the computed fracture parameters are most accurate. As the degree of the accuracy of the fields near the crack depends on the type and refinement of the elements in that region, it is expected that the optimum r_m depends mainly on the type and size of the elements in the crack front region. In an arbitrary mesh around the crack front, the size of the elements may vary significantly, and therefore an approximate (nominal) value shall be used to represent the average size of the elements. The nominal crack front element size can be defined as $L_n = L_f/N_f$ where L_f and N_f are the length of the crack front and number of segments used to discretize it, respectively.

In order to evaluate the idea of the presence of an optimum r_m, an extensive parametric study was carried out to relate the SIF computation error to r_m in different mesh refinements. The SIFs of the different crack configurations were computed while the points of correlation moved further away from crack front in different mesh densities. Fig. 3.8 shows the variation of the total SIF computation error e_{t}, computed from Eq. (3.10), versus the normalized distance of the correlation point from the crack front, r_m/L_n, for different mesh refinements expanding from coarse meshes $a/L_n \approx 10$ to fine meshes $a/L_n \approx 45$. The main feature of the results in these plots is that for all crack configurations except very coarse meshes, e_{t} slightly drops by increasing r_m, reaching its minimum between $r_m = L_n$ and $r_m = 2L_n$, and then increases gradually for points further from the crack front. The

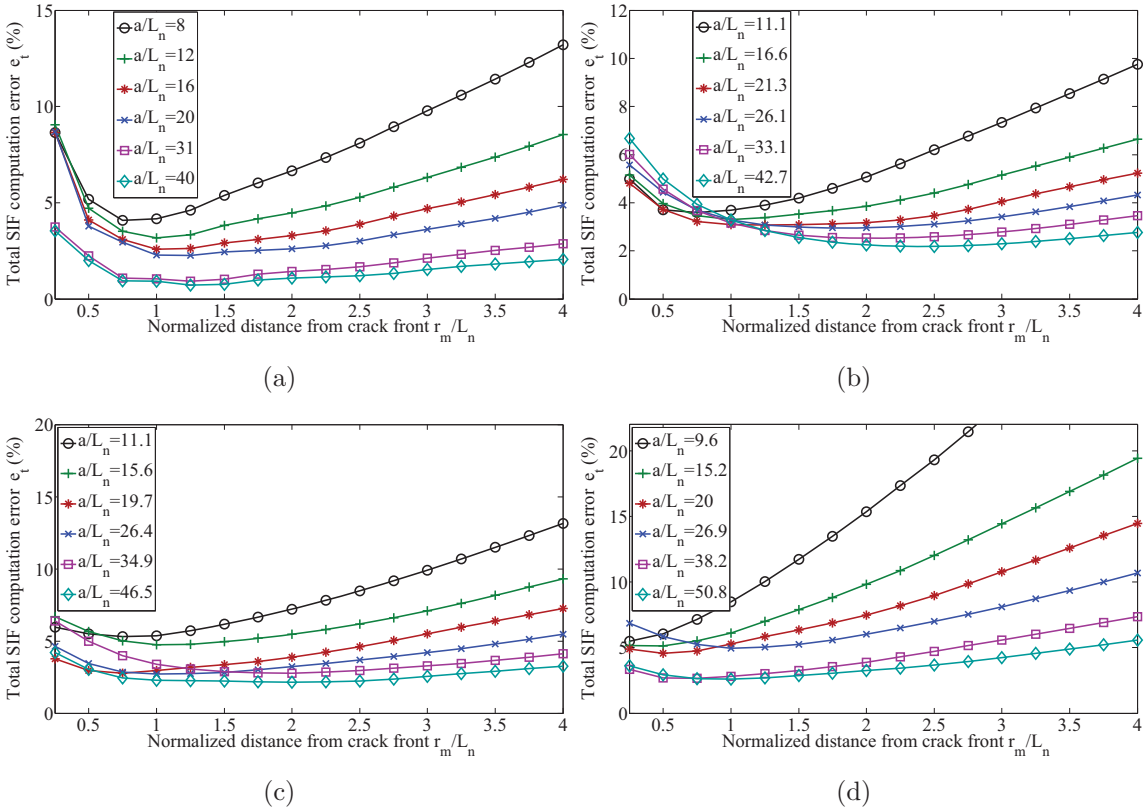

Figure 3.9: Average SIF computation error of the DC method with quarter-point tetrahedral elements. The variation of the total numerical error e_t against the normalized distance from the crack front r_m/L_n for (a) through-the-thickness, (b) penny-shaped, (c) elliptical ($b/a = 0.7$), (d) elliptical ($b/a = 0.4$) cracks in different mesh refinements ($\beta = 45°$).

decreasing trend in the beginning is explained by the fact that high numerical errors and displacement inaccuracies exist near the crack front, generating large relative numerical error due to the small magnitude of the displacements there. By correlating at points further away, this relative numerical error drops, and more accurate SIFs are computed. The growth trend is because the displacements at point far from the crack front is more likely to include the influence of higher order terms, and also due to the fact that the plane strain condition no longer prevails at those points. The plots clearly show that there exists an optimum value of r_m in the range of $L_n \leq r_m \leq 2L_n$ where the SIF computation error hits its minimum. The optimum distance approaches $r_m = L_n$ and $r_m = 2L_n$ for coarse and fine meshes, respectively. A distance of $r_m = 1.5L_n$ can be chosen as the best choice that works for both fine and coarse meshes.

A domain integral approach is introduced in Chapter 4 that computes SIFs with an average error of about 1%. A comparison of the SIF values from DC and domain integral methods indicates that their dependency on the size of quarter-point elements is similar.

Similar to the concept of optimum sampling distance for the DC method, there is an optimum mesh size-dependent domain size for the domain integral method. The only difference is that results from the domain integral method for the through-the-thickness crack show that the error drops slightly from $R_d = 0.5L_n$ to $R_d = 1.5L_n$, at which point it stabilizes (see Fig. 4.14). In contrast, when using the DC method, as seen in Fig. 3.9, the error starts increasing at $r_m = L_n$. The reason for this behavior lies in the main difference between these methods. In the through-the-thickness crack the whole plate is under plane strain, and the 3D solution fields approach the fields obtained from a 2D plane strain crack problem. It is well known that the J-integral exhibits path-independence for a 2D crack problem [Rice, 1968]. Therefore, higher-order terms cannot influence the SIFs obtained from the domain integral method, even when very large domains are employed. This is not the case for the DC method, where the effect of higher-order terms are assumed to be negligible in Eq. (3.2), while the higher-order terms may have a significant influence on the FE displacements far from the crack front. Therefore, there is an increasing trend of the SIF error with r_m due to the higher order terms which influence FE displacements far from the crack front. It is noteworthy that, as compared to the DC method, the SIFs obtained using the domain integral approach require less dense meshes.

Fig. 3.10 demonstrates the variation of the total SIF computation error e_{t} versus the normalized distance of the correlation point from the crack front r_m/L_n, when standard tetrahedral elements are employed at the crack front region, instead of quarter-point elements. The following are the main features in these plots: (i) The SIF computation error is significantly higher in these plots compared to the ones in Fig. 3.9, especially at small values of r_m. The errors in these plots are approximately two to three times larger than the errors in Fig. 3.9. This highlights the efficiency of the quarter-point elements in improving the numerical solution of the crack tip fields. It is noteworthy that the results of the domain integral approach in Chapter 4 also demonstrate the significant improvement of the accuracy of the SIFs by quarter-point tetrahedra, reducing the error two to three times as opposed to standard tetrahedra. (ii) Similar trends are observed in these plots as those shown in Fig. 3.9. One important difference is that the errors for points close to crack front are significantly higher than those in Fig. 3.9. This indicates that when standard tetrahedral elements are used, a larger r_m should be preferred to compute accurate SIF values.

3.5.4 Poisson's ratio value

The SIFs obtained from the DC method proposed by Ingraffea and Manu [1980] exhibited dependency on the value of Poisson's ratio. This dependency is justifiable when analyzing

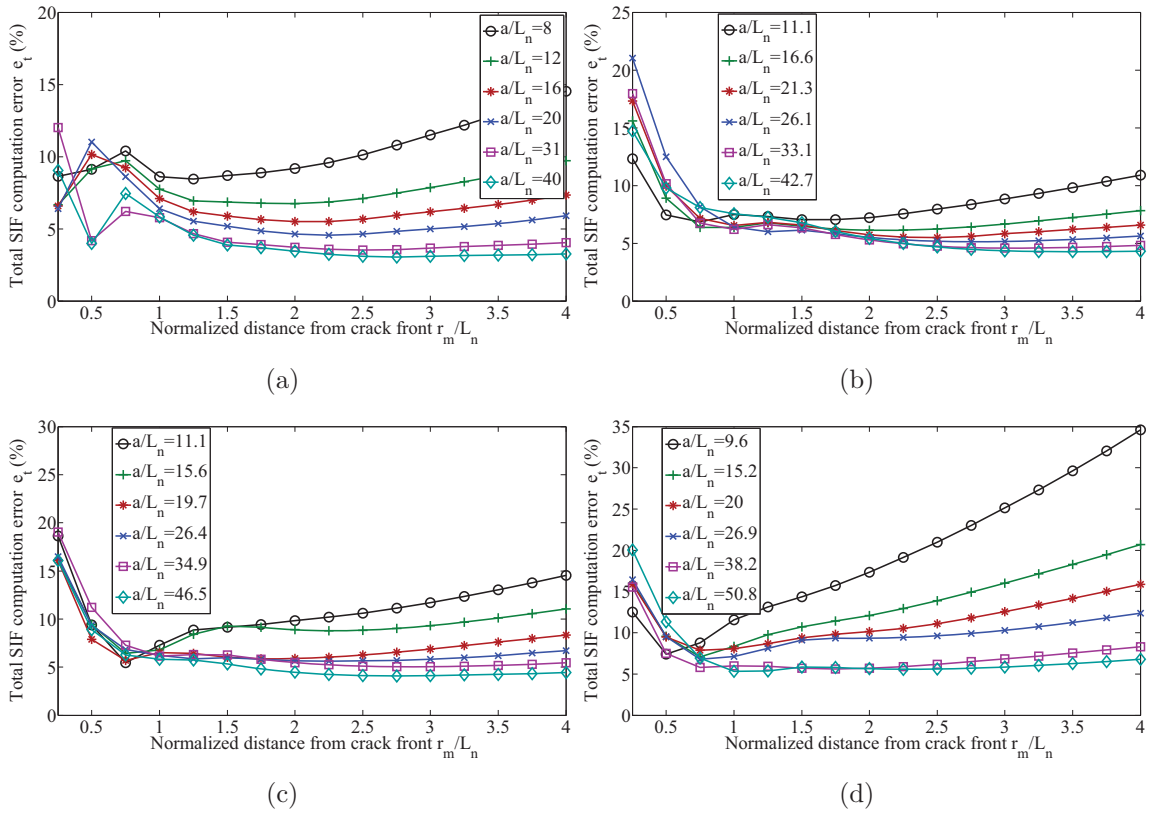

Figure 3.10: Average SIF computation error of the DC method in the absence of quarter-point tetrahedral elements. The variation of the total numerical error e_{t} against the normalized distance from the crack front r_m/L_n for (a) through-the-thickness, (b) penny-shaped, (c) elliptical ($b/a = 0.7$), (d) elliptical ($b/a = 0.4$) cracks in different mesh refinements.

the SIFs near a corner point, i.e., the meeting point of a crack front and a free surface. This is because at these points a corner singularity occurs, where the order of singularity, which depends on Poisson's ratio as well as loading conditions, is different from the crack singularity [Benthem, 1977; Bažant and Estenssoro, 1979]. Therefore, the SIFs near the corner points differs from one value of the Poisson's ratio to another one. However, the analytical mode I stress intensity factor of an embedded penny-shaped crack does not depend on the value of Poisson's ratio, whereas the numerical results of Ingraffea and Manu [1980] show significant dependency of the SIFs on this material property. The reason for this dependency is not explained in that paper.

All the previous SIF results in this chapter are obtained by considering $\nu = 0.3$. In order to evaluate the influence of Poisson's ratio, two other values, $\nu = 0.15$ and $\nu = 0.45$, were considered to compute the SIFs of the penny-shaped crack under mixed-mode loading. Fig. 3.11 shows the variation of the total SIF computation error e_{t} versus the normalized distance of the correlation point from the crack front r_m/L_n for different mesh refinements

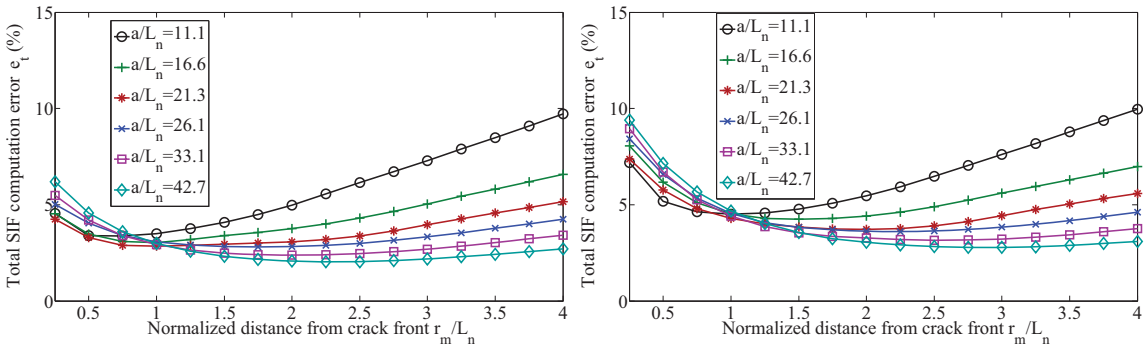

Figure 3.11: The effect of Poisson's ratio value on the variation of the total numerical error e_{t} against the normalized distance from the crack front r_m/L_n for penny-shaped under mixed-mode loading ($\beta = 45°$): (a) $\nu = 0.15$, (b) $\nu = 0.45$.

and Poisson's ratios. A comparison of these two plots and Fig. 3.9b, in which the results for $\nu = 0.3$ are reported, demonstrates that the error of the SIF values obtained by the proposed DC method in this chapter are barely influenced by Poisson's ratio value. For example, at the distance $r_m = 2L_n$, $e_{\mathrm{t}} = 0.024$, $e_{\mathrm{t}} = 0.025$, and $e_{\mathrm{t}} = 0.033$, are the errors corresponding to Poisson's ratio values of $\nu = 0.15$, $\nu = 0.3$, $\nu = 0.45$, respectively. It is also seen in these plots that the optimum distance from the crack front is not influenced by the value of Poisson's ratio. In fact, unlike the results of Ingraffea and Manu [1980], which suggest an optimum Poisson's ratio dependent element size, the results from the proposed DC method here suggest that the optimum distance from the crack front is independent of Poisson's ratio, and only depends on the mesh refinement near the crack front.

3.5.5 The method for non-matched meshes

All the previous proposed DC schemes rely on the generation of matched elements over the crack surfaces, as they use the displacements of matched nodes to compute the relative displacements between the two surfaces. The proposed DC approach in this chapter, however, does not require the crack surface elements to be matched. This is of great importance, as a considerable constraint is removed from meshing procedures by allowing non-matched meshes over the crack surfaces. The penny-shaped crack in a mixed-mode loading condition ($\beta = 45°$), as shown in Fig. 3.3b, was considered in order to evaluate the results of the DC method for non-matched meshes. The crack surface mesh structure is shown in Fig. 3.12a. Fig. 3.12b presents the variation of pointwise mixed-mode SIFs along the crack front. The average total error e_{t} is about 0.02. These results demonstrate the efficiency of the proposed DC approach for computing accurate SIFs from arbitrary meshes with non-matched crack surface elements.

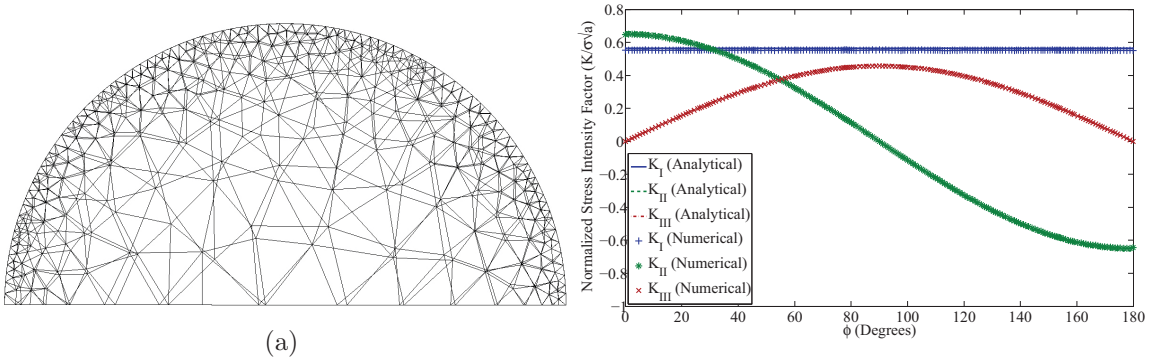

(a) (b)

Figure 3.12: (a) Non-matched mesh over the crack surfaces, (b) The variation of normalized mixed-mode ($\beta = 45°$) analytical and numerical SIFs along the fronts of penny-shaped crack with non-matched elements over the crack surfaces. $a/L_n = 30.2$, $r_m = 2L_n$, $e_{\mathrm{I}} = 0.02$, $e_{\mathrm{II}} = 0.021$, $e_{\mathrm{III}} = 0.0177$, $e_{\mathrm{t}} = 0.02$.

3.6 Conclusions

An efficient displacement correlation (DC) method is proposed for computing accurate approximations of the SIFs. This DC method is computationally very cheap, can be readily implemented in any FE code, and can be applied on unstructured meshes even when the elements on the crack surfaces are non-matched. The results of this method have been validated for a number of crack configurations in mode I and mixed-mode loadings, where the average SIF computation error varies from 1% for through-the thickness crack, to about 4% for elongated elliptical ones. A comparison of the results from the DC method for standard and quarter-point elements also reveals that the average SIF computation error more than doubles when using standard tetrahedra instead of quarter-point ones at the crack front region. The numerical results on the relative displacements over the crack surfaces also clearly demonstrate very good performance of the quarter-point tetrahedra in reproducing a square root displacement variation near the crack front. The results from an extensive parametric study suggest that there is an optimum mesh-dependent distance from the crack front at which the average SIF computation error by the DC method hits its minimum. This distance is about once to twice the average (nominal) size of the elements at the crack front region. The results of this chapter provide further evidence to the applicability, efficiency and accuracy of unstructured meshes to analyze cracked bodies.

Chapter 4

A disk-shaped domain integral method for the computation of SIFs

Contents

4.1 Abstract

A novel domain integral approach is introduced for the accurate computation of pointwise J-integral and stress intensity factors (SIFs) of 3D cracks using tetrahedral elements. This method is efficient and easy to implement, and does not require a structured mesh around the crack front. The method relies on the construction of virtual disk-shaped integral domains at points along the crack front, and the computation of domain integrals using a series of virtual triangular elements. The accuracy of the numerical results computed for through-the-thickness, penny-shaped, and elliptical crack configurations has been validated by using the available analytical formulations. The average error of computed SIFs remains below 1% for fine meshes, and between $2-3\%$ for coarse ones. The results of an extensive parametric study suggest that there exists an optimum mesh-dependent domain radius at which the computed SIFs are the most accurate. Furthermore, results provide evidence that tetrahedral elements are efficient, reliable and robust instruments for accurate linear elastic fracture mechanics calculations.

4.2 Introduction

Chapter 2 discussed the efficiency and effectiveness of quarter-point tetrahedra in reproducing the strain singularity along the crack front of three-dimensional cracks. A simple and straightforward displacement correlation method was also introduced in Chapter 3, and the efficiency of the quarter-point tetrahedra in reproducing singularity was evaluated in detail. This chapter introduces a new domain integral approach to compute the stress intensity factors and J-integral from unstructured meshes. Existing methods to extract J-integrals and SIFs using tetrahedral elements are complex and suffer from oscillations [Červenka and Saouma, 1997; Rajaram et al., 2000; Paluszny and Zimmerman, 2011], while others require very fine meshes near the crack front, rely on complicated numerical procedures, and are applied on arbitrary domain shapes and sizes [Okada et al., 2008; Daimon and Okada, 2014]. These methods mainly rely on volumetric actual [Rajaram et al., 2000; Daimon and Okada, 2014] and virtual [Červenka and Saouma, 1997; Paluszny and Zimmerman, 2011] domains to compute the SIFs from the evaluated J- and interaction integrals. Therefore, accurate, efficient and reliable methods based on crack conservative integrals have yet to be introduced.

As was mentioned earlier, techniques for SIF computation from FE results fall into two categories. (i) Direct approaches, such as stress/displacement extrapolation and correlation, which are based on the correlation between the FE stress/displacement distribution around the crack and the analytical field expressions. Displacement extrapolation method proposed

by Chan et al. [1970], displacement correlation approach suggested by Barsoum [1976] and further developed by Shih et al. [1976]; Ingraffea and Manu [1980], as well as recently developed least-square based finite element over-deterministic method (FEOD) by Ayatollahi and Nejati [2011a,b] fall into this category. (ii) Energy approaches are based on the computation of energy released rate $\mathcal{G}$ [Irwin, 1956]. The SIFs are computed indirectly by using the relationships between $\mathcal{G}$ and the SIFs. In the context of LEFM, three main methods have been proposed to compute $\mathcal{G}$: 1) the J-integral: J, which is equivalent to $\mathcal{G}$ for elastic materials, is defined as a contour integral around the crack tip [Cherepanov, 1967; Rice, 1968; Budiansky and Rice, 1973]. DeLorenzi [1982] and Li et al. [1985] then transformed this contour integral into an equivalent domain integral. 2) Virtual crack extension: VCE was suggested by Parks [1974], and computes the rate of the change of the total potential energy of the system, for a small virtual extension of the crack. This technique is mathematically equivalent to the domain version of J-integral, and can be interpreted as a virtual crack extension technique [DeLorenzi, 1982; Shih et al., 1986; Banks-Sills and Sherman, 1992; Banks-Sills, 2010]. 3) Virtual crack closure technique: The VCCT was originally proposed by Rybicki and Kanninen [1977] for two-dimensional problem, and Shivakumar et al. [1988] extended it for three-dimensional cracks. The VCCT uses Irwin's crack closure integral and computes the energy required to close the crack for one finite element length by multiplying the nodal reaction forces and the opening displacements [Okada et al., 2008]. This chapter introduces an efficient, accurate and straightforward disk-shaped domain integral method to extract J-integral and SIFs from unstructured meshes. This method does not require a very fine mesh near the crack front, and no oscillation is seen in the computed pointwise fracture parameters.

4.3 Volumetric domain integral method

The J-integral has been the most used crack tip parameter in fracture mechanics, and plays an important role in linear and nonlinear fracture mechanics. Under pure modes I, II or III, the extraction of SIFs from the J-integral is straightforward. However, a technique is required to separate SIFs due to different deformation modes in a mixed-mode crack deformation, as the J-integral gives the *total* energy release rate. There have been two main strategies for separating the SIFs. The first strategy uses decomposed crack tip fields to compute separate energy release rates for different deformation modes [Bui, 1983]. This approach has been frequently used along with the domain representation of the J-integral for the computation of SIFs [Raju and Shivakumar, 1990; Shivakumar and Raju, 1992; Nikishkov and Atluri, 1987b; Huber et al., 1993]. However, decomposing the crack tip field into symmetric and antisymmetric fields introduces error, and is mainly applicable to a

mesh that is symmetric with respect to the crack face. The second method is called the interaction integral method, which was initially developed for 2D cracks by Chen and Shield [1977] and Yau et al. [1980], and then extended to 3D crack configurations by Nakamura and Parks [1989]. In this method, the contribution of the interaction of two different stress fields, a real field and an auxiliary field, to the J-integral defines a new integral which is able to compute separate SIFs. Interaction integral methods have emerged as the most accurate and readily implementable approach to extract SIFs in mixed-mode crack deformation [Walters et al., 2005]. This section discusses the available domain integral approaches of computing J-integral and interaction-integral from FE results. All of these approaches are based on using volumetric domains for the computation of three-dimensional crack parameters.

4.3.1 J-integral

Let us consider a two-dimensional elastic body containing a crack which lies in the direction of x_1 as shown in Fig. 4.1. Restricting the crack to advance along the x_1 axis, the energy release rate per unit crack advance, $\mathcal{G}$, is equivalent to the J-integral [Rice, 1968; Shih et al., 1986]:

$$\mathcal{G} = J = \lim_{\Gamma \to 0} \int_{\Gamma} \Big(W\delta_{1i} - \sigma_{ij} \frac{\partial u_j}{\partial x_1} \Big) n_i d\Gamma = \lim_{\Gamma \to 0} \int_{\Gamma} P_{1i} n_i \mathrm{d}\Gamma \tag{4.1}$$

where $W = \int_0^{\epsilon} \sigma_{ij}\epsilon_{ij} d\epsilon$ is the strain energy density, σ_{ij}, ϵ_{ij} and u_i are the Cartesian components of the stress tensor, strain tensor and displacement vector in the local x_1x_2 coordinate system, respectively, δ_{ij} is the Kronecker delta, and n_i is the unit vector normal to Γ which is an arbitrary path beginning at the bottom crack face and ending on the top face. $\Gamma \to 0$ indicates that the contour Γ is shrinking onto the crack tip. The bracketed quantity is in fact the x_1 component of Eshelby's energy-momentum tensor $P_{1i} = W\delta_{1i} - \sigma_{ij}\partial u_j/\partial x_1$ [Eshelby, 1970]. In the absence of body force and thermal strains, the energy density W does not depend explicitly on the system coordinates, and the divergence of P_{1i} vanishes ($P_{1i,i} = 0$). Assuming that the vector m is normal to a closed contour $\Gamma_c = \Gamma_0 + \Gamma_+ + \Gamma_- - \Gamma$ such that $m = -n$ on Γ, $m = n$ on Γ_0, $m_2 = -1$ on Γ_+ , and $m_2 = 1$ on Γ_-, then according to the divergence theorem the integral in Eq. (4.1) vanishes for Γ_c, $\int_{\Gamma_c} P_{1i} m_i \mathrm{d}\Gamma = 0$, and the J-integral can be expressed as

$$J = \int_{\Gamma_0} \Big(W\delta_{1i} - \sigma_{ij} \frac{\partial u_j}{\partial x_1} \Big) n_i \mathrm{d}\Gamma - \int_{\Gamma_+ + \Gamma_-} \sigma_{2j} \frac{\partial u_j}{\partial x_1} m_2 \mathrm{d}\Gamma \tag{4.2}$$

Eq. (4.2) indicates that in the absence of body force and thermal strains, the J-integral is path-independent as long as the contribution of crack face tractions is considered. In fact, the J-integral does not depend on a limiting process in which the crack tip contour Γ is shrunk onto the crack tip, and can be accurately extracted from contours remote from

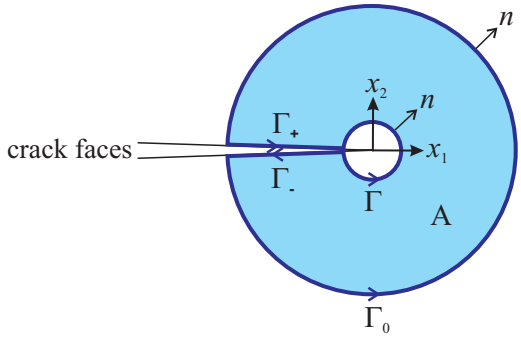

Figure 4.1: Contour and domain integrals for the evaluation of J-integral in 2D cracks.

the crack tip. This formulation allows one to use contours remote from the crack tip, which results in the computation of more accurate values for J-integral. However, the evaluation of contour integrals in Eq. (4.2) is cumbersome in the FE scheme as the contour is preferably selected to pass through Gauss points where stresses are expected to be the most accurate. To circumvent this difficulty, the line-integral form of J can be recast as a domain integral [DeLorenzi, 1982; Li et al., 1985]. Let us assume q is a sufficiently smooth scalar function in the region enclosed by $\Gamma_c = \Gamma_0 + \Gamma_+ + \Gamma_- - \Gamma$, holding unity on Γ and vanishing on Γ_0. Eq. (4.1) can be rewritten as

$$J = \int_A \left(\sigma_{ij}\frac{\partial u_j}{\partial x_1} - W\delta_{1i}\right)\frac{\partial q}{\partial x_i}\mathrm{d}A - \int_{\Gamma_+ + \Gamma_-} \sigma_{2j}\frac{\partial u_j}{\partial x_1} m_2 q \mathrm{d}\Gamma \tag{4.3}$$

where the closed contour integral is transformed to an equivalent domain integral by applying the divergence theorem and making use of the relation ($P_{1i,i} = 0$). Due to the scalar function q, the contour integrals in Eq. (4.2) is now transformed to an area integral over A together with contour integral over the crack faces. The process of recasting the contour integral into an area integral is advantageous for numerical purposes, as a domain integral is compatible with the finite element formulations and can be readily implemented in FE codes. Also as the integral is evaluated over a domain of elements surrounding the crack, errors in local solution parameters have less effect on the evaluated quantity of J-integral. It has been shown that the domain version of the J-integral has superior path independence than does the line integral, yielding much more accurate results for the crack field parameters [Nikishkov and Atluri, 1987a; Raju and Shivakumar, 1990]. The domain integral method corresponds to a continuum formulation of the finite-element virtual crack extension technique [DeLorenzi, 1982]. One can refer to Moran and Shih [1987a,b] for a general discussion on crack-tip contour integrals and their associated domain integral representation.

For a 3D crack configuration, the J-integral generalizes to a surface integral where two definitions of the J-integral have been proposed: (i) the average value which gives the

average of the energy release rate per unit crack advance at the whole crack front; and (ii) the pointwise value which gives the energy release rate due the extension of the crack front locally at a given point on the crack front [Budiansky and Rice, 1973; DeLorenzi, 1982; Li et al., 1985]. The pointwise J-integral reveals the variation of the strength of the energy release rate along the crack front, and can be used to compute the SIFs at any point on the crack front. Consider point s on the curved crack front of a 3D planar crack. A local orthogonal coordinate system is defined at point s such that the local x_2 axis is perpendicular to the plane of the crack, and the x_1, and x_3 axes are normal and tangent to the crack front, respectively (Fig. 4.2). The pointwise energy release rate due to the unit local crack advancement at the point s is given by

$$J(s) = \lim_{\Omega\to 0,\, L_c\to 0} \frac{1}{L_c} \int_{\Omega} P_{1i} n_i \mathrm{d}\Omega = \lim_{\Gamma\to 0} \int_{\Gamma} P_{1i} n_i \mathrm{d}\Gamma \tag{4.4}$$

where Γ is a contour that lies on a plane passing through point s and is perpendicular to the crack front, Ω is the surface of a tube connecting the top and bottom crack faces, and n_i is the unit vector normal to Ω. $\Omega \to 0$ indicates that the surface Ω is shrinking onto the crack front segment L_c. Although the shape of surface Ω may be arbitrary as it collapses onto the crack front, an equivalent path independent integral such as Eq. (4.2) does not exist for 3D cracks. This is because the two-dimensional plane strain fields are only asymptotically approached at the crack front, and a general 3D state of stress prevails far from the crack front [Nakamura and Parks, 1989]. Therefore, for the J-integral to capture the effects of plane strain conditions, the surface must be very close to the crack front. Furthermore, if the surface Ω that is used for the J-integral is too large, then it is influenced by singular fields from other points of the crack front and not just the position of interest [Shivakumar and Raju, 1992; Rigby and Aliabadi, 1998]. The presence of two limits and integration over surface make it very cumbersome and error-prone to evaluate the J-integral from its original definition in Eq. (4.4). However, two steps can be taken to recast the integral into a more compatible formulation within the FE context. In the first step it is assumed that $J(s)$ varies slowly over a small segment of the crack front L_c which has undergone a crack advancement of $\delta l(s)$, and reformulate Eq. (4.4) as

$$J(s) = \frac{1}{\displaystyle\int_{L_f} \delta l(s) \mathrm{d}s} \lim_{\Omega\to 0} \int_{\Omega} P_{1i} \delta l(s) n_i \mathrm{d}\Omega \tag{4.5}$$

where the crack advance $\delta l(s)$ is continuously differentiable arbitrary function that equals zero at the two ends of L_c (Fig. 4.2). The second step is to recast the surface integral into a domain integral version. Consider a tubular domain V surrounding the crack segment L_c, which is enclosed by the closed manifold $\Omega_c = \Omega + \Omega_0 + \Omega_L + \Omega_R + \Omega_+ + \Omega_-$ with the

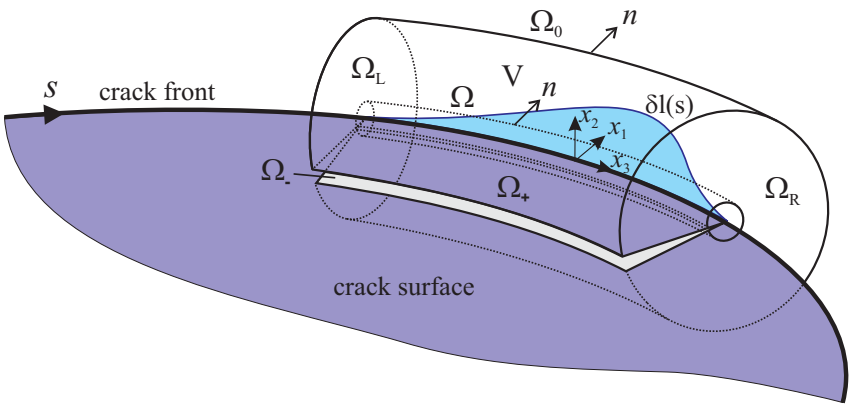

Figure 4.2: The tubular domain V surrounding the crack segment L_c, which is enclosed by the closed manifold $\Omega_c = \Omega + \Omega_0 + \Omega_L + \Omega_R + \Omega_+ + \Omega_-$ where Ω shrinks onto the crack front.

outward-point normal vector m where $m = -n$ on Ω, $m = n$ on Ω_0, $m_2 = -1$ on Ω_+ and $m_2 = 1$ on Ω_- (see Fig. 4.2). These surfaces are formed by translating the contour Γ, Γ_0, Γ_+ and Γ_- in Fig. 4.1 along the curved crack front segment L_c. Now introduce an arbitrary continuously differentiable, class C^1, scalar function q in the neighborhood of V, which is equal to $\delta l(s)$ on the surface Ω, and zero on Ω_0, Ω_R and Ω_L. Applying the divergence theorem, and knowing that in the absence of thermal strains and body forces, and when the equilibrium conditions are satisfied throughout the whole domain V ($\partial\sigma_{ij}/\partial x_j = 0$), P_{1i} is divergence free ($\partial P_{1i}/\partial x_i = 0$), Eq. (4.5) is reformulated to

$$J(s) = \frac{1}{\int_{L_c} q(s)\mathrm{d}s}\left[\int_V \left(\sigma_{ij}\frac{\partial u_j}{\partial x_1} - W\delta_{1i}\right)\frac{\partial q}{\partial x_i}\mathrm{d}V - \int_{\Omega_+ + \Omega_-} \sigma_{2j}\frac{\partial u_j}{\partial x_1} m_2 q \mathrm{d}\Omega\right] \tag{4.6}$$

By separately advancing various small segments of the crack front, the pointwise J-integral can be computed along the crack front [Shih et al., 1986; Nikishkov and Atluri, 1987b; Shivakumar and Raju, 1992]. Volume integration is performed over a volumetric domain around the crack front; a special concentric mesh is required to define a structured domain around the crack front.

4.3.2 Interaction integral to extract SIFs

The three SIFs K_{I}, K_{II}, and K_{III} cannot be calculated separately from the J-integral. The interaction integral, however, is able to extract the separated SIFs from the FE results. Chen and Shield [1977] and Yau et al. [1980] introduced this method for 2D cracks, and Nakamura and Parks [1989] extended it to 3D crack configurations. Interaction integral methods are perhaps the most accurate, reliable and readily implementable methods to extract SIFs in mixed-mode 2D and 3D crack problems [Walters et al., 2005; Banks-Sills,

2010; Bremberg and Faleskog, 2015]. Consider two states of equilibrium for the cracked body deformation: (i) an actual state obtained by the FE solution of the actual boundary value problem $(u_i, \epsilon_{ij}, \sigma_{ij})$; and (ii) an auxiliary state given by the known asymptotic fields which are functions of the SIFs $(u_i^{\text{aux}}, \epsilon_{ij}^{\text{aux}}, \sigma_{ij}^{\text{aux}})$. Except at points that are very close to the intersection point of a crack front with free surfaces, the two-dimensional plane strain fields are asymptotically approached at the crack front [Nakamura and Parks, 1988, 1989]. Therefore, the first terms of the Williams series expansions for stresses, strains and displacements in 2D cracks are usually chosen as the auxiliary fields in the vicinity of the crack front. The so-called Williams series expansions describe the linear elastic stress fields for a 2D cracked plate subjected to an arbitrary load [Williams, 1957]. In the region close to the crack tip, the first terms in these expansions are dominant. The auxiliary fields for 3D embedded cracks are therefore considered to be in the form of these singular fields in the plane strain condition ($\sigma_{33}^{\text{aux}} = \nu(\sigma_{11}^{\text{aux}} + \sigma_{22}^{\text{aux}})$). Eqs. (4.7) and (4.8) give these stress fields when in-plane and anti-plane loads are applied, respectively [Anderson, 2005]:

$$\begin{Bmatrix} \sigma_{11}^{\text{aux}} \\ \sigma_{22}^{\text{aux}} \\ \sigma_{12}^{\text{aux}} \\ \sigma_{33}^{\text{aux}} \end{Bmatrix} = \frac{K_{\text{I}}^{\text{aux}}}{\sqrt{2\pi r}} \begin{Bmatrix} \cos\frac{\theta}{2}\left(1 - \sin\frac{\theta}{2}\sin\frac{3\theta}{2}\right) \\ \cos\frac{\theta}{2}\left(1 + \sin\frac{\theta}{2}\sin\frac{3\theta}{2}\right) \\ \cos\frac{\theta}{2}\sin\frac{\theta}{2}\cos\frac{3\theta}{2} \\ 2\nu\cos\frac{\theta}{2} \end{Bmatrix} + \frac{K_{\text{II}}^{\text{aux}}}{\sqrt{2\pi r}} \begin{Bmatrix} \sin\frac{\theta}{2}\left(-2 - \cos\frac{\theta}{2}\cos\frac{3\theta}{2}\right) \\ \sin\frac{\theta}{2}\cos\frac{\theta}{2}\cos\frac{3\theta}{2} \\ \cos\frac{\theta}{2}\left(1 - \sin\frac{\theta}{2}\sin\frac{3\theta}{2}\right) \\ -2\nu\sin\frac{\theta}{2} \end{Bmatrix} \tag{4.7}$$

$$\begin{Bmatrix} \sigma_{13}^{\text{aux}} \\ \sigma_{23}^{\text{aux}} \end{Bmatrix} = \frac{K_{\text{III}}^{\text{aux}}}{\sqrt{2\pi r}} \begin{Bmatrix} -\sin\frac{\theta}{2} \\ \cos\frac{\theta}{2} \end{Bmatrix} \tag{4.8}$$

Here r and θ are the polar coordinates in a local Cartesian coordinate system $x_1x_2x_3$ which is perpendicular to the crack front, as shown in Fig. 4.3. The displacement fields adjacent to the crack tip due to the in-plane and anti-plane loadings conditions, respectively, are given by [Anderson, 2005]

$$\begin{aligned} \begin{Bmatrix} u_1^{\text{aux}} \\ u_2^{\text{aux}} \end{Bmatrix} = {} & \frac{K_{\text{I}}^{\text{aux}}}{2\mu}\sqrt{\frac{r}{2\pi}} \begin{Bmatrix} \cos\frac{\theta}{2}\left(\kappa - 1 + 2\sin^2\frac{\theta}{2}\right) \\ \sin\frac{\theta}{2}\left((\kappa + 1 - 2\cos^2\frac{\theta}{2}\right) \end{Bmatrix} \\ & + \frac{K_{\text{II}}^{\text{aux}}}{2\mu}\sqrt{\frac{r}{2\pi}} \begin{Bmatrix} \sin\frac{\theta}{2}\left(1 + \kappa + 2\cos^2\frac{\theta}{2}\right) \\ \cos\frac{\theta}{2}\left(1 - \kappa + 2\sin^2\frac{\theta}{2}\right) \end{Bmatrix} \end{aligned} \tag{4.9}$$

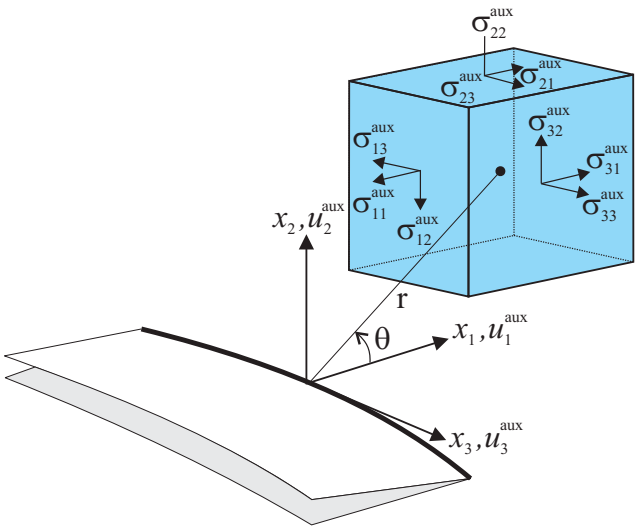

Figure 4.3: Local Cartesian coordinate system at a point along crack front and crack tip auxiliary fields.

$$u_3^{\text{aux}} = \frac{2K_{\text{III}}^{\text{aux}}}{\mu}\sqrt{\frac{r}{2\pi}}\sin\frac{\theta}{2} \tag{4.10}$$

where κ is a function of Poisson's ratio, and under plane strain conditions, $\kappa = 3 - 4\nu$. Under plane strain conditions, the out-of-plane displacement u_3^{aux} vanishes when applying in-plane loads, and in-plane displacements (u_1^{aux} and u_2^{aux}) are zero when anti-plane loads are applied. The derivatives of the displacement fields with respect to x_1 are readily obtained from Eqs. (4.9) and (4.10) as

$$\begin{Bmatrix} \dfrac{\partial u_1^{\text{aux}}}{\partial x_1} \\ \dfrac{\partial u_2^{\text{aux}}}{\partial x_1} \end{Bmatrix} = \frac{K_{\text{I}}^{\text{aux}}}{4\mu\sqrt{2\pi r}} \begin{Bmatrix} \cos\dfrac{\theta}{2}\Big(\kappa - 1 - \cos\theta + \cos 2\theta\Big) \\ \sin\dfrac{\theta}{2}\Big(-\kappa - 1 + \cos\theta + \cos 2\theta\Big) \end{Bmatrix} + \frac{K_{\text{II}}^{\text{aux}}}{4\mu\sqrt{2\pi r}} \begin{Bmatrix} -\sin\dfrac{\theta}{2}\Big(\kappa + 1 + \cos\theta + \cos 2\theta\Big) \\ \cos\dfrac{\theta}{2}\Big(-\kappa + 1 - \cos\theta + \cos 2\theta\Big) \end{Bmatrix} \tag{4.11}$$

$$\frac{\partial u_3^{\text{aux}}}{\partial x_1} = -\frac{K_{\text{III}}^{\text{aux}}}{\mu\sqrt{2\pi r}}\sin\frac{\theta}{2} \tag{4.12}$$

A linear combination of actual fields (or finite element fields) with auxiliary fields (field expressions as functions of SIFs) constitutes a third, superimposed, equilibrium state. From Eq. (4.4), the J-integral for this superimposed equilibrium state is given by

$$J^{\text{sup}}(s) = \lim_{\Gamma\to 0}\int_{\Gamma}\Big[\frac{1}{2}(\sigma_{ij}+\sigma_{ij}^{\text{aux}})(\epsilon_{ij}+\epsilon_{ij}^{\text{aux}})\delta_{1i} - (\sigma_{ij}+\sigma_{ij}^{\text{aux}})(\frac{\partial u_j}{\partial x_1} + \frac{\partial u_j^{\text{aux}}}{\partial x_1})\Big]n_i d\Gamma \tag{4.13}$$

Consider $J^{\text{sup}}(s) = J^{\text{act}}(s) + J^{\text{aux}}(s) + I(s)$, where $J^{\text{act}}(s)$ and $J^{\text{aux}}(s)$ are the energy release rates due to the actual and auxiliary fields, and $I(s)$ is the interaction integral for the two states of equilibrium. By comparing the energy release rate for the superimposed state with the energy release rates for the separate actual and auxiliary fields, the interaction integral is formulated as

$$I(s) = \lim_{\Gamma \to 0} \int_{\Gamma} \Big[W_{\text{I}} \delta_{1i} - \Big(\sigma_{ij} \frac{\partial u_j^{\text{aux}}}{\partial x_1} + \sigma_{ij}^{\text{aux}} \frac{\partial u_j}{\partial x_1} \Big) \Big] n_i d\Gamma \tag{4.14}$$

where $W_{\text{I}} = 1/2(\epsilon_{ij}^{\text{aux}} \sigma_{ij} + \epsilon_{ij} \sigma_{ij}^{\text{aux}})$ is the mutual strain density, and as the actual and auxiliary fields provide two solutions for the same elastic solid with the same constitutive tensor, according to the reciprocal theorem $W_{\text{I}} = \epsilon_{ij}^{\text{aux}} \sigma_{ij} = \epsilon_{ij} \sigma_{ij}^{\text{aux}}$. In the context of LEFM, the two very important fracture parameters, namely the energy release rate $\mathcal{G}$, which gives the change in the potential energy that accompanies an increment of crack extension, and the stress intensity factors K_{I}, K_{II} and K_{III}, which characterize the stresses, strains, and displacement near the crack front for different modes, are uniquely related by [Anderson, 2005]

$$\mathcal{G} = J = \frac{K_{\text{I}}^2 + K_{\text{II}}^2}{E'} + \frac{K_{\text{III}}^2}{2\mu} \tag{4.15}$$

where $E' = E$ and $E' = E/(1-\nu^2)$ for plane stress and plane strain conditions, respectively, and E, ν and $\mu = E/2(1+\nu)$ are the Young's modulus, Poisson's ratio, and shear modulus of the material. As plane strain condition prevails very close to the crack front at any point on the crack front except points very close to the intersection of the crack front and free surfaces [Nakamura and Parks, 1988, 1989], a plane strain condition must be assumed in order to relate $\mathcal{G}(s)$ to the SIFs. Using Eq. (4.15) the energy release rate for the superimposed state in terms of SIFs will be

$$\begin{aligned} &J^{\text{sup}}(s) = J^{\text{act}}(s) + J^{\text{aux}}(s) + I(s) \\ &= \frac{\big(K_{\text{I}}(s) + K_{\text{I}}^{\text{aux}}(s)\big)^2 + \big(K_{\text{II}}(s) + K_{\text{II}}^{\text{aux}}(s)\big)^2}{E'} + \frac{\big(K_{\text{III}}(s) + K_{\text{III}}^{\text{aux}}(s)\big)^2}{2\mu} \end{aligned} \tag{4.16}$$

where $K_{\text{I}}(s)$, $K_{\text{II}}(s)$ and $K_{\text{III}}(s)$ are the SIFs due to the actual state, and $K_{\text{I}}^{\text{aux}}(s)$, $K_{\text{II}}^{\text{aux}}(s)$ and $K_{\text{III}}^{\text{aux}}$ are the SIFs due to the auxiliary states. The interaction energy integral is then developed in terms of SIFs as

$$I(s) = \frac{2}{E'} \Big(K_{\text{I}}(s) K_{\text{I}}^{\text{aux}}(s) + K_{\text{II}}(s) K_{\text{II}}^{\text{aux}}(s) \Big) + \frac{1}{\mu} K_{\text{III}}(s) K_{\text{III}}^{\text{aux}}(s) \tag{4.17}$$

By using following three equilibrium auxiliary states of pure mode I $(K_{\text{I}}^{\text{aux}}, K_{\text{II}}^{\text{aux}}, K_{\text{III}}^{\text{aux}}) = (1, 0, 0)$, pure mode II $(K_{\text{I}}^{\text{aux}}, K_{\text{II}}^{\text{aux}}, K_{\text{III}}^{\text{aux}}) = (0, 1, 0)$, and pure mode III $(K_{\text{I}}^{\text{aux}}, K_{\text{II}}^{\text{aux}}, K_{\text{III}}^{\text{aux}}) = (0, 0, 1)$, three corresponding interaction integral values $I_{\text{I}}(s)$, $I_{\text{II}}(s)$ and $I_{\text{III}}(s)$ are obtained from Eq. (4.14), and the SIFs are extracted from the following expressions:

$$K_{\text{I}}(s) = \frac{E'}{2} I_{\text{I}}(s), \quad K_{\text{II}}(s) = \frac{E'}{2} I_{\text{II}}(s), \quad K_{\text{III}}(s) = \mu I_{\text{III}}(s) \tag{4.18}$$

Equation (4.14) is not in a form well suited for finite element calculations. The same approach that was used in Section 4.3.1 can be used to recast this integral into a domain integral, which is more compatible with the context of finite elements. Again consider the tubular domain V surrounding the crack segment L_c, which is enclosed by the closed manifold Ω_c, with the outward-point normal vector m, and also consider the scalar function q as explained in Section 4.3.1 (Fig. 4.2). Applying the divergence theorem, Eq. (4.14) is reformulated to

$$
\begin{aligned}
I(s) = \frac{1}{\int_{L_c} q(s)\mathrm{d}s}\Bigg[& \int_V \left(\sigma_{ij}\frac{\partial u_j^{\mathrm{aux}}}{\partial x_1} + \sigma_{ij}^{\mathrm{aux}}\frac{\partial u_j}{\partial x_1} - W_{\mathrm{I}}\delta_{1i}\right)\frac{\partial q}{\partial x_i}\mathrm{d}V \\
& + \int_V \left(\sigma_{ij}\frac{\partial}{\partial x_1}\left(\frac{\partial u_j^{\mathrm{aux}}}{\partial x_i} - \epsilon_{ij}^{\mathrm{aux}}\right) + \frac{\partial \sigma_{ij}^{\mathrm{aux}}}{\partial x_i}\frac{\partial u_j}{\partial x_1}\right) q\mathrm{d}V \\
& - \int_{\Omega_+ + \Omega_-} \sigma_{2j}\frac{\partial u_j^{\mathrm{aux}}}{\partial x_1} m_2 q \mathrm{d}\Omega\Bigg]
\end{aligned}
\tag{4.19}
$$

Equation (4.19) is derived for isothermal loading without body forces, assuming that in the actual state the equilibrium and compatibility conditions are satisfied throughout the entire domain V ($\partial\sigma_{ij}/\partial x_j = 0, \partial u_j/\partial x_i - \epsilon_{ij} = 0$). For a straight crack front, the 2D plane strain auxiliary fields also satisfy compatibility and equilibrium equations, and therefore, the second integral in Eq. (4.19) vanishes. In the case of curved crack fronts, however, special care must be taken, as Williams 2D plane strain auxiliary fields do not satisfy compatibility ($\partial u_j^{\mathrm{aux}}/\partial x_i - \epsilon_{ij}^{\mathrm{aux}} \neq 0$) and equilibrium ($\partial\sigma_{ij}^{\mathrm{aux}}/\partial x_i \neq 0$) in curvilinear coordinates and the second integral remains non-zero [Nahta and Moran, 1993; Gosz et al., 1998; Gosz and Moran, 2002]. The main difficulty in calculating the interaction energy integral from the domain form in Eq. (4.19) lies in the evaluation of the gradients and higher order gradients of the auxiliary fields that appear in the second integrand in Eq. (4.19). Nahta and Moran [1993]; Gosz et al. [1998] presented a method to evaluate this integral by introducing curvilinear coordinates in the definition of deformation gradients. Kim et al. [2001] proposed a method to calculate the two-state integral in Eq. (4.19) through imposing displacement of the two dimensional asymptotic solution on the nodes in the finite element model. Both methods involve the computation of highly accurate values of the coordinates of the integration points with respect to the curved crack front, which usually require a Newton scheme and an analytical definition for the local crack front geometry. Walters et al. [2005] proposed another strategy in which elements with straight edges are used along the crack front. This approach eliminates this additional integral appearing in the interaction integral formulation for curvilinear coordinates. It has been demonstrated that it is crucial to maintain this integrand, especially when the local crack

front curvature is high [Gosz et al., 1998; Kim et al., 2001]. The third terms in Eq. (4.19) also involves the evaluation of surface integrals, which include singular terms. An accurate evaluation of this integral ensures that it does not contribute numerical error to the SIF results.

The existing volumetric domain integral approaches use Eqs. (4.6) and (4.19) to evaluate the J-integral and interaction integrals, respectively. As they evaluate integrals over tubular domains built by a set of volumetric elements, a structured mesh is required around the crack front. The main advantage of these versions of domain integrals is that they can be readily implemented in the FE codes when a structured mesh is used near the crack front. The main disadvantages of these forms are: (i) Implementation of these methods on an unstructured mesh is very cumbersome; (ii) The method requires the crack tip fields to be obtained in a curvilinear coordinate system by the computation of accurate values of the coordinates of the integration points with respect to the curved crack front, which usually requires a Newton scheme and an analytical definition for the local crack front geometry; (iii) The computation of the second integral in Eq. (4.19) requires computation of the higher-order gradients of crack tip fields, which is not trivial. The question arises as to whether this is the best domain form choice to be used in the case of an unstructured mesh around the crack front.

4.4 Disk-shaped domain integral approach

Consider a cracked body under mechanical loading only, in the absence of body forces and thermal strains. The arbitrarily-shaped planar crack is assumed to lie in a plane described by $X_p(X_1, X_2, X_3) = 0$ whose crack front is of length L_f, as shown in Fig. 4.4. The crack front is a smooth plane curve that is described by the position vector $X_f(s)$, where $0 \leq s \leq L_f$ parameterizes the points along the crack front. The unit normal vector to the crack surface is constant ($N_p = \nabla X_p / \|\nabla X_p\|$), but the unit tangent vector to the crack front will be a function of s ($T(s) = X_f'(s)/\|X_f'(s)\|$). The unit normal to the crack front which lies in the crack plane and is in the direction of crack extension is also a function of s and is defined by $N_f(s) = N_p \times T(s)$. A right-handed orthogonal curvilinear coordinate system $x_1x_2x_3$ is constructed in a way that the x_3 axis coincide with the curved crack front. In this coordinate system, $x_3 = s$ indicates a plane normal to the crack front, and the local unit base vectors at the point s along the crack front are $b_1 = N_f(s)$, $b_2 = N_p$, and $b_3 = T(s)$.

4.4.1 J-integral

Assume a virtual crack advance of $\delta l(s) = \delta(x_3 - s)b_1$ in the curvilinear coordinate system $x_1x_2x_3$. Here $\delta(x_3 - s)$ is the Dirac delta function, which is zero along the crack front except

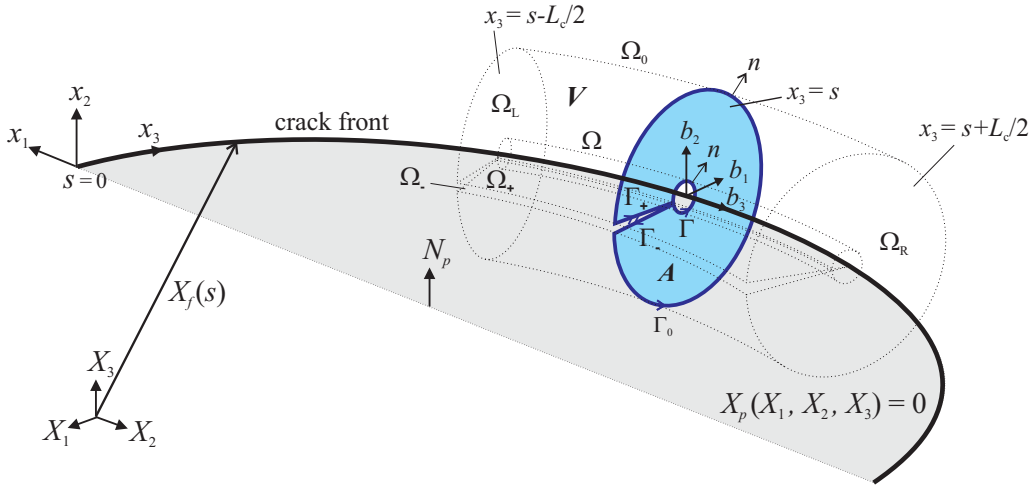

Figure 4.4: Disk-shaped domain for the evaluation of J- and interaction integrals in 3D crack configurations.

at the point s, and gives a pointwise crack extension at the point s on the crack front. Due to this virtual crack extension, the negative of the change of the potential energy of the body (Π) is equivalent to the pointwise energy release rate:

$$-\delta\Pi = \int_0^{L_f} \mathcal{G}(x_3)\delta(x_3 - s)\mathrm{d}x_3 = \mathcal{G}(s) \tag{4.20}$$

Equation (4.20) implies that the Dirac delta function is a proper choice for the virtual crack extension in order to evaluate the pointwise energy release rate as the unit crack extension occurs at the point s only, remaining elsewhere at its original length. Now consider an arbitrary path Γ beginning at the bottom crack face and ending on the top face, with n_i being its unit normal vector (Fig. 4.4). Both contour path Γ and its normal n_i lie in the plane $x_3 = s$, which is normal to the crack front at the point s. The tubular surface Ω is now formed by translating the contour Γ along the curved crack front segment L_c (Fig. 4.4). From Eq. (4.4), the pointwise energy release rate $\mathcal{G}$ is equivalent to the well-known J-integral:

$$\mathcal{G}(s) = J(s) = \lim_{\Gamma\to 0}\int_\Gamma P_{1i}n_i\mathrm{d}\Gamma = \lim_{\Omega\to 0}\int_\Omega P_{1i}n_i\delta(x_3 - s)\mathrm{d}\Omega \tag{4.21}$$

where $\Gamma \to 0$ and $\Omega \to 0$ indicate that the contour Γ and the surface Ω are shrinking down to the point $x_3 = s$, and crack segment L_c, respectively.

Let us consider a tubular domain V surrounding the crack segment L_c, which is enclosed by the closed manifold $\Omega_c = \Omega + \Omega_0 + \Omega_L + \Omega_R + \Omega_+ + \Omega_-$ with the outward-point normal vector m where $m = -n$ on Ω, $m = n$ on Ω_0, $m_2 = -1$ on Ω_+ and $m_2 = 1$ on Ω_- (see Fig. 4.4). These surfaces are formed by translating the enclosed contour $\Gamma_c = \Gamma_0 + \Gamma_+ + \Gamma_- - \Gamma$ at the plane $x_3 = s$ along the curved crack front segment L_c. Let us also introduce an

arbitrary continuously differentiable scalar function $q(x_1, x_2)$, which is equal to unity on Ω, and zero on Ω_0. $q(x_1, x_2)\delta(x_3 - s)$ is therefore a continuously differentiable scalar function which is equal to $\delta l(x_3) = \delta(x_3 - s)$ on Ω, and zero on Ω_0. In the absence of thermal strains and body forces, and when the equilibrium conditions are satisfied throughout the whole domain A ($\partial\sigma_{ij}/\partial x_j = 0$), P_{1i} is divergence-free on A ($\partial P_{1i}/\partial x_i = 0$). Applying the divergence theorem, the surface integral in Eq. (4.21) is reformulated to a domain integral as

$$J(s) = \int_A \left(\sigma_{ij}\frac{\partial u_j}{\partial x_1} - W\delta_{1i}\right)\frac{\partial q}{\partial x_i}\mathrm{d}A - \frac{\partial}{\partial x_3}\int_A \sigma_{3j}\frac{\partial u_j}{\partial x_1}\, q\mathrm{d}A - \int_{\Gamma_+ + \Gamma_-} \sigma_{2j}\frac{\partial u_j}{\partial x_1} m_2 q \mathrm{d}\Gamma \quad (4.22)$$

where A is a disk-shaped area in the plane orthogonal to the crack front at point s, and Γ_+ and Γ_- are the contours on the crack faces with $m_2 = -1$ and $m_2 = 1$, respectively. Here the fundamental equation that defines derivatives of the delta function ($\int f(x)\delta'(x)\mathrm{d}x = -\int f'(x)\delta(x)\mathrm{d}x$) has been used. The limiting process is approximated by the q function, which is equal to unity on Γ, and zero on Γ_0. As 2D plane strain conditions are approached asymptotically near crack tip field, the integration area A must be very close to the crack front. It is noteworthy that $\partial q/\partial x_3 = 0$ as q is a function of only x_1 and x_2.

Now consider the following two states of equilibrium superimposed on top of each other over the disk A: (**a**) an equilibrium state generated due to in-plane loads ($u^{\mathbf{a}} = \{u_1, u_2, 0\}^T, \epsilon^{\mathbf{a}} = \{\epsilon_{11}, \epsilon_{22}, \epsilon_{33}, \epsilon_{12}, 0, 0\}^T, \sigma^{\mathbf{a}} = \{\sigma_{11}, \sigma_{22}, \sigma_{33}, \sigma_{12}, 0, 0\}^T$); (**b**) an equilibrium state generated due to anti-plane loads ($u^{\mathbf{b}} = \{0, 0, u_3\}^T, \epsilon^{\mathbf{b}} = \{0, 0, 0, 0, \epsilon_{13}, \epsilon_{23}\}^T, \sigma^{\mathbf{b}} = \{0, 0, 0, 0, \sigma_{13}, \sigma_{23}\}^T$). The actual fields within the area A are obtained by superimposing the states **a** and **b** (see Fig. 4.5). The state **a** produces a mixed-mode I/II crack deformation only, while the state **b** can produce mode III deformation only. In fact, neither can state **a** produce mode III deformation ($K_{\mathrm{III}} = 0$ for state **a**), nor is state **b** able to generate in-plane crack deformation ($K_{\mathrm{I}} = K_{\mathrm{II}} = 0$ for state **b**). As a result, the two states are fully decoupled and cannot interact with each other, and therefore the J-integral of the superimposed state is equivalent to the sum of the J-integrals obtained from the fields in states **a** and **b** separately ($J = J^{\mathbf{a}} + J^{\mathbf{b}}$). As the second integral in Eq. (4.22) vanishes for each of equilibrium states **a** and **b**, the J-integral is simplified to

$$J(s) = \int_A \left(\sigma_{ij}\frac{\partial u_j}{\partial x_1} - W\delta_{1i}\right)\frac{\partial q}{\partial x_i}\mathrm{d}A - \int_{\Gamma_+ + \Gamma_-} \sigma_{2j}\frac{\partial u_j}{\partial x_1} m_2 q \mathrm{d}\Gamma \quad (4.23)$$

4.4.2 Interaction integral to extract SIFs

Again assume a virtual crack advance of $\delta l(s) = \delta(x_3 - s)b_1$ in the curvilinear coordinate system $x_1x_2x_3$, and the arbitrary path Γ with unit normal n_i which lies in the plane $x_3 = s$. The tubular surface Ω is formed by translating the contour Γ along the curved crack front

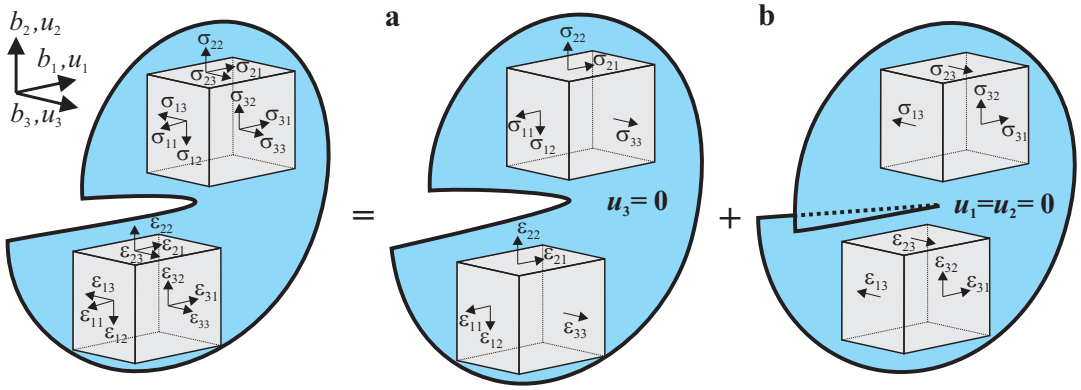

Figure 4.5: Decomposition of crack tip fields into state **a**: fields from in-plane loads, and state **b**: fields from anti-plane loads.

segment L_c (Fig. 4.4). From Eq. (4.14), and by defining $P'_{1i} = W_{\mathrm{I}}\delta_{1i} - (\sigma_{ij}\partial u_j^{\mathrm{aux}}/\partial x_1 + \sigma_{ij}^{\mathrm{aux}}\partial u_j/\partial x_1)$, the pointwise interaction integral is given by

$$I(s) = \lim_{\Gamma\to 0}\int_{\Gamma} P'_{1i}n_i \mathrm{d}\Gamma = \lim_{\Omega\to 0}\int_{\Omega} P'_{1i}n_i\delta(x_3 - s)\mathrm{d}\Omega \tag{4.24}$$

Again consider a tubular domain V as shown in Fig. 4.4, and the arbitrary continuously differentiable scalar function $q(x_1, x_2)$ which is equal to unity on Ω, and is zero on Ω_0. $q(x_1, x_2)\delta(x_3 - s)$ is therefore a continuously differentiable scalar function which is equal to $\delta l(x_3) = \delta(x_3 - s)$ on Ω, and is zero on Ω_0. It can be easily shown that $(\partial P'_{1i}/\partial x_i = 0)$ in the whole domain A, since for both actual and auxiliary fields the equilibrium conditions $(\partial\sigma_{ij}/\partial x_j = 0, \partial\sigma_{ij}^{\mathrm{aux}}/\partial x_j = 0)$ and compatibility conditions $(\partial u_j/\partial x_i - \epsilon_{ij} = 0, \partial u_j^{\mathrm{aux}}/\partial x_i - \epsilon_{ij}^{\mathrm{aux}} = 0)$ are satisfied. Applying the divergence theorem, the surface integral in Eq. (4.24) is reformulated to a domain integral as

$$\begin{aligned} I(s) = &\int_A \left(\sigma_{ij}\frac{\partial u_j^{\mathrm{aux}}}{\partial x_1} + \sigma_{ij}^{\mathrm{aux}}\frac{\partial u_j}{\partial x_1} - W_{\mathrm{I}}\delta_{1i}\right)\frac{\partial q}{\partial x_i}\mathrm{d}A \\ &-\frac{\partial}{\partial x_3}\int_A \left(\sigma_{3j}\frac{\partial u_j^{\mathrm{aux}}}{\partial x_1} + \sigma_{3j}^{\mathrm{aux}}\frac{\partial u_j}{\partial x_1}\right)q\mathrm{d}A - \int_{\Gamma_+ + \Gamma_-}\sigma_{2j}\frac{\partial u_j^{\mathrm{aux}}}{\partial x_1}m_2 q\mathrm{d}\Gamma \end{aligned} \tag{4.25}$$

where A is the disk-shaped domain in the plane orthogonal to the crack front at point s, and Γ_+ and Γ_- are the contours on the crack faces with $m_2 = -1$ and $m_2 = 1$, respectively. Again consider two following states of equilibrium superimposed on top of each other over the very small area A: (**a**) an equilibrium state generated due to in-plane loads ($u^{\mathbf{a}} = \{u_1, u_2, 0\}^T, \epsilon^{\mathbf{a}} = \{\epsilon_{11}, \epsilon_{22}, \epsilon_{33}, \epsilon_{12}, 0, 0\}^T, \sigma^{\mathbf{a}} = \{\sigma_{11}, \sigma_{22}, \sigma_{33}, \sigma_{12}, 0, 0\}^T$); (**b**) an equilibrium state generated due to anti-plane loads ($u^{\mathbf{b}} = \{0, 0, u_3\}^T, \epsilon^{\mathbf{b}} = \{0, 0, 0, 0, \epsilon_{13}, \epsilon_{23}\}^T, \sigma^{\mathbf{b}} = \{0, 0, 0, 0, \sigma_{13}, \sigma_{23}\}^T$). The actual fields within the area A are

obtained by superposing the states **a** and **b** (see Fig. 4.5). The state **a** produces a mixed-mode I/II crack deformation only, while the state **b** can produce mode III deformation only. Consider now the auxiliary fields for mode I as ($u^{\text{aux}} = \{u_1^{\text{aux}}, u_2^{\text{aux}}, 0\}^T, \epsilon^{\text{aux}} = \{\epsilon_{11}^{\text{aux}}, \epsilon_{22}^{\text{aux}}, \epsilon_{33}^{\text{aux}}, \epsilon_{12}^{\text{aux}}, 0, 0\}^T, \sigma^{\text{aux}} = \{\sigma_{11}^{\text{aux}}, \sigma_{22}^{\text{aux}}, \sigma_{33}^{\text{aux}}, \sigma_{12}^{\text{aux}}, 0, 0\}^T$).

K_{I} can now be computed by substituting superimposed states and the mode I auxiliary fields in Eq. (4.25). From the equilibrium states **a** and **b**, only state **a** contributes to the crack deformation in mode I, and the equilibrium state **b** shall be ignored. Considering the auxiliary fields, and equilibrium state **a** only, the second integral in Eq. (4.25) vanishes. The same logic can be applied for formulating the interaction integral associated with modes II and III to eliminate the second integral in Eq. (4.25). The interaction integral formulation in Eq. (4.25) therefore simplifies to

$$I(s) = \int_A \left(\sigma_{ij} \frac{\partial u_j^{\text{aux}}}{\partial x_1} + \sigma_{ij}^{\text{aux}} \frac{\partial u_j}{\partial x_1} - W_{\text{I}} \delta_{1i} \right) \frac{\partial q}{\partial x_i} \mathrm{d}A - \int_{\Gamma_+ + \Gamma_-} \sigma_{2j} \frac{\partial u_j^{\text{aux}}}{\partial x_1} m_2 q \mathrm{d}\Gamma \qquad (4.26)$$

By using the following auxiliary states of mode I $(K_{\text{I}}^{\text{aux}}, K_{\text{II}}^{\text{aux}}, K_{\text{III}}^{\text{aux}}) = (1, 0, 0)$, mode II $(K_{\text{I}}^{\text{aux}}, K_{\text{II}}^{aux}, K_{\text{III}}^{\text{aux}}) = (0, 1, 0)$, and mode III $(K_{\text{I}}^{\text{aux}}, K_{\text{II}}^{\text{aux}}, K_{\text{III}}^{\text{aux}}) = (0, 0, 1)$, three corresponding interaction integral values $I_{\text{I}}(s)$, $I_{\text{II}}(s)$ and $I_{\text{III}}(s)$ are obtained from Eq. (4.26), and the SIFs are extracted from Eq. (4.18).

4.5 Volumetric vs. disk-shaped domain integrals

New versions of domain integrals for computing J- and interaction integrals in 3D cracks were developed in Eqs. (4.23) and (4.26). These versions are similar to the domain integral formulations developed for 2D cracks. The main advantage of the volumetric domain integrals is that the domain can be built by a set of elements around the crack front. As a result, the numerical integration is readily implemented using the integration points of the elements. This is a major advantage of the volumetric domain approach, if a structured mesh provides a well-defined tubular region around the crack front. However, for the case of an unstructured mesh where the domain integral is most likely to be independent of the mesh structure, the volumetric domain integral may not be the best option.

The advantages of the disk-shaped domain integrals over the volumetric ones are as follows: (1) They can be readily implemented for unstructured meshes. (2) They directly use the original definition of the pointwise J integral and interaction integrals in Eqs. (4.4) and (4.14) without using any approximation. This is not the case in the volumetric domain integrals, where an error may arise from the assumption of the small variation of fracture parameters along the local crack segment L_c. (3) The new versions perform the integration over a disk perpendicular to the crack front, and therefore determining the position

of the integration points with respect to the curved crack front is very simple. In fact, in these domains, expressing the stress, strain and displacement fields in a curvilinear coordinate system is no longer required. This is not the case for the volumetric domains, where expressing the fields in a curvilinear coordinate system requires determining the position of integration points with respect to a curved crack front, which is usually performed by minimizing the distance of the integration point from the crack front through a Newton procedure. (4) As the 2D plane strain auxiliary fields do not satisfy the compatibility and equilibrium equations in the curvilinear coordinates, a new term containing the higher order gradients of the auxiliary fields emerges in the volumetric domain integral formulation (the second term in Eq. (4.19)). In the disk-shaped domain integral formulation, however, such a term does not exist as the 2D plane strain auxiliary fields satisfy the compatibility and equilibrium equations throughout a disk-shaped domain. (5) The new formulation requires less computational cost, as it performs integration over a disk rather than a tube. Moreover, unlike the volumetric approach, the disk-shaped domain integrals do not require performing iterative procedures to obtain the fields in curvilinear coordinates, which significantly reduces computational effort. (6) In the disk-shaped domain integral, the in-plane and anti-plane fields are separated, and cannot influence each other in the computation of fracture parameters. In fact, the in-plane numerical results cannot affect the computation of out-of-plane mode III stress intensity factor, and anti-plane numerical fields cannot also influence the computation of in-plane mode I and II stress intensity factors.

4.6 Finite element implementation details

New formulations for the evaluation of pointwise J- and interaction integrals using disk-shaped domains were presented in Section 4.4. As this type of domain cannot be represented by a set of volumetric elements, the existing elements cannot be directly used in the integration process. A novel, efficient and accurate approach for the evaluation of domain integrals, based on using a set of virtual triangular and line elements, is now presented. In this approach, the disk-shaped domain A is filled with virtual quadratic triangular elements, while the contours on the crack surfaces, Γ_- and Γ_+, are discretized by line elements (see Fig. 4.7). These elements are referred to as *virtual* since they are not used while performing the finite element solution of the boundary value problem. In fact, these elements are constructed in the post-processing stage, and discarded after the domain integrals are evaluated at the point s along the crack front. The presented domain integration can be readily implemented in any FE code. Moreover, these virtual elements make the process of integrating over the domain completely independent of the mesh structure and resolution around the crack front. This is a great advantage, as accurate domain integrals can be

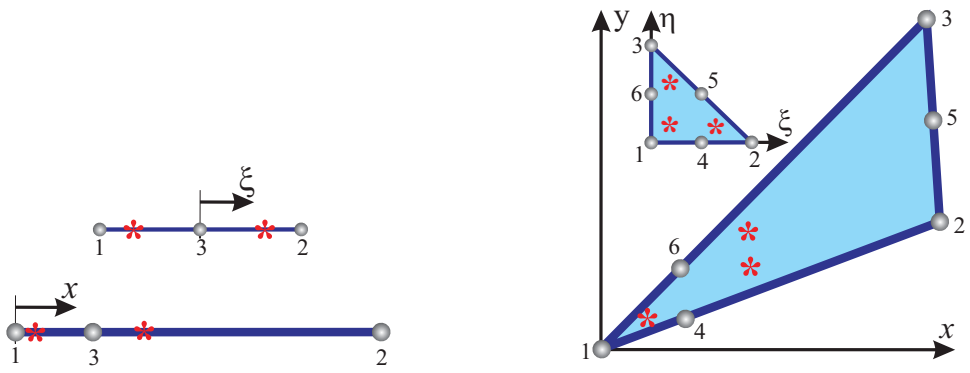

Figure 4.6: Configuration of nodes and integration points in (a) quarter-point line element and (b) quarter-point triangular element.

evaluated by using fine virtual elements, although a coarse mesh discretization may have been used for the finite element solution.

Consider point s along the crack front with the local coordinate system $x_1x_2x_3$. Due to the domain symmetry, only one-quarter of the disk of radius R_d is discretized with virtual triangular elements, and the contour Γ_+ is discretized by line elements. The integration over the other three quarters is readily evaluated by the reflection of integrating points of the generated virtual elements (see Fig. 4.7). Quarter-point tetrahedra reproduce square root singular $(1/\sqrt{r})$ fields in the vicinity of the crack front; therefore, the evaluation of line and area integrals in Eqs. (4.23) and (4.26) requires numerical integration of singular integrands of types $1/\sqrt{r}$, and $1/r$, respectively. Standard Gauss-quadrature integration scheme performs well only when the integrand varies gradually; in fact, the use of standard quadrature rules to compute the integration of singular functions results in significant errors unless the domain is subdivided into many subdivisions. Here it is proposed that the mid-side nodes of the virtual triangular/line elements attached to the crack front be moved to the quarter-point position (see Fig. 4.7). These quarter-point virtual elements significantly improve the accuracy of the numerical integration as explained below.

Consider $x_1 = 0$, $x_2 = L$, and $x_3 = L/4$ being the positions of nodes 1, 2 and 3 of the isoparametric quarter-point line element shown in Fig. 4.6a. Considering the element shape functions $N_1 = \xi(\xi-1)/2$, $N_2 = \xi(\xi+1)/2$, $N_3 = (1-\xi)(1+\xi)$, the mapping of the geometry from the local coordinate system x into the natural element coordinate system ξ, where $-1 \le \xi \le +1$, is given by $x(\xi) = \sum_{i=1}^{3} N_i x_i = (\xi+1)^2 L/4$. This mapping has a Jacobian of $\partial x/\partial\xi = (\xi+1)L/2$, which cancels out the square-root singular term in the integrand $(\int_0^L \mathrm{d}x/\sqrt{x} = \int_{-1}^{+1} \sqrt{L}\mathrm{d}\xi)$. The standard quadrature rule is now able to compute the exact value of the integral.

Consider now that the corner nodes 1, 2 and 3 of the quarter-point triangular element shown in Fig. 4.6b are located at $(0,0)$, (x_2,y_2), and (x_3,y_3), respectively. The positions of the mid-side node 5 and the quarter-point nodes 4 and 6 are $((x_2+x_3)/2,(y_2+y_3)/2)$, $(x_2/4,y_2/4)$, and $(x_3/4,y_3/4)$, respectively. Considering the natural coordinates $0\leq\xi\leq 1$, $0\leq\eta\leq 1$ and $\gamma=1-\xi-\eta$, the element shape functions are $N_1=\gamma(2\gamma-1)$, $N_2=\xi(2\xi-1)$, $N_3=\eta(2\eta-1)$, $N_4=4\gamma\xi$, $N_5=4\xi\eta$, $N_6=4\gamma\eta$, and the mapping of the geometry from the local coordinate system xy into the natural coordinate system $\xi\eta$ is given by

$$\begin{aligned} x(\xi,\eta)&=\textstyle\sum_{i=1}^{6}N_i x_i=(\xi+\eta)(\xi x_2+\eta x_3)\\ y(\xi,\eta)&=\textstyle\sum_{i=1}^{6}N_i x_i=(\xi+\eta)(\xi y_2+\eta y_3)\\ r(\xi,\eta)&=(\xi+\eta)^2\sqrt{\left[\frac{\xi x_2+\eta x_3}{\xi+\eta}\right]^2+\left[\frac{\xi y_2+\eta y_3}{\xi+\eta}\right]^2} \end{aligned} \tag{4.27}$$

where r denotes the radial distance from the node 1 (crack tip). This mapping gives the determinant of the Jacobian matrix $\mathbf{J}=\partial(x,y)/\partial(\xi,\eta)$ as $|\mathbf{J}|=2(\xi+\eta)^2(x_2y_3-x_3y_2)$ which cancels out the singular term in the integrand:

$$\int_A\frac{\mathrm{d}A}{r}=\int_0^1\int_0^1\frac{2(x_2y_3-x_3y_2)}{\sqrt{\left[\frac{\xi x_2+\eta x_3}{\xi+\eta}\right]^2+\left[\frac{\xi y_2+\eta y_3}{\xi+\eta}\right]^2}}\mathrm{d}\xi\mathrm{d}\eta \tag{4.28}$$

in which A is the area of the triangular element. This transformation significantly improves the accuracy of the numerical integration using a standard quadrature-rule procedure. In fact, the integration points are placed closer to the singular point in quarter-point elements, which helps them to efficiently capture the high gradients of singular integrands near the singular point. It is noteworthy that these virtual quarter-point triangular elements have to be used only when quarter-point tetrahedral elements have been employed in the FE solution; virtual standard triangular elements would suffice when standard tetrahedral elements are used in the vicinity of the crack front.

Using the virtual elements, evaluation of the domain integrals in Eqs. (4.23) and (4.26) follows the same standard Gauss-quadrature integration scheme available in any FE code:

$$\begin{aligned} J(s)=&\sum_{A}^{\text{elems}}\sum_{p}^{\text{gpts}}\left\{\left[\left(\sigma_{ij}\frac{\partial u_j}{\partial x_1}-W\delta_{1i}\right)\frac{\partial q}{\partial x_i}\right]|\mathbf{J}|\right\}_p w_p\\ &-\sum_{\Gamma_-+\Gamma_+}^{\text{elems}}\sum_{p}^{\text{gpts}}\left[\left(\sigma_{2j}\frac{\partial u_j}{\partial x_1}m_2 q\right)|\mathbf{J}|\right]_p w_p \end{aligned} \tag{4.29}$$

$$\begin{aligned} I(s)=&\sum_{A}^{\text{elems}}\sum_{p}^{\text{gpts}}\left\{\left[\left(\sigma_{ij}\frac{\partial u_j^{\text{aux}}}{\partial x_1}+\sigma_{ij}^{\text{aux}}\frac{\partial u_j}{\partial x_1}-W_{\text{I}}\delta_{1i}\right)\frac{\partial q}{\partial x_i}\right]|\mathbf{J}|\right\}_p w_p\\ &-\sum_{\Gamma_-+\Gamma_+}^{\text{elems}}\sum_{p}^{\text{gpts}}\left[\left(\sigma_{2j}\frac{\partial u_j^{\text{aux}}}{\partial x_1}m_2 q\right)|\mathbf{J}|\right]_p w_p \end{aligned} \tag{4.30}$$

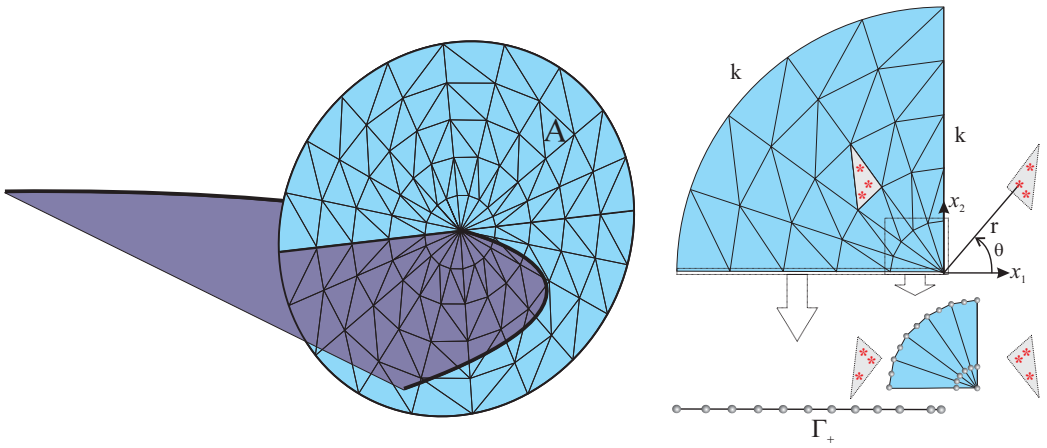

Figure 4.7: (a) Virtual second-order triangular and line elements constitute the integration domain, (b) details of the virtual mesh.

where the summations over area A and contour $\Gamma_- + \Gamma_+$ include all the virtual triangular and line elements, respectively. The sum over p includes element integration points, 'gpts', of the virtual elements, 'elems', where the bracketed quantities $\{\}_p$ and $[]_p$ are evaluated and multiplied by the corresponding weight w_p. Repeated indices imply summation, and $|\mathbf{J}|$ denotes the determinant of the coordinate Jacobian matrix of the virtual triangular and line elements.

The computation of area integrals in Eqs. (4.29) and (4.30) requires the computation of the stress, strain and displacement gradient tensors at the integration points of the virtual elements. These values have to be extracted from the FE solution over the tetrahedral element that contains the integration point of the virtual element. This requires the following steps: (i) The tetrahedral element containing the virtual integration point p is identified by using a search algorithm explained in Section 2.6. (ii) The local coordinates of the point p inside the tetrahedral element are computed using the expressions in Section 2.6. (iii) The stress, strain and displacement gradient tensors of these integration points are directly obtained from the FE displacement solution over the tetrahedral element. All these quantities must be expressed in the local coordinate system $x_1x_2x_3$ located at point s on the crack front (see Fig. 4.5). The evaluation of line integrals also requires the computation of surface traction σ_{2j} and displacement gradient $\partial u_j/\partial x_1$ at the virtual integration point p on the crack surface. Computing these values also requires the following steps: (i) The triangular element that contains p is identified; (ii) The local coordinates of the point p in the triangular element are computed; (iii) σ_{2j} and $\partial u_j/\partial x_1$ at p are computed by interpolating the nodal tractions and displacement derivatives using the element shape functions (see Section 2.6). It is also straightforward to compute the values for q-function and its

derivative, and the auxiliary fields σ_{ij}^{aux}, and $\partial u_j^{\text{aux}}/\partial x_1$ at the virtual integration point p. This only requires substituting the position of p in the local coordinate system located at s into the q-function and analytical auxiliary fields expressions given in Eqs. (4.7-4.12). As q is a function of x_1 and x_2 only, the derivative with respect to x_3 vanishes ($\partial q/\partial x_3 = 0$). The procedure of computing J-integral and the SIFs is demonstrated in Algorithm (1).

Algorithm 1 Evaluation of the pointwise J-integral and SIFs using the disk-shaped domain integral method

Generate a local coordinate system $x_1x_2x_3$ at the point s using the unit vectors b_1, b_2 and b_3.
Create a virtual disk-shaped integration domain using quadratic triangular and line elements.
for $e := 1 \rightarrow \mathrm{N_{tr}}$ **do**
  for $p := 1 \rightarrow \mathrm{N_P}$ **do**
    Find the tetrahedral element which contains the point p.
    Compute the local coordinates (ξ, η, ζ) of p in the tetrahedral element.
    Compute σ_{ij}, ϵ_{ij}, $\nabla \times u$ at p in the local coordinate system.
    Compute the auxiliary fields σ_{ij}^{aux}, and $\partial u_j^{\text{aux}}/\partial x_1$ at p .
    Compute $\partial q/\partial x_i$ at p.
    Compute $|\mathbf{J}|$ at p using virtual triangular element coordinate matrix.
    Accumulate: $J(s) \leftarrow J(s) + \left[\left(\sigma_{ij}\dfrac{\partial u_j}{\partial x_1} - W\delta_{1i}\right)\dfrac{\partial q}{\partial x_i}\right]|\mathbf{J}|\, w_p$
    Accumulate: $I_{\mathrm{z}}(s) \leftarrow I_{\mathrm{z}}(s) + \left[\left(\sigma_{ij}\dfrac{\partial u_j^{\text{aux}}}{\partial x_1} + \sigma_{ij}^{\text{aux}}\dfrac{\partial u_j}{\partial x_1} - W_{\mathrm{I}}\delta_{1i}\right)\dfrac{\partial q}{\partial x_i}\right]|\mathbf{J}|\, w_p$
  end for
end for
for $e := 1 \rightarrow \mathrm{N_{li}}$ **do**
  for $p := 1 \rightarrow \mathrm{N_P}$ **do**
    Find the triangular surface element which contains the point p.
    Compute the local coordinates (ξ, η) of p in the triangular element.
    Compute the traction σ_{ij}, and $\nabla \times u$ at p in the local coordinate system.
    Compute the auxiliary field $\partial u_j^{\text{aux}}/\partial x_1$ at p.
    Compute q at p.
    Compute $|\mathbf{J}|$ at p using virtual line element coordinate matrix.
    Accumulate: $J(s) \leftarrow J(s) - \left(\sigma_{2j}\dfrac{\partial u_j}{\partial x_1}m_2 q\right)|\mathbf{J}|\, w_p$
    Accumulate: $I_{\mathrm{z}}(s) \leftarrow I_{\mathrm{z}}(s) - \left(\sigma_{2j}\dfrac{\partial u_j^{\text{aux}}}{\partial x_1}m_2 q\right)|\mathbf{J}|\, w_p$
  end for
end for
Compute SIFs from Eq. (4.18)

▷ $\mathrm{N_{tr}}$, $\mathrm{N_{li}}$, and $\mathrm{N_P}$ are the numbers of virtual triangular elements, virtual line elements, and the element's integration points, respectively. ▷ $I_{\mathrm{z}}(s)$ is computed using the auxiliary fields of crack deformation mode z ($\mathrm{z} = \mathrm{I}, \mathrm{II}, \mathrm{III}$).

All procedures employed in this work were implemented into the IC Geomechanics

toolkit, a geomechanical module [Paluszny and Matthäi, 2009; Paluszny and Zimmerman, 2011] of the Complex System Modeling Platform (CSMP++), an object-oriented finite element based API developed for the simulation of complex geological processes [Matthäi et al., 2001]. The system of equations resulting from the finite element method accumulation is solved using the Fraunhofer SAMG Solver [Stüben, 2001].

4.7 Numerical examples

In order to demonstrate the efficiency and accuracy of the proposed approach, the J-integral and stress intensity factors were computed for the following three crack configurations: (i) through-the-thickness crack in a large thin plate with lateral constraint (plane strain condition); (ii) penny-shaped crack embedded in an infinite solid; and (iii) elliptical crack embedded in an infinite solid, as shown in Fig. 4.8.

4.7.1 Experimental setup

All the crack bodies are subjected to a uniform uniaxial tension in the X_2 direction over the top and bottom surfaces. The cracks lie in the plane $X_2 = X_1 \cot \beta$ which generates the angle of β with the direction of applied load. A horizontal crack configuration ($\beta = 90°$) produces pure mode I crack deformation, while the inclined one ($0° < \beta < 90°$) provokes a mixed-mode condition. In these configurations, a denotes half of the crack length for the through crack, crack radius for the penny-shaped crack, and semi-major axis for the elliptical crack. The semi-minor axis b of the elliptical crack is perpendicular to the X_1X_2 plane. The crack length to body width ratio of $a/w = 0.1$ was used for all the cracked bodies. The crack length to the plate thickness of $a/t = 1$ was considered for the through-the-thickness crack. As the fracture parameters of these crack configurations are independent of the value of Young's modulus, an arbitrary value of $E = 1\,\text{MPa}$ was used in all models. The choice of Poisson's ratio is not arbitrary, as the mode II and III SIFs of embedded cracks depend strongly on the value of this material property (see analytical solutions in Appendix). In this work, a Poisson's ratio of $\nu = 0.3$ was used for all simulations.

Boundary conditions

Due to the symmetry in geometry and loading conditions, only one-eighth ($X_1 > 0, X_2 > 0, X_3 < 0$) and one-half ($X_3 < 0$) of the cracked bodies were modeled for pure mode I ($\beta = 90°$) and mixed-mode ($\beta = 45°$) conditions, respectively. The following boundary conditions were applied for mode I models: $u_1 = 0$ over the plane $X_1 = 0$, $u_2 = 0$ over the plane $X_2 = 0$ except over the crack surface, $u_3 = 0$ over the plane $X_3 = 0$, and $\sigma = 1$ over the plane $X_2 = w$. The applied boundary conditions for the mixed-mode models are also as

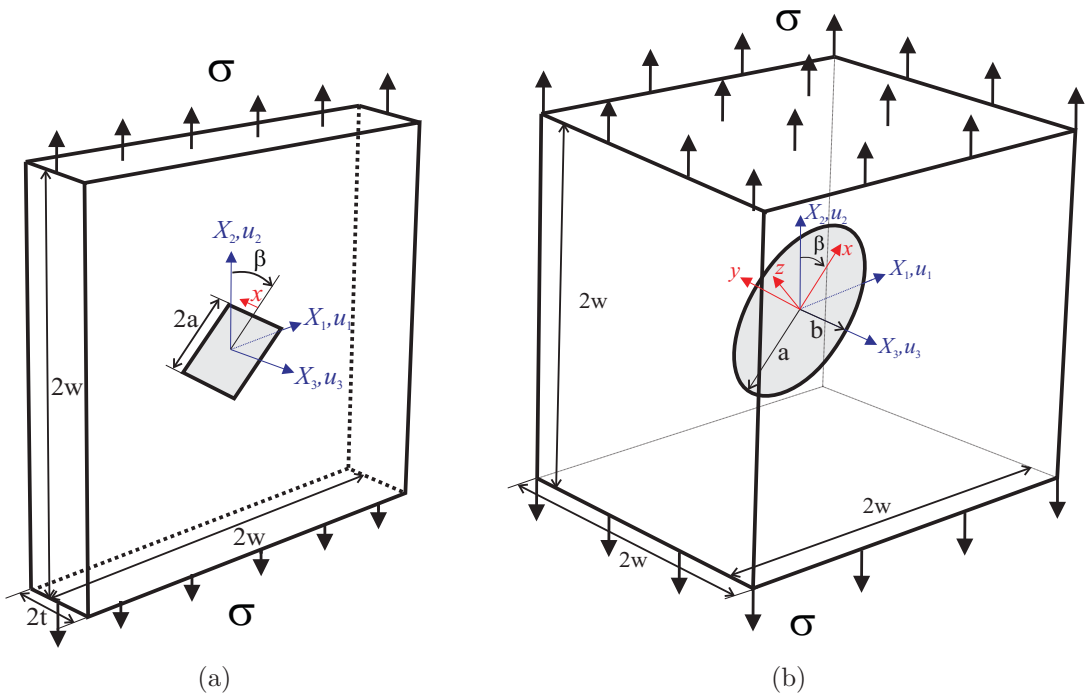

Figure 4.8: Schematics of (a) Through-the-thickness crack in a large thin plate under uniaxial tension; (b) Penny-shaped/elliptical crack embedded in an infinite solid under uniaxial tension.

follows: $u_1 = 0$ at the point $X_1 = X_2 = -w, X_3 = 0$, $u_2 = 0$ over the plane $X_2 = -w$, $u_3 = 0$ over the plane $X_3 = 0$, and $\sigma = 1$ over the plane $X_2 = w$. For the through-the-thickness crack, the following additional boundary condition was also applied, to ensure zero lateral displacement: $u_3 = 0$ over the plane $X_3 = -t$. This boundary condition imposes a plane strain condition over the cracked plate, where the pointwise SIFs at any point on the crack front follows the solution of the equivalent 2D problem of an inclined central crack in a large plane. This solution gives the SIFs as follows: $K_{\mathrm{I}} = \sigma\sqrt{\pi a}\sin^2\beta$, $K_{\mathrm{II}} = \sigma\sqrt{\pi a}\sin\beta\cos\beta$, and $K_{\mathrm{III}} = 0$. These formulas along with the analytical solutions for the SIFs of embedded inclined penny-shaped and elliptical cracks in infinite solids given in Appendix will be used to validate the numerical results.

Mesh

An octree-based mesh generation software was employed to generate arbitrary meshes for all specimens, using 10-noded isoparametric tetrahedral elements. For the elements attached to the crack front, the nodes near the front are moved from the mid-side point to the quarter-point position to produce inverse square root singular fields near the front. The curved crack fronts impose one curved edge for the tetrahedral elements sharing an edge with the crack front. When using quarter-point elements, the Jacobian determinant over a small

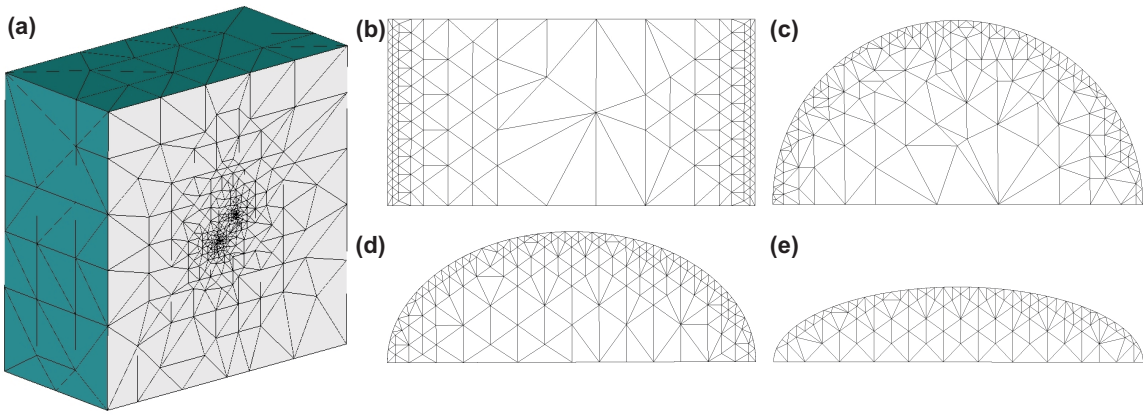

Figure 4.9: (a) Finite element mesh discretizing one-half of an embedded penny-shaped crack; Details of mesh in crack-front region for (b) through-the thickness, (c) penny-shaped, (d) elliptical ($b/a = 0.7$), (e) elliptical ($b/a = 0.4$) cracks. For all cases $L_n \approx a/20$.

volume near the curved edges becomes negative. To avoid this, as suggested in Chapter 2, the curve edges were straightened by moving the mid-side nodes of the curved segments. The refinement of the mesh near the crack front was controlled by assigning the number of segments along the crack front. Assume that the crack front of length L_f is discretized by N_f segments. A parameter called the nominal length (size) of the elements in the crack front region can be defined as $L_n = L_f/N_f$. The nominal element length L_n represents the approximate length of the elements' sides near the crack front, and therefore gives an approximate for the average size of the tetrahedral elements in the crack front region. In all models, the degree of mesh refinement in the crack front region was controlled by keeping the nominal crack front element size about one twentieth of the crack length ($L_n \approx a/20$). As estimations suggest that the size of the singular dominant zone depends mainly on the crack length, ranging between $a/10$ and $a/50$ [Kuna, 2013], keeping $L_n \approx a/20$ ensures that the quarter-point elements at the crack front predominantly remain in the singular dominant zone where the fields have the inverse square root singularity. Four-point, three-point, and two-point Gaussian quadrature rules were employed for the numerical integration over tetrahedral, triangular, and line elements, respectively. Figure (4.9) shows the finite element mesh of the penny-shaped crack problem together with the local mesh refinements near the crack front in different crack configurations.

Domain size and virtual mesh

For all crack configurations, the mesh-dependent domain radius of $R_d = L_n$ has been used to generate the virtual domains and compute the fracture parameters. Domains were built at the locations of both corner and mid-side nodes of the segments along the crack front.

The refinement of the virtual mesh is controlled by the number of domain elements in the radial direction k as shown in Fig. 4.7. A similar virtual mesh structure as the one shown in Fig. 4.7, with four elements in radial direction ($k = 4$), was used to compute the fracture parameters. This choice yields 112 quadratic triangular elements, containing 112×3 integration points, together with 8 quadratic line elements, containing 8×2 integration points. The reasons for these choices are explained in Sections 4.8.1 and 4.8.2.

The scalar function q

In order to compute the fracture parameters, a smooth function q must be defined over the domain (disk) area. All the numerical results in this chapter are determined by using $q = 1 - r/R_d$, where $r = \sqrt{x_1^2 + x_2^2}$ is the distance from disk center and R_d is the domain radius (see Fig. 4.7). The derivatives of this function ($\partial q/\partial x_1 = -x_1/rR_d$ and $\partial q/\partial x_2 = -x_2/rR_d$) are directly evaluated at the integration points of the virtual triangular elements. Section 4.8.3 explains how the numerical results are influenced by changing this function.

After the computation of the pointwise SIFs along the crack fronts, the average numerical error of SIF computation for individual modes e_{i} ($\mathrm{i} = \mathrm{I}, \mathrm{II}, \mathrm{III}$) and average total error e_{t} were evaluated by using Eq. (4.31). In these expressions, K_{i}^A and K_{i}^N are the pointwise analytical and numerical mode i SIFs, respectively, and L_f is the crack front length. Wherever closed form integration was not available, a trapezoidal rule has been employed to evaluate the integrals numerically.

$$e_{\mathrm{i}} = \frac{\displaystyle\int_{L_f} |K_{\mathrm{i}}^A - K_{\mathrm{i}}^N| \mathrm{d}l}{\displaystyle\int_{L_f} |K_{\mathrm{i}}^A| \mathrm{d}l} \quad \mathrm{i} = \mathrm{I}, \mathrm{II}, \mathrm{III} \qquad e_{\mathrm{t}} = \frac{\displaystyle\sum_{\mathrm{i}=\mathrm{I}}^{\mathrm{III}} \int_{L_f} |K_{\mathrm{i}}^A - K_{\mathrm{i}}^N| \mathrm{d}l}{\displaystyle\sum_{\mathrm{i}=\mathrm{I}}^{\mathrm{III}} \int_{L_f} |K_{\mathrm{i}}^A| \mathrm{d}l} \tag{4.31}$$

4.7.2 Pure mode I SIFs

Fig. 4.10 shows the variation of the pointwise mode I stress intensity factor along the crack front of different crack configurations when $\beta = 90°$. Analytical solutions for a 2D plane strain central crack problem, and 3D penny-shaped and elliptical cracks embedded in infinite solids (Appendix) are also plotted. Here, ϕ and ω are the polar angle of the circle, and the parametric angle of the ellipse, respectively. The numerical K_{I} values have been computed by the evaluation of J- and interaction integrals in Eqs. (4.29) and (4.30), and their substitution into Eqs. (4.15) and (4.18) for the following loading conditions: (i) the specimens are subjected to original far field load σ as shown in Fig. 4.8; (ii) instead of applying the load at the far field, σ was applied over the fracture surface. These loading conditions are equivalent according to the superposition principle, generating identical SIFs.

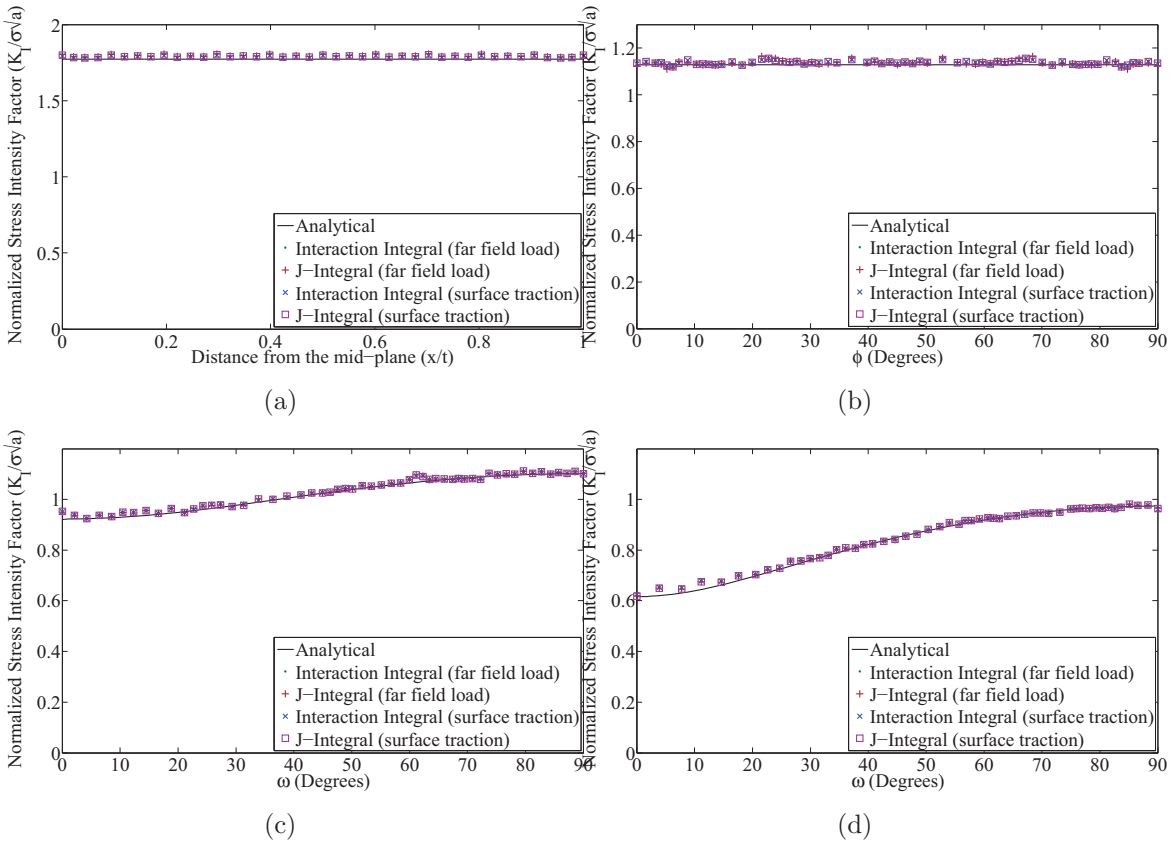

Figure 4.10: The variation of normalized mode I ($\beta = 90°$) analytical and numerical SIFs along the fronts of (a) through-the-thickness, (b) penny-shaped, (c) elliptical ($b/a = 0.7$), (d) elliptical ($b/a = 0.4$) cracks using J- and interaction integrals. The mode I average error is as follows: (a) $e_{\mathrm{I}} = 0.011$, (b) $e_{\mathrm{I}} = 0.008$, (c) $e_{\mathrm{I}} = 0.008$, (d) $e_{\mathrm{I}} = 0.008$.

The average error e_{I} for any of these four sets of results is about 1%. Highly accurate values in the case of surface tractions demonstrate the efficiency of line elements for accurate numerical computation of surface traction integrals.

4.7.3 Mixed-mode SIFs

Fig. 4.11 shows the variation of pointwise mixed-mode SIFs along the crack front of four different crack configurations, when $\beta = 45°$. The average total error e_{t} for all the cases is about 1%. These results are obtained from a relatively coarse mesh (see Fig. 4.9), and a finer mesh will result in the computation of even more accurate SIFs. These results demonstrate the efficiency of the disk-shaped domains to accurately compute the interaction integral from arbitrary meshes. Section 4.8 discusses the effects of actual and virtual mesh refinements as well as domain radius on these results.

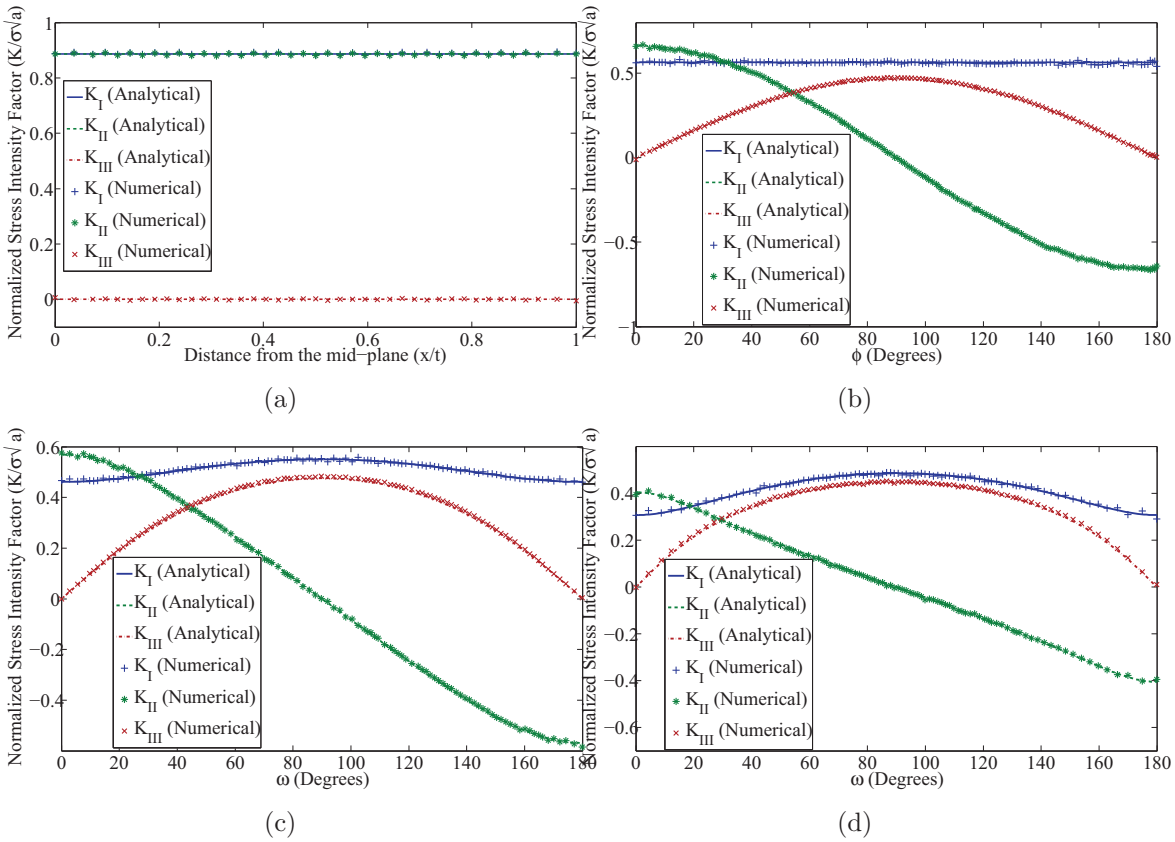

Figure 4.11: The variation of normalized mixed-mode ($\beta = 45°$) analytical and numerical SIFs along the fronts of (a) through-the-thickness, (b) penny-shaped, (c) elliptical ($b/a = 0.7$), (d) elliptical ($b/a = 0.4$) cracks. The average total SIF computation error is as follows: (a) $e_{\mathrm{t}} = 0.005$, (b) $e_{\mathrm{t}} = 0.011$, (c) $e_{\mathrm{t}} = 0.012$, (d) $e_{\mathrm{t}} = 0.013$.

4.7.4 SIFs near corner points

Consider the through-the-thickness crack problem, when no lateral constraint is applied to the plate, leaving the lateral surfaces traction free. The main characteristics of the behavior in this cracked body are: (i) At the intersection of the crack front and free surface a corner singularity occurs, where the order of the singularity, which depends on Poisson's ratio as well as on the loading conditions, is different from the crack singularity [Benthem, 1977; Bažant and Estenssoro, 1979]. As a result, at the exact corner point, the definition of crack stress intensity factor loses its meaning, since an inverse square root singular field no longer exists [Nakamura and Parks, 1988, 1989]. (ii) Modes II and III become coupled, meaning that applying primary shear or anti-plane loading on the plate also generates a coupled mode III, or mode II crack deformation, respectively [Bažant and Estenssoro, 1979; Nakamura and Parks, 1988, 1989; Kotousov et al., 2013]. This coupling occurs due to the Poisson's ratio effect or the redistribution of stresses near the free surfaces [Kotousov et al., 2010, 2013; Pook et al., 2014]. For example, when a primary mode II crack deformation

($K_{\mathrm{II}} > 0$) is applied to the cracked plate, a coupled mode III deformation also occurs due to the Poisson's effect, as the plate above the crack plane is expanded along thickness direction, while the region below the crack plane is contracted. It has been shown that the intensities of the coupled modes can be as strong as those of primary modes [Kotousov et al., 2013]. Because of these two characteristics, the strong 3D effects influences the stress fields near the crack front, and a classical two-dimensional (plane) elasticity solution is no longer able to reproduce the stress intensities along the crack front.

Now assume that a primary mixed-mode I/II load is applied on a through-the-thickness crack with traction-free surfaces. A few characteristics of the SIF variation along the crack front must be noted: (i) As explained earlier, although the cracked plate is primarily subjected to a mixed-mode I/II loading condition, a couple mode III crack deformation is also created due to the Poisson effects. (ii) Under symmetric loading, the corner singularity is weaker than the crack singularity, and therefore the local K_{I} must approach zero at the free surface [Nakamura and Parks, 1988; Benthem, 1977; Bažant and Estenssoro, 1979; Benthem, 1980; He et al., 2015]. This does not mean that the stress is finite at the corner point, but it demonstrates that K_{I} cannot be used to characterize the fields at the corner point. (iii) On the other hand, for the antisymmetric loading condition, the corner singularity is stronger than a crack singularity, and therefore the local K_{II} approaches infinity at the free surfaces [Nakamura and Parks, 1989; Benthem, 1977; Bažant and Estenssoro, 1979; Benthem, 1980; He et al., 2015]. (iv) The coupled mode III deformation behaves differently compared to K_{I} and K_{II}, since K_{III} must be zero at mid-plane and free surfaces, due to the symmetry and traction free boundary conditions, respectively. In fact, K_{III} is zero at the mid-plane, reaches its maximum value near the free surface, and drops back to zero at the corner point [Harding et al., 2010; Kotousov et al., 2010, 2013]. This behavior is not observed in the results of Nakamura and Parks [1989] as the coupled mode III SIF, which is computed using the volumetric domain integral approach, appears to approach infinity at the free surface. Such behavior is inconsistent with the free boundary conditions and zero anti-plane shear stress at the free surfaces. This inconsistency has been noticed by Harding et al. [2010]; Kotousov et al. [2010], as the K_{III} values they computed using the stress extrapolation method deviates from the ones obtained by Nakamura and Parks [1989] for the points very close to the corner point. The reason for this inconsistency has not been previously investigated.

The proposed method is now used to compute the SIFs of a plate with traction-free lateral surfaces containing an inclined through-the-thickness crack with $\beta = 45°$. A very fine mesh ($L_n = a/400$) was generated, and the SIFs at nodes along the crack front were computed using the disk-shaped domains of radius $R_d = 2L_n$. Fig. 4.12a shows the variation of SIFs against the normalized distance from the mid-plane, x/t. The specimen was also

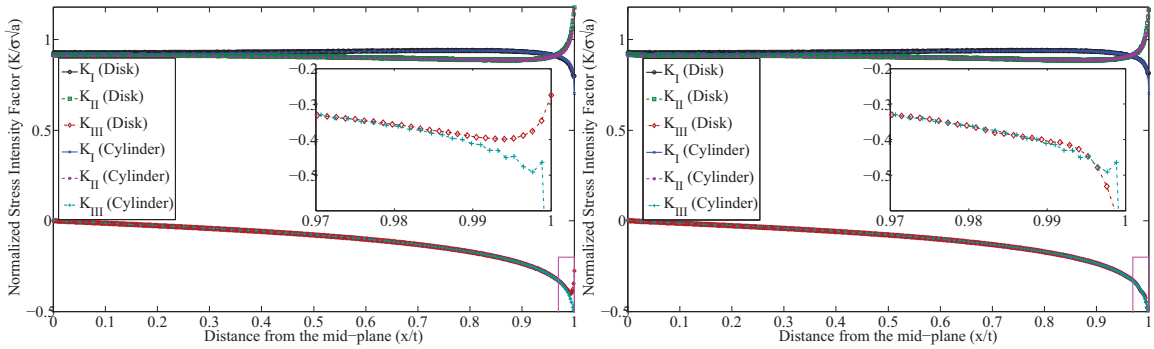

Figure 4.12: The variation of normalized numerical SIFs along the through-the-thickness crack front when the lateral surfaces are traction-free ($\beta = 45°$). For both plots the cylinder results are computed from cylindrical domains using Abaqus contour integral module. Eqs. (4.26) and (4.25) are used respectively to compute disk results for (a) and (b).

modeled and analyzed with SIMULIA Abaqus FEA, where a structured mesh by collapsed quarter-point hexahedral elements with an equivalent crack front region mesh density was used. The SIFs were computed using an equivalent cylinder radius of $R_d = 2L_n$ in the contour integral module of this commercial FE package. The module uses the volumetric cylindrical domains explained in Section 4.3 to compute the SIFs [Abaqus, 2012]. These results are plotted against the normalized distance from the mid-plane in Fig. 4.12a. A comparison of the two methods shows that the results are in very close agreement, except very near the corner point, $x/t = 1$. The results from both methods demonstrate that K_{I} and K_{II} approach zero and infinity, respectively. However, the coupled K_{III} results from the cylindrical domains tend to infinity, similar to the trend reported in Nakamura and Parks [1989], while those from disk-shaped domains seem to approach zero, which is consistent with the trend reported by Harding et al. [2010]; Kotousov et al. [2010, 2013]. Let us now use Eq. (4.25) instead of Eq. (4.26) to evaluate the integrals for the disk-shaped domains. Eq. (4.25) contains one more term, the second term, where in-plane and anti-plane crack tip fields are coupled in the process of SIF computation. This term vanishes in Eq. (4.26) by employing the superposition principle, as discussed in Section 3. The following steps were taken to compute this term: (i) the integral associated with this term was computed at the points along the crack fronts; (ii) at each point a polynomial equation was fitted locally to the integral values using the least square scheme; (3) the derivative of the polynomial was computed at the point. Fig. 4.12b shows the variation of SIFs computed by Eq. (4.25) against the normalized distance from the mid-plane. As seen, the results of the disk-shaped domains are now consistent with cylindrical domains, providing questionable trend for K_{III} near the corner point.

Consider the integral term developed by substituting $i = 3$ into Eq. (4.6). This integral term is evaluated over the tubular domain shown in Fig. 4.2. Also consider the function q over the volume V as $q = q'(x_1, x_2)q''(x_3)$, where $q'(x_1, x_2)$ describes the variation of q over a disk-shaped area A, and $q''(x_3)$ describes the variation of q along the small crack front segment L_c (see Fig. 4.4). If the crack fields vary slightly along L_c, the integral $\int_A \sigma_{3j}\partial u_j/\partial x_1 q'(x_1, x_2)$ can be assumed to behave linearly along L_c. Using integration by parts, therefore, the term $i = 3$ in Eq. (4.6) can be expressed in the form of an area integral as

$$\frac{\displaystyle\int_V \sigma_{3j}\frac{\partial u_j}{\partial x_1}\frac{\partial q}{\partial x_3}\mathrm{d}V}{\displaystyle\int_{L_c} q(x_3)\mathrm{d}x_3} = -\frac{\partial}{\partial x_3}\int_A \sigma_{3j}\frac{\partial u_j}{\partial x_1}\, q'(x_1, x_2)\mathrm{d}A \tag{4.32}$$

where A is the disk-shaped area developed when an orthogonal plane to the crack front intersects the tubular region V at the mid-point of L_c (see Fig. 4.4). A similar equivalent area integral can be found for the term developed when $i = 3$ is substituted in the first term of Eq. (4.19). These relations indicate that the volumetric versions of domain integrals in Eq. (4.6) and (4.19) approximately evaluate the second terms of the disk-shaped domain integral formulas in Eqs. (4.22) and (4.25). As discussed in Sections 4.4.1 and 4.4.2 these terms couple the fields from in-plane and anti-plane loads. It was then shown that, by applying the superposition principle, these terms can be eliminated, and Eqs. (4.23) and (4.26) were suggested for the disk-shaped domain integral formulations. The inaccurate trend of K_{III} near the corner point when using volumetric domain integrals can be attributed to the presence of these terms in their formulation. Strong variation of modes I/II fields occurs near the corner point, and the gradients of these fields with respect to x_3 are high enough to influence K_{III} significantly via the coupling term developed by substituting $i = 3$ in Eq. (4.19), or the second term in Eq. (4.25). Such an influence is not allowed in the disk-shaped domain formulation proposed in this chapter, i.e. Eq. (4.26); therefore this formulation can reproduce a more accurate variation of SIFs near the corner point. It must be noted that the values of SIFs in Fig. 4.12a may vary slightly by using a finer mesh, but the trend remains the same. It is generally advised that a more refined mesh is used to compute more accurate values of the SIFs near the corner point.

4.8 Discussion

Three parameters mainly influence the computation of the fracture parameters using the proposed method: mesh refinement at the crack front region, virtual mesh refinement of the disk, and domain (disk) size. The domains must remain in the singular-dominant region, where a plane strain condition prevails. Thus, one should avoid using large domains

compared to the crack sizes. However, a very small domain may also capture only the FE fields which are not accurate enough due to the high local numerical errors to represent crack tip fields. Therefore, for every mesh resolution, there will be an optimum domain size at which the computed fracture parameters are the most accurate. As the degree of the accuracy of the fields near the crack depends on the type and refinement of the elements in that region, it is expected that the optimum domain size depends mainly on the type and size of the elements in the crack front region. To clarify the dependency of the proposed domain integral approach on these three parameters, an extensive parametric study is carried out in this Section. The SIFs of the crack configurations described in the previous section were computed while changing these three parameters, and the formulas in Eq. (4.31) were used to evaluate the average of total SIF computation error.

4.8.1 Refinement of virtual mesh

Consider the virtual mesh structure shown in Fig. 4.7 with k and $4 \times k$ grids in the radial and circumferential directions, respectively. In this mesh structure, k controls the virtual mesh refinement by generating $(4 \times k)[(2 \times k) - 1]$ virtual triangular elements and $2 \times k$ line elements. The crack front of length L_f is discretized by N_f segments. The nominal size of the elements in the crack front region is defined as $L_n = L_f/N_f$, which quantifies the refinement of the actual mesh in the crack front region. Figure (4.13) shows the variation of average total SIF error e_{t} for different actual mesh refinements, a/L_n, versus the number of virtual elements in radial direction, k, used to compute the SIFs of the penny-shaped crack for two domain radiuses $R_d = a/10$ and $R_d = a/20$. In both the virtual and actual meshes, quarter-point elements have been used at the immediate crack front region. These graphs demonstrate the following: (i) The virtual elements are very efficient in capturing the crack fields, as accurate values can be computed for the SIFs even when very coarse virtual elements are employed ($k = 1$), and using a more refined mesh does not significantly change the SIFs. This is mainly because the quarter-point virtual elements are very accurate and efficient in numerical integration of singular fields. (ii) The SIF computation error drops slightly by increasing k to 4, remaining steady for greater values of k. A similar behavior was also observed in other crack configurations and other choices of the domain radius. This suggests that the choice of $k = 4$ generates a sufficiently refined virtual mesh that is able to capture all the crack tip field variations that a very refined actual mesh can reproduce. This finding allows the virtual mesh density to be chosen independent of the actual mesh refinement, and of the domain size. It is recommended that $k = 3, 4$ be used for the fast and efficient computation of SIFs, and $k = 5, 6$ for a more robust SIFs computation.

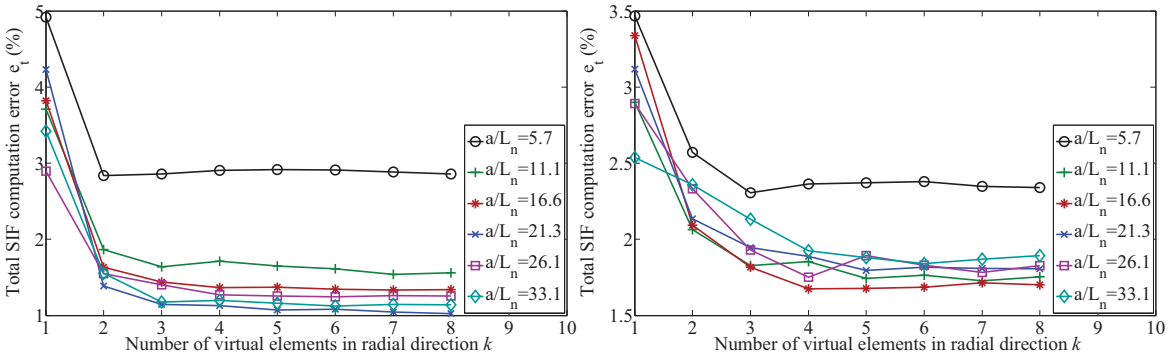

Figure 4.13: The variation of the total SIF computation error e_t of the penny-shaped crack under mixed-mode loading condition ($\beta = 45°$) versus the number of the virtual elements in the radial direction k in different mesh refinements: (a) $R_d = a/20$, (b) $R_d = a/10$.

4.8.2 Disk (domain) radius

An optimum size is expected to exist, which depends on the local actual mesh refinement in the front region. A very large domain compared to the crack size leads to the violation of the basic assumption of having a plane strain condition within the domain. The domain radius, therefore, must be chosen to be as small as possible. The size of the singular-dominant zone can be considered as an upper bound for the domain radius. This requires the domain radius to be smaller than the size of the singular dominant zone which mainly depends on the characteristic crack length, ranging between a/10 and a/50 [Kuna, 2013]. However, very small domains might also introduce high errors, since the closer to the crack front, the higher the error of FE fields [Paluszny and Zimmerman, 2011]. In addition, crack tip fields are obtained from the FE solution, where the equilibrium equations are satisfied on average within the element. Therefore, domains significantly smaller than crack front elements may not capture the crack tip fields properly. Given these facts, the appropriate domain size is found to be a balance between the satisfaction of prior assumption of plain strain fields and the accuracy of FE fields in the domain. In an arbitrary mesh around the crack front, the size of the elements may vary significantly, and an approximate (nominal) value should be used to represent the average size of the elements. The nominal element size $L_n = L_f/N_f$ is defined, where L_f and N_f are the length of the crack front and number of segments used to discretize it, respectively. To investigate the idea of an optimum domain size, an extensive parametric study was carried out to relate the SIF computation error to the domain radius in different mesh refinements. The SIFs of the different crack configurations were computed for different domain radii for different actual mesh densities, while the virtual mesh density was kept constant by $k = 6$. This fine virtual mesh ensures that all the field variation in

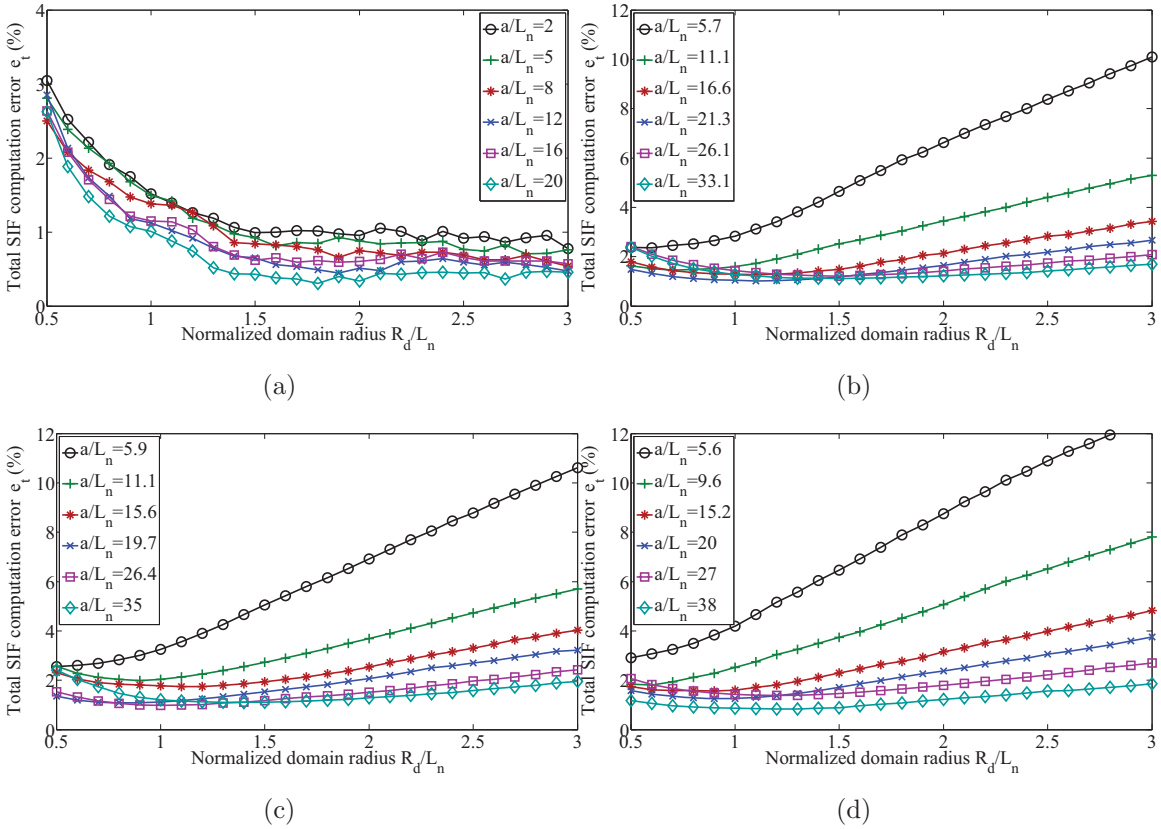

Figure 4.14: The variation of the total numerical error e_{t} against normalized domain radius R_d/L_n for (a) through-the-thickness, (b) penny-shaped, (c) elliptical ($b/a = 0.7$), (d) elliptical ($b/a = 0.4$) cracks in different mesh refinements when using quarter-point tetrahedral elements.

different actual mesh refinements and domain radiuses are captured. Quarter-point elements were employed in the crack front region in both actual and virtual meshes.

Figure (4.14) shows the variation of the average total SIF computation error versus the normalized domain radius R_d/L_n for different actual mesh refinements expanding from very coarse meshes $a/L_n \approx 5$ to very fine meshes $a/L_n \approx 35$. The main features of the results in these graphs are as follows: (i) For the through crack, the error e_{t} drops slightly from $R_d = 0.5L_n$ to $R_d = 1.5L_n$, at which point it stabilizes. As the whole plate is under plane strain conditions, 2D plane strain crack tip fields are developed ahead of the crack front, and therefore the fracture parameters can be computed very accurately, even when using very large domains. This is not the case for the other crack configurations, where the plane strain condition prevails only close to the crack front. (ii) For the embedded penny-shaped and elliptical cracks, except very coarse meshes, e_{t} slightly drops by increasing the domain radius, reaching its minimum between $R_d = L_n$ and $R_d = 1.5L_n$, and then increases gradually for larger domain sizes. The decreasing trend in the beginning is explained by the fact that increasing the domain size allows the capture of more representative crack tip

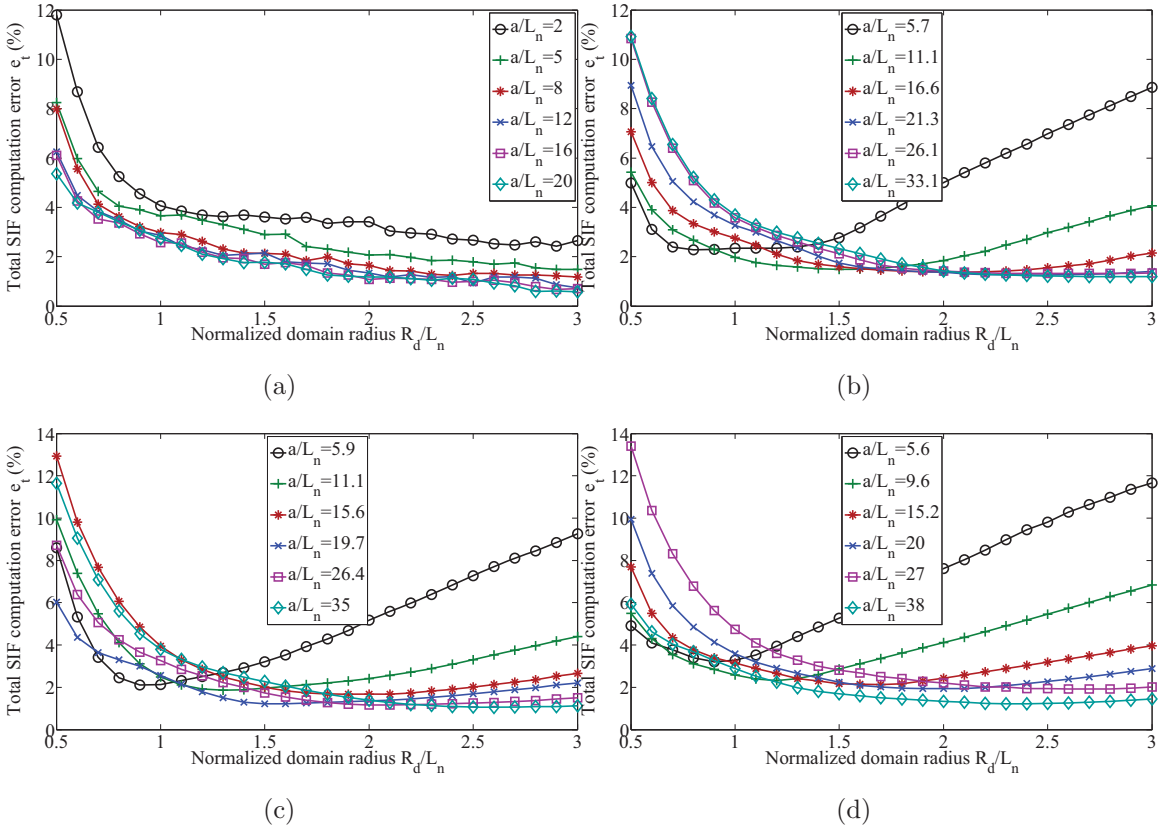

Figure 4.15: The variation of the total numerical error e_t against the normalized domain radius R_d/L_n for (a) through-the-thickness, (b) penny-shaped, (c) elliptical ($b/a = 0.7$), (d) elliptical ($b/a = 0.4$) cracks in different mesh refinements and in the absence of quarter-point tetrahedral elements.

fields, and also, the overall influence of local numerical errors decreases as integration is performed over a larger domain. The growth trend is because a larger domain is more likely to include the areas at which the plane strain condition no longer prevails. The plots clearly show that there exists an optimum domain radius at which the error is minimized. This behavior is not observed for the very coarse mesh, as the domains are already very large compared to the crack size, and the minimum error is more likely to occur at $R_d \approx 0.5L_n$. According to these results, it can be concluded that there exists a mesh-dependent optimum domain radius in the range of $0.5L_n \leq R_d \leq 1.5L_n$, where the SIF computation error is minimum. The optimum radius approaches $R_d = 0.5L_n$ and $R_d = 1.5L_n$ for coarse and fine meshes, respectively, and a domain radius of $R_d = L_n$ is the best choice that works for both fine and coarse meshes.

Figure (4.15) presents the variation of the total SIF computation error versus the normalized domain radius R_d/L_n, when standard tetrahedral elements are employed at the crack front region instead of quarter-point ones. Equivalently, instead of quarter-point tri-

angular elements, standard quadratic triangular elements are used at the first row in the virtual mesh. The main features of the results in these plots are as follows: (i) The SIF computation error is significantly higher in these plots as compared to the ones in Fig. 4.14, especially for small domain sizes. The errors in these plots are approximately two to three times larger than the errors in Fig. 4.14. This highlights the efficiency of the quarter-point elements in improving the numerical solution of the crack tip fields. (ii) Similar trends are observed in these plots to those shown in Fig. 4.14. One important difference is that the errors for the small domains are significantly higher than those shown in Fig. 4.14. This indicates that when standard tetrahedral elements are used, larger domains should be preferred to compute accurate SIF values. (iii) The plots clearly demonstrate the existence of an optimum mesh-dependent domain radius at which the SIF computation error hits its minimum. This optimum domain radius is generally in the range of $L_n \leq R_d \leq 3L_n$ approaching $R_d = L_n$ and $R_d = 3L_n$ for very coarse and fine meshes, respectively. A domain radius of $R_d = 1.5L_n$ is suggested as the best choice, that works for both fine and coarse meshes.

4.8.3 The choice of the q-function

As was explained in Sections 4.3 and 4.4, an arbitrary continuously differentiable, the class C^1, scalar function q has to be defined over the domain. In order to assess the influence of different q functions, the SIFs of the penny-shaped crack were computed using the q function $q = 1 - (r/R_d)^n$ with the following four different powers: $n = 0.5, 1, 1.5, 2$. The model specifications such as actual mesh refinement, virtual mesh refinement and domain radius are the same as the ones given in Section 5.6.1. The average total SIF error e_{t} is as follows: $e_{\mathrm{t}} = 5\%$ for $n = 0.5$; $e_{\mathrm{t}} = 1.1\%$ for $n = 1, 1.5$; and $e_{\mathrm{t}} = 1.2\%$ for $n = 2$. The reason for the high numerical error in the case $n = 0.5$ seems to be due to the fact that the derivatives of q function become singular at the disk center. This results in a less accurate numerical integration over the domain. Additionally, due to the singularity at the disk center, the sampling points near the disk center contributes to the entire integral much more than do the points near the disk boundaries. As the numerical error near the crack front is larger, it is expected that such a weighing process will lead to a larger numerical error in the computation of the SIFs. The accuracy of the results for the other three cases $n = 1, 1.5, 2$ seems to be about the same. However, an increase in n results in a higher average error, e_{t}. In particular, the individual mode III error e_{III} grows significantly for $n > 2$. The reason for such behavior is that increasing n makes the contribution of the sampling point near the boundaries more significant than that of the points near the crack front. This induces another source of error, due to the fact that only near the crack

front a plane strain state prevails, and far from the crack front a 3D stress state is more likely to exist. To summarize, it is concluded that q function should be chosen in a way that all sampling points contribute evenly to the entire integral. Therefore, the function $q = 1 - (r/R_d)$ is a suitable choice since (i) the linear variation of its derivatives can be captured well in the numerical integration, and (ii) the sampling points all over the domain contribute evenly to the entire integral.

4.8.4 The choice of crack front points

In this chapter the pointwise SIFs are reported at the position of both corner and mid-side nodes of the crack front segments. However, disk-shaped domains can be constructed at any point along the crack front, and not necessarily at the position of crack front nodes. To assess the influence of the choice of points on the numerical results, the pointwise SIFs of the penny-shaped crack, whose specifications are explained in Section 5.6.1, were computed for the following sets of points separately: (i) positions of corner nodes of crack front segments; (ii) positions of mid-side nodes of crack front nodes; (iii) positions of midpoints between corner and mid-side nodes of the crack front segments. The average SIF error remains about 1% for all cases. This indicates the choice of the points on the crack front does not influence the accuracy of the SIFs, and therefore the pointwise SIFs can be computed accurately at any point along the crack front.

4.9 Conclusions

A novel, efficient and accurate domain integral approach is proposed for computing pointwise J-integral and stress intensity factors of 3D crack configurations from unstructured meshes. This method is based on the evaluation of domain integrals over disk-shaped domains, and has the following advantages over volumetric domain approaches that are based on tubular domains:

1. It can be directly applied to arbitrary tetrahedral meshes.

2. It requires less computational cost, as it performs integration over a disk rather than a tube. For example, a simple integration scheme over a virtual cylinder requires integrating over three disks, and therefore requires three times more integration points, as compared to using the proposed disk-shaped domain.

3. It directly applies the original definition of the pointwise J- and interaction integrals.

4. Integration is performed over a disk perpendicular to the crack front, which is easy to generate and low in cost, and expressing the field in curvilinear coordinates is no longer required for curved cracks.

5. As 2D plane strain auxiliary fields satisfy compatibility and equilibrium equations over a disk, the term containing the higher order gradients of the auxiliary fields vanishes in this new formulation.

6. The in-plane and anti-plane fields are separated, and cannot influence each other in the computation of fracture parameters.

This method utilizes disk-shaped domains discretized with virtual triangular elements, which can be readily implemented in any FE code. The results of this method have been validated for a number of crack configurations in mode I and mixed-mode loading conditions, where the SIF computation error remains within 1% for fine meshes and 2-3% for coarse ones. The results of an extensive parametric study also suggests that an optimum mesh-dependent domain radius exists at which the SIF computation error hits its minimum. This optimum radius is roughly equal to the nominal size of the elements at the crack front region. It was also shown that employing quarter-point tetrahedral elements can improve the FE solution of the crack tip fields significantly. These results provide further evidence of the applicability, efficiency and accuracy of unstructured meshes to analyze cracked bodies.

Chapter 5

A gap-based augmented Lagrangian method for modeling frictional contact between crack surfaces

Contents

5.1 Abstract

This chapter introduces a three-dimensional finite element (FE) formulation to accurately model the linear elastic deformation of fractured media under compressive loading. The FE model is based on unstructured meshes using quadratic tetrahedral elements, and includes three novel components: (i) The singular stress field near the crack front is modeled using quarter-point tetrahedra. (ii) The frictional contact between the crack faces in high contact precisions is modeled using isoparametric contact discretization, and a gap-based augmented Lagrangian method. (iii) Stress intensity factors of three-dimensional cracks under compression are computed using displacement correlation and disk-shaped domain integral methods. The main contributions in the contact treatment algorithm are: (i) A square root singular variation of the penalty parameter near the crack front is proposed to accurately model the contact tractions near the crack front. (ii) A gap-based augmented Lagrangian algorithm is introduced for updating the contact forces obtained from the penalty method to more accurate estimates. The results of contact and stress intensity factors are validated for several numerical examples of cubes containing single and multiple cracks.

5.2 Introduction

Understanding the mechanical behavior of fractured media under different mechanical loads is of vital importance and great interest to a variety of engineering fields. Examples at the micro-scale are materials such as rock and concrete which contains a large number of micro-cracks. Not only elastic deformation features of this class of materials such as nonlinearity and hysteresis, but also inelastic processes such as yielding, failure, fracturing, and fragmentation are attributed to the presence of micro-cracks and crack-like voids [Walsh, 1965; Shockey et al., 1974; Kachanov, 1982b; Einstein and Dershowitz, 1990; Lawn and Marshall, 1998; Aleshin and Van Den Abeele, 2007a; Khanal et al., 2008; David et al., 2012]. Geological formations are examples of fractured media at larger scales, where rock joints extend to lengths ranging from hundreds to thousands of meters [Bonnet et al., 2001]. Pre-existing natural fractures in geological media act as local mechanical weaknesses and main flow pathways, and therefore determine not only their deformation and strength behavior but also their flow and transport properties [Segall and Pollard, 1983; Gudmundsson, 1987; Pyrak-Nolte and Morris, 2000; Bonnet et al., 2001; Nick et al., 2011]. Many of these fractured media are often subjected to compression, and applications including rock fracturing and fragmentation and fault growth, require analyzing crack under compressive loads. The crack surfaces are most likely to go into contact under compressive loading states, and re-

liable and accurate numerical methods are required to model the contact process between crack surfaces.

The use of the finite element method to model contact between crack surfaces has been mainly limited to XFEM formulations. XFEM allows modeling of the entire crack geometry independently of the finite element mesh [Dolbow et al., 2001]. Both LATIN, LArge Time INcrement, [Dolbow et al., 2001; Ribeaucourt et al., 2007; Pierrès et al., 2010; Baietto et al., 2010; Trollé et al., 2012] and Newton-Raphson [Elguedj et al., 2007; Khoei and Nikbakht, 2007; Liu and Borja, 2010] iterative strategies have been employed in dealing with the non-linearity of the contact problem. However, Liu and Borja [2008] demonstrated the superior convergence performance of the Newton-Raphson method as compared to the LATIN strategy. This previous work is mainly focused on XFEM modeling of two-dimensional cracks and interfaces which are initially closed, yielding a low contact precision model. Moreover, the accuracy of the contact tractions near the crack tip/front has not been investigated. This accuracy directly influences the computation of stress intensity factors when using an energy-based method such as the interaction integral. No validation of the accuracy of the stress intensity factors has been reported in previous work. The proposed finite element formulation here is based on unstructured tetrahedral elements, where the contact constraints are enforced on 3D initially open cracks in high density fractured media. Also, special attention is devoted to the accurate resolution of contact tractions near the crack front and accurate computation of stress intensity factors.

An exact geometric representation of naturally fractured media is challenging, and stochastic models are often required to investigate deformation/flow characteristics of fractured media [Bonnet et al., 2001]. These models often use idealized fracture shapes based on a statistic description of key parameters such as distributions of size and orientation [Dershowitz and Einstein, 1988; Huseby et al., 1999, 2000; Malinouskaya et al., 2014]. Despite great geometrical simplifications, such approximated statistical representations are sufficient for estimating effective values of engineering parameters. This is the original idea behind Discrete Fracture Network (DFN) models, in which a natural fractured medium is represented by a set of discrete individual fractures in a continuum environment. The concept of DFN was first introduced by Long et al. [1982] for homogenizing complex fracture networks and has been extensively used for flow/transport applications [Min et al., 2004; Baghbanan and Jing, 2007; Leung and Zimmerman, 2012; De Dreuzy et al., 2012; Lang et al., 2014]. A similar concept to DFN has also been extensively applied in solid mechanics to estimate the mechanical deformation of micro-structured materials [Walsh, 1965; Lawn and Marshall, 1998; Aleshin and Van Den Abeele, 2007a; David et al., 2012]. A discrete fracture network is often defined stochastically by a set of fractures with random shape,

size, orientation, locations, and initial apertures embedded in a continuum medium. Due to the explicit representation of fractures, these networks have complex geometrical configurations, and hence specific meshing schemes and numerical algorithms are required for analyzing their mechanical deformation.

Due to the geometrical complexity of fractured media, unstructured meshes using tetrahedral elements are preferred. Meshing procedures for tetrahedra are much simpler, and these elements are best suited to mesh complicated geometries automatically [Paluszny and Zimmerman, 2011]. Unstructured meshes have been successfully used in the context of FE simulation of crack propagation [Paluszny and Matthäi, 2009; Paluszny and Zimmerman, 2011, 2013] as well as fragmentation [Paluszny et al., 2013]. This chapter presents a finite element formulation based on unstructured quadratic tetrahedral meshes to model internal contact in fractured media. A sophisticated algorithm is developed for the treatment of frictional contact between the fracture surfaces, based on isoparametric discretization of the contact contribution. The contact constraints are enforced by using a gap-based augmented Lagrange method. The frictional contact algorithm proposed here is novel because (i) a singular variation of the penalty parameter is suggested near the crack front to circumvent the difficulty of zero gaps on the crack front nodes; (ii) a gap-based augmented Lagrangian algorithm is introduced to update contact tractions obtained from the penalty solution to new, better estimates. As opposed to the conventional traction-based augmented Lagrangian method, in which Lagrange multipliers are augmented, in this proposed methodology gaps are augmented, which allows one to circumvent the difficulty of defining and augmenting Lagrange multipliers at crack front nodes. In order to model the strain singularity along the crack front of fractures, quarter-point tetrahedral elements are used at the crack front region. Displacement correlation and domain integral methods are also explained and used for computing the point-wise stress intensity factors. The proposed FE formulation is able to compute fracture contact tractions and high stress gradients near the crack front very accurately. Therefore, the deformation response of the fractured media can be obtained more accurately using this FE framework.

5.3 Problem description

Consider a body containing randomly distributed cracks, some of which are isolated and some of which are intersecting with others or the boundaries as shown in Fig. (5.1). The continuum medium, referred to as the matrix, is assumed to behave elastically, and the deformation is assumed to be in the range of infinitesimal strain theory. Cracks are modeled as discontinuities of the material over discrete areas, generating two smooth surfaces for each crack. They can be initially closed or open, with a certain aperture distribution over the

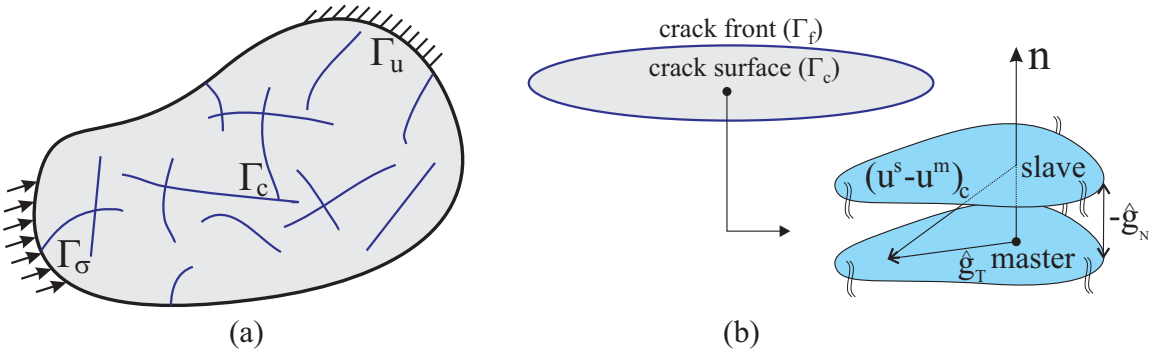

Figure 5.1: (a) Schematics of an elastic medium containing random distributed discrete fractures, (b) Kinematics of master and slave points over the crack surfaces.

crack surfaces. The crack surfaces are assumed traction-free and cohesion-free while the crack is open. Once the crack surfaces go into contact, a frictional contact constitutive law based on the Coulomb frictional law governs the boundary conditions over the crack surfaces. The two surfaces of each crack intersect at a curve called the crack front, at which a strain singularity occurs. The body is subjected to Dirichlet and Neumann conditions applied on the outer boundaries of the solid. Quasi-static loading condition is assumed, where the loading is applied sufficiently slowly so that inertial effects can be neglected.

5.3.1 Strong form

The main governing equations of the deformation are firstly developed in a strong form, building the partial differential equations which satisfy the equilibrium condition throughout the solid based on the equations of balance, kinematic relations, and constitutive equations. Consider a body containing randomly distributed cracks as schematically shown in Fig. (5.1). The domain of the body $\Omega \subset \mathbb{R}^3$ has external boundary Γ which is divided into two non-overlapping sets: a Dirichlet boundary Γ_u with pre-defined displacements, and a Neumann boundary Γ_σ with predefined tractions. Additionally, the domain Ω has internal boundaries produced by the surfaces of embedded cracks, Γ_c, which are subjected to potential contact boundary conditions. Although the body is subjected to quasi-static loads, a time discretization over $[0, T]$ is necessary due to contact-induced nonlinearity and path-dependency of frictional forces. The body undergoes small deformation described by the mapping $X \mapsto x = \varphi(X, t)$, where $t \in [0, T]$ and $\varphi : \Omega \times [0, T] \to \mathbb{R}^3$. This maps material points $X \in \Omega$ of the reference configuration to $x \in \Omega_t$ of the current configuration. The displacement field is therefore defined as $u(X, t) = \varphi(X, t) - X$. The quasi-static boundary

value problem is therefore given by [Ibrahimbegovic, 2009]

$$\begin{array}{lll} \nabla \cdot \sigma + b = 0 & in & \Omega \times [0,T] \\ u = \bar{u} & on & \Gamma_u \times [0,T] \\ \sigma n = \bar{t} & on & \Gamma_\sigma \times [0,T] \end{array} \tag{5.1}$$

Here $\sigma = D\varepsilon$ is the Cauchy stress tensor, where D is the elasticity matrix constituted by the material properties Young's modulus E and Poisson's ratio ν, and $\varepsilon = 1/2[\nabla u + (\nabla u)^T]$ is the infinitesimal strain tensor. The differential equation describes the balance of linear momentum, where $\nabla \cdot \sigma$ denotes the internal forces, and b is the vector of body forces per unit volume. $\bar{u}$ and $\bar{t}$ are the pre-defined displacements and surface tractions on the external boundaries with unit normal n. The local balance of angular momentum yields $\sigma = \sigma^T$, which indicates the symmetry of the Cauchy stress tensor.

The contact conditions are enforced on Γ_c through applying contact constraints between the two surfaces of each crack; one is referred to as the so-called *master* surface, Γ^m, while the other is denoted as the *slave* surface, Γ^s ($\Gamma_c = \Gamma^m \cup \Gamma^s$). The curves at which slave and master surfaces meet belong to the crack front, ($\Gamma_f = \Gamma^m \cap \Gamma^s$). Consider X^m, the position vector of the points on the crack master surface in the reference configuration. The crack slave surface can then be defined as $X^s = X^m - \hat{g}_{\mathrm{N}}(X^m)\boldsymbol{n}(X^m)$, where $\hat{g}_{\mathrm{N}} \leq 0$ is a scalar function defining the initial normal gaps over the crack surface, and $n(X_c^m)$ is the unit normal to the master surface in the reference configuration. Assuming small deformations, the unit normal is time-independent, and the normal gap function between the crack master and slave surfaces is given by

$$g_{\mathrm{N}} = (x^s - x^m) \cdot \boldsymbol{n} = (u^s - u^m) \cdot \boldsymbol{n} - \hat{g}_{\mathrm{N}} \tag{5.2}$$

where x^m, x^s, u^m, and u^s are the position vectors and displacement vectors of master and slave surfaces in the current configuration. This gap function is employed to detect the contact and enforce displacement constraints in the normal direction. The kinematics of the contact surfaces in the tangential direction also involves the calculation of initial tangential gap between the crack surfaces. Consider the time that a point on the slave surface first touches the master surface. The relative displacement at this time is referred to as $(u^s - u^m)_c$, where $(u^s - u^m)_c \cdot \boldsymbol{n} = \hat{g}_{\mathrm{N}}$. The inital tangential gap vector $\hat{g}_{\mathrm{T}}$ is defined as the relative tangental displacement of the two mapped points on the slave and master surfaces when they come into contact, and is computed by $\hat{g}_{\mathrm{T}} = (\mathbb{I} - \boldsymbol{n} \otimes \boldsymbol{n})(u^s - u^m)_c$. Assuming small deformations, the tangential gap function, which describes the relative tangential displacement of slave point with respect to master point during contact, is given by

$$g_{\mathrm{T}} = (\mathbb{I} - \boldsymbol{n} \otimes \boldsymbol{n})\,(x^s - x^m) - \hat{g}_{\mathrm{T}} = (\mathbb{I} - \boldsymbol{n} \otimes \boldsymbol{n})\,(u^s - u^m) - \hat{g}_{\mathrm{T}} \tag{5.3}$$

which will be used in conjunction with an interfacial constitutive law to enforce the contact constraints in the tangential direction. The contact traction acting on the master surface t^m is split into its normal and tangential components $p = t^m \cdot \boldsymbol{n}$, and $\tau = (\mathbb{I} - \boldsymbol{n} \otimes \boldsymbol{n})\, t^m$, respectively. The traction acting on the slave surface obeys Cauchy's first law, ($t^s = -t^m$). The most frequently used frictional constitutive equation is the classical law of Coulomb, describing the tangential frictional traction as

$$\begin{array}{ll} g_{\mathrm{T}} = 0 \Leftrightarrow \dot{g}_{\mathrm{T}} = 0 & if \quad \tau \leq \mu|p| + \tau_c \\ \tau = (\mu|p| + \tau_c)\dfrac{\dot{g}_{\mathrm{T}}}{|\dot{g}_{\mathrm{T}}|} & if \quad \tau > \mu|p| + \tau_c \end{array} \tag{5.4}$$

where μ and τ_c are the friction coefficient and cohesive stress, respectively, and $\dot{g}_{\mathrm{T}} = (\mathbb{I} - \boldsymbol{n} \otimes \boldsymbol{n})\,(\dot{u}^s - \dot{u}^m)$ is the rate of change of the tangential gap with time. Coulomb's law suggests two states of contact: *stick* condition, where no tangential displacement is allowed, and the contact traction is defined by enforcing kinematic constraints; and *slip* condition, where no kinematic constraint is applied, but the value and the direction of frictional traction is defined by the constitutive law. In fact, a constraint has to be applied to ensure tangential traction is in the opposite direction of the rate of change in the tangential gap. Assuming the slip of the slave points take place with the rate $\dot{\gamma}$, the frictional traction applied on the master points has to lie in the direction of slip according to the slip rule ($\dot{g}_{\mathrm{T}} = \dot{\gamma}\tau/|\tau|$). Consider the function $f_s(\tau, p) = |\tau| - (\mu|p| + \tau_c)$ which bounds the contact frictional stress, the normal and tangential contact conditions can be described in Kuhn-Tucker form as [Wriggers, 2006]

$$\begin{array}{llll} g_{\mathrm{N}} \geq 0, & p \leq 0, & p g_{\mathrm{N}} = 0 & on \quad \Gamma_c \times [0, T] \\ \dot{\gamma} \geq 0, & f_s(\tau, p) \leq 0, & \dot{\gamma} f_s(\tau, p) = 0 & on \quad \Gamma_c \times [0, T] \end{array} \tag{5.5}$$

The strong form of equilibrium equation in Eq. (5.1) constitutes a set of differential equations to be solved simultaneously with respect to inequality boundary conditions in Eq. (5.5) for the deformation field u. The strong form of the governing equations requires strong continuity of the displacement field, and is not suitable for numerical approximations.

Remark 1: The boundary of the cracked body is divided into three sets of Dirichlet, Neumann and contact boundaries, $\Gamma = \Gamma_u \cup \Gamma_\sigma \cup \Gamma_c$, as shown in Fig. (5.1). The boundaries Γ_σ and Γ_c can generally have overlap regions at the intersection of cracks with external boundaries. However, special care has to be taken when Γ_u and Γ_c overlap as the kinematic constraints of one region can prevent enforcing the constraints by the other. In fact, the Dirichlet boundary conditions on contact surfaces can prevent p and τ from satisfying the inequality conditions in Eq. (5.5). Therefore, in addition to $\Gamma_u \cap \Gamma_\sigma = \varnothing$, the restriction $\Gamma_u \cap \Gamma_c = \varnothing$ must be applied.

Remark 2: The crack front, Γ_f, where master and slave surfaces meet, can only provide the boundaries of the contact region for each embedded crack, and is excluded from the contact area, $\Gamma_f \notin \Gamma_c$. Therefore, no contact traction is defined or applied on the crack front. However, the limit of the contact traction as the crack front is approached, $r \to 0$ where r is the normal distance from the crack front, can be nonzero:

$$\lim_{r\to 0} ||t^m(r)|| \geq 0 \tag{5.6}$$

Remark 3: The state of strain is singular along the crack front. This indicates that considerable stresses occur adjacent to the crack front even when very small penetration occurs between the fracture surfaces. Therefore, penetration has to be strictly penalized in a penalty treatment so that accurate contact tractions can be obtained.

5.3.2 Weak form

Consider a solid in its equilibrium configuration to be deformed by an arbitrary virtual infinitesimal displacement field δu which satisfies the displacement boundary condition $\delta u = \bar{u}$. This virtual displacement has also to be admissible with regard to the displacement constraints of the contact condition. By applying the principle of virtual work to the material points of Ω, the weak form of the equilibrium equation in Eq. (5.1) is formed as an integral equation:

$$\delta\Pi = \underbrace{\int_\Omega \Big(\sigma : \delta\varepsilon - b \cdot \delta u\Big)\, \mathrm{d}\Omega}_{\delta\Pi_\Omega} - \underbrace{\int_{\Gamma_\sigma} \bar{t} \cdot \delta u \, \mathrm{d}\Gamma}_{\delta\Pi_\sigma} + \underbrace{\int_{\Gamma^m} \Big(p\delta g_{\mathrm{N}} + \tau \cdot \delta g_{\mathrm{T}}\Big)\mathrm{d}\Gamma}_{\delta\Pi_c} = 0 \tag{5.7}$$

subjected to the inequality conditions in Eq. (5.5) being satisfied for the normal and tangential tractions, p and τ, on the contact master surfaces Γ^m. Here, $\delta\varepsilon = 1/2[\nabla\delta u + (\nabla\delta u)^T]$ is the strain tensor of the virtual displacement field δu. The virtual normal and tangential gaps are also developed based on the virtual displacement field as $\delta g_{\mathrm{N}} = (\delta u^s - \delta u^m) \cdot \boldsymbol{n}$ and $\delta g_{\mathrm{T}} = (\mathbb{I} - \boldsymbol{n} \otimes \boldsymbol{n})\,(\delta u^s - \delta u^m)$. The term $\delta\Pi_\Omega$ indicates the contribution of internal stresses and body forces to the total virtual work $\delta\Pi$, and the terms $\delta\Pi_\sigma$ and $\delta\Pi_c$ include the virtual work of pre-defined tractions and contact forces, respectively. In contrast to strong form in Eq. (5.1), which is a set of differential equations with respected boundary conditions, the weak form is in the form of an integral equation which requires a weaker continuity on the displacement. The weak form also holds the pre-defined boundary conditions of the boundary value problem, and is best suited to be the basis of numerical approximations. The weak form integral statements of the form of Eq. (5.7) constrained with inequality conditions in Eq. (5.5) will be the foundation of the subsequent finite element formulation.

5.4 Treatment of contact constraints

Two main numerical methodologies for incorporating contact constraints into the contact contribution $\delta\Pi_c$ are the Lagrange multiplier and penalty methods. Both methods are borrowed from optimization theory, and are often applied with active set strategies to deal with the inequality conditions. The classical method of Lagrange multipliers adds the active constraints to the weak formulation by introducing normal and tangential Lagrange multipliers λ_{N} and λ_{T} as unknown contact tractions. The important advantage of this method is that exact kinematic contact constraints are enforced. However, this is achieved at the cost of an additional effort required to compute the additional unknowns. Zeros are also introduced in the diagonal of the system of equations, which leads to difficulties in the direct solution of the system. Recent applications of Lagrange multipliers can be found in Fischer and Wriggers [2005]; Hartmann and Ramm [2008] and Tur et al. [2009]. On the other hand, the penalty method avoids the exact solution and additional unknowns by introducing an approximation of the constraint conditions. In fact, the penalty method exploits the advantage of removing the constraints explicitly from the formulation. The violation of the constraint condition is then penalized by using a large positive penalty parameter ϵ. Small penalty parameters results in considerable violation of constraints, and as the penalty parameter tends to infinity, the contact constraint is enforced exactly. However, the system of equations may become ill-conditioned as the penalty parameter increases, and therefore, an appropriate penalty parameter is found to be a balance between accuracy and stability. Due to ill-conditioning, the penalty method performs poorly for high precision contact problems. Recent applications of the penalty method can be found in [Fischer and Wriggers, 2006; Yang et al., 2005; Zavarise and De Lorenzis, 2009].

The application of any of these methods for the contact treatment in heavily fractured media is problematic, as it is likely that the system becomes ill-conditioned due to high contact precisions. The augmented Lagrangian method, however, is able to enforce the contact constraint accurately in high contact precisions. This method, which was originally proposed and applied in the context of mathematical programming problems subjected to equality constraints, provides advantages over the more traditional Lagrange multiplier and penalty methods. It combines Lagrange multiplier and penalty methods to exploit the merits of both approaches [Wriggers and Zavarise, 1993; Puso and Laursen, 2004]. The advantages of the augmented Lagrangian over the penalty method include decreased ill-conditioning of the system, and essentially exact satisfaction of constraints with finite penalties. The advantage over Lagrange multipliers is that it avoids introducing unknowns to the problem by using current fixed estimates of the Lagrange multipliers. Applying

the augmented Lagrange method often yields a double loop algorithm in which constant Lagrange multipliers are used with penalty terms during the inner loop to enforce the contact constraints. Then, within an outer loop, the Lagrange multipliers are updated to new values based on the computed tractions in the inner loop. This procedure increases the number of iterations, but allows enforcing contact constraints accurately by using small penalty parameters (see Simo and Laursen [1992]; Laursen and Simo [1993]; Zavarise et al. [1995]). This type of algorithm has been referred to as nested augmented Lagrangian algorithm [Simo and Laursen, 1992], or Uzawa-type algorithm [Wriggers, 2006].

5.4.1 Traction-based (standard) augmented Lagrangian method

In order to describe the formulation of the augmented Lagrangian method, the weak form of the equilibrium equation in Eq. (5.7) is rewritten as $\delta\Pi_\Omega - \delta\Pi_\sigma + \delta\Pi_c = 0$. The solution to this equation must provide values for the normal and tangential contact tractions p and τ under the contact constraints in Eq. (5.5). Based on the augmented Lagrangian treatment, contact tractions include contributions due to both the penalization by penalty terms and Lagrange multipliers. The normal traction is defined as $p = \langle \lambda_{\mathrm{N}} + \epsilon g_{\mathrm{N}} \rangle$, where the introduction of the Macauley bracket, defined as $\langle x \rangle = (x - |x|)/2$, ensures the satisfaction of the constraint $p \leq 0$ in Eq. (5.5). The penalty parameter ϵ is chosen as large as possible without making the system ill-conditioned. The terms ϵg_{N} penalizes the violation of the constraint $g_{\mathrm{N}} \geq 0$, denoting that this constraint is satisfied approximately. However, this approximation of contact traction approaches the exact solution through an augmentation procedure where the fixed estimates of Lagrange multiplier λ_{N} are employed and updated in an outer loop. The same concept is used for enforcing the contact constraints in the tangential direction. According to the constraints in Eq. (5.5), the vector of slip rate has to equal the tangential velocity in the slip condition ($\dot{g}_{\mathrm{T}} = \dot{\gamma}\tau/|\tau|$ when $f_s(\tau, p) = 0$), while the tangential velocity remains zero in the case of stick ($\dot{g}_{\mathrm{T}} = 0$ when $f_s(\tau, p) < 0$). In both case, the tangential contact traction can be decomposed into Lagrange multiplier and penalty parts. Assume λ_{T} is the Lagrange multiplier part of τ. Since λ_{T} is an estimate of contact traction, the tangential displacement constraints are satisfied approximately, resulting in a slight difference between the vectors of slip rate and tangential velocity. However, this approximate solution approaches the exact values by updating the Lagrange multipliers through an augmentation process. The augmented Lagrangian treatment reformulates the

contact constraint in Eq. (5.5) as [Simo and Laursen, 1992]

$$\begin{aligned} &p = \langle \lambda_{\mathrm{N}} + \epsilon g_{\mathrm{N}} \rangle \\ &f_s(\tau, p) = |\tau| - (\mu |p| + \tau_c) \leq 0 \\ &\dot{g}_{\mathrm{T}} - \dot{\gamma} n_{\mathrm{T}} = \frac{1}{\epsilon}(\dot{\tau} - \dot{\lambda}_{\mathrm{T}}) \\ &\dot{\gamma} \geq 0 \\ &\dot{\gamma} f_s(\tau, p) = 0 \end{aligned} \tag{5.8}$$

where $n_{\mathrm{T}} = \partial f_s(\tau, p)/\partial \tau = \tau/|\tau|$. If λ_{N} and λ_{T} are correct multipliers, then the displacement constraints associated with the contact conditions are satisfied exactly ($g_{\mathrm{N}} = 0$ and $\dot{g}_{\mathrm{T}} = \dot{\gamma} n_{\mathrm{T}}$), and an exact penalization occurs. The main idea of the augmented Lagrangian method is that fixed current estimates are considered for Lagrange multipliers. Then the problem is solved to penalize any violation from contact constraint using the penalty method, and the estimates of the Lagrange multipliers are updated based on the result of penalty solution.

The quasi-static problem is solved in an incremental manner over the time interval $[0, T] = \bigcup_{n=0}^{N-1} [t_n, t_{n+1}]$ by which the loads are applied over N increments. In each time increment $[t_n, t_{n+1}]$, the solution u_n at the beginning of the increment t_n is known from Eq. (5.7) being satisfied. The aim is to find the deformation through the increment Δu which yields the solution $u_{n+1} = u_n + \Delta u_n$ at the time t_{n+1}. The algorithmic update of the frictional contact traction is often performed by a return mapping strategy based on the integration of Eq. (5.8) between t_n and t_{n+1} using a backward Euler integration scheme [Giannakopoulos, 1989; Simo and Laursen, 1992; Yastrebov, 2013]. Consider $\{u_n, p_n, \tau_n\}$ to be given through the satisfaction of Eq. (5.7) at t_n:

$$\delta \Pi_{\Omega+\sigma}(u_n, \delta u) + \int_{\Gamma^m} \Big(p_n \delta g_{\mathrm{N}} + \tau_n \cdot \delta g_{\mathrm{T}} \Big) \mathrm{d}\Gamma = 0 \tag{5.9}$$

where $\delta \Pi_{\Omega+\sigma} = \delta \Pi_{\Omega} - \delta \Pi_{\sigma}$. The solution at t_{n+1}, i.e. $\{u_{n+1}, p_{n+1}, \tau_{n+1}\}$, is then obtained by enforcing the satisfaction of Eq. (5.7) subject to the laws of evolution in Eq. (5.8) as

$$\delta \Pi_{\Omega+\sigma}(u_{n+1}, \delta u) + \int_{\Gamma^m} \Big(p_{n+1} \delta g_{\mathrm{N}} + \tau_{n+1} \cdot \delta g_{\mathrm{T}} \Big) \mathrm{d}\Gamma = 0 \tag{5.10}$$

where

$$\begin{aligned} &p_{n+1} = \langle \lambda^k_{\mathrm{N}_{\mathrm{n+1}}} + \epsilon g_{\mathrm{N}_{\mathrm{n+1}}} \rangle \\ &\tau^{\mathrm{tr}}_{n+1} = \lambda^k_{\mathrm{T}_{\mathrm{n+1}}} + \epsilon g_{\mathrm{T}_{\mathrm{n+1}}} \\ &n^{\mathrm{tr}}_{\mathrm{T}_{\mathrm{n+1}}} = \tau^{\mathrm{tr}}_{n+1}/|\tau^{\mathrm{tr}}_{n+1}| \\ &f^{\mathrm{tr}}_s = |\tau^{\mathrm{tr}}_{n+1}| - (\mu |p_{n+1}| + \tau_c) \\ &\tau_{n+1} = \tau^{\mathrm{tr}}_{n+1} - \epsilon \, \Delta\gamma \, n^{\mathrm{tr}}_{\mathrm{T}_{\mathrm{n+1}}}, \quad \text{where} \quad \Delta\gamma = \begin{cases} 0, & \text{if} f^{\mathrm{tr}}_s \leq 0 \text{ (stick).} \\ f^{\mathrm{tr}}_s/\epsilon, & \text{otherwise (slip).} \end{cases} \end{aligned} \tag{5.11}$$

Here, the application of the return mapping algorithm regularizes the frictional traction and the law of evolution in Eq. (5.8) in order to fulfil the inequality restriction for the slip surface ($f_s(\tau, p) \leq 0$). The backward Euler integration scheme is used to approximate the relative tangential slip in the time increment. $\lambda^k_{\mathrm{N}_{n+1}}$ and $\lambda^k_{\mathrm{T}_{n+1}}$ are the kth fixed estimate of Lagrange multipliers at t_{n+1}, where $k = 0, 1, 2, ...$ are iterations in the outer loop of the augmented Lagrangian method to search for the correct multipliers. $g_{\mathrm{N}_{n+1}}$ and $g_{\mathrm{T}_{n+1}}$ are also the normal and tangential gap functions in Eqs. (5.2) and (5.3) based on the solution u_{n+1} .

Algorithm (2) demonstrates the application of return mapping strategy and augmentation procedure for updating the contact tractions in a time increment. The contact tractions are known at t_n, and are stored at the corresponding Lagrange multipliers: $p_n = \lambda_{\mathrm{N}_n}$ and $\tau = \lambda_{\mathrm{T}_n}$. These values are the first estimates of the Lagrange multipliers at t_{n+1}. A trial solution is obtained by assuming stick condition over the active contact zones. The frictional forces are then updated through the return mapping strategy, and Eq. (5.7) is solved using Newton's method in an inner loop, before the Lagrange multipliers are updated to new estimates in the augmentation stage. The augmentation process is performed only after the solution in the inner loop has converged. This procedure ensures the quadratic convergence of Newton-Raphson solution scheme at the inner loop. In the first iteration ($k = 0$) all the change in contact tractions during the step is stored in the penalty terms. By continuing augmentation, however, the penalty contributions to contact tractions are transferred into multipliers, yielding better estimates for the Lagrange multipliers. The augmentation process continues until the normal gap and relative tangential displacement in stick condition become less than certain thresholds $\mathrm{Tol_N}$ and $\mathrm{Tol_T}$. At this stage, the multipliers are the contact tractions, while the penalty terms are essentially zero. The main advantage of augmented Lagrangian treatment is that the satisfaction of contact constraints is improved by the augmentation procedure, outer loop, and not by the application of very large penalty parameters. In practice, the penalty parameter should be as large as possible without inducing ill-conditioning. The augmented Lagrangian method reduces to penalty regularization if no augmentation is performed in the time steps.

Employing Algorithm (2), however, is problematic when dealing with contact between crack surfaces. The reason is that no contact traction is available for the points on the crack front, since the crack front is excluded from the contact domain. Lagrange multipliers are often defined at finite element nodes and interpolated over the contact elements using the shape functions. Therefore, values of traction on the crack front nodes are required in order to distribute the traction over the contact elements attached to the crack front.

Algorithm 2 Traction-based (standard) augmented Lagrangian approach for the evolution of frictional contact in the time step $[t_n, t_{n+1}]$

1. Initialization:

$k = 0$

$\lambda^{k}_{\mathrm{N}_{n+1}} = \lambda_{\mathrm{N}_n}$

$\lambda^{k}_{\mathrm{T}_{n+1}} = \lambda_{\mathrm{T}_n}$

2. Return Mapping and Solution:

$p_{n+1} = \langle \lambda^{k}_{\mathrm{N}_{n+1}} + \epsilon g_{\mathrm{N}_{n+1}} \rangle$

$\tau^{\mathrm{tr}}_{n+1} = \lambda^{k}_{\mathrm{T}_{n+1}} + \epsilon g_{\mathrm{T}_{n+1}}$

$n^{\mathrm{tr}}_{\mathrm{T}_{n+1}} = \tau^{\mathrm{tr}}_{n+1} / |\tau^{\mathrm{tr}}_{n+1}|$

$f^{\mathrm{tr}}_s = |\tau^{\mathrm{tr}}_{n+1}| - (\mu |p_{n+1}| + \tau_c)$

$\Delta\gamma = -\langle -f^{\mathrm{tr}}_s / \epsilon \rangle$

$\tau_{n+1} = \tau^{\mathrm{tr}}_{n+1} - \epsilon\, \Delta\gamma\, n^{\mathrm{tr}}_{\mathrm{T}_{n+1}}$

$\delta\Pi_{\Omega+\sigma}(u_{n+1}, \delta u) + \int_{\Gamma^m} \Big(p_{n+1} \delta g_{\mathrm{N}} + \tau_{n+1} \cdot \delta g_{\mathrm{T}} \Big) \mathrm{d}\Gamma = 0$

3. Augmentation:

$\lambda^{k+1}_{\mathrm{N}_{n+1}} = \langle \lambda^{k}_{\mathrm{N}_{n+1}} + \epsilon g^{k}_{\mathrm{N}_{n+1}} \rangle$

$n^{k+1}_{\mathrm{T}_{n+1}} = n^{\mathrm{tr}}_{\mathrm{T}_{n+1}}$

$$\lambda^{k+1}_{\mathrm{T}_{n+1}} = \begin{cases} \lambda^{k}_{\mathrm{T}_{n+1}} + \epsilon g^{k}_{\mathrm{T}_{n+1}} & \text{if } f^{\mathrm{tr}}_s \leq 0 \ \text{(stick)}. \\ \left(\mu |\lambda^{k+1}_{\mathrm{N}_{n+1}}| + \tau_c\right) n^{k+1}_{\mathrm{T}_{n+1}} & \text{otherwise (slip)}. \end{cases}$$

4. Convergence check:

IF $\left(|g_{\mathrm{N}_{n+1}}| \geq \mathrm{Tol}_{\mathrm{N}} \text{ or } |g_{\mathrm{T}_{n+1}}| \geq \mathrm{Tol}_{\mathrm{T}} \text{ over } \Gamma^m_{\mathrm{st}} \right)$

$k \leftarrow k + 1$

GOTO 2

ELSE

$\hat{g}_{\mathrm{T}_{n+1}} \leftarrow \hat{g}_{\mathrm{T}_n} + g_{\mathrm{T}_{n+1}}$

Converge (EXIT).

5.4.2 Gap-based augmented Lagrangian method

In the context of LEFM, FE crack analyses consider single nodes over the crack front as cracks are assumed to remain sharp. The gaps, therefore, remain zero on the crack front nodes, and increase according to a square root variation with the normal distance from the crack front (see Fig. (5.2)). On the other hand, the penalty solution is formulated based on the gap distribution over the contact elements. As discussed earlier, the contact traction can have a non-zero limit when the crack front is approached. This behavior cannot be modeled with a standard penalty formulation with constant penalty parameter, since the variation of contact traction near the crack front is dictated by the variation of the gap there. This is a major issue, since the penalty formulation enforces the traction to decay

near the crack front while the crack front is approached. A penalty solution based on a constant penalty parameter, therefore, fails to determine a correct variation of traction near the crack front unless special treatment is considered in that region.

The numerical solutions suggest that near the crack front of an arbitrary 3D crack configuration, a plane strain condition prevails locally, so that the three-dimensional deformation fields approach the two-dimensional plane strain fields [Nakamura and Parks, 1988, 1989]. According to these fields, the displacement adjacent to the crack front and over a perpendicular plane to the crack front are given as square root functions of distance from the crack front [Anderson, 2005]. Therefore, the distribution of relative displacement of the top crack surface with respect to the bottom surface also follows a square root variation, giving the total gap function of a point located at normal distance r from the crack front as

$$g(r) = \left(\frac{\kappa+1}{\mu}\right)\sqrt{\frac{r_0}{2\pi}}\left[K_{\mathrm{I}}e_2 + K_{\mathrm{II}}e_1 + K_{\mathrm{III}}\left(\frac{4}{\kappa+1}\right)e_3\right]\sqrt{r/r_0} = \bar{g}\sqrt{r/r_0} \tag{5.12}$$

where K_{i}, $\mathrm{i} = \mathrm{I}, \mathrm{II}, \mathrm{III}$ is the mode i point-wise stress intensity factor, $\mu = E/2(1+\nu)$ is the shear modulus, E and ν are the Young's modulus and Poisson's ratio, and Kolosov constant κ is equal to $3-4\nu$ for plane strain condition, e_i is the unit vector along the x_i axis of the local coordinate system located on the crack front, and $\bar{g}$ is the gap at the distance r_0 from the crack front. Numerical results from quarter-point tetrahedral elements also capture this type of gap variation near the crack front, as shown in Chapters 2 and 3. This gap variation significantly influences the contact tractions obtained from a penalty formulation near the crack front. To avoid gap values influencing the contact reactions, it is suggested that a singular square root variation of penalty parameter with r is used. Let ϵ_0 be a constant nominal penalty parameter at the distance r_0 from the crack front. The distribution of penalty parameter near the crack front can then be defined as $\epsilon = \epsilon_0/\sqrt{r/r_0}$, generating a square root singularity of penalty parameter near the crack front. This regularization of the penalty parameter cancels out the influence of gap variation on the contact traction variation, ensuring a finite value of stick traction very close to the crack front, as shown in Fig. (5.2):

$$t^m = \lim_{r\to 0}\epsilon(r)g(r) = \epsilon_0\bar{g} \tag{5.13}$$

It can also be shown for the slip condition that finite values of traction are obtained very close to the crack front using this treatment. Although this proposed regularization of the penalty parameter improves the contact tractions near the crack front, the difficulty of defining Lagrange multipliers distribution over the element attached to the crack front remains. This is because contact tractions cannot be defined and updated over the crack front, and contact tractions over the master elements attached to the crack front cannot

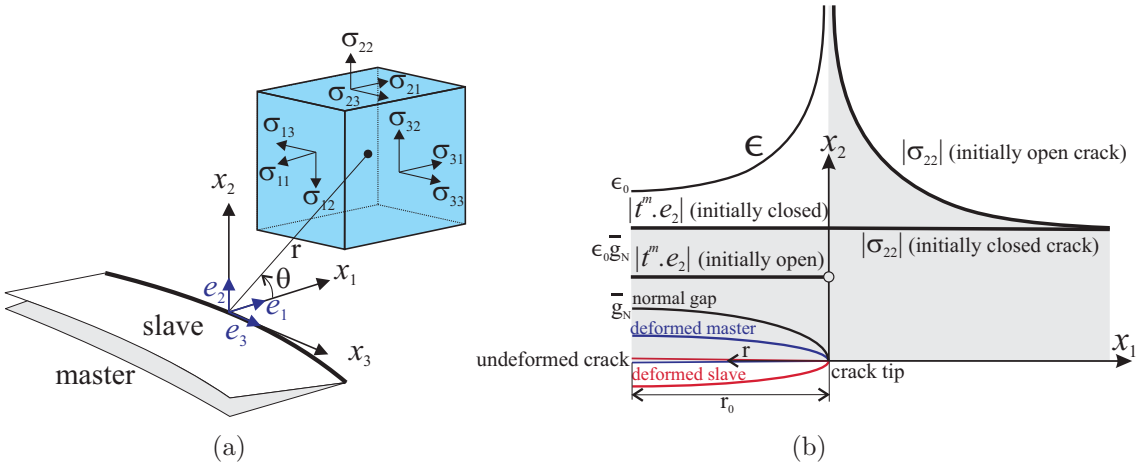

Figure 5.2: (a) Local coordinate system at a point along the crack front, and schematics of stresses, (b) Variations of normal gap, penalty parameter, normal contact traction, and the normal stress component σ_{22} at an orthogonal plane to the crack front.

be directly obtained from the tractions at nodal values. This difficulty, however, can be circumvented by introducing a gap-based augmented Lagrangian method which relies on the augmentation of gaps rather than contact tractions. In this type of treatment, the normal and tangential Lagrange multipliers are defined as

$$\lambda_{\mathrm{N}} = \epsilon g^*_{\mathrm{N}} \qquad , \qquad \lambda_{\mathrm{T}} = \epsilon g^*_{\mathrm{T}} \tag{5.14}$$

where g^*_{N} and g^*_{T} are augmented normal and tangential gaps. The augmented gaps are constant during the penalty solution, inner loop, and are updated in the augmentation process, outer loop, based on the penalty solution. In this strategy, thanks to the singularity of penalty parameter, the augmented gaps are able to determine very accurate contact tractions near the crack front. Algorithm (3) demonstrates the application of the proposed gap-based augmentation Lagrangian treatment in the combination of return mapping strategy for updating the contact tractions in a time increment.

An active strategy is often used to update the regions in contact in every iteration in the inner loop. This strategy identifies the regions in contact by using the value of the normal traction $p_{n+1} = \epsilon(g^{*k}_{\mathrm{N}_{n+1}} + g_{\mathrm{N}_{n+1}})$, where $p_{n+1} \leq 0$ denotes active contact zone. The slip or stick condition is also determined based on the value of f^{tr}_s in Algorithm (3). Consider Γ^m_{st} and Γ^m_{sl} being respectively stick and slip zones of the contact master surface. $\Gamma^m_{\mathrm{st}} \cup \Gamma^m_{\mathrm{sl}}$ therefore constitutes the active contact zone. According to the augmented Lagrangian treatment in Algorithm (3), the normal, tangential stick and tangential slip tractions are defined by $p = \epsilon(g^*_{\mathrm{N}} + g_{\mathrm{N}})$, $\tau_{\mathrm{st}} = \epsilon(g^*_{\mathrm{T}} + g_{\mathrm{T}})$, and $\tau_{\mathrm{sl}} = (\mu\epsilon|g^*_{\mathrm{N}} + g_{\mathrm{N}}| + \tau_c)n_{\mathrm{T}}$, respectively. Here, the superscript k and subscript $n+1$ are removed for simplicity. Using these expressions,

Algorithm 3 Gap-based augmented Lagrangian approach for the evolution of frictional contact in the time step $[t_n, t_{n+1}]$

1. Initialization:

$k = 0$

$g^{*k}_{\mathrm{N}_{n+1}} = g^{*}_{\mathrm{N}_n}$

$g^{*k}_{\mathrm{T}_{n+1}} = g^{*}_{\mathrm{T}_n}$

2. Return Mapping and Solution:

$p_{n+1} = \epsilon\langle g^{*k}_{\mathrm{N}_{n+1}} + g_{\mathrm{N}_{n+1}}\rangle$

$\tau^{\mathrm{tr}}_{n+1} = \epsilon(g^{*k}_{\mathrm{T}_{n+1}} + g_{\mathrm{T}_{n+1}})$

$n^{\mathrm{tr}}_{\mathrm{T}_{n+1}} = \tau^{\mathrm{tr}}_{n+1}/|\tau^{\mathrm{tr}}_{n+1}|$

$f^{\mathrm{tr}}_s = |\tau^{\mathrm{tr}}_{n+1}| - (\mu|p_{n+1}| + \tau_c)$

$\Delta\gamma = -\langle -f^{\mathrm{tr}}_s/\epsilon\rangle$

$\tau_{n+1} = \tau^{\mathrm{tr}}_{n+1} - \epsilon\,\Delta\gamma\, n^{\mathrm{tr}}_{\mathrm{T}_{n+1}}$

$\delta\Pi_{\Omega+\sigma}(u_{n+1}, \delta u) + \int_{\Gamma^m}\Big(p_{n+1}\delta g_{\mathrm{N}} + \tau_{n+1}\cdot\delta g_{\mathrm{T}}\Big)\mathrm{d}\Gamma = 0$

3. Augmentation:

$g^{*k+1}_{\mathrm{N}_{n+1}} = \langle g^{*k}_{\mathrm{N}_{n+1}} + g^{k}_{\mathrm{N}_{n+1}}\rangle$

$n^{k+1}_{\mathrm{T}_{n+1}} = n^{\mathrm{tr}}_{\mathrm{T}_{n+1}}$

$$g^{*k+1}_{\mathrm{T}_{n+1}} = \begin{cases} g^{*k}_{\mathrm{T}_{n+1}} + g^{k}_{\mathrm{T}_{n+1}} & \text{if } f^{\mathrm{tr}}_s \le 0 \ \text{ (stick).} \\ \left(\mu|g^{*k+1}_{\mathrm{N}_{n+1}}| + \tau_c/\epsilon\right) n^{k+1}_{\mathrm{T}_{n+1}} & \text{otherwise (slip).} \end{cases}$$

4. Convergence check:

IF $\left(|g_{\mathrm{N}_{n+1}}| \ge \mathrm{Tol}_{\mathrm{N}} \text{ or } |g_{\mathrm{T}_{n+1}}| \ge \mathrm{Tol}_{\mathrm{T}} \text{ over } \Gamma^m_{\mathrm{st}}\right)$

$k \leftarrow k+1$

GOTO 2

ELSE

$\hat{g}_{\mathrm{T}_{n+1}} \leftarrow \hat{g}_{\mathrm{T}_n} + g_{\mathrm{T}_{n+1}}$

Converge (EXIT).

Eq. (5.7) is rewritten as

$$\begin{aligned} &\delta\Pi_{\Omega+\sigma}(u, \delta u) + \underbrace{\int_{\Gamma^m_{\mathrm{st}}+\Gamma^m_{\mathrm{sl}}} \epsilon\big(g^{*}_{\mathrm{N}} + g_{\mathrm{N}}\big)\delta g_{\mathrm{N}}\,\mathrm{d}\Gamma}_{\delta\Pi_{\mathrm{Normal}}} \\ &+ \underbrace{\int_{\Gamma^m_{\mathrm{st}}} \epsilon\big(g^{*}_{\mathrm{T}} + g_{\mathrm{T}}\big)\cdot\delta g_{\mathrm{T}}\,\mathrm{d}\Gamma}_{\delta\Pi_{\mathrm{Stick}}} + \underbrace{\int_{\Gamma^m_{\mathrm{sl}}} \big(\mu\epsilon|g^{*}_{\mathrm{N}} + g_{\mathrm{N}}| + \tau_c\big)\, n_{\mathrm{T}}\cdot\delta g_{\mathrm{T}}\,\mathrm{d}\Gamma}_{\delta\Pi_{\mathrm{Slip}}} = 0 \end{aligned} \tag{5.15}$$

Eq. (5.15) has to be solved in an iterative manner using Newton's method, which constitutes an inner loop in Algorithm (3). Since the augmented gaps are fixed within the inner loop, the linearization of Eq. (5.15) depends only on the normal and tangential gaps

g_{N} and g_{T}, and the direction of tangential traction n_{T}. The finite element discretization, and the linearization procedure, will be described in Section 5.5.

The augmentation process makes it possible to strictly penalize any violation of contact constraints by using a small penalty parameter. It is noteworthy that due to the singularity, even a slight violation of contact constraints can cause considerable stresses near the cracks. Therefore, the contact constraints have to be applied as accurately as possible. This requires the augmentation to continue until the normal gap g_{N} and the tangential stick gap g_{T} become smaller than reasonable values of thresholds $\mathrm{Tol}_{\mathrm{N}}$ and $\mathrm{Tol}_{\mathrm{T}}$, which are dependent on the crack size.

5.5 Finite element formulation

Due to the complex geometrical constraints of the explicitly represented fractures, a fully unstructured mesh based on tetrahedral elements is the best choice to discretize an arbitrary fractured media. It is well known that meshing procedures by tetrahedra are much simpler, and these elements are best suited to mesh arbitrary domains and complicated geometries automatically. Additionally, adaptive meshing procedures can be applied to discretize the domain efficiently. Quadratic elements are preferred over linear ones in such complex deformation states, since high stress gradients occur in the domain, particularly near the crack fronts. Consider the problem domain Ω to be discretized using quadratic tetrahedral finite elements. Accordingly the domain boundaries and fracture surfaces are discretized by quadratic triangular elements. Most meshing schemes are able generate matched meshes over the fracture surfaces. Therefore, an isoparametric discretization of the contact area based on quadratic triangular elements is applicable. Such discretizations are preferred in geometrically linear problems where the change in the geometry is trivial due to small deformations. In general, procedures based on non-matched meshes such as node-to-surface and surface-to-surface mortar-based methods are computationally more expensive [Wriggers, 2006].

5.5.1 Domain discretization

The entire domain of the problem is discretized with quadratic ten-noded tetrahedral elements as shown in Fig. (5.3). The geometry and displacement of a ten-noded isoparametric tetrahedral element is mapped from the global coordinate system xyz into the natural coordinate system $\xi\eta\zeta$ $(0 \leq \xi, \eta, \zeta \leq 1)$ by

$$X(\xi,\eta,\zeta) = \sum_{i=1}^{10} N_i X_i \quad , \quad u(\xi,\eta,\zeta) = \sum_{i=1}^{10} N_i u_i \tag{5.16}$$

where N_i is the shape function corresponding to the node i with the position vector $X_i = (x_i, y_i, z_i)$ in the global space, and u_i is the displacement vector of the node i in the global space. The shape functions of a ten-noded tetrahedral finite element are given by

$$\begin{aligned} &N_1 = \lambda(2\lambda - 1)\ ,\ N_2 = \xi(2\xi - 1)\ ,\ N_3 = \eta(2\eta - 1)\ ,\ N_4 = \zeta(2\zeta - 1) \\ &N_5 = 4\lambda\xi\ ,\ N_6 = 4\xi\eta\ ,\ N_7 = 4\lambda\eta\ ,\ N_8 = 4\lambda\zeta\ ,\ N_9 = 4\xi\zeta\ ,\ N_{10} = 4\eta\zeta \end{aligned} \tag{5.17}$$

where $\lambda = 1 - \xi - \eta - \zeta$. The boundaries of the problem, including the external boundaries and internal crack surfaces, are discretized with isoparametric quadratic six-noded triangular elements as shown in Fig. (5.3). In these elements, the mapping from the global coordinate system xyz into the natural coordinate system $\xi\eta$ $(0 \leq \xi, \eta \leq 1)$ is

$$X(\xi, \eta) = \sum_{i=1}^{6} N_i X_i \ \ , \ \ u(\xi, \eta) = \sum_{i=1}^{6} N_i u_i \tag{5.18}$$

where the shape functions are

$$N_1 = \lambda(2\lambda - 1)\ ,\ N_2 = \xi(2\xi - 1)\ ,\ N_3 = \eta(2\eta - 1)\ ,\ N_4 = 4\lambda\xi\ ,\ N_5 = 4\xi\eta\ ,\ N_6 = 4\lambda\eta \tag{5.19}$$

where $\lambda = 1 - \xi - \eta$. According to the linear elastic solution, the state of strain is singular over the crack front of 3D fractures [Anderson, 2005]. Conventional finite elements including standard tetrahedra employ polynomials to interpolate field variables in the domain. Therefore, these elements are not able to reproduce the crack tip square root singular strain field near the crack front, which leads to their poor performance in FE analyses of crack problems. The efficiency and applicability of quarter-point tetrahedral finite elements in reproducing the strain singularity near the crack front were demonstrated in Chapters 2 and 3. The numerical results in Chapter 3 suggest that employing quarter-point tetrahedral element in an unstructured mesh layout improves the FE solution near the crack front considerably.

Quarter-point tetrahedral elements are employed at the immediate neighborhood of crack fronts, while the remainder of the domain is discretized with the standard tetrahedral elements as shown in Fig. (5.3). The introduction of quarter-point elements to the fractured media is straightforward. Tetrahedral elements attached to the crack front are identified, and mid-side nodes are shifted to the quarter-point position near the crack front. The internal node numbering of the elements is then adapted to become consistent with the numbering in Section 2.6. This allows one to use simple relations for obtaining the local coordinates of a given point inside a quarter-point element. The use of quarter-point tetrahedra also introduces quarter-point triangular elements over the crack surfaces near the crack front as is shown in Fig. (5.3). The internal node numbering of these elements

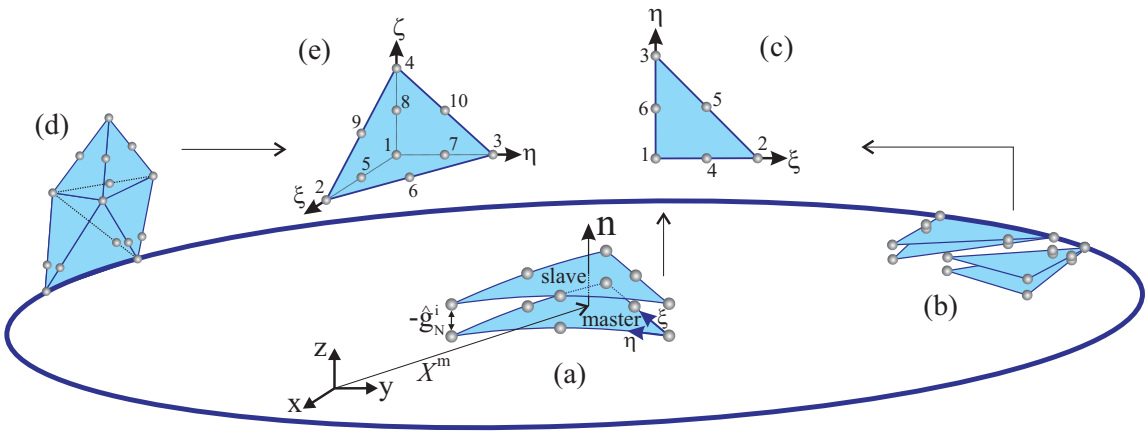

Figure 5.3: (a, b) Schematics of matched contact master and slave standard and quarter-point triangular elements which are mapped from xyz into the natural space $\xi\eta$ in (c). (d) Schematics of standard and quarter-point tetrahedral elements which are mapped from xyz into $\xi\eta\zeta$ space in (e).

are also changed in order to make the orientations of quarter-point triangular elements consistent (see Section 2.6). As is seen in Fig. (5.3), the remainder of surfaces is discretized with standard quadratic triangular elements.

5.5.2 The contribution of internal/external forces

In order to describe the kinematics of tetrahedral and triangular elements, the vectors of displacements, u_i, virtual displacements, δu_i, and incremental displacements, Δu_i are introduced for every node i. The virtual work due to internal stresses and body forces throught the domain is given by

$$\delta\Pi_{\Omega+\sigma}(u,\delta u) = \int_{\Omega}\Big(\sigma:\delta\varepsilon - b\cdot\delta u\Big)\,\mathrm{d}\Omega - \int_{\Gamma_\sigma}\bar{t}\cdot\delta u\,\mathrm{d}\Gamma \approx \sum_{\Omega}^{\text{elems}}\sum_{i=1}^{10}\delta u_i^T G_i^{\Omega} - \sum_{\Gamma_\sigma}^{\text{elems}}\sum_{i=1}^{6}\delta u_i^T G_i^{\sigma}$$

$$G_i^{\Omega} = \int_{\Omega_e}\Big(B_i^T D B_j u_j - N_i b\Big)\,\mathrm{d}\Omega \approx \sum_{p=1}^{\text{gpts}}\Big[\Big(B_i^T D B_j u_j - N_i b\Big)|\mathbf{J}|\Big]_p w_p$$

$$G_i^{\sigma} = \int_{\Gamma_e} N_i\bar{t}\,\mathrm{d}\Gamma \approx \sum_{p=1}^{\text{gpts}}\Big[N_i\,\bar{t}\,|\mathbf{J}|\Big]_p w_p \tag{5.20}$$

The summations over domains Ω and Γ_σ include all tetrahedral elements, and triangular elements which are subjected to pre-defined external tractions, respectively. Ω_e and Γ_e denote the domain of tetrahedral and triangular elements. The sum over p includes element integration points where the bracketed quantities $\{\}_p$ and $[]_p$ are evaluated and multiplied by the corresponding weight w_p. $|\mathbf{J}|$ also denotes the determinant of the coordinate Jacobian matrix of the elements. Matrix B_i contains the derivative of the shape functions associated

with node i in local coordinate, and D is the elasticity matrix containing the material properties [Zienkiewicz and Taylor, 1989]. The contribution is linearly dependent on the displacement, and the associated tangent matrix is the so-called stiffness matrix, given by

$$K_{ij}^{\Omega} = \frac{\partial G_i^{\Omega}}{\partial u_j} = \int_{\Omega_e} B_i^T D B_j \, \mathrm{d}\Omega \approx \sum_{p=1}^{\text{gpts}} \Big[B_i^T D B_j |\mathbf{J}| \Big]_p w_p \tag{5.21}$$

5.5.3 Contact kinematics and contribution

Consider two conformed quadratic triangular elements on the crack surfaces. One is referred to as *master* element, m, and the other is denoted as *slave* element, s, as shown in Fig. (5.3). Considering the global coordinate system in Fig. (5.3), all the top and bottom crack surfaces are assigned as slave and master surfaces, respectively. Each node i on the master element is paired with the matched node i on the slave surface, constructing the nodal pair i. Assuming small deformation, the geometry of the contact surface can be represented by the reference configuration of master surface X^m. The expression of the unit normal to the master surface is given by

$$\boldsymbol{n}\left(\xi,\eta\right) = \frac{\partial X^m/\partial\xi \times \partial X^m/\partial\eta}{||\partial X^m/\partial\xi \times \partial X^m/\partial\eta||} \tag{5.22}$$

where $\partial X^m/\partial\alpha = \sum_{i=1}^{6} X_i^m \partial N_i/\partial\alpha$, $\alpha = \xi, \eta$ are the tangent vectors to the master surface. Depending on the internal node numbering of the master element, two normals with opposite directions are obtained from Eq. (5.22). A normal vector that makes an acute angle with the z direction of global coordinate system shall be used ($\boldsymbol{n} \cdot e_z > 0$ where $e_z = (0,0,1)$ in Fig. (5.3)). The two elements are separated by a small initial aperture, leading to an initial normal gap $-\hat{g}_{\mathrm{N}}$. Since the initial distance between the contact elements is small compared to the size of contact elements, it is not necessary to explicitly apply this gap between the elements in the geometrical specification. In fact, the implicit presence of the gap in the gap formulation would suffice, leaving the geometry of the domain unchanged during the entire contact analysis. Considering a certain fracture aperture distribution, the initial normal gap is distributed over the master nodes of the fracture surface. Considering the slave node i with the initial normal gap $\hat{g}_{\mathrm{N}}^i$, the initial normal gap distribution over the contact element is given by

$$\hat{g}_{\mathrm{N}}\left(\xi,\eta\right) = \sum_{i=1}^{6} N_i \hat{g}_{\mathrm{N}_i} \tag{5.23}$$

On the other hand, the initial tangential gap has to be computed by taking into account the displacement field at the time that the master and slave surfaces first come into contact. Consider that the slave element penetrates the master surface during the current time

increment $t_c = [t_n, t_{n+1}]$, when the relative displacement at the penetrating nodal pair i in the first iteration is $(u_i^s - u_i^m)_c$. The initial tangential gap distribution over the contact element is then approximated by

$$\hat{g}_{\mathrm{T}}(\xi,\eta) = \frac{\hat{g}_{\mathrm{N}}(\xi,\eta)}{\boldsymbol{n}\cdot\sum_{i=1}^{6} N_i(u_i^s - u_i^m)_c}\,(\mathbb{I}-\boldsymbol{n}\otimes\boldsymbol{n})\sum_{i=1}^{6} N_i(u_i^s - u_i^m)_c \tag{5.24}$$

at the end of the first iteration and is used in the following iterations of this increment to apply the contact constraints. This initial tangential gap then remains constant until the time at which the nodes in the nodal pair lose their contact again. The distribution of total initial gap over the master element will therefore be

$$\hat{g}(\xi,\eta) = \hat{g}_{\mathrm{N}}\cdot\boldsymbol{n} + \hat{g}_{\mathrm{T}} \tag{5.25}$$

In order to describe the kinematics of each nodal pair, the vectors of displacements, virtual displacements and incremental displacements are introduced as

$$u_i^c = \begin{Bmatrix} u_i^s \\ u_i^m \end{Bmatrix} \;,\; \delta u_i^c = \begin{Bmatrix} \delta u_i^s \\ \delta u_i^m \end{Bmatrix} \;,\; \Delta u_i^c = \begin{Bmatrix} \Delta u_i^s \\ \Delta u_i^m \end{Bmatrix} \tag{5.26}$$

In addition, the following vector and matrix are introduced based on the local normal at the master element as

$$C(\xi,\eta) = \begin{Bmatrix} n \\ -n \end{Bmatrix} \;,\; T(\xi,\eta) = \begin{bmatrix} (\mathbb{I}-\boldsymbol{n}\otimes\boldsymbol{n}) \\ -(\mathbb{I}-\boldsymbol{n}\otimes\boldsymbol{n}) \end{bmatrix} \tag{5.27}$$

Based on these definitions and employing Eq. (5.26), the discretized version of gap functions in Eqs. (5.2) and (5.3) in normal and tangential directions are given by

$$g_{\mathrm{N}}(\xi,\eta) = C^T\sum_{i=1}^{6} N_i u_i^c - \hat{g}_{\mathrm{N}}(\xi,\eta) \;,\; g_{\mathrm{T}}(\xi,\eta) = T^T\sum_{i=1}^{6} N_i u_i^c - \hat{g}_{\mathrm{T}}(\xi,\eta) \tag{5.28}$$

The variation of the gap functions due to virtual displacement, δg, and the variation of gap function due to incremental displacement, Δg, in normal and tangential directions are also given as

$$\begin{aligned} \delta g_{\mathrm{N}}(\xi,\eta) &= C^T\sum_{i=1}^{6} N_i\delta u_i^c \;,\; \delta g_{\mathrm{T}}(\xi,\eta) = T^T\sum_{i=1}^{6} N_i\delta u_i^c \\ \Delta g_{\mathrm{N}}(\xi,\eta) &= C^T\sum_{i=1}^{6} N_i\Delta u_i^c \;,\; \Delta g_{\mathrm{T}}(\xi,\eta) = T^T\sum_{i=1}^{6} N_i\Delta u_i^c \end{aligned} \tag{5.29}$$

As was explained in Section 5.4, the accurate computation of contact traction near the crack front requires a square-root singular variation of the penalty parameter near the crack front. This type of variation can be applied simply over the entire fracture surface, in the

case of well-defined crack shapes such as penny-shaped and elliptical cracks. For example, for an elliptical crack defined by the equation $x'^2/a^2 + y'^2/b^2 = 1$, where a and b are the minor and major axis of the ellipse in the local $x'y'$ coordinate system, the parameter $\epsilon_r = \sqrt{1-(x'^2/a^2+y'^2/b^2)^{1/2}}$ is defined, and corresponding values are applied on nodes over the master surface. The distribution of the penalty parameters over any master element is then obtained by

$$\epsilon(\xi,\eta) = \frac{\epsilon_0}{\sum_{i=1}^{6} N_i \epsilon_r^i} \tag{5.30}$$

where ϵ_r^i holds the value of ϵ_r at the node i. In the cases of complex fracture geometries, the singular square root variation of penalty parameter can be applied only adjacent to the crack front, perhaps over the quarter-point triangular elements only. In this case, the application of a constant penalty parameter $\epsilon = \epsilon_0$ would suffice for the remainder of the fracture surface.

Augmented gaps are also obtained based on the gap discretization in Eq. (5.28). The $(k+1)$th augmented gaps are given by

$$\begin{aligned} g_{\mathrm{N}}^{*k+1}(\xi,\eta) &= g_{\mathrm{N}}^{*k}(\xi,\eta) + g_{\mathrm{N}}^{k}(\xi,\eta) \\ g_{\mathrm{T}}^{*k+1}(\xi,\eta) &= \begin{cases} g_{\mathrm{T}}^{*k}(\xi,\eta) + g_{\mathrm{T}}^{k}(\xi,\eta), & \text{if} f_s^{\mathrm{tr}} \le 0 \text{ (stick).} \\ \left(\mu |g_{\mathrm{N}}^{*k+1}(\xi,\eta)| + \tau_c/\epsilon\right) n_{\mathrm{T}}^{k+1}, & \text{otherwise (slip).} \end{cases} \end{aligned} \tag{5.31}$$

where

$$g_{\mathrm{N}}^{k}(\xi,\eta) = C^T \sum_{i=1}^{6} N_i u_i^{ck} - \hat{g}_{\mathrm{N}}(\xi,\eta) \quad , \quad g_{\mathrm{T}}^{k}(\xi,\eta) = T^T \sum_{i=1}^{6} N_i u_i^{ck} - \hat{g}_{\mathrm{T}}(\xi,\eta) \tag{5.32}$$

where u_i^{ck} is the displacement associated with the nodal pair i at kth iteration. n_{T}^{k+1} is also the direction of tangential traction at the $(k+1)$th augmentation iteration. It is obtained through the return mapping process by using the trial tangential gap of the kth augmentation iteration. Consider n_{T}^{k} and g_{T}^{k} to be respectively the direction of tangential slip traction and the tangential gap at kth augmentation iteration. The direction of tangential traction for the next iteration is then obtained as

$$n_{\mathrm{T}}^{k+1} = \frac{g_{\mathrm{T}}^{*k} + g_{\mathrm{T}}^{k}}{||g_{\mathrm{T}}^{*k} + g_{\mathrm{T}}^{k}||} \tag{5.33}$$

where $g_{\mathrm{T}}^{*k} = \left(\mu |g_{\mathrm{N}}^{*k}| + \tau_c/\epsilon\right) n_{\mathrm{T}}^{k}$. As gaps are evaluated at the integration points of the contact elements, the direction of the trial tangential traction is also evaluated there, and updated during the augmentation process. For a planar crack, however, as the normals to all master elements are identical for each fracture, the directions of tangential traction can be stored and updated at the nodal pairs and then interpolated to the integration points as

$$g_{\mathrm{T}}^{*k} + g_{\mathrm{T}}^{k} = \sum_{i=1}^{6} N_i \big(g_{\mathrm{T}_i}^{*k} + g_{\mathrm{T}_i}^{k} \big) \tag{5.34}$$

Here gaps and augmented gaps corresponding to the nodal pair i are defined as

$$\begin{aligned} g_{\mathrm{N}_i}^{k} &= C^T u_i^{ck} - \hat{g}_{\mathrm{N}_i} \quad , \quad g_{\mathrm{N}_i}^{*k} = g_{\mathrm{N}_i}^{*k-1} + C^T u_i^{ck-1} - \hat{g}_{\mathrm{N}_i} \\ g_{\mathrm{T}_i}^{k} &= T^T u_i^{ck} - \hat{g}_{\mathrm{T}_i} \quad , \quad g_{\mathrm{T}_i}^{*k} = \begin{cases} g_{\mathrm{T}_i}^{*k-1} + T^T u_i^{ck-1} - \hat{g}_{\mathrm{T}_i}, & \text{(stick).} \\ \big(\mu | g_{\mathrm{N}_i}^{*k} | + \tau_c / \epsilon \big) \, n_{\mathrm{T}_i}^{k}, & \text{(slip).} \end{cases} \end{aligned} \tag{5.35}$$

In this case the augmented nodal gaps are stored for each nodal pair i in $g_{\mathrm{N}_i}^{*k}$ and $g_{\mathrm{T}_i}^{*k}$ and updated in the augmentation process.

The contribution of the normal, stick and slip contact tractions are approximated by integrating numerically over the master elements. Using Eqs. (5.26) and (5.29), the contact contributions in Eq. (5.15) is given by

$$\begin{aligned} \delta\Pi_{\mathrm{Normal}} &= \int_{\Gamma_{\mathrm{st}}^m + \Gamma_{\mathrm{sl}}^m} \epsilon \big(g_{\mathrm{N}}^{*} + g_{\mathrm{N}} \big) \delta g_{\mathrm{N}} \, \mathrm{d}\Gamma \approx \sum_{\Gamma_{\mathrm{st}}^m + \Gamma_{\mathrm{sl}}^m}^{\mathrm{elems}} \sum_{i=1}^{6} \delta u_i^{cT} G_i^{\mathrm{N}} \\ \delta\Pi_{\mathrm{Stick}} &= \int_{\Gamma_{\mathrm{st}}^m} \epsilon \big(g_{\mathrm{T}}^{*} + g_{\mathrm{T}} \big) \cdot \delta g_{\mathrm{T}} \, \mathrm{d}\Gamma \approx \sum_{\Gamma_{\mathrm{st}}^m}^{\mathrm{elems}} \sum_{i=1}^{6} \delta u_i^{cT} G_i^{\mathrm{St}} \\ \delta\Pi_{\mathrm{Slip}} &= \int_{\Gamma_{\mathrm{sl}}^m} \big(\mu \epsilon | g_{\mathrm{N}}^{*} + g_{\mathrm{N}} | + \tau_c \big) \, n_{\mathrm{T}} \cdot \delta g_{\mathrm{T}} \, \mathrm{d}\Gamma \approx \sum_{\Gamma_{\mathrm{sl}}^m}^{\mathrm{elems}} \sum_{i=1}^{6} \delta u_i^{cT} G_i^{\mathrm{Sl}} \end{aligned} \tag{5.36}$$

where the residual vectors are defined as

$$\begin{aligned} G_i^{\mathrm{N}} &= \int_{\Gamma_{\mathrm{e}}} \epsilon (g_{\mathrm{N}}^{*} + g_{\mathrm{N}}) N_i C \, \mathrm{d}\Gamma \approx \sum_{p=1}^{\mathrm{gpts}} \Big[\epsilon (g_{\mathrm{N}}^{*} + g_{\mathrm{N}}) N_i C |\mathbf{J}| \Big]_p w_p \\ G_i^{\mathrm{St}} &= \int_{\Gamma_{\mathrm{e}}} T \epsilon (g_{\mathrm{T}}^{*} + g_{\mathrm{T}}) N_i \, \mathrm{d}\Gamma \approx \sum_{p=1}^{\mathrm{gpts}} \Big[T \epsilon (g_{\mathrm{T}}^{*} + g_{\mathrm{T}}) N_i |\mathbf{J}| \Big]_p w_p \\ G_i^{\mathrm{Sl}} &= \int_{\Gamma_{\mathrm{e}}} \Big(\mu \epsilon | g_{\mathrm{N}}^{*} + g_{\mathrm{N}} | + \tau_c \Big) N_i T n_{\mathrm{T}} \, \mathrm{d}\Gamma \approx \sum_{p=1}^{\mathrm{gpts}} \Big[\Big(\mu \epsilon | g_{\mathrm{N}}^{*} + g_{\mathrm{N}} | + \tau_c \Big) N_i T n_{\mathrm{T}} |\mathbf{J}| \Big]_p w_p \end{aligned} \tag{5.37}$$

Summations over area Γ_{st}^m and Γ_{sl}^m include all the elements domains Γ_{e} in stick and slip conditions, respectively. The sum over p includes element integration points, 'gpts', of the master triangular elements, 'elems', where the bracketed quantities $\{\}_p$ and $[]_p$ are evaluated and multiplied by the corresponding weight w_p. $|\mathbf{J}|$ denotes the determinant of the coordinate Jacobian matrix of the triangular elements. Eqs. (5.27), (5.28), (5.30) and (5.31) are used to evaluate the parameters in Eq. (5.37) at integration points. The direction of slip at integration point is also evaluated using Eq. (5.33). Linearization of Eq. (5.37)

gives the tangent matrices as

$$
\begin{aligned}
K_{ij}^{\mathrm{N}} &= \frac{\partial G_i^{\mathrm{N}}}{\partial u_j} = \int_{\Gamma_{\mathrm{e}}} \epsilon N_i N_j C C^T \,\mathrm{d}\Gamma \approx \sum_{p=1}^{\mathrm{gpts}} \Big[\epsilon N_i N_j C C^T |\mathbf{J}|\Big]_p w_p \\
K_{ij}^{\mathrm{St}} &= \frac{\partial G_i^{\mathrm{St}}}{\partial u_j} = \int_{\Gamma_{\mathrm{e}}} \epsilon N_i N_j T T^T \,\mathrm{d}\Gamma \approx \sum_{p=1}^{\mathrm{gpts}} \Big[\epsilon N_i N_j T T^T |\mathbf{J}|\Big]_p w_p \\
K_{ij}^{\mathrm{Sl}} &= \frac{\partial G_i^{\mathrm{Sl}}}{\partial u_j} = \frac{\partial G_i^{\mathrm{Sl}}}{\partial n_{\mathrm{T}}} \frac{\partial n_{\mathrm{T}}}{\partial u_j} + \frac{\partial G_i^{\mathrm{Sl}}}{\partial g_{\mathrm{N}}} \frac{\partial g_{\mathrm{N}}}{\partial u_j} \\
&= \int_{\Gamma_{\mathrm{e}}} \epsilon N_i N_j \Big(\frac{\mu |g_{\mathrm{N}}^* + g_{\mathrm{N}}| + \tau_c/\epsilon}{||g_{\mathrm{T}}^* + g_{\mathrm{T}}||} T(\mathbb{I} - n_{\mathrm{T}} \otimes n_{\mathrm{T}}) T^T - \mu T n_{\mathrm{T}} C^T \Big) \,\mathrm{d}\Gamma \\
&\approx \sum_{p=1}^{\mathrm{gpts}} \Big[\epsilon N_i N_j \Big(\frac{\mu |g_{\mathrm{N}}^* + g_{\mathrm{N}}| + \tau_c/\epsilon}{||g_{\mathrm{T}}^* + g_{\mathrm{T}}||} T(\mathbb{I} - n_{\mathrm{T}} \otimes n_{\mathrm{T}}) T^T - \mu T n_{\mathrm{T}} C^T \Big) |\mathbf{J}| \Big]_p w_p
\end{aligned}
\tag{5.38}
$$

Remark 4: Some of the tangent matrix components in Eq. (5.38) are associated with the virtual or actual displacement variation of the gap at the crack front nodes, which are essentially zero. Therefore, the rows and columns corresponding to the crack front nodes must be eliminated from the tangent matrices of the contact elements attached to the crack front.

5.5.4 Contact algorithm and implementation

The Newton-Raphson method is often used to solve the system of nonlinear equations associated with the nonlinear characteristic of contact problems. Once the element residual vectors and tangent matrices are obtained, the residual vector and tangent matrix of the entire system of elements is developed through an assembling process. Let $u = \{u_1, u_2, ..., u_{\mathrm{N}}\}$ be the solution vector containing the displacements of all the nodes of the system, N. Equivalently, $\delta u^T = \{\delta u_1, \delta u_2, ..., \delta u_{\mathrm{N}}\}$ can be defined to include the virtual displacement of the nodes in the system. By substituting Eqs. (5.20), (5.21), (5.37) and (5.38) into (5.15), the virtual work of the entire system is developed as

$$
\begin{aligned}
\delta\Pi(u, \delta u) = \delta u^T G = &\sum_{\Omega}^{\mathrm{elems}} \sum_{i=1}^{10} \delta u_i^{cT} G_i^{\Omega} - \sum_{\Gamma_\sigma}^{\mathrm{elems}} \sum_{i=1}^{6} \delta u_i^{cT} G_i^{\sigma} \\
&+ \sum_{\Gamma_{\mathrm{st}}^m + \Gamma_{\mathrm{sl}}^m}^{\mathrm{elems}} \sum_{i=1}^{6} \delta u_i^{cT} G_i^{\mathrm{N}} + \sum_{\Gamma_{\mathrm{st}}^m}^{\mathrm{elems}} \sum_{i=1}^{6} \delta u_i^{cT} G_i^{\mathrm{St}} + \sum_{\Gamma_{\mathrm{sl}}^m}^{\mathrm{elems}} \sum_{i=1}^{6} \delta u_i^{cT} G_i^{\mathrm{Sl}} = 0
\end{aligned}
\tag{5.39}
$$

where

$$
G = \underbrace{\sum_{\Omega}^{\mathrm{elems}} \sum_{i=1}^{10} G_i^{\Omega} - \sum_{\Gamma_\sigma}^{\mathrm{elems}} \sum_{i=1}^{6} G_i^{\sigma}}_{G^{\Omega+\sigma}} + \underbrace{\sum_{\Gamma_{\mathrm{st}}^m}^{\mathrm{elems}} \sum_{i=1}^{6} \Big(G_i^{\mathrm{N}} + G_i^{\mathrm{St}} \Big) + \sum_{\Gamma_{\mathrm{sl}}^m}^{\mathrm{elems}} \sum_{i=1}^{6} \Big(G_i^{\mathrm{N}} + G_i^{\mathrm{Sl}} \Big)}_{G^C}
\tag{5.40}
$$

Here G is the residual vector of the entire system, where $\delta u^T G = 0$ indicates that a zero residual vector defines the solution vector u, constituting a set of $3 \times N$ nonlinear equations. Here the application of Newton-Raphson method involves the convergence of a trial solution vector iteratively as

$$\begin{aligned} K\Delta u &= -G \\ u &\leftarrow u + \Delta u \end{aligned} \tag{5.41}$$

where $\Delta u = \{\Delta u_1, \Delta u_2, ..., \Delta u_{\mathrm{N}}\}^T$ is vector of displacement corrections, and K is the tangent matrix of the entire system:

$$K = \underbrace{\sum_{\Omega}^{\text{elems}} \sum_{i=1}^{10} \sum_{j=1}^{10} K_{ij}^{\Omega}}_{K^{\Omega}} + \underbrace{\sum_{\Gamma_{\mathrm{st}}^m}^{\text{elems}} \sum_{i=1}^{6} \sum_{j=1}^{6} \Big(K_{ij}^{\mathrm{N}} + K_{ij}^{\mathrm{St}}\Big) + \sum_{\Gamma_{\mathrm{sl}}^m}^{\text{elems}} \sum_{i=1}^{6} \sum_{j=1}^{6} \Big(K_{ij}^{\mathrm{N}} + K_{ij}^{\mathrm{Sl}}\Big)}_{K^{\mathrm{C}}} \tag{5.42}$$

K and G are updated in each iteration to include the contribution of all the regions in contact. The Newton-Raphson iteration continues until the norm of Δu becomes less than some tolerance value. Algorithm (4) demonstrates all necessary steps associated with the contact algorithm. The initial opening of the fractures in this algorithm is modeled by applying an initial fluid (normal) pressure p_0 on the fracture surfaces, and solving for the deformation. The induced initial normal gaps are then saved as nodal values over the crack surfaces. Afterwards the fluid pressure is removed, the solid deformation due to fluid pressure is discarded, and the simulation begins by applying external compressive stress to the cube, where as a result the crack surfaces might go into contact. This process of introducing initial gap agrees well with the opening process of the natural fractures in geomechanical systems.

Remark 5: The elements of the tangent matrix in Eq. (5.38) require integration of polynomials of a maximum order of four. The Jacobian determinants of the straight-sided standard and quarter-point triangular elements are polynomials of order zero and two, respectively. Therefore, full-integration of the elements of the tangent matrix requires the integration of sixth-order polynomials, which can be achieved by a seven-point integration rule [Zienkiewicz and Taylor, 1989]. It is noteworthy that a rule with integration points on the sides cannot be employed, as the Jacobian determinant is zero along the crack front, due to the nonlinear mapping in quarter-point tetrahedra. A four-point Gauss rule computes exactly the elements of stiffness matrix of straight-sided standard tetrahedral elements. However, quarter-point tetrahedra introduce a Jacobian determinant in the form of polynomials of order three. Therefore, a four-point Gauss rule provides a reduced integration scheme for these elements. It has been demonstrated that a five-point Gauss rule can integrate the elements of the stiffness matrix with the level of accuracy that is compatible with the full integration of the components of the tangent matrices of quarter-point triangles.

In this work, five-point and seven-point Gauss rules are used for tetrahedral and triangular elements, respectively.

Algorithm 4 A frictional contact algorithm for analyzing 3D fractured media using a gap-based augmented Lagrangian method

Initialization:
  $u = 0$, $g^* = 0$
  Initialize fractures: Define $\epsilon, \mu, \tau_c, p_0$ for each fracture
  Identify master and slave elements and nodes pairs
  Identify all node pairs and crack front nodes
  Generate quarter-point tetrahedra
  Update $\hat{g}_{\mathrm{N}}$ based on the solution of the system under p_0 only
  Save K^{Ω} in the form of a sparse matrix
Loop over N load increments:
for $n := 1 \rightarrow N$ **do**
  Identify all nonactive node pairs NNP
  Update the boundary conditions $\bar{u}$ and $\bar{t}$ at t_n
  Trial solution based on updated boundary conditions
  Update $\hat{g}_{\mathrm{T}}$ for NNP based on the trial solution
  Loop over A augmentations:
  for $k := 1 \rightarrow A$ **do**
    Loop over Newton-Raphson iterations:
    while $||\Delta u|| >$ THRESHOLD **do**
      Update $G^{\Omega+\sigma}$
      Update G^{C} and K^{C}
      Solve $K\Delta u = -G$
      Update u : $u \leftarrow u + \Delta u$
    end while
    Update augmented gaps g^*
  end for
  Update $\hat{g}_{\mathrm{T}}$ for slipping node pairs
  Compute SIFs along all crack fronts
end for

5.5.5 The computation of fracture parameters

A major step in analyzing crack behavior is the accurate computation of fracture mechanics parameters such as the J-integral and stress intensity factors (SIFs). In the context of linear elastic fracture mechanics (LEFM), the SIFs characterize the stress state adjacent to the crack, and therefore their accurate determination is of great importance for predicting the onset and characteristics of brittle crack growth. Unlike the vast amount of research that has been carried out on the computation of fracture parameters for open cracks, crack behavior

under compression has not been well investigated. Many fractured media are subjected to compression, and many applications, including rock fracturing and fragmentation and fault growth, require analyzing cracks under compressive loads. Two efficient, accurate and straightforward methods to compute fracture parameters from unstructured meshes were presented in Chapters 3 and 4. One is a straightforward and computationally cheap displacement correlation (DC) scheme, which is employed in combination with quarter-point elements. This method is based on correlating the displacement of points over the crack faces at a fixed distance r_m from the crack front. The use of this method for compressive stresses requires no adaptation for closed cracks. The second method is an energy-based domain integral approach, which computes J- and interaction integrals over disk-shaped domains along the crack front. Since this method involves integration of crack surface tractions, a brief description of the method and the process of integration of contact tractions is described here.

In the absence of body forces, the disk-shaped domain representation of point-wise J-integral and interaction integral at any point along the crack front of a planar 3D crack is given by (see Chapter 4)

$$J(s) = \int_A \left(\sigma_{kl}\frac{\partial u_l}{\partial x_1} - W\delta_{1k}\right)\frac{\partial q}{\partial x_k}\mathrm{d}A - \int_{C_-+C_+} \sigma_{2l}\frac{\partial u_l}{\partial x_1} m_2 q \mathrm{d}C \tag{5.43}$$

$$I(s) = \int_A \left(\sigma_{kl}\frac{\partial u_l^{\mathrm{aux}}}{\partial x_1} + \sigma_{kl}^{\mathrm{aux}}\frac{\partial u_l}{\partial x_1} - W_{\mathrm{I}}\delta_{1k}\right)\frac{\partial q}{\partial x_k}\mathrm{d}A - \int_{C_-+C_+} \sigma_{2l}\frac{\partial u_l^{\mathrm{aux}}}{\partial x_1} m_2 q \mathrm{d}C \tag{5.44}$$

where A is a disk-shaped area in the plane orthogonal to the crack front at point s, and C_+ and C_- are the contours on the top (slave) and bottom (master) crack surfaces with the outward unit normal $m = (0, -1, 0)$ and $m = (0, 1, 0)$, respectively as shown in Fig. (5.4). σ_{kl}, ε_{kl} and u_k are the Cartesian components of the stress tensor, strain tensor and displacement vector in the local $x_1x_2x_3$ coordinate system, respectively. $\sigma_{kl}^{\mathrm{aux}}$, $,\varepsilon_{kl}^{\mathrm{aux}}$, and u_k^{aux} are the components of stress tensor, strain tensor and displacement vector due to an auxiliary state which includes the dominant terms in the linear elastic solution of a crack problem. The auxiliary fields are therefore the first terms of the Williams series expansion of crack tip fields [Williams, 1957]. $W = \int_0^{\varepsilon} \sigma_{kl}\varepsilon_{kl} d\varepsilon$ and $W_{\mathrm{I}} = 1/2(\varepsilon_{kl}^{\mathrm{aux}}\sigma_{kl} + \varepsilon_{kl}\sigma_{kl}^{\mathrm{aux}})$ are the actual and mutual strain energy densities, respectively. δ_{kl} is the Kronecker delta, and q is a smooth scalar function defined within the area A, taking the value of unity on the disk's circumference, and vanishing on the crack front. After the interaction integrals corresponding to different auxiliary modes are computed, the stress intensity factors are computed from simple relations.

Once the boundary value problem subjected to the contact constraints is solved, and the required augmentation steps are performed, Lagrange multipliers provide the contact

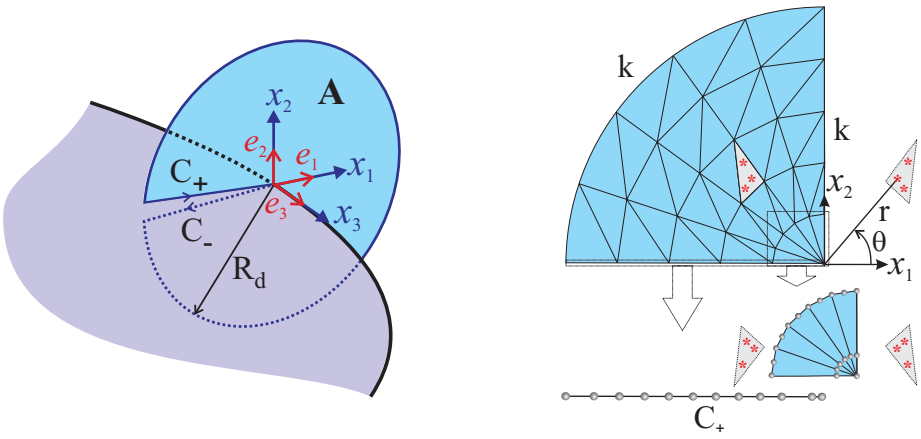

Figure 5.4: Schematics of integration over disk-shape domains using virtual triangular and line elements.

tractions, and the penalty terms are essentially zero. In this case, the normal and tangential tractions are obtained by $p = \epsilon g_{\mathrm{N}}^*$ and $\tau = \epsilon g_{\mathrm{T}}^*$, respectively. The contact traction over the master (bottom) surface is therefore given by $t^m = p \cdot \boldsymbol{n} + \tau = \epsilon g^*$, where $g^* = g_{\mathrm{N}}^* \boldsymbol{n} + g_{\mathrm{T}}^*$. The traction over the slave (top) surface is also opposite the one applied on the master surface ($t^s = -t^m$). The stress components σ_{2l} applied on both master and slave surfaces is therefore equal to $\sigma_{2l} = \epsilon g^* \cdot e_l$ where e_l is the unit vector of local axis x_l in local coordinate system as shown in Fig. (5.4). The domain integrals in Eqs. (5.43) and (5.44) are rewritten as

$$J(s) = \int_A \left(\sigma_{kl} \frac{\partial u_l}{\partial x_1} - W\delta_{1k}\right) \frac{\partial q}{\partial x_k} \mathrm{d}A - \int_{C_- + C_+} \epsilon g^* \cdot e_l \frac{\partial u_l}{\partial x_1} m_2 q \mathrm{d}C \tag{5.45}$$

$$I(s) = \int_A \left(\sigma_{kl} \frac{\partial u_l^{\mathrm{aux}}}{\partial x_1} + \sigma_{kl}^{\mathrm{aux}} \frac{\partial u_l}{\partial x_1} - W_{\mathrm{I}}\delta_{1k}\right) \frac{\partial q}{\partial x_k} \mathrm{d}A - \int_{C_- + C_+} \epsilon g^* \cdot e_l \frac{\partial u_l^{\mathrm{aux}}}{\partial x_1} m_2 q \mathrm{d}C \tag{5.46}$$

The line integral involves the evaluation of singular integrands defined by the displacement gradients multiplied by the contact tractions. This implies that any small inaccuracy of contact tractions very close to the crack front could potentially influence the value of line integral significantly via the singular terms. Since the contributions of line integrals are significant to the entire J- and interaction integrals, these inaccuracies are most likely to influence the accuracy of the total value of J- and interaction integrals. Therefore, the accuracy of the results of the J-integral and stress intensity factors are heavily dependent on the accuracy of the contact traction near the fracture front. Although the choice of singular penalty parameter makes it possible to obtain accurate contact tractions even very close to the crack front, local inaccuracies near the crack front may still be observed. This is because contact tractions in a penalty solution are directly affected by the local displacement inaccuracies near the crack front which are mainly due to low quality of randomly placed

elements at a region with high stress gradients. These small inaccuracies can then greatly influence the results of J- and interaction integrals, due to the presence of singular displacement gradients. This vulnerability of the domain integrals to potential inaccuracies of the contact traction can however be circumvented by recasting the line integral. As explained earlier, the crack boundary condition dictates a square root displacement variation of the crack surfaces near the crack front. Employing a singular square root penalty parameter ensures that the contact traction is held constant at the region very close to the crack front. Since the domain integrals are evaluated over small region near the crack front, a constant contact traction over $C_- + C_+$ is therefore expected. Define $\Delta u_l = u_l|_{\theta=\pi} - u_l|_{\theta=-\pi}$ and $\Delta u_l^{\text{aux}} = u_l^{\text{aux}}|_{\theta=\pi} - u_l^{\text{aux}}|_{\theta=-\pi}$ as the relative actual and auxiliary displacement of slave crack surface with respect to the master crack surface. Δu and q vanish at the beginning and the end of C_-, which helps to recast integrals in Eqs. (5.45) and (5.46) using integration by parts as

$$\begin{aligned} \int_{C_-+C_+} \epsilon g^* \cdot e_l \frac{\partial u_l}{\partial x_1} m_2 q \mathrm{d}C &= \int_{C_-} \epsilon g^* \cdot e_l \, \Delta u_l \frac{\partial q}{\partial x_1} \mathrm{d}C \\ \int_{C_-+C_+} \epsilon g^* \cdot e_l \frac{\partial u_l^{\text{aux}}}{\partial x_1} m_2 q \mathrm{d}C &= \int_{C_-} \epsilon g^* \cdot e_l \, \Delta u_l^{\text{aux}} \frac{\partial q}{\partial x_1} \mathrm{d}C \end{aligned} \tag{5.47}$$

Here, it is assumed that the contour C_- is a straight line opposite to the x_1 direction ($\mathrm{d}C_- = -\mathrm{d}x_1$), and the contact traction is constant, in value and direction, over the small contour C_-. Recasting the contour integral in Eq. (5.47) is advantageous for numerical purposes, as the local contact inaccuracies are no longer able to influence the J- and interaction integrals through the singular displacement gradients. Using these new formulations of the contour integrals, the domain integrals are rewritten as

$$J(s) = \int_A \left(\sigma_{kl} \frac{\partial u_l}{\partial x_1} - W \delta_{1k} \right) \frac{\partial q}{\partial x_k} \mathrm{d}A - \int_{C_-} \epsilon g^* \cdot e_l \, \Delta u_l \frac{\partial q}{\partial x_1} \mathrm{d}C \tag{5.48}$$

$$I(s) = \int_A \left(\sigma_{kl} \frac{\partial u_l^{\text{aux}}}{\partial x_1} + \sigma_{kl}^{\text{aux}} \frac{\partial u_l}{\partial x_1} - W_{\text{I}} \delta_{1k} \right) \frac{\partial q}{\partial x_k} \mathrm{d}A - \int_{C_-} \epsilon g^* \cdot e_l \, \Delta u_l^{\text{aux}} \frac{\partial q}{\partial x_1} \mathrm{d}C \tag{5.49}$$

The area and contour integrals in Eqs. (5.48) and (5.49) are evaluated using a set of virtual quadratic triangular and line elements. These elements are referred to as *virtual* since they are not used while performing the finite element solution of the boundary value problem. Consider a point s along the crack front with the local coordinate system $x_1x_2x_3$. Due to the domain symmetry, only one-quarter of the disk of radius R_d is discretized with virtual triangular elements, and the contour C_- is discretized by line elements. The integration over the other three quarters is readily evaluated by the reflection of integrating points of the generated virtual elements as shown in Fig. (5.4). Using the virtual elements, evaluation of the domain integrals in Eqs. (5.48) and (5.49) follows the same standard

Gauss-quadrature integration scheme available in any FE code:

$$\begin{aligned} J(s) = &\sum_{A}^{\text{elems}} \sum_{p}^{\text{gpts}} \left\{ \left[\left(\sigma_{kl} \frac{\partial u_l}{\partial x_1} - W \delta_{1k} \right) \frac{\partial q}{\partial x_k} \right] |\mathbf{J}| \right\}_p w_p \\ &- \sum_{C_-}^{\text{elems}} \sum_{p}^{\text{gpts}} \left[\left(\epsilon g^* \cdot e_l \, \Delta u_l \frac{\partial q}{\partial x_1} \right) |\mathbf{J}| \right]_p w_p \end{aligned} \tag{5.50}$$

$$\begin{aligned} I(s) = &\sum_{A}^{\text{elems}} \sum_{p}^{\text{gpts}} \left\{ \left[\left(\sigma_{kl} \frac{\partial u_l^{\text{aux}}}{\partial x_1} + \sigma_{kl}^{\text{aux}} \frac{\partial u_l}{\partial x_1} - W_{\text{I}} \delta_{1k} \right) \frac{\partial q}{\partial x_k} \right] |\mathbf{J}| \right\}_p w_p \\ &- \sum_{C_-}^{\text{elems}} \sum_{p}^{\text{gpts}} \left[\left(\epsilon g^* \cdot e_l \, \Delta u_l^{\text{aux}} \frac{\partial q}{\partial x_1} \right) |\mathbf{J}| \right]_p w_p \end{aligned} \tag{5.51}$$

5.6 Numerical examples

In order to demonstrate the efficiency and accuracy of the proposed contact algorithm and the SIF computation procedure, the deformation behavior of the following fractured body configurations are analyzed under uniaxial uniform compression: (i) Single penny-shaped and elliptical cracks embedded in large cubes; (ii) Two interacting/intersecting penny-shaped cracks embedded in a cube; and (iii) Multiple randomly oriented, randomly placed, penny-shaped cracks in a cube. All these cracked bodies are subjected to a uniaxial compression. All procedures employed in this work are implemented into the Imperial College Geomechanics Toolkit, a geomechanics module [Paluszny and Matthäi, 2009; Paluszny and Zimmerman, 2011] of the Complex System Modeling Platform (CSMP++), an object-oriented finite element based API developed for the simulation of complex geological processes [Matthäi et al., 2001]. The system of equations resulting from the finite element accumulation is solved using the Fraunhofer SAMG Solver [Stüben, 2001].

For the cases for which analytical values are available, the numerical error in the computation of the contact tractions, e_{c}, and the SIFs, e_{t}, are respectively evaluated by

$$e_{\text{c}} = \frac{\displaystyle\int_{\Gamma^m} ||t_A^m - t_N^m|| \text{d}\Gamma}{\displaystyle\int_{\Gamma^m} ||t_A^m|| \text{d}\Gamma} \quad , \quad e_{\text{t}} = \frac{\displaystyle\sum_{\text{i=I}}^{\text{III}} \int_{L_f} |K_{\text{i}}^A - K_{\text{i}}^N| \text{d}l}{\displaystyle\sum_{\text{i=I}}^{\text{III}} \int_{L_f} |K_{\text{i}}^A| \text{d}l} \tag{5.52}$$

Here, t_A^m and t_N^m are respectively the analytical and numerical contact tractions on master surfaces, K_{i}^A and K_{i}^N are the pointwise analytical and numerical mode i SIFs respectively, and integrations are performed over the master surface Γ^m and the crack front L_f. Single and double vertical bars indicate the absolute value of a scalar and the length of a vector, respectively. Wherever closed form integration was not available, a trapezoidal rule has been employed to evaluate the integrals numerically. The analytical solutions for the SIFs

of embedded initially-open inclined penny-shaped and elliptical cracks in infinite solids under uniaxial compression are obtained in Appendix.

5.6.1 Experimental setup

Consider a cube of length $2w$ containing single or multiple cracks as shown in Figs. (5.5a) and (5.12a,c). The cube is subjected to a uniform uniaxial compression in the X_2 direction over the top and bottom surfaces. The cracks lie in the plane $X_2 = X_1 \cot\beta$ which generates the angle of β with the direction of applied load. A horizontal single crack configuration ($\beta = 90°$) produces pure mode I crack deformation in the case of initially open cracks, while the inclined one ($0° < \beta < 90°$) provokes a mixed-mode condition. In these configurations, a denotes the crack radius for the penny-shaped crack, and semi-major axis for the elliptical crack. The semi-minor axis b of the elliptical crack is perpendicular to the X_1X_2 plane. Young's modulus and Poisson's ratio values of $E = 10\,\text{GPa}$ and $\nu = 0.3$ are used in all models. The penalty parameter ϵ_0 over each fracture is determined individually as the Young's modulus divided by the average size of elements at the crack front region, $\epsilon_0 = E/L_n$. The average length of the elements L_n is defined as the crack front length L_f divided by the number of crack front segments N_f ($L_n = L_f/N_f$). This choice of penalty parameter generates a well-conditioned system of equations, where the values of the members corresponding to the fracture nodes in the global stiffness matrix are comparable to the value of the members corresponding to nearby nodes.

Mesh

An octree-based mesh generation software was employed to generate arbitrary meshes for all geometries, using ten-noded isoparametric tetrahedral and six-noded triangular elements. This mesh generator is able to split the walls of fractures and generate matched surface elements over the two surfaces of the cracks. For the elements attached to the crack front, the nodes near the front are moved from the mid-side point to the quarter-point position to produce inverse square root singular fields near the front. The curved crack fronts impose one curved edge for the tetrahedral elements sharing an edge with the crack front. When using quarter-point elements, the Jacobian determinant over small volumes near the curved edges becomes negative, as explained in Chapter 2. To avoid this, the curved edges are straightened by moving the mid-side nodes to the center. The refinement of the mesh near the crack front is controlled by assigning the number of segments along the crack front. Assume that the crack front of length L_f is discretized by N_f segments. A parameter called the nominal length (size) of the elements in the crack front region can be defined as $L_n = L_f/N_f$. The nominal element length L_n represents the approximate length of

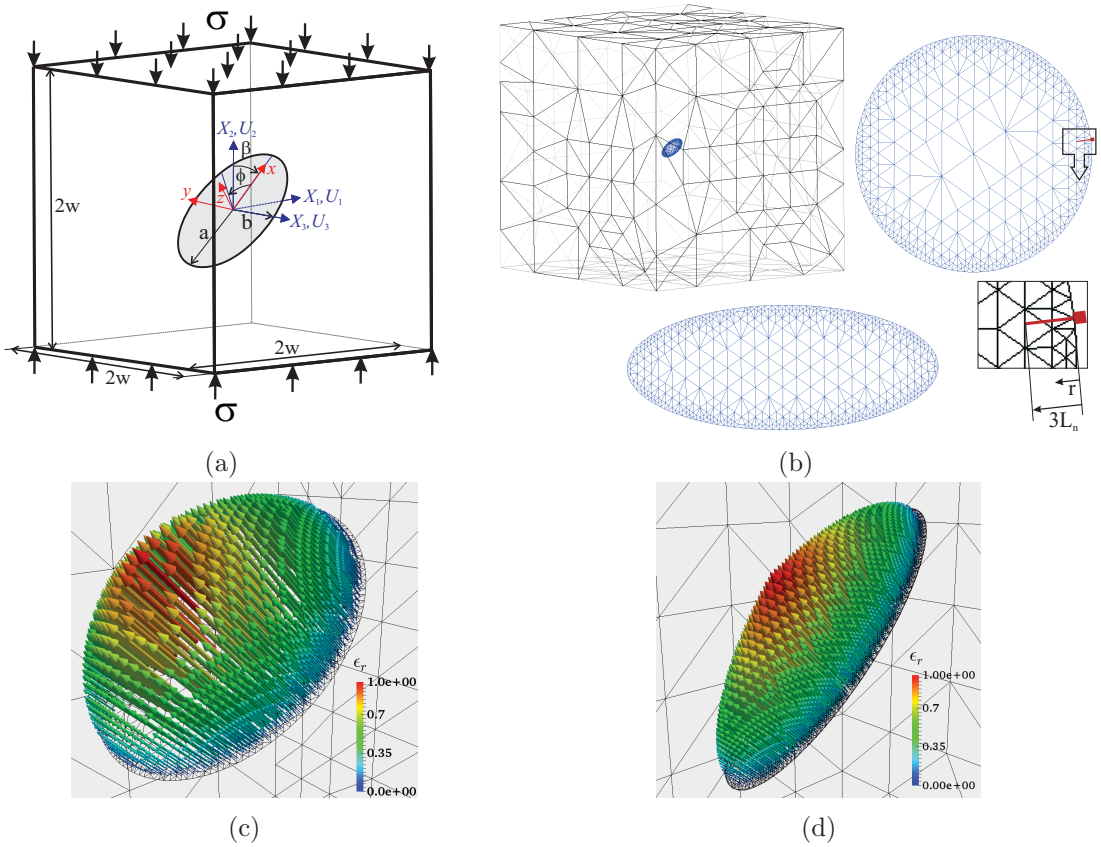

Figure 5.5: (a) Schematic of single penny-shaped/elliptical crack embedded in a large cube under uniaxial compression; (b) Finite element mesh discretizing an embedded penny-shaped crack in a cube, and the details of the matched meshes over the crack surfaces of penny-shaped ($a/w = 0.1$) and elliptical ($a/w = 0.1, b/a = 0.4$) cracks. For the two cases $L_n \approx a/20$; (c,d) The distribution of ϵ_r over the penny-shaped and elliptical cracks, which reproduces a singular square root penalty parameter near the crack front ($\epsilon = \epsilon_0/\epsilon_r$).

the element sides near the crack front, and therefore gives an approximate for the average size of the quarter-point tetrahedral elements in the crack front region. The degree of mesh refinement in the crack front region is controlled by keeping the nominal crack front element size about one twentieth of the crack length ($L_n \approx a/20$). Since estimations suggest that the size of the singular dominant zone depends mainly on the crack length, ranging between $a/10$ and $a/50$ [Kuna, 2013], keeping $L_n \approx a/20$ ensures that the quarter-point elements at the crack front predominantly remain in the singular dominant zone, where the fields have the inverse square root singularity. Five-, seven-, and two-point Gaussian quadrature rules are employed for the numerical integration over tetrahedral, triangular, and line elements, respectively.

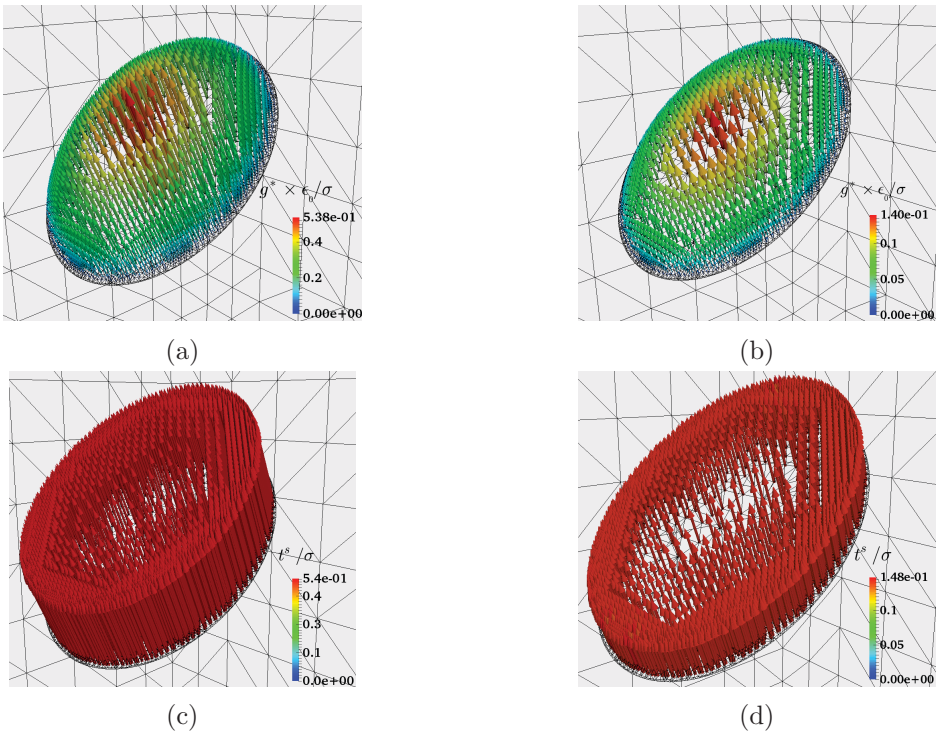

Figure 5.6: The distribution of normalized augmented gap (a,b) and contact traction (c,d) over the slave surfaces of a slipping penny-shaped crack with the geometrical configuration of $a/w = 0.1$ and $\beta = 45°$; Contact details: $\epsilon_0 = E/L_n$ with three augmentations; (a,c) Initially closed crack with $p_0/\sigma = 0$, $\tau_c/\sigma = 0.1$, $\mu = 0.2$; (b,d) Initially open crack with $p_0/\sigma = 3/8$, $\tau_c/\sigma = 0$, $\mu = 0.5$. The average contact traction errors are $e_c = 0.00013$, and $e_c = 0.00079$ for initially closed (c) and initially open (d) cracks, respectively.

Details of the SIF computation

For all crack configurations, the mesh-dependent domain radius of $R_d = L_n$ has been used to generate the virtual domains and compute the fracture parameters. Domains are built at the locations of both corner and mid-side nodes of the segments along the crack front. A similar virtual mesh structure as the one proposed in Chapter 4, with four elements in the radial direction ($k = 4$), was used to compute the SIFs. This choice yields 112 quadratic triangular elements, containing 112×3 integration points, together with 8 quadratic line elements, containing 8×2 integration points. The reasons for these choices are explained in Chapter 4. In order to compute the fracture parameters, a smooth function q must be defined over the integration domain. All numerical results here are determined by using $q = 1 - r/R_d$, where $r = (x_1^2 + x_2^2)^{1/2}$ is the distance from the disk center, and R_d is the domain radius. The derivatives of this function ($\partial q/\partial x_1 = -x_1/rR_d$ and $\partial q/\partial x_2 = -x_2/rR_d$) are directly evaluated at the integration points of the virtual triangular elements. For the SIF computation from the DC method, the diplacements are correlated at points located at the fixed distance of $r_m = L_n$ from the crack front (see Section 3.5.3).

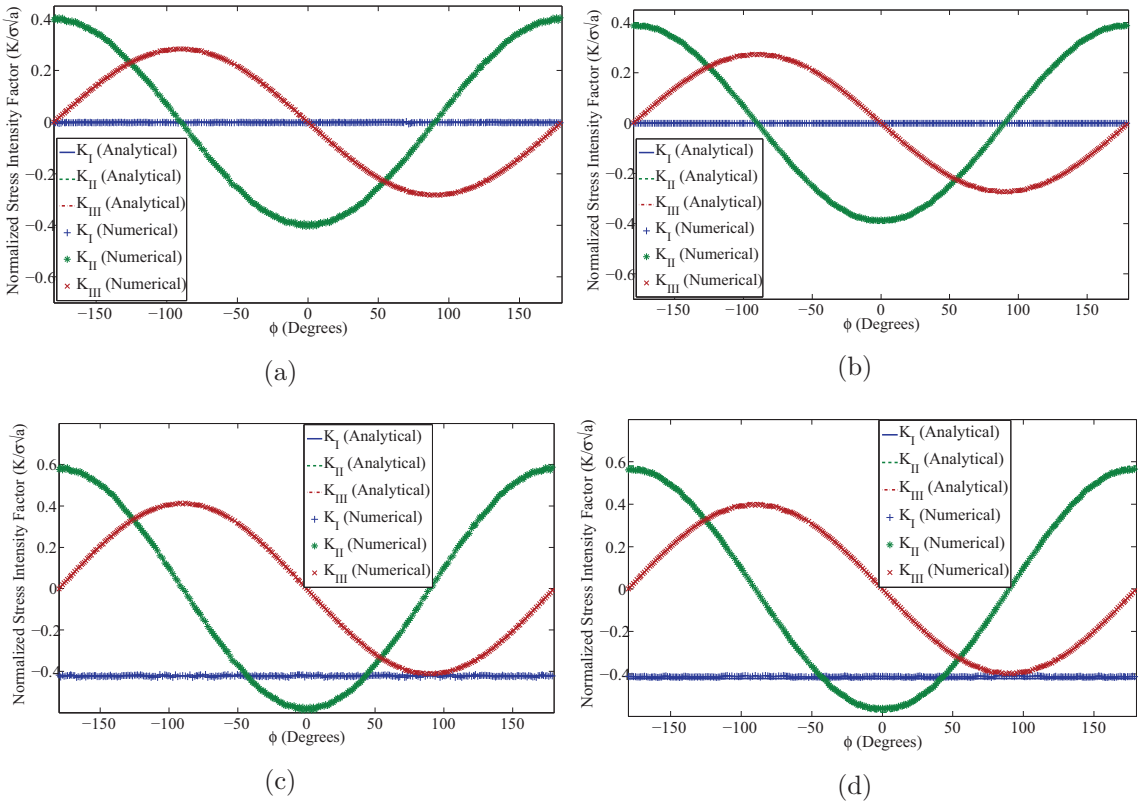

Figure 5.7: The variation of normalized mixed mode analytical and numerical SIFs along the front of a slipping penny-shaped crack using domain integral, (a) and (c), and displacement correlation, (b) and (d), methods; (a,b) Initially closed crack, (c,d) Initially open crack; Details of geometry, mesh and contact are given in Figs. (5.5) and (5.6). The analytical solutions for the SIFs are given in Appendix. The average SIF computation error is as follows: (a) $e_{\mathrm{t}} = 0.01$, (b) $e_{\mathrm{t}} = 0.022$, (c) $e_{\mathrm{t}} = 0.015$, (d) $e_{\mathrm{t}} = 0.024$.

5.6.2 Single penny-shaped and elliptical crack

Consider a single penny-shaped/elliptical crack in a large cube subjected to uniform compression as shown in Fig. (5.5a). A crack length to body width ratio of $a/w = 0.1$ was used in order to eliminate any influence of the cube boundaries on the crack fields. Figure (5.5b) shows the finite element mesh of the penny-shaped crack, together with two close-up pictures of the mesh structure over the penny-shaped and elliptical ($b/a = 0.4$) cracks. The following boundary conditions are applied for this configuration: $u_1 = 0$ over the edge $X_1 = X_2 = -w$, $u_2 = 0$ over the plane $X_2 = -w$, $u_3 = 0$ over the edge $X_2 = X_3 = -w$, and $\sigma = 1$ over the plane $X_2 = w$. Figures (5.5c) and (5.5d) also show the distribution of ϵ_r over the surfaces of the penny-shaped and elliptical cracks. This variation generates a square root singular penalty variation near the crack front ($\epsilon = \epsilon_0/\epsilon_r$), which makes it possible to compute accurate contact tractions very close to the crack front.

Figure 5.6 shows the distribution of normalized augmented gap and contact traction over

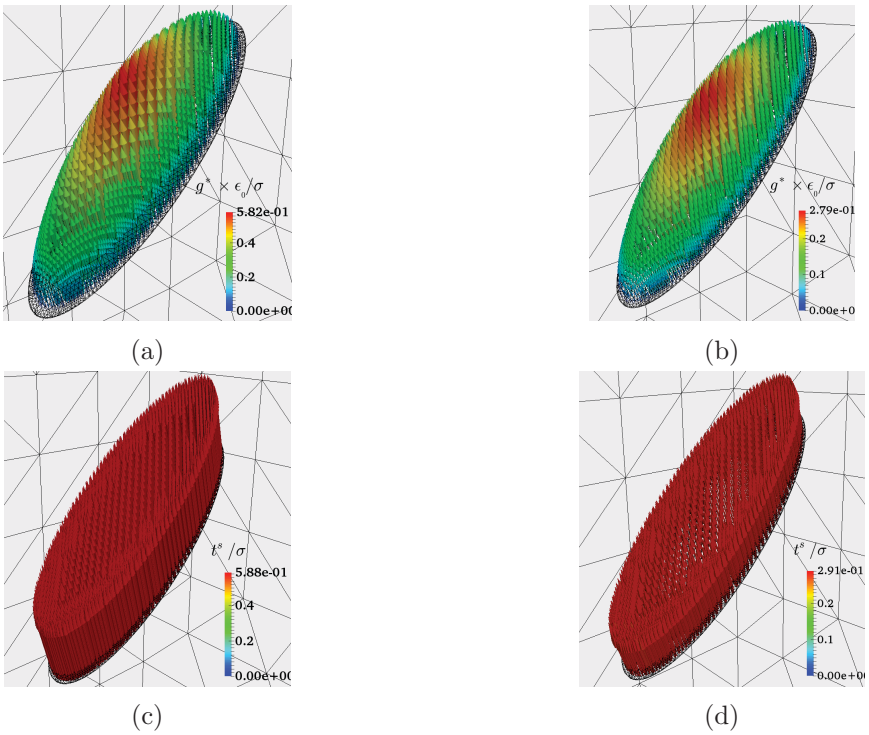

Figure 5.8: The distribution of normalized augmented gap (a,b) and contact traction (c,d) over the slave surfaces of a slipping elliptical crack with the geometrical configuration of $a/w = 0.1, b/a = 0.4$ and $\beta = 45°$; Contact details: $\epsilon_0 = E/L_n$ with three augmentations; (a,c) Initially closed crack with $p_0/\sigma = 0$, $\tau_c/\sigma = 0.2$, $\mu = 0.2$; (b,d) Initially open crack with Initially open crack with $p_0/\sigma = 0.25$, $\tau_c/\sigma = 0$, $\mu = 0.5$. The average contact traction errors are $e_c = 0.00015$, and $e_c = 0.00053$ for initially closed (c) and initially open (d) cracks, respectively.

the slave surfaces of a slipping penny-shaped crack. As is seen, the augmented gap maintains zero magnitude along the crack front, increasing towards the center of the crack where it attains its maximum. The application of an inverse singular penalty parameter variation near the crack front allows computing very accurate contact tractions for the elements attached to the crack front. Application of a constant penalty parameter over the crack surface, however, would not compute accurate contact tractions near the crack front, where the contact traction tends to zero when the crack front is approached. The more accurate the displacements over the fracture surface near crack front, the more accurate the contact tractions. Therefore, for more accurate contact tractions, a more accurate FE displacement solution near the crack front is required. Although the accuracy of displacements increases by using quarter-point tetrahedra at the crack front region, some inaccuracies may still remain due to the low quality of the element resulting from the random size, shape and orientation of the elements in the crack front region (see Section 3.5). A more structured mesh, in which significant variation of the size of quarter-point tetrahedral elements along the crack front is avoided, is therefore expected to produce more accurate contact tractions.

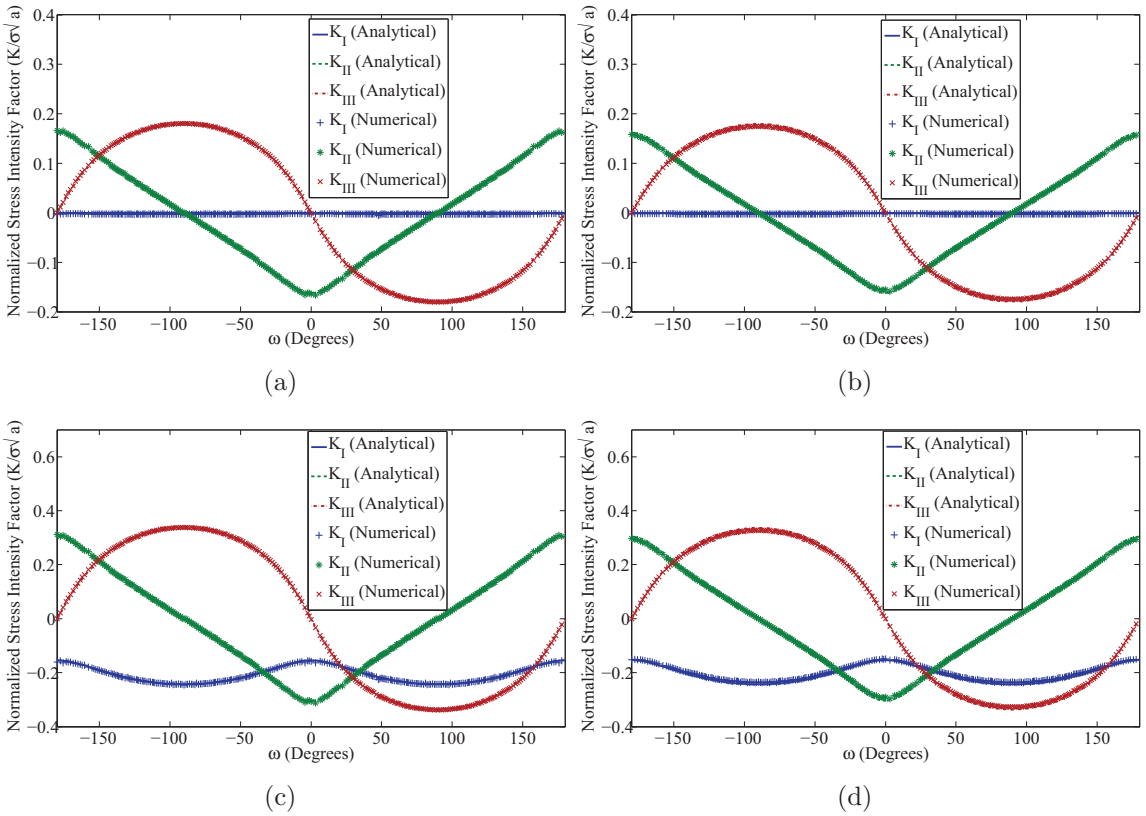

Figure 5.9: The variation of normalized mixed mode analytical and numerical SIFs along the front of a slipping elliptical crack using domain integral, (a) and (c), and displcement correlation, (b) and (d), methods; (a,b) Initially closed crack, (c,d) Initially open crack; Details of geometry, mesh and contact are given in Figs. (5.5) and (5.8). The average SIF computation error is as follows: (a) $e_{\mathrm{t}} = 0.011$, (b) $e_{\mathrm{t}} = 0.027$, (c) $e_{\mathrm{t}} = 0.013$, (d) $e_{\mathrm{t}} = 0.028$.

Figure 5.7 also shows the variation of the numerical pointwise mixed-mode SIFs along the crack fronts of the penny-shaped crack under two different contact conditions. Analytical solutions for 3D penny-shaped and elliptical cracks embedded in infinite solids (Appendix) are also plotted. Here, ϕ and ω are the polar angle of the circle, and the parametric angle of the ellipse, respectively. These results demonstrate the efficiency of the disk-shaped domain integral and displacement correlation to accurately compute the SIFs from arbitrary meshes even when crack surfaces are in contact.

Figure (5.8) shows the distribution of normalized augmented gap and contact traction over the slave surfaces of a slipping elliptical crack. As is seen, the application of an inverse singular penalty parameter variation near the crack front has resulted in very accurate contact tractions. Figure 5.9 also shows the variation of the numerical pointwise mixed-mode SIFs along the crack fronts of the elliptical crack subjected to two different contact conditions. One important feature in Figs. 5.7 and 5.9 is the mode I crack deformation for the initially open cracks. This significant negative K_{I}, which is due to the crack deformation

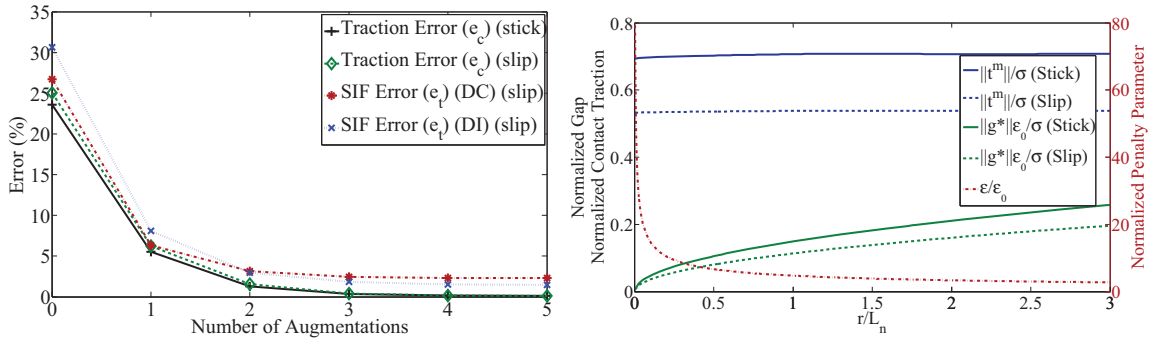

(a) (b)

Figure 5.10: (a) The variation of the computation error of contact traction and SIFs during the augmentation process in a single penny-shaped crack embedded in a large cube under uniaxial compression; (b) The variation of the master contact tractions, t^m, augmented gaps, g^* and penalty parameter along in a radial ray emanating from the crack front of the penny-shaped crack shown in Fig (5.5b). Geometrical details: $a/w = 0.1$, $\beta = 45°$; Mesh details: $L_n \approx a/20$; Contact details: $\epsilon_0 = E/a$, Stick condition: $p_0/\sigma = 0$, $\tau_c/\sigma = 0$, $\mu = 1.2$, Slip condition: $p_0/\sigma = 0$, $\tau_c/\sigma = 0$, $\mu = 0.2$. Results in (b) are obtained after three augmentations.

before the crack closure, can significantly influence the growth behavior of cracks under compression. It is noteworthy that open cracks accounts for a large percentage of the cracks in the subsurface, even at great depths.

Figure (5.10a) shows the convergence of the contact tractions through the augmentation process. A very low penalty parameter ($\epsilon_0 = E/a$) has been considered, where the role of the augmentation procedure in enforcing the contact constraints is significant. The errors in the contact traction and the SIFs drop considerably in the first two augmentations, indicating that very efficient enforcement of the contact constraints is achieved by only two augmentations. More than four augmentations enforce the contact constrains almost exactly by strictly penalizing any penetration on the contact surfaces. It is evident that a larger value of the penalty parameter yields a faster convergence of the contact tractions to the exact values. In order to make the augmentation procedure most efficient, the penalty parameter has to be chosen as large as possible without making the system of equations ill-conditioned. The contact precision for heavily fractured media can attain very high values, and therefore a lower bound of the penalty parameter, for which no ill-conditioned behavior occurs in the system, has to be defined irrespective of the contact precision. A penalty parameter based on the ratio of Young's modulus to the average crack surface element size introduces penalty terms into the system which are comparable to the values of the members in stiffness matrix corresponding to the nodes near the contact surfaces. As defined previously, L_n indicates the average size of the elements at the crack front region. A penalty parameter defined as the ratio of Young's modulus to this average size

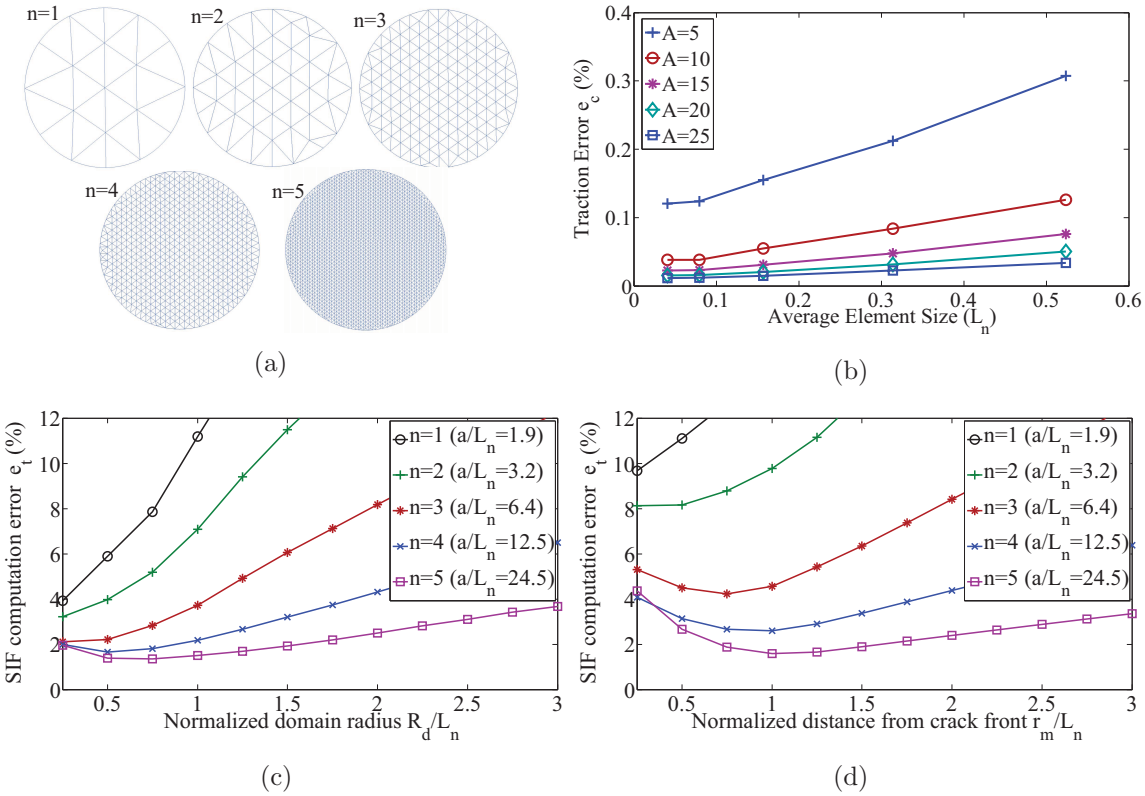

Figure 5.11: (a) Finite element mesh discretizing an embedded penny-shaped crack in a cube with different degrees of mesh refinement n ($a/w = 0.1$, $\beta = 45°$); (b) The variation of contact traction error e_c defined in Eq. (5.52) against the average size of elements (L_n) for different number of augmentations (A) in stick condition at an initially closed crack ($p_0/\sigma = 0$); (c) The variation of SIF computation error e_t defined in Eq. (5.52) computed from the domain integral method against the normalized domain radius R_d/L_n for different degrees of mesh refinement; (d) The variation of e_t computed from the displacement correlation method against the normalized distance of correlation point from crack front r_m/L_n in different degrees of mesh refinement. The results in (b)-(d) are obtained using $\epsilon_0 = E/a$ and five augmentations. Details of contact parameters in (c) and (d) are $\tau_c/\sigma = 0$, $\mu = 0.5$ and $p_0/\sigma = 0$.

($\epsilon_0 = E/L_n$) can therefore be recommended as the lower bound for the value of the penalty parameter for individual cracks. For a reasonably fine mesh, suitable for the crack problems, this proposed value for the penalty parameter yields less contact traction errors and faster convergence than the one shown in Fig. (5.10a). Therefore, a penalty parameter $\epsilon_0 = E/L_n$ defined individually for each fracture, together with 2-3 augmentations, enforces the contact constraints accurately and efficiently.

Consider a ray emanating from an arbitrary point on the crack front, lying on the surface of the penny-shaped crack and extending in a direction normal to the crack front, as shown in Fig. (5.5b). Figure (5.10b) presents the variation of the magnitude of the augmented gap, penalty parameter, and the magnitude of the contact traction after three augmentations along this ray against the normalized distance from the crack front. This plot clearly shows

how a singular square root variation of the penalty parameter forces the contact traction to have finite values very close to the crack front. As is seen in the plot, the magnitude of the gap vector tends to zero when the crack front is approached ($\lim_{r\to 0}||g^*|| = 0$), and a square root singular penalty parameter $\epsilon = \epsilon_0/\epsilon_r = \epsilon_0/\sqrt{r/a}$ makes it possible to obtain a non-zero limit for the magnitude of contact traction ($\lim_{r\to 0}||t^m|| = \lim_{r\to 0}\epsilon||g^*|| \neq 0$). Such a variation of contact traction cannot be reproduced when a constant penalty parameter is considered. In fact, the contact traction approaches zero in the case of constant penalty, as a result of the influence of zero magnitude gap along the crack front.

A mesh sensitivity analysis was conducted to demonstrate the efficiency of the proposed contact and stress intensity factor computation algorithms. Figure (5.11a) shows five crack surface meshes with different degrees of refinement, ranging from a coarse mesh ($n = 1$) to a fine one ($n = 5$). Figure (5.11b) presents the variation of the contact traction error e_{c} against the average element size for stick condition. A similar convergence behavior is seen for slip condition as well. These results confirm that the contact tractions are accurate irrespective of the degree of mesh refinement over the crack surface. Figures (5.11c) and (5.11d) also show the variation of SIF computation error e_{t} against the normalized domain size R_d/L_n and normalized distance of correlation point from the crack front r_m/L_n in DI and DC methods, respectively. The main features of these plots are as follows: (1) For coarse meshes, domain integral computes more accurate SIFs than displacement correlation, provided that the domain integral is small enough with respect to the mesh size. (2) For fine meshes, both methods compute very accurate SIFs, with an error in the range of $e_{\mathrm{t}} \approx 1-2\%$. (3) The dependencies of the SIF error on the correlation point distance in DC method and domain size in DI method are similar. This suggests that the mesh-dependent values of $r_m = R_d \approx L_n/4$ and $r_m = R_d \approx L_n$ compute the most accurate SIFs in very coarse and very fine meshes, respectively. The general recommendation for the mesh size near the crack front is that the quarter-point element must be entirely inside the singular-dominant zone. The size of the singular-dominant zone mainly depends on the characteristic crack length, ranging between $a/10$ and $a/50$ [Kuna, 2013]. Therefore, a suitable mesh size for a penny-shaped crack requires $L_n < a/10$ for which $r_m = R_d = L_n$ is recommended for computing accurate SIFs from DC and DI methods. Similar values have been suggested for r_m and R_d in the case of cracks under tensile loadings (see Chapetrs 3 and 4). It is noteworthy that for the purpose of accurate SIF computation, a local refinement at the crack front region suffices. Therefore, coarse meshes should be used for the regions far from the crack front to avoid unnecessary computational cost (see mesh structures in Fig. (5.5b)).

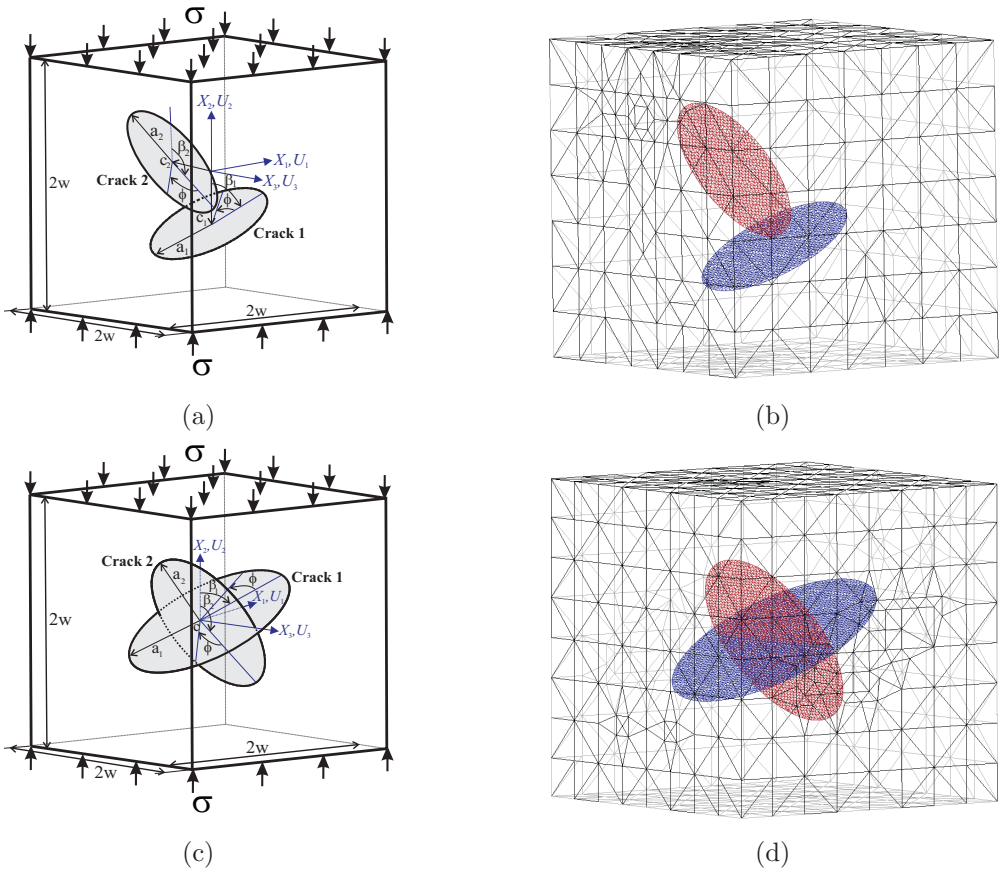

Figure 5.12: (a) Schematic of two interacting penny-shaped cracks embedded in a cube subjected to uniaxial compression; (b) Finite element mesh discretizing it; Geometrical details: $a_1/w = a_2/w = 0.5$, $\beta_1 = 60°, \beta_2 = 150°$, $c_1 = (0, 0, -3), c_2 = (-3, 0, 2)$; Mesh details: $L_n \approx a/20$; (c) Schematic of two intersecting penny-shaped cracks embedded in a cube subjected to uniaxial compression; (d) Finite element mesh discretizing it; Geometrical details: $a_1/w = 0.7, a_2/w = 0.6$, $\beta_1 = 60°, \beta_2 = 150°$, $c = (0, 0, 0)$; Mesh details: $L_n \approx a/20$.

5.6.3 Two penny-shaped cracks

Consider two cubes, one with a pair of interacting penny-shaped cracks (Fig. (5.12a)), another one with a pair of intersecting penny-shaped cracks (Fig. (5.12c)). Each cube is subjected to uniform compression in the X_2 direction over the top and bottom surfaces. The geometrical details of the cracks in both configurations are given in Fig. (5.12). Both cracks lie in the plane $X_2 = X_1 \cot \beta$ which generates the angle β with the direction of applied load. Figures (5.12b) and (5.12d) show the finite element mesh of these crack configurations. The same boundary conditions as in the single crack problem are applied.

Figure (5.13) shows the distribution of contact traction over the master surfaces of these penny-shaped cracks in the slip condition. The details of the contact parameters are given in Fig. (5.13). The main features are as follows: (i) Figure (5.13a) depicts how the singular field of one crack can influence the contact tractions enforced on the surfaces

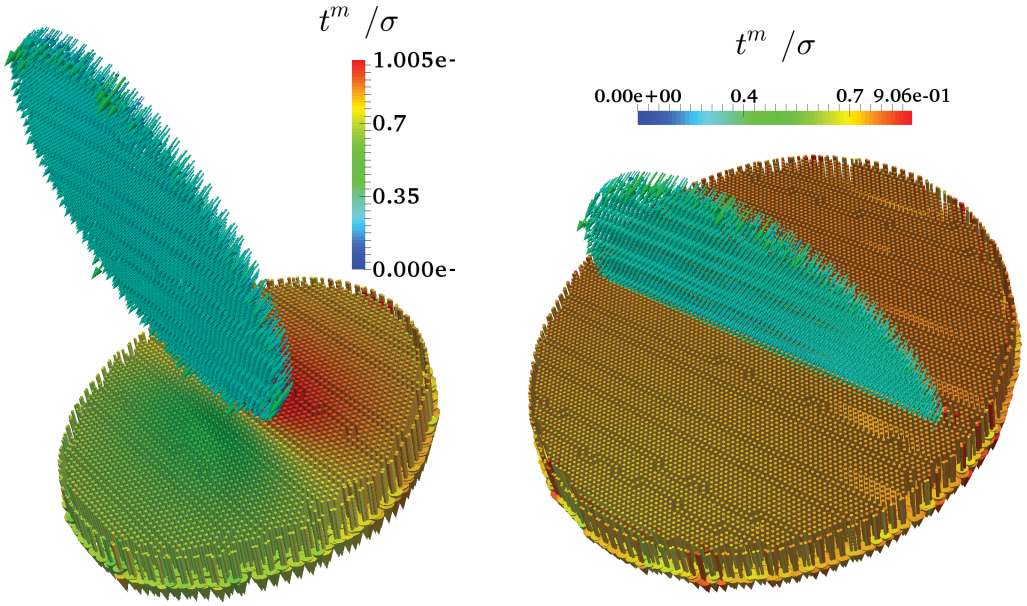

(a) (b)

Figure 5.13: (a) The distribution of contact tractions over the master surfaces of two interacting cracks described in Fig. (5.12a); Contact details: $\epsilon_0 = E/L_n$ with three augmentations, crack 1: $p_0/\sigma = 0$, $\tau_c/\sigma = 0$, $\mu = 0.2$., crack 2: $p_0/\sigma = 0$, $\tau_c/\sigma = 0$, $\mu = 0.4$; (b) The distribution of contact tractions over the master surface for two intersecting fractures described in Fig. (5.12c); Contact details for both fractures: $\epsilon_0 = E/L_n$ with three augmentations, $p_0/\sigma = 0$, $\tau_c/\sigma = 0$, $\mu = 0.2$.

of another crack when two close cracks are slipping next to each other. This interaction cannot be captured well unless the singular stress state along the crack front is modeled accurately. (ii) Figure (5.13b) demonstrates the efficiency of the proposed contact algorithm in enforcing the contact constraints, even for very complex configurations involving crack intersections. The main difficulty is dealing with the corner singularity at the points where crack 2 intersects the surfaces of crack 1. (iii) Some limited inaccuracies in contact traction are visible near the crack fronts in both configurations. As was mentioned previously, these inaccuracies result from the low quality of some elements due the random placement of quarter-point tetrahedra near the crack front. Nevertheless, these slight inaccuracies are limited to a few quarter-point nodes, and the contact tractions are obtained with a high level of accuracy elsewhere. Overall, these results demonstrate the applicability and efficiency of the proposed methodology in the contact treatment of very complex contact configurations.

Figure (5.14) shows the variation of the pointwise mixed-mode SIFs along the crack fronts of the penny-shaped cracks of the interacting and intersecting configurations shown in Fig. (5.12). The results are obtained from the displacement correlation and domain integral methods. Here, ϕ is the polar angle of the circle as shown in Fig. (5.12). A few characteristics of the SIF variation along the crack front must be noted: (i) The results from

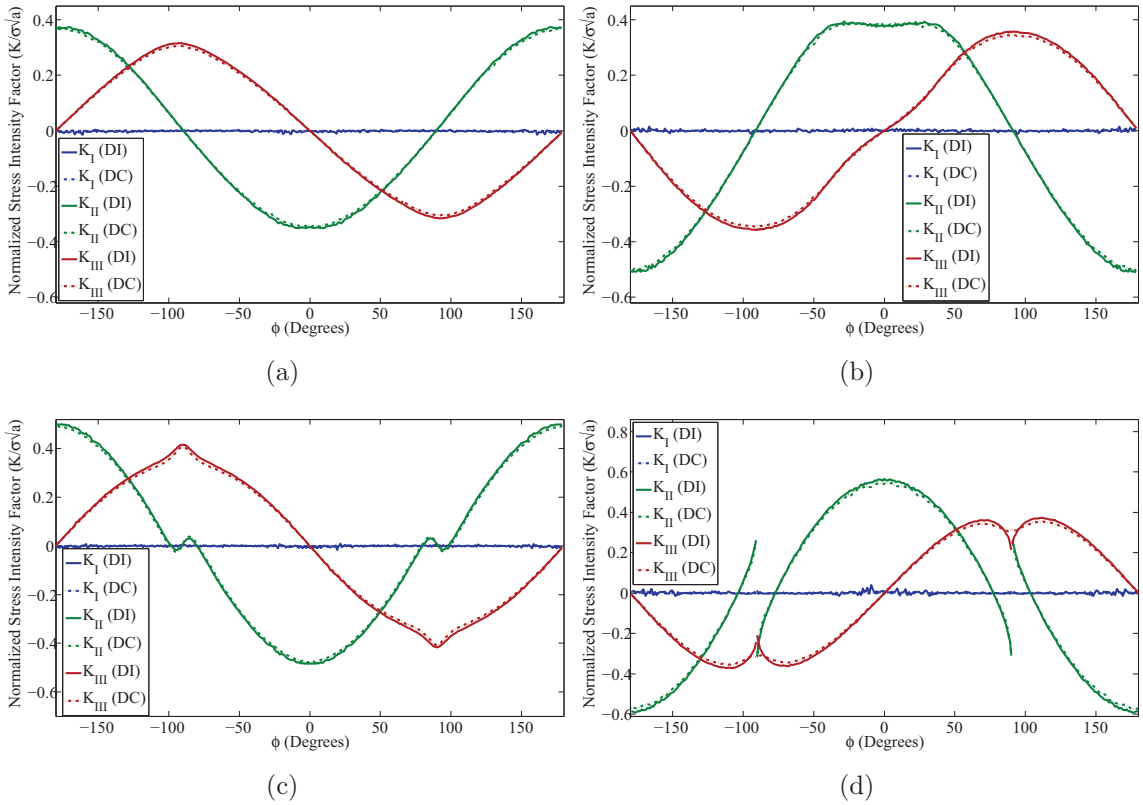

Figure 5.14: The variation of normalized mixed mode numerical SIFs along the front of interacting/intersecting penny-shaped cracks using domain integral (DI) and displacement correlation (DC) methods; (a) and (b) show the SIF variation along cracks 1 and 2 at two interacting cracks configuration, respectively (see Figs. (5.12) and (5.13) for geometrical and contact details); (c) and (d) plot the SIF variation along cracks 1 and 2 at two intersecting crack configurations (see Figs. (5.12) and (5.13) for geometrical and contact details).

displacement correlation and domain integral methods are in good agreement everywhere, except very close to the corner points, i.e. near $\phi = -90°$ and $\phi = 90°$ in Fig. (5.14d). The reason is the complex stress state near these points. In fact, the stress intensity factor loses its meaning at the exact corner points, since the order of singularity at this point is different from the order of singularity of the crack. The reader is referred to Section 4.7.4 for more details. (ii) The interaction of the singular fields of one crack with the singular field or enforced contact conditions in the other one, significantly influences the SIF variation along the crack front. For example, one can see these considerable interactions about $\phi = 0°$ in Fig. (5.14b), due to the interaction of singular field of crack 1 with boundary conditions over surfaces of crack 2, and near $\phi = -90°$ and $\phi = 90°$ (see Figs. (5.14c) and (5.14d)). (iii) Slight oscillations are visible in mode I SIF values obtained from the domain integral method. These are due to the existence of inaccuracies in the contact tractions near the crack front. However, by using the proposed new version of line integral in Eq. (5.47), the influence

of these inaccuracies on the computation of SIFs is significantly reduced. Overall, these results demonstrate the efficiency of both disk-shaped domain integral and displacement correlation methods to accurately compute the SIFs of complex crack configurations.

5.6.4 Multiple planar cracks

Figures (5.15) and (5.16) present the results of the contact simulation of two networks of fractures, where solid cubes are filled with randomly oriented, randomly placed, penny-shaped cracks. For both cases, the cube is subjected to a uniform compression in the X_2 direction over the top surface, and the same boundary conditions as in Section 5.6.2 are applied. This boundary condition requires that no crack intersects the bottom face of the cube, where a Dirichlet boundary condition is applied. Figure (5.15a) shows the finite element discretization of a network of twenty four cracks with a power-law size distribution, while Fig. (5.16a) presents the FE mesh of a network of seventy five cracks of the same size. Figures (5.15b) and (5.16b) illustrate the distribution of normalized stick contact tractions over the slave surfaces, where the average contact traction error for both cases remains less than $e_c = 0.0003$. This indicates the efficiency of the proposed contact algorithm for enforcing accurate contact constraints with small penalty parameters in high contact precision problems. In fact, assigning an individual penalty parameter based on the local mesh refinement of each fracture avoids the system to become ill-conditioned, yet performing augmentation enssures high accuracy enforcement of the contact tractions. Figures (5.15c) and (5.16c) also show the contact tractions over the slave surfaces when contact conditions $\tau_c = 0.1, \mu = 0.4$ and $\tau_c = 0, \mu = 0.6$ are applied for networks with power-law and uniform size distributions, respectively. For these cases, the distributions of normalized tangential gap (slip) over the crack surfaces are presented in Figs. (5.15d) and (5.16d). The ratio of external load to the Young's modulus (σ/E) is very small in the context of infinitesimal strain theory. Therefore, according to the normalized slip values in Figs. (5.15d) and (5.16d), the values of tangential slip remain very small compared to the size of the cracks. This indicates the applicability of isoparametric contact discretizations in geometrically linear applications such as the linear elastic simulation of fractured media.

5.7 Conclusions

A tetrahedral-based finite element formulation is presented for the treatment of contact between fracture surfaces in high density fractured media. In this framework, the application of a singular square root penalty parameter near the crack front ensures the enforcement of contact constraint accurately close to the crack front. The introduced gap-based augmented Lagrangian approach also circumvents the difficulty of not being able to define contact

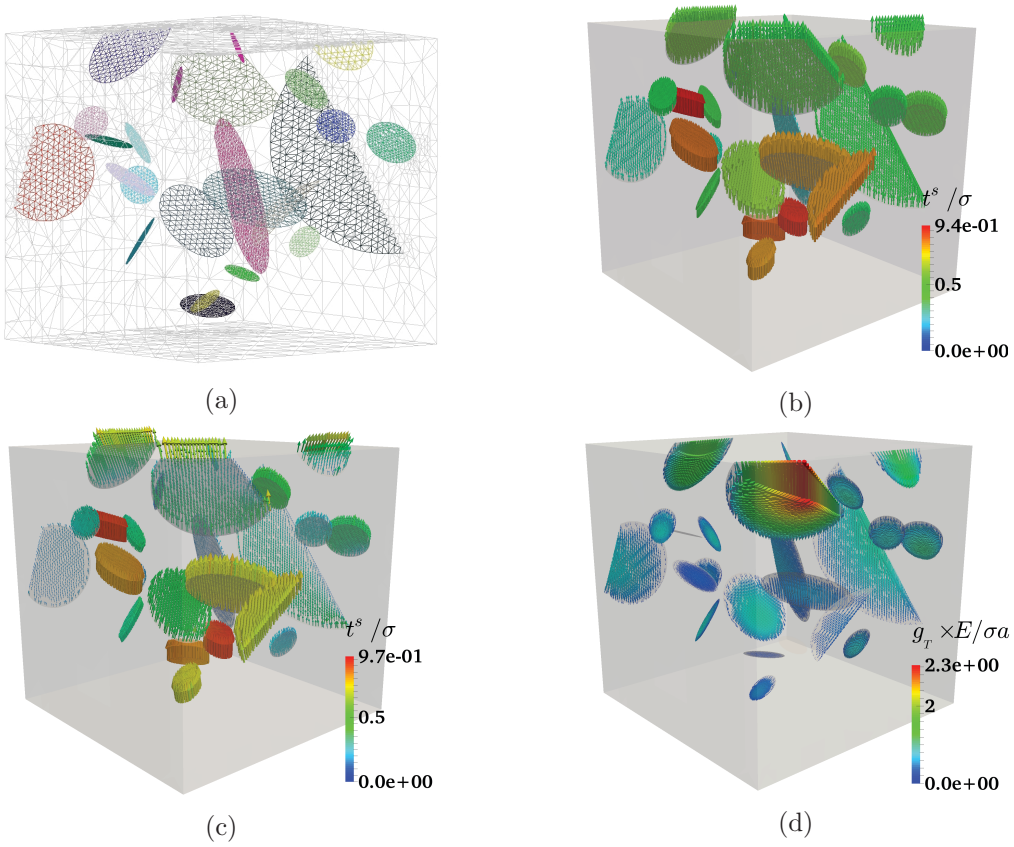

Figure 5.15: Finite element mesh discretizing a network of 24 randomly-oriented penny-shaped cracks inside a cube of length 2w. The size of cracks follows a power-law size distribution where the minimum and maximum of crack radius are $r_{min} = 0.1w$ and $r_{min} = w$, respectively. (b) The distribution of normalized contact traction over the slave surfaces when all cracks are in stick condition. The average contact traction error for this case is $e_c = 0.0003$. (c,d) The distribution of normalized contact traction and tangential gap (slip) over the slave surfaces when $p_0/\sigma = 0$, $\tau_c/\sigma = 0.1$, $\mu = 0.4$ govern the contact condition of the cracks; For all cases, a penalty parameter of $\epsilon_0 = E/L_n$ is assigned individually for each fracture, and three augmentations are performed.

tractions at the nodes located along the crack front. The proposed contact algorithm is able to enforce the contact constraint accurately over the crack surfaces of densely fractured media even with small penalty parameters. Results from numerical experiments on a cube containing single, and multiple cracks indicate the efficiency, accuracy and reliability of the FE framework introduced in this paper. Employing a suggested version of the line integral for computing the SIFs from domain integral method also prevents a possible significant influence of contact traction inaccuracies on the SIF computation. Accurately computed SIFs using the displacement correlation and disk-shaped domain integral methods indicate the efficiency and accuracy of these methods using unstructured meshes.

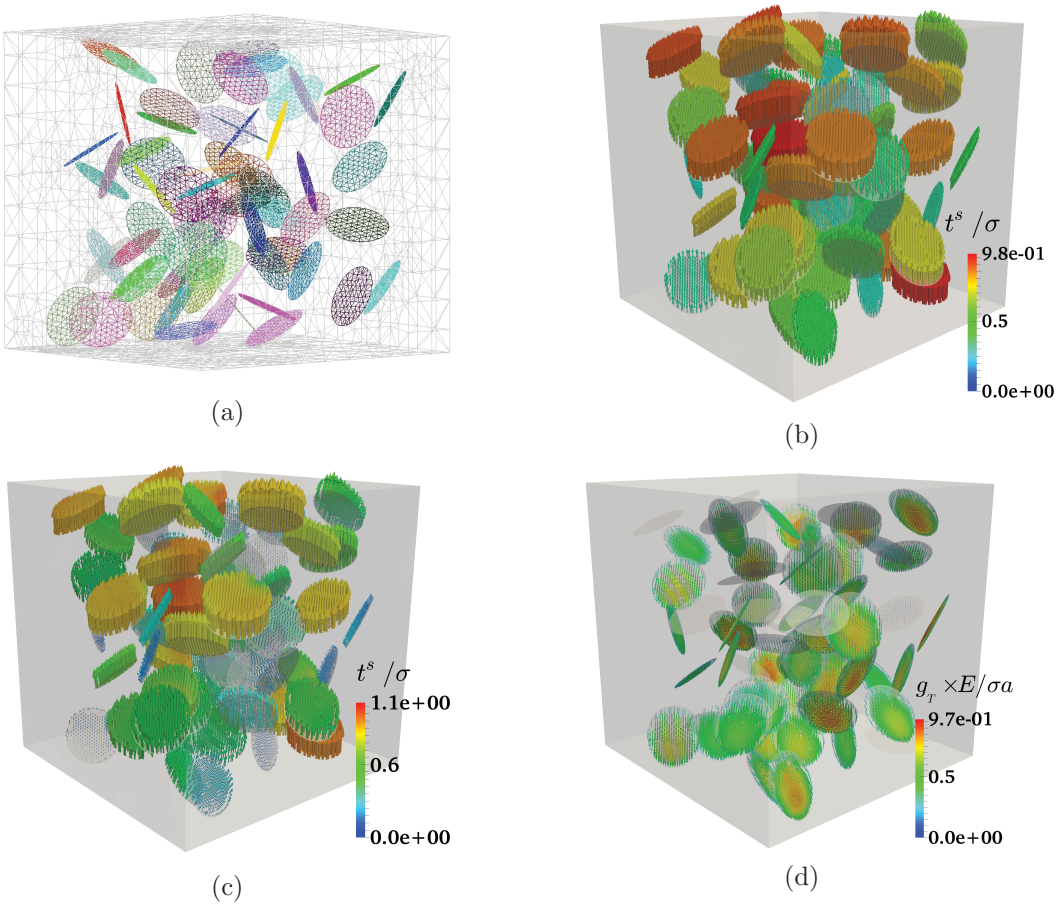

Figure 5.16: Finite element mesh discretizing a network of 70 randomly-oriented penny-shaped cracks inside a cube of length 2w. Cracks are of the same size of $r/w = 0.2$ where r is the crack radius. (b) The distribution of normalized contact traction over the slave surfaces when all cracks are in stick condition. The average contact traction error for this case is $e_c = 0.0003$. (c,d) The distribution of normalized contact traction and tangential gap (slip) over the slave surfaces when $p_0/\sigma = 0$, $\tau_c/\sigma = 0$, $\mu = 0.6$ govern the contact condition of the cracks. For all cases, a penalty parameter of $\epsilon_0 = E/L_n$ is assigned individually for each fracture, and three augmentations are performed.

Chapter 6

Applications in modeling rock hysteresis and brittle crack growth

Contents

6.1 Abstract

This chapter discusses two applications of the numerical methodology developed in this thesis in rock deformation problems. These include: (i) Understanding the hysteretic behavior in rock deformation with regards to the frictional contact in micro-cracks; and (ii) Simulating three-dimensional brittle crack growth under mixed-mode loading conditions. The numerical results indicate the applicability and efficiency of the proposed numerical methodology for a better understanding of elastic and inelastic processes in rock deformation.

6.2 Modeling rock hysteresis

Nonlinearity and hysteresis, which are two key features of elastic rock deformation, are often attributed to the presence of cracks and crack-like voids. The hysteretic behavior of rocks is related to the concept of unrecovered energy, where mainly two processes are involved: (i) the work of frictional forces and (ii) the strain energy trapped in the solid [Jaeger et al., 2007]. In this section, a literature review is presented to address the previous research in this area. Then, finite element analyses are performed to evaluate the sliding crack model in reproducing hysteretic behavior in rock deformation.

6.2.1 Introduction

Many geomaterials, such as volcanic and sedimentary rocks (granite, basalt, sandstones, limestones, and slates), and artificial materials such as concrete and mortar, have impurities, inclusions, and defects, which are inherent properties of their micro-structure. Generally, all solids that are not single crystals can be regarded as materials with an inherent random structure at a mesoscopic scale, i.e., a scale that significantly exceeds the atomic size, but is still small compared to macroscopic dimensions [Aleshin and Van Den Abeele, 2007b]. The presence of micro-cracks can be attributed not only to mechanical or thermal damage, but also to the process of formation, such as solidification and deposition, which results in shrinkage due to drying and chemical reactions. Internal defects can be roughly categorized into three classes: dislocations (regarded as one-dimensional or 1D), internal contacts (2D) and pores and voids (3D). The internal contacts and crack-like voids are the most essential ones contributing to non-linearity and hysteresis [Aleshin and Van Den Abeele, 2007b]. If a microcrack suddenly appears during these processes, its surfaces will be separated over distances significantly exceeding the atomic size [Aleshin and Van Den Abeele, 2005]. It is generally believed that the mechanical behavior of this class of materials, in both elastic deformation and inelastic processes such as yielding and failure, is controlled by these defects and imperfections. Hysteresis, in particular, is believed to be one of the main features of deformation in this class of solid materials.

In micro-structured materials, when cracks are all open and randomly distributed, the overall response is isotropic. When some cracks close and undergo frictional sliding, however, the overall response becomes anisotropic and dependent on the loading conditions, as well as on the loading history [Horii and Nemat-Nasser, 1983]. This anisotropy is highly load-dependent, and may even be affected by the sequence of load applications [Walsh, 1965; Kachanov, 1982a]. Hence, it is expected that the overall shear modulus depends on the hydrostatic pressure, and the overall bulk modulus is influenced by the applied overall shear

stresses. To simulate the elastic behavior of micro-structured materials, the characterization of the stress–strain constitutive equations is of great importance. Only a few investigations have established constitutive laws of micro-structured materials based on frictional contact of the internal cracks [Walsh, 1965; Kachanov, 1982a; Horii and Nemat-Nasser, 1983; Lawn and Marshall, 1998]. In these publications, the interaction between cracks is neglected. Most of them consider the loading stage only, and none has addressed the energy loss mechanisms and sources. The cracks were generally considered to be initially closed, as well. In addition, no numerical simulation has been carried out to verify the analytical results. There remains a need for precise numerical simulation of the stress–strain behavior of elastic bodies containing interacting frictional cracks. These numerical simulations can eventually help to build more precise constitutive models that can capture the nature of the micro-structured materials under a general loading conditions.

The classic work of Walsh [1965], was among the first to describe the role of frictional contact at the microscale in inducing nonlinear and hysteretic behavior. According to the proposed sliding crack model, hysteresis occurs due to the sliding of closed micro-cracks in the loading stage, which is followed by a delayed reverse-sliding in the unloading stage. The hysteretic behavior of materials introduces the concept of unrecovered energy via two main processes: (i) the work of frictional forces, and (ii) the strain energy trapped in the solid. The work of the frictional forces is lost as heat energy, while the trapped strain energy remains available in the solid, and may be recovered at a later loading stage. David et al. [2012] extended Walsh's formulation to consider initially open cracks, and analyzed the behavior of a body containing a system of micro-cracks during both loading and unloading, under uniaxial compression. They compared a two-dimensional analytical formulation against experimental data on sandstones and thermo-mechanically loaded granite specimens, and concluded that the elastic deformation of the rock subjected to uniaxial compression can be fully characterized by four microstructural parameters: the modulus of the uncracked rock, the crack density, an initial crack aspect ratio, and a friction coefficient.

The formulation developed by David et al. [2012] is able to reproduce residual strain as a part of the hysteretic behavior of rock, and therefore the analytical results fit the experimental stress–strain curves. However, this formulation needs to be re-examined as it lacks proper use of the reciprocal theorem. This was highlighted in [Nejati et al., 2013], where the results of the analytical formulation and numerical simulation on a solid cube containing 3D penny-shaped cracks under uniaxial compression clearly show that frictional contact between the faces of initially open cracks lead to only frictional energy loss, and no residual strain is reproduced after complete unloading. Therefore, one can conclude the results from a sliding crack model based on initially open cracks cannot possibly agree with

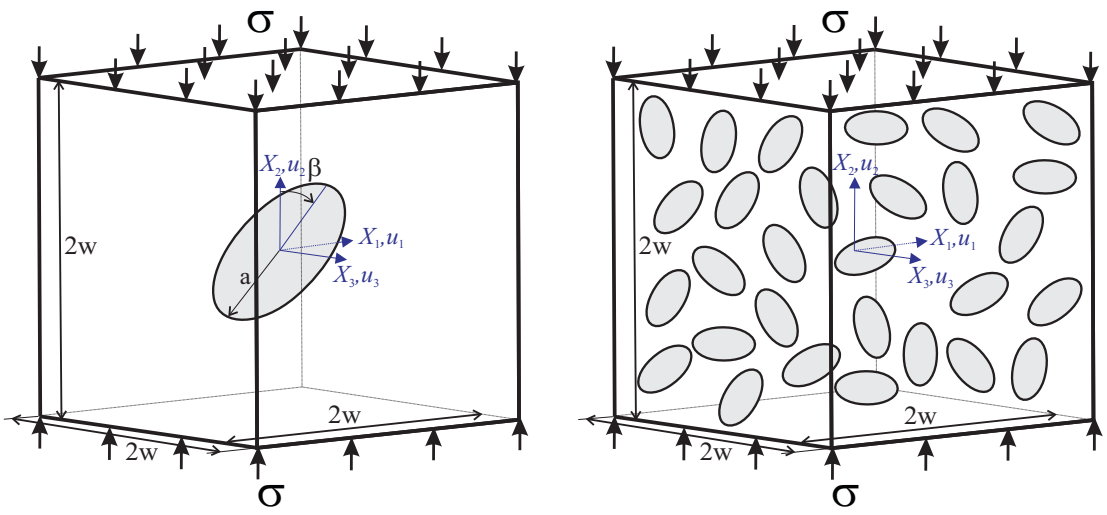

Figure 6.1: Schematics of (a) A cube containing a penny-shaped crack under uniaxial compression; (b) A cube containing a set of randomly-oriented penny-shaped cracks under uniaxial compression.

the experimental stress–strain curves for rock materials. In this section, we investigate the influence of a cohesion term in the frictional constitutive law on the hysteretic behavior of cracked bodies. The results from various finite element simulations show that in order to be able to fit the experimental results, a cohesion term in the frictional constitutive law is necessary to reproduce the residual strain.

6.2.2 Methodology

Assume a cube of edge length $2w$ which contains single or multiple cracks and is subjected to the uniaxial compression σ as shown in Fig. 6.1. Due to the applied load in X_2 direction, the crack surfaces might undergo frictional sliding, where the effective Young's modulus of the cube is influenced by the excess energy input into the body [Nejati et al., 2013]. During the unloading stage, reverse-sliding does not begin immediately due to the change of the direction of frictional force. Therefore, the overall stress–strain curve of these cracked bodies exhibits a hysteretic behavior. The response of the cube to the applied load is nonlinear due to the frictional sliding, and therefore the load must be applied incrementally in a numerical simulation. Consider the maximum compressive stress σ_m is applied over n increments, followed by the complete removal of the load in another set of n increments. The incremental load applied in each increment is $\Delta\sigma = \sigma_m/n$ and $\Delta\sigma = -\sigma_m/n$ in loading and unloading stages, respectively. Here, positive stress implies compression. In each increment, the load $\Delta\sigma$ results in the relative displacement of the top surface with respect to the bottom surface in the direction of applied load, Δu_2. The effective Young's

modulus of $E_e = \Delta\sigma/\Delta\varepsilon_{av}$ is then computed in each increment, where $\Delta\varepsilon_{av}$ is the average of overall strain in the direction of applied load:

$$\Delta\varepsilon_{av} = \frac{1}{8w^3}\int_A \Delta u_2 \mathrm{d}A \tag{6.1}$$

Here, A is the top/bottom surface of the cube. Assuming the bottom surface is fixed in the load direction, X_2, in the numerical model, the average strain is obtained using the numerical integration of displacement over the top surface as

$$\Delta\varepsilon_{av} \approx \frac{1}{8w^3}\sum_{A}^{\text{elems}}\sum_{p}^{\text{gpts}}\left\{\Delta u_2|\mathbf{J}|\right\}_p w_p \tag{6.2}$$

where summation over area A includes all the element, 'elems', over the top surface, the sum over p includes element integration points, 'gpts', where the bracketed quantities $\{\}_p$ are evaluated and multiplied by the corresponding weight w_p. $|\mathbf{J}|$ denotes the determinant of the coordinate Jacobian matrix of the elements, and the incremental displacement at integration points can be ready obtained using the shape functions ($\Delta u = \sum_i^{\text{nodes}} N_i \Delta u_{2i}$). After the computation of Δu in each increment, the incremental effective Youngs modulus is readily computed, and the overall stress–strain curve is obtained by plotting stress against the average total strain.

6.2.3 Numerical examples

Consider two cubes, one with a single large penny-shaped crack with the crack radius to the cube edge length of $a/2w = 0.5$, and another with 70 randomly-oriented penny-shape cracks of the same size (a/w=0.2). The crack in the single configuration is oriented at angle $\beta = 45°$ relative to the direction of the uniaxial compression load σ. The finite element

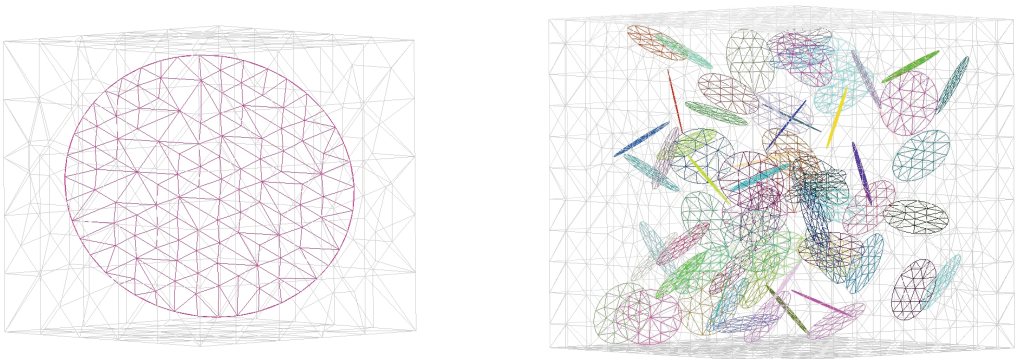

(a) (b)

Figure 6.2: Finite element mesh of (a) a cube with a large penny-shape crack and (b) a cube with 70 randomly-oriented penny-shape cracks.

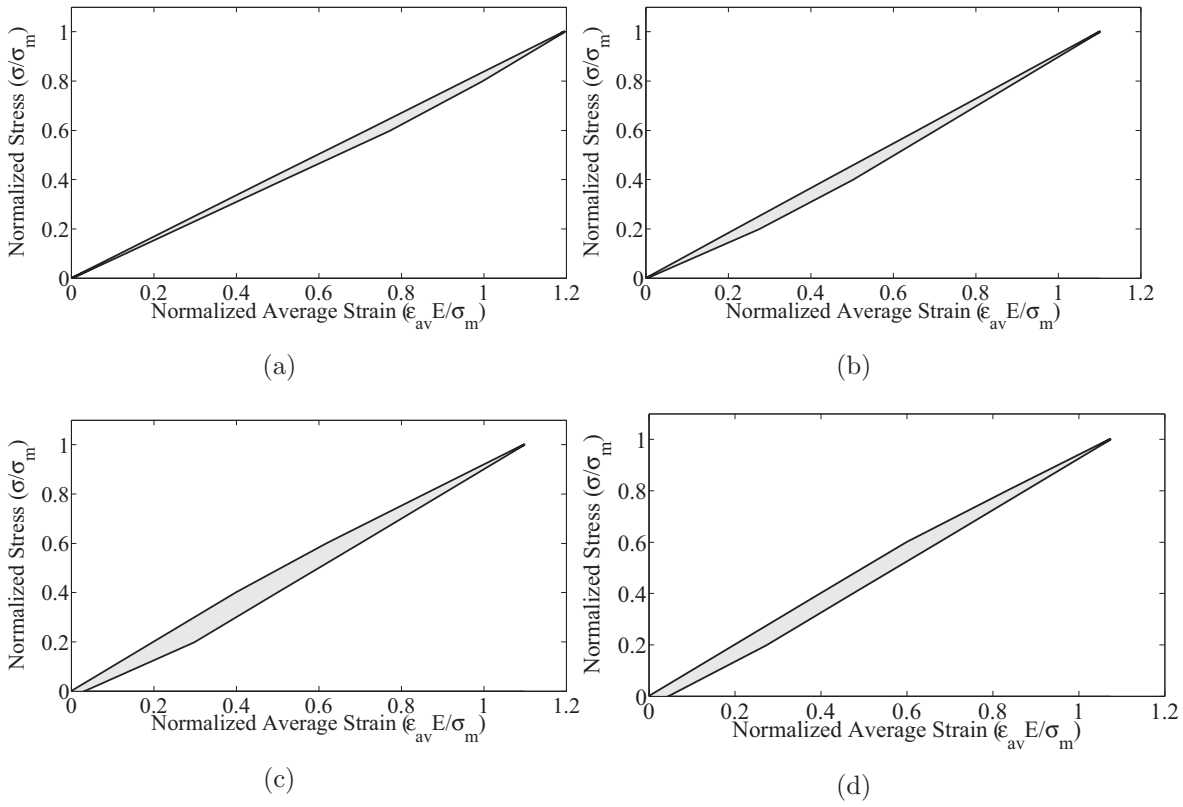

Figure 6.3: Stress–strain curves for a cube containing a large closed penny-shaped crack. (a) $\mu = 0.2, \tau_c/\sigma_m = 0$; (b) $\mu = 0.6, \tau_c/\sigma_m = 0$; (c) $\mu = 0.2, \tau_c/\sigma_m = 0.2$; (d) $\mu = 0.2, \tau_c/\sigma_m = 0.25$.

meshes of these cracked bodies are shown in Fig. 6.2. The following displacement boundary conditions are applied: $u_1 = 0$ over the edge $X_1 = X_2 = -w$, $u_2 = 0$ over the plane $X_2 = -w$, and $u_3 = 0$ over the edge $X_2 = X_3 = -w$. The Coulomb frictional constitutive law, $\tau_f = \mu|p| + \tau_c$, is used over the crack surfaces, where τ_f is the frictional resistive traction, p is the normal traction, and μ and τ_c are the friction coefficient and cohesive stress, respectively. Arbitrary values of $E = 10\,\text{GPa}$, and $\nu = 0.3$ were used for Young's modulus and Poisson's ratio, respectively. The maximum compressive stress of $\sigma_m = 1$ is gradually applied over the top surfaces in five increments ($n = 5$). This is followed by five more increments to remove the load completely, adding up to ten total increments.

Figures 6.3 and 6.4 present the stress–strain curves for the cubes with single and multiple cracks, respectively. Different choices of frictional contact parameters are used in the simulations. At the end of each increment, the average strain is computed from Eq. (6.2), and eventually the stress is plotted against the average strain. The following features in these plots are highlighted: (1) A hysteretic behavior is seen in all the plots, due to the work of frictional forces. (2) The plots in Fig. 6.3a,b and Fig. 6.4a show the results in the absence of the cohesive stress ($\tau_c = 0$). These plots clearly show that although a hysteretic energy loss

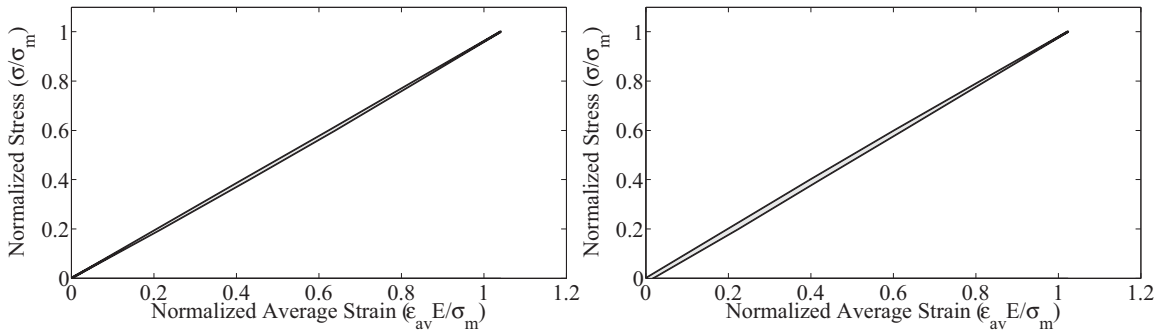

(a) (b)

Figure 6.4: Stress–strain curves for a cube containing 70 randomly-oriented closed penny-shaped cracks of the same size ($a/w = 0.2$). (a) $\mu = 0.4, \tau_c/\sigma_m = 0$; (b) $\mu = 0.2, \tau_c/\sigma_m = 0.2$.

is apparent in the solid deformation, no residual strain occurs after the complete removal of the load. This is because after the removal of the load, no resistive frictional force exists to prevent the solid from relaxing the strains. (3) The results for the cases with cohesive stress in Figs. 6.3c,d and 6.4b, however, show that a residual strain appears at the end of unloading stage. This is because the resistive cohesive stress can prevent the strain energy from being released. The uniaxial compression tests of rocks often demonstrate a hysteretic behavior with significant residual strains at the end of unloading stage [David et al., 2012]. Therefore, a cohesion term appears to be necessary in the frictional constitutive law when one describes the hysteretic behavior based on the sliding of micro-cracks.

6.2.4 Conclusions

Simulation results of the deformation of a cube containing large number of randomly-oriented cracks provide significant evidence that the frictional sliding along micro-cracks causes the hysteretic behavior of rock. The results also show that a cohesion term is necessary in the frictional constitutive law of micro-cracks in order to reproduce the residual strain feature of hysteretic stress–strain curves.

6.3 Modeling brittle crack growth

Simulating crack growth in brittle solids is of vital importance and great interest to a variety of scientific and engineering fields. Brittle crack growth is a complex process in which cracks propagate with very high speeds, and the solid might fragment into smaller parts due to crack coalescence and/or crack extension to the solid boundaries. In this section, a few examples of finite element modeling of growth of three-dimensional crack configurations are discussed.

6.3.1 Introduction

Brittle crack growth is one of main processes leading to sudden failure. One of the simplest numerical methodologies to model the crack propagation is the erosion element algorithm. This method is based on the deletion of elements, and once a certain damage criterion is met within an element, the stiffness of the element is reduced to model the reduced stiffness of the damaged material [Fan and Fish, 2008; Rabczuk et al., 2010]. Modeling cracks explicitly is not required in this method, which is advantageous because of low computational cost. However, the results of this method may exhibit mesh-dependency unless an appropriate energy-based failure criterion is used [Beissel et al., 1998]. In addition, this method is not able to model the strain singularity at the front of sharp cracks in elastic materials. The cohesive element approach is another attractive tool to model crack growth without modeling the crack singularity [Ortiz and Pandolfi, 1999]. This method allows the separation of finite element boundaries once a local failure criterion is met at the inter-element boundaries. The crack advance is then updated by the detachment of elements. One of the main weaknesses of this method is that non-smooth crack growth path is obtained, and the results are vulnerable to mesh-sensitivity unless very fine meshes are employed [Fan and Fish, 2008]. In addition, the crack path must conform to the boundaries of elements in the pre-existing mesh.

The classical modeling of brittle crack propagation involves the explicit representation of crack as sharp material discontinuity, and handling the crack evolution and geometry change by using remeshing techniques. In this approach, new crack surfaces are inserted along the computed crack path, and the new geometry is remeshed to allow separation between the elements over the new crack surfaces [Shephard et al., 1985]. The main weakness of this method is that remeshing accounts for a significant portion of the computational cost, particularly in three-dimensional models. A mesh modification, which uses a local remeshing rather than a complete one, can reduce the computational costs due to remeshing, but requires specific re-meshing techniques to be implemented as part of the numerical code [Li et al., 2005]. Full remeshing, however, allows the FE implementation and the meshing procedure to remain independent of each other. Several commercial fracture growth codes such as FRANC3D use local mesh modification technique to propagate explicit fractures in solids [Carter et al., 2000]. However, these software use either hybrid meshes [Carter et al., 2000; Bremberg and Dhondt, 2008, 2009; Bremberg and Faleskog, 2015] or submodeling technique [Schöllmann et al., 2003; Rabold and Kuna, 2014] to accurately model the strain singularity at the crack front. Complications may arise in both methodologies due to the incompatibility of different element types in hybrid meshes, or significant computational cost in sub-modeling procedures.

A very popular method to model the crack growth is the extended finite element method (X-FEM). X-FEM was proposed by Moës et al. [1999] and Sukumar et al. [2000], and allows one to model the crack independent of the mesh, which alleviates the need for remeshing during crack propagation. X-FEM uses enrichment functions, which makes it possible for the crack to pass arbitrary through elements. The level set method proposed by Osher and Sethian [1988] is often used with X-FEM to simplify the selection of enriched nodes, and the definition of enriched functions. Due to the simplicity of modeling crack propagation by X-FEM, this method has become very popular. However, defining enrichment functions for very close cracks may be problematic, and difficulties may arise when cracks interact or intersect.

Another methodology is the use of unstructured tetrahedral meshes to model crack growth in solids. This method lies between the classical methods based on hybrid meshes or submodeling techniques, and the more recent advanced enrichment-based X-FEM. This methodology uses quarter-point tetrahedra to model the crack singularity, and therefore does not require different types of elements, sub-models, or enrichment functions to model singularity at the crack front. This methodology has been successfully applied in the context of crack propagation [Paluszny and Matthäi, 2009; Paluszny and Zimmerman, 2011] as well as fragmentation [Paluszny et al., 2013]. It is well known that meshing procedures using unstructured tetrahedra are much simpler, and these elements are best suited to automatically mesh arbitrary domains and complicated geometries. Additionally, adaptive meshing procedures can be applied to discretize the domain efficiently [Pain et al., 2001]. The efficiency of quarter-point tetrahedral elements for reproducing square root strain singularity was discussed in Chapter 2. Also, accurate, efficient and reliable methods were introduced in Chapters 3 and 4 to extract the fracture parameters from the FE solution of tetrahedra. In this section, the tools developed in this thesis are used to model of mixed mode brittle crack growth in solids.

6.3.2 Methodology

The development of algorithms for growing cracks involves three steps: (i) Solving the boundary value problem for the current loading conditions, and computing the fracture parameters such as the stress intensity factor and the J-integral for all cracks in the domain. (ii) Employing a well-validated crack propagation criterion to estimate the angle and the extent of the crack growth of segments over the crack front. (iii) Change the geometry by extending the crack and continue the simulation from step i. In this algorithm the crack growth process is subdivided into several increments where the cracks advance until the energy released due to crack growth is not large enough to overcome the surface energy

required to advance the crack. During all the increments, the boundary value problem is solved to satisfy the equilibrium condition throughout the model. For a fixed set of boundary conditions, the model is iteratively deformed, until no more growth is registered. Since the mesh is dependent on the geometry of the crack, after crack advance in each increment the domain has to be remeshed in order to capture the emerging crack geometry. In every increment the geometry changes, the previous stress state is invalidated and new updated stresses are re-computed. In summary, the simulation of fracture growth involves the following steps [Paluszny and Zimmerman, 2011]:

1. Generate the geometry of cracked body
2. Generate mesh automatically
3. Apply boundary conditions
4. Solve for deformation
5. Compute fracture parameters
6. Compute propagation angle and length
7. Extend cracks
8. Remesh the new geometry and map the variables
9. Go to step 3 unless no growth is registered for the current increment

There have been mainly three criteria to estimate the angle of crack growth as well as the critical conditions required for the onset of crack growth in brittle materials: Maximum tangential stress (MTS) [Erdogan and Sih, 1963], minimum strain energy density (SED) [Sih, 1974] and maximum energy release rate ($\mathcal{G}$) [Nuismer, 1975]. The MTS criterion has been used extensively because of its simplicity and consistency with the experimental results on brittle fracture growth [Ayatollahi et al., 2006]. An extension of this method for mixed mode I/II/III loading in three-dimensional cracks has been introduced in [Schöllmann et al., 2002]. Based on this criterion, once the value of tangential stress in this direction reaches its critical value, the crack propagates along the direction of maximum tangential stress. This criterion is used in this research for estimating the extent and the direction of crack propagation. Once the stress intensity factors are computed along the crack front, the magnitude and the direction of crack growth can be estimated. More detail about fracture geometric representation and remeshing process can be found in Paluszny and Zimmerman [2011].

Simulating the propagation of a three-dimensional crack requires another criterion to estimate the extent of crack advance in different locations over the crack front. This is because the crack extension speed differs from one point to another along the crack front. Numerical studies show that within a group of cracks, and in order to reproduce patterns found in

the growth experiments, cracks must grow at different speeds [Renshaw and Pollard, 1994]. Generally, the extension rate of crack front points can be benchmarked against the highest extension rate. In this research, the weighing of the speeds and crack advances per points is formalized by a propagation criterion proposed by Charles [1958], and further extended by Renshaw and Pollard [1994]. This criterion proposes that the extension of crack front points is proportional to the point-wise energy released rate. The point with the maximum energy released rate grows fastest, while other points with less energy released rate grow slower proportionally. At each increment, the point with the highest energy released rate attains a fixed distance of extension, and the extensions of the other points are estimated proportionally according to variation of point-wise energy released rate. This means that the point with the highest released energy advances most in one increment, while points with less energy released rate grow to a lower extent [Paluszny and Matthäi, 2009].

6.3.3 Results and discussion

In order to demonstrate the efficiency and accuracy of the crack growth simulation using unstructured tetrahedral elements, penny-shaped and elliptical cracks embedded in large cubes are considered for growth experiments (Fig. 6.5a). Initially, the crack planes are at an angle of $\beta = 45°$ with respect to the direction of applied load. a denotes crack radius for the penny-shaped crack, and semi-major axis for the elliptical crack. The semi-minor axis b of the elliptical crack is perpendicular to the X_1X_2 plane. The geometrical specifications $a/w = 0.1$ and $b/w = 0.4$, and Young's modulus and Poisson's ratio values of $E = 1\,\text{GPa}$ and $\nu = 0.3$ are considered. The following boundary conditions are also applied: $u_1 = 0$ over the edge $X_1 = X_2 = -w$, $u_2 = 0$ over the plane $X_2 = -w$, $u_3 = 0$ over the edge $X_2 = X_3 = -w$, and $\sigma = 1\,\text{MPa}$ over the plane $X_2 = w$. Unstructured meshes based on 10-noded isoparametric tetrahedral elements are used to discretize the specimens, and quarter-point elements are employed at the crack front region. In all increments of simulation, the degree of mesh refinement in the crack front region was controlled by keeping the average crack front element size at about one twentieth of the crack length ($L_n \approx a/20$). This restriction ensures that the quarter-point elements at the crack front predominantly remain in the singular dominant zone [Kuna, 2013]. Figure 6.5b shows the finite element mesh of the penny-shaped crack configuration.

All crack growth procedures including incremental geometry change, remeshing, and mapping have been previously implemented into the Imperial College Geomechanics Tool (ICGT) [Paluszny and Matthäi, 2009; Paluszny and Zimmerman, 2011]. The procedures to estimate the crack parameters in this tool were upgraded in the ICGT by employing the displacement correlation and disk-shaped domain integral methods described in Chapters

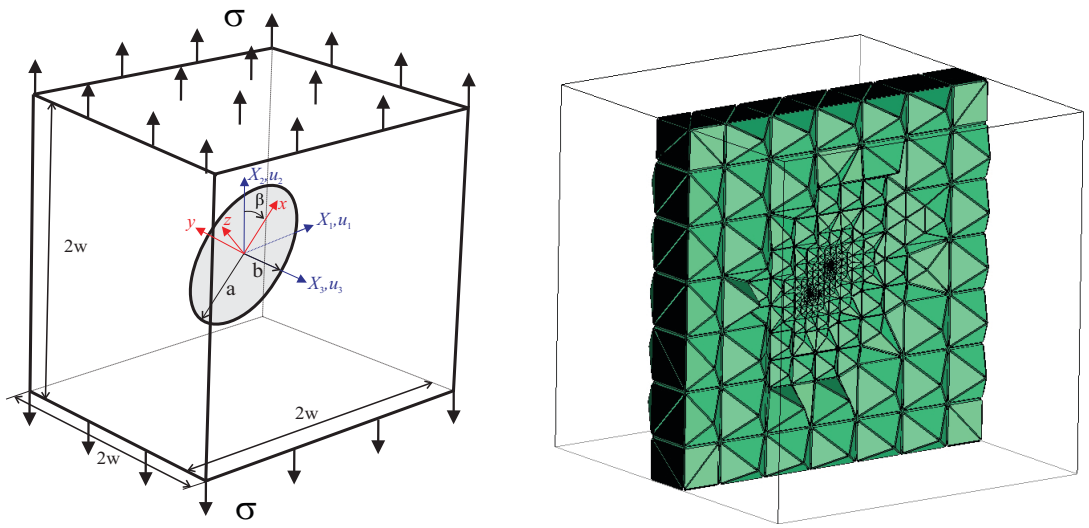

Figure 6.5: (a) Schematics of penny-shaped and elliptical crack embedded in a large cube under uniaxial tension; (b) Unstructured tetrahedral mesh.

3 and 4. Figures 6.6 and 6.7 show the incremental growth of penny-shaped and elliptical cracks under uniaxial tension. The incremental growth is simulated using eight steps. In both configurations, although cracks are initially under mixed mode loading, the change of geometry aligns the cracks normal to the load direction in a predominantly mode I loading condition. This behavior agrees with the results of growth experiments. The reason for this behavior is that the crack path follows the direction in which maximum energy is released to overcome the surface energy of new crack faces, and therefore an inclined crack reorients itself to grow in mode I, in alignment with the boundary conditions. Cracks extended towards pure mode I seem to release the maximum amount of strain energy compared to alternative crack path configurations. The mixed mode elliptical crack also gradually extends to a penny-shaped crack normal to the load direction. This shows that a penny-shaped crack is a more stable crack configuration as compared to an elliptical one. The same approach can be used to grow multiple interacting fractures. Figures 6.8 and 6.9 show the incremental growth of cubes with ten and fifty interacting randomly-oriented penny-shaped cracks under uniaxial tension. In such a model, the interaction of nearby cracks can considerably influence the growth path.

6.3.4 Conclusions

The results of the simulation of crack growth show that a growth simulator based on tetrahedral elements is efficient and accurate to predict paths of single and interacting cracks. Since tetrahedral meshes are suitable for meshing complex geometries with multiple cracks,

a growth simulator based on tetrahedrals can be potentially used to investigate the influence of crack interactions on the growth behavior.

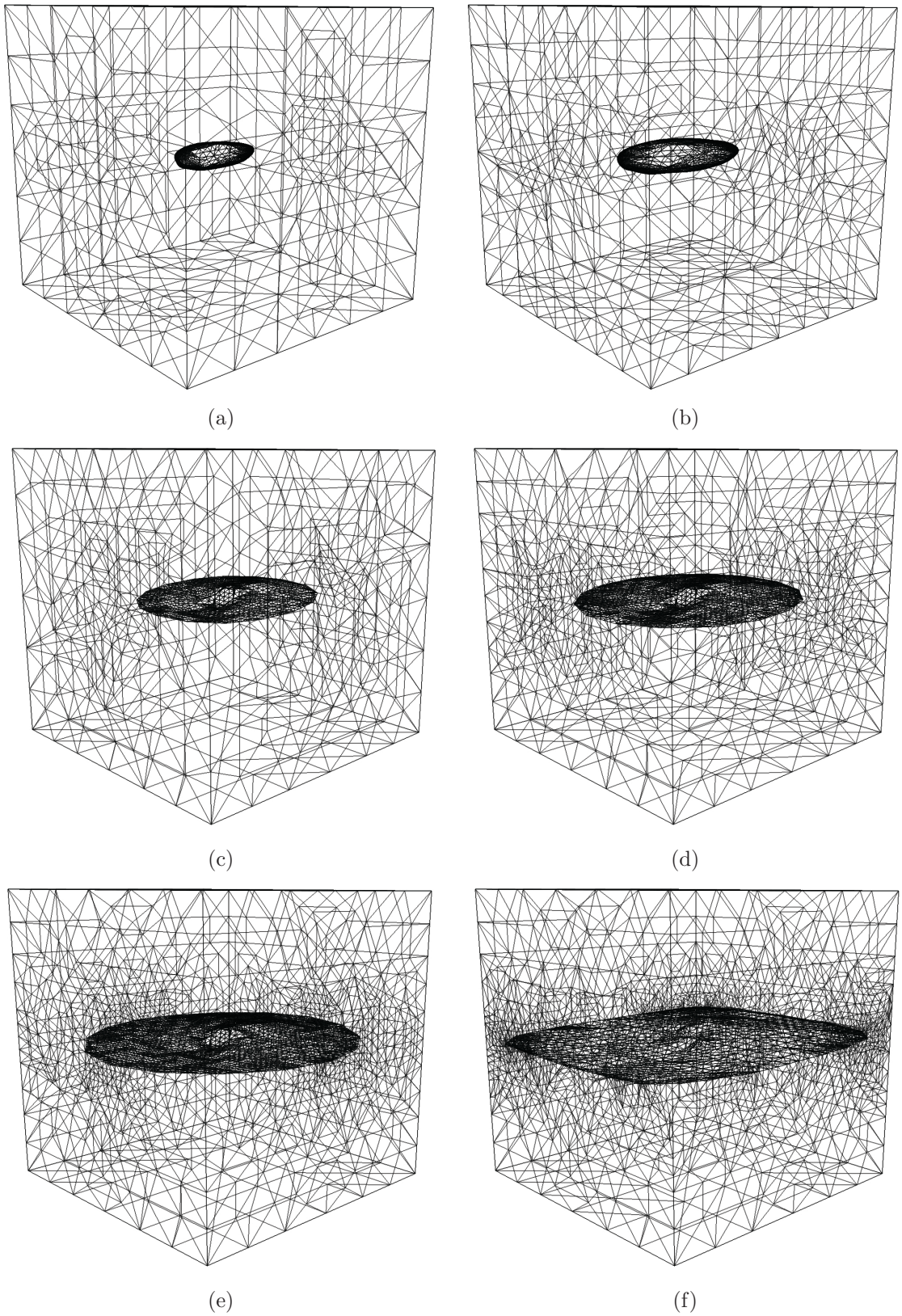

Figure 6.6: Incremental growth of an inclined penny-shaped crack in a large cube subjected to uniaxial tension.

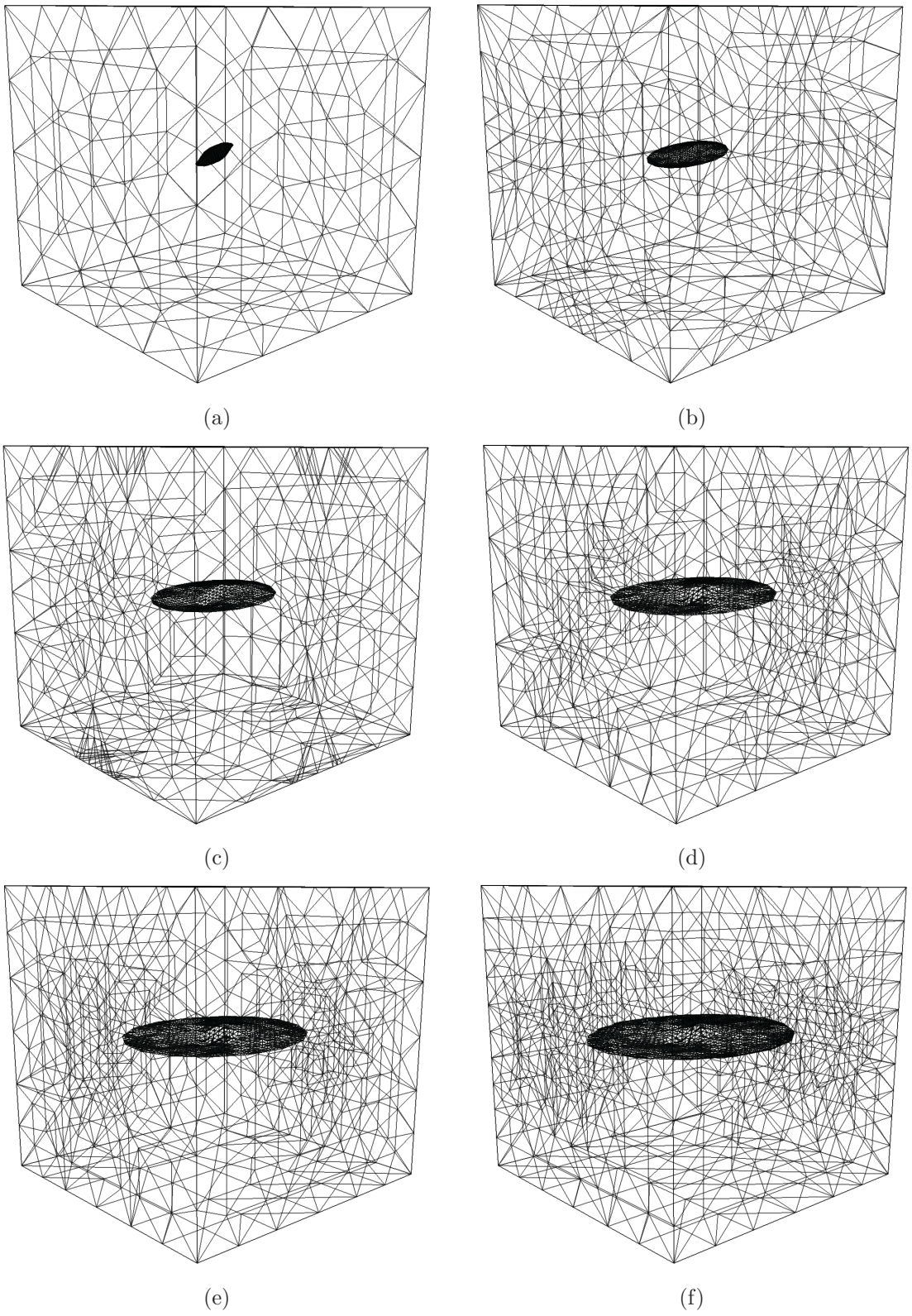

Figure 6.7: Incremental growth of an inclined elliptical crack in a large cube subjected to uniaxial tension ($a/b = 0.4$).

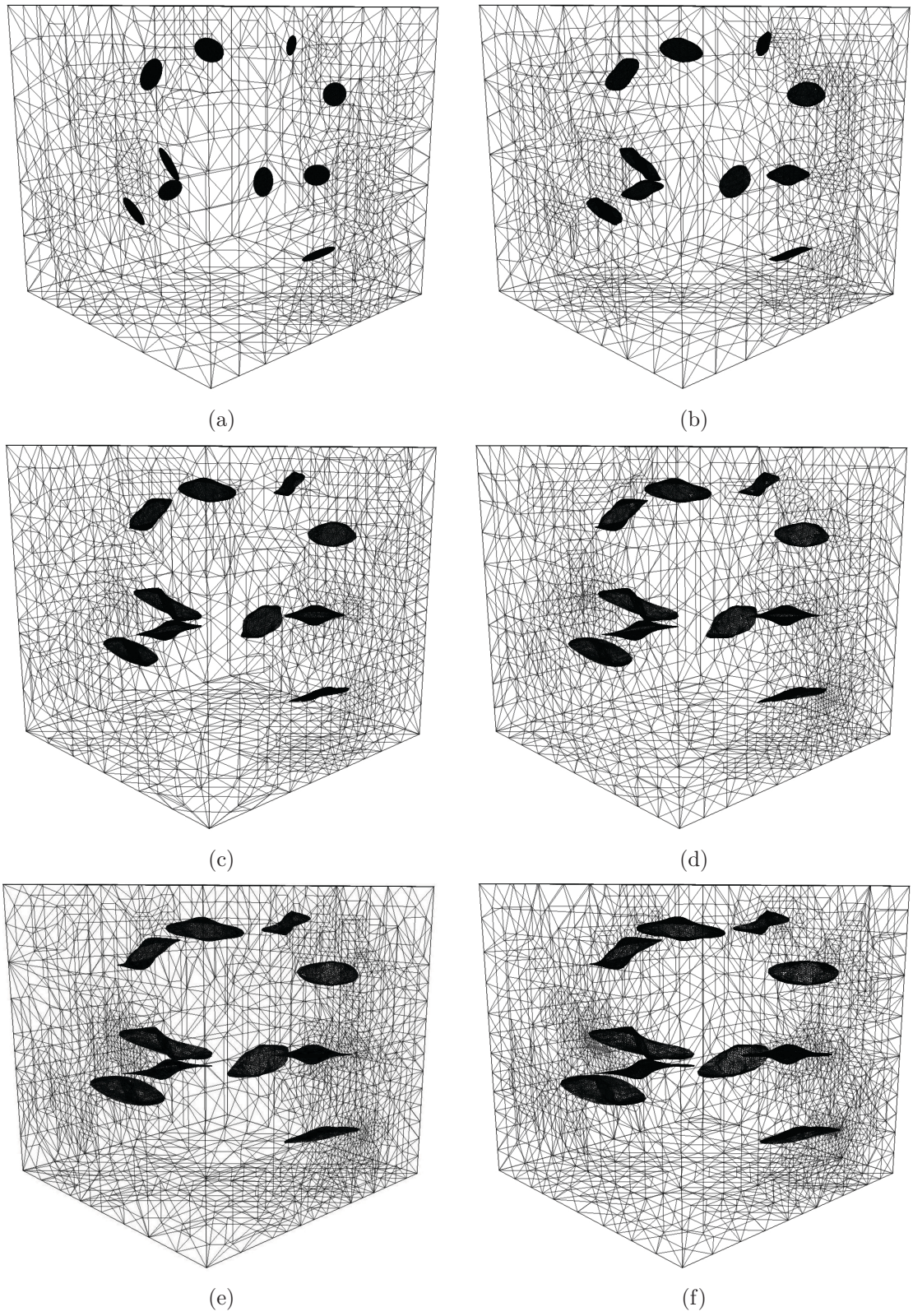

Figure 6.8: Incremental growth of ten interacting randomly-oriented penny-shaped cracks in a large cube subjected to uniaxial tension.

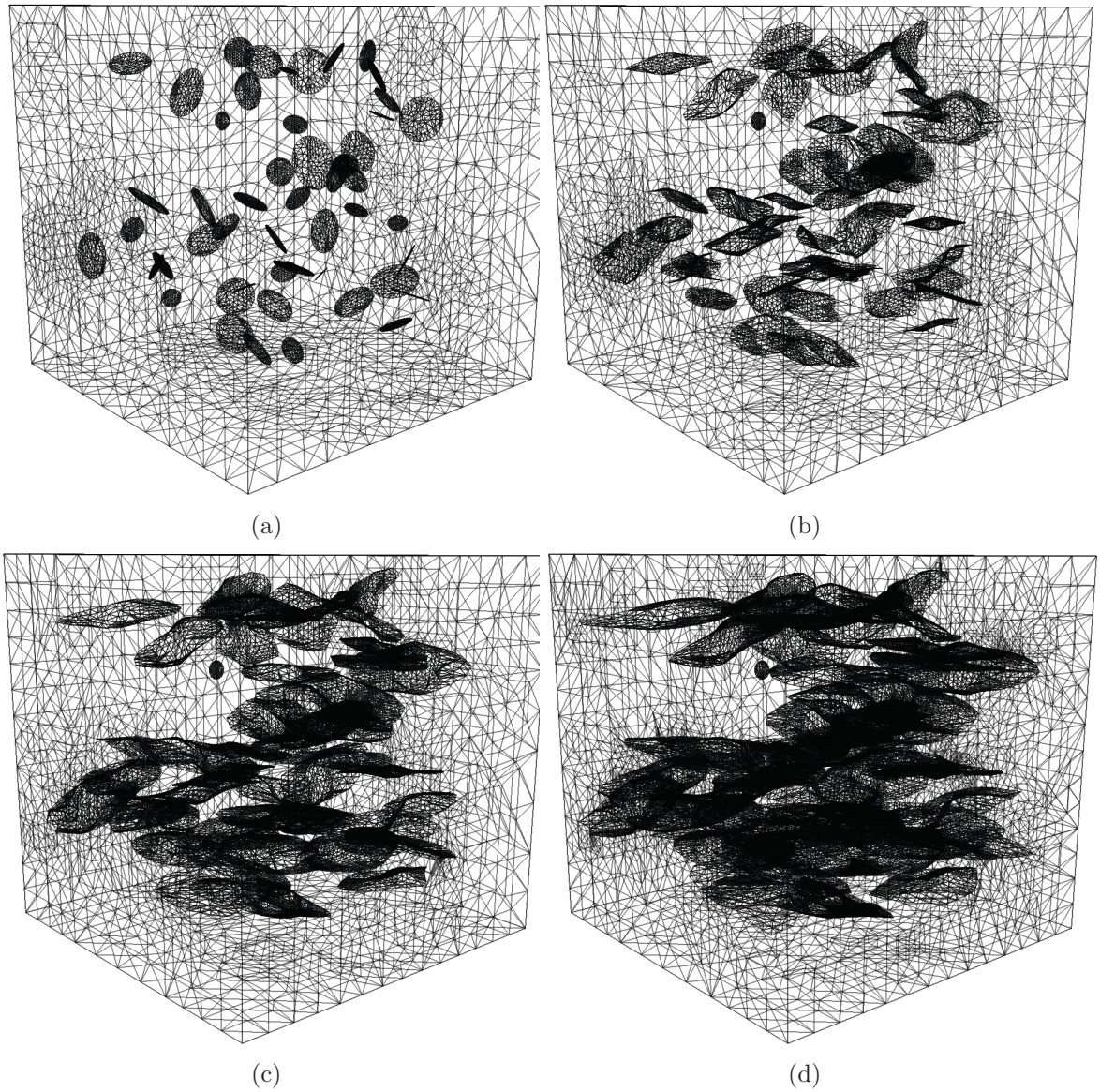

Figure 6.9: Incremental growth of fifty interacting randomly-oriented penny-shaped cracks in a large cube subjected to uniaxial tension.

Chapter 7

Conclusions

This thesis introduces a novel three-dimensional finite element formulation using unstructured tetrahedral meshes to accurately model the linear elastic deformation of fractured media under tensile and compressive loadings. Overall, this research provides significant evidence to the applicability, efficiency and accuracy of unstructured tetrahedral meshes to analyze fractured media. The main contributions of this work include:

- **Quarter-point tetrahedral finite elements [Nejati et al., 2015c]:**

  It is mathematically proven that quarter-point tetrahedral finite elements reproduce a square-root strain singularity along the crack front. This advancement enables one to model the crack strain singularity using unstructured tetrahedral meshes, which results in a considerable decrease in the computational cost. It is shown that the Jacobian becomes negative in a small region near the curved side of the quarter-point tetrahedra attached to the curved crack fronts. To avoid this, it is suggested to make these curve sides straight when using the quarter-point tetrahedra along the curved crack fronts. The numerical results on the relative displacements over the crack surfaces clearly demonstrate very good performance of quarter-point tetrahedra in reproducing a square root displacement variation near the crack front. Overall, quarter-point tetrahedra are efficient, accurate and reliable in linear elastic fracture mechanics applications.

- **Displacement correlation method for tetrahedra [Nejati et al., 2015c]:**

  An efficient displacement correlation (DC) method is proposed for extracting the SIFs from the FE solution of tetrahedral meshes. This method is based on correlating displacement at a fixed distance from the crack front. It is computationally very cheap, can be readily implemented in any FE code, and can be applied on unstructured meshes even for non-conforming crack surface elements. The application of the method

on several crack configurations in tension and compression shows that the average SIF computation error remains about 2-3%. A comparison of the results from the DC method for standard and quarter-point elements also reveals that the average SIF computation error more than doubles when using standard tetrahedra instead of quarter-point ones at the crack front region. The results from an extensive parametric study also suggest that there is an optimum mesh-dependent distance from the crack front at which the average SIF computation error hits its minimum. This distance is roughly equal to the average size of the elements at the crack front region.

- **Disk-shaped domain integral approach [Nejati et al., 2015a]:**

  A novel, efficient and accurate domain integral approach is proposed for computing pointwise J-integral and stress intensity factors. This method is based on the evaluation of domain integrals over disk-shaped domains discretized with virtual triangular elements. The main advantages of this method over classic volumetric domain approaches based on tubular domains are: (1) It can be directly applied to arbitrary tetrahedral meshes. (2) It requires less computational cost, as it performs integration over a disk rather than a tube. (3) It directly applies the original definition of the pointwise J- and interaction integrals. (4) Integration is performed over a disk perpendicular to the crack front, which is easy to generate and low in cost, and expressing the fields in curvilinear coordinates is no longer required for curved cracks. (5) As 2D plane strain auxiliary fields satisfy compatibility and equilibrium equations over a disk, the term containing the higher order gradients of the auxiliary fields vanishes in this new formulation. (6) The in-plane and anti-plane fields are separated, and cannot influence each other in the computation of fracture parameters. Based on the numerical results of several crack configurations, the SIF computation error remains within 1% for fine meshes, and 2-3% for coarse ones. The results of an extensive parametric study also suggests that an optimum mesh-dependent domain radius exists at which the SIF computation error hits its minimum. This optimum radius is roughly equal to the nominal size of the elements at the crack front region.

- **Singular penalty parameter on the crack front [Nejati et al., 2015b]:**

  It is shown that the application of a singular square root penalty variation near the crack front ensures the enforcement of contact constraints accurately close to the crack front. The gaps vanish on the crack front nodes, and the application of a constant (standard) penalty near the crack front enforces the contact tractions to follow the variation of the gaps there. The use of a singular square root penalty variation, however, compensates for the gradual decrease of the gaps near the crack front, and leads

to the computation of accurate contact tractions. Results from numerical experiments demonstrated the efficiency of the singular penalty variation for obtaining accurate contact tractions near the crack front.

- **Gap-based augmented Lagrangian approach [Nejati et al., 2015b]:**

  A gap-based augmented Lagrangian algorithm is introduced for updating contact forces over the crack fronts. This algorithm is based on the augmentation of gaps rather than the augmentation of Lagrange multipliers, and circumvents the difficulty of not being able to define contact tractions at the nodes located along the crack front. The crack front is excluded from the contact region, and therefore no traction is available for the nodes along the crack front. Therefore, Lagrange multipliers cannot be defined for the crack front nodes, and this causes a difficulty in using standard traction-based augmented Lagrangian method. The introduced gap-based augmented Lagrangian approach, however, is based on gaps and does not require the nodal tractions. Therefore, it can be effectively used to update the contact forces over the crack surfaces. The results from several numerical experiments demonstrated the efficiency of the gap-based augmented Lagrangian algorithm in accurately enforcing the contact constraints.

- **Efficient contact algorithm for fractured media [Nejati et al., 2015b]:**

  An efficient algorithm is presented for the treatment of contact between fracture surfaces in high density fractured media. In this algorithm, the contribution of the internal forces is accumulated once at the start, and is repeatedly used throughout the simulation. The penalty parameter is chosen for each fracture individually based on the value of Young's modulus and the average size of the elements over that fracture. This ensures that no ill-conditioning occurs in the system. The fracture parameters such as J-integral and stress intensity factor are computed for each fracture using the domain integral and displacement correlation methods. The recommended value for the domain radius and sampling distance in these methods is the average size of the quarter-point elements. The algorithm is efficient, reliable, and accurate for resolving internal contact in heavily fractured media.

- **Hysteresis and crack growth [Nejati et al., 2013]:**

  The numerical simulations demonstrated that a cohesive stress is required in the constitutive frictional law in order to model the hysteretic behavior of rocks based on sliding of micro-cracks. The results clearly show that no residual strain is reproduced when the cohesive stress is zero. The residual strain is a very important feature

of hysteretic behavior of rock, and these numerical simulations provide interesting insights on how it can be reproduced. The research on this topic is still ongoing, and more detailed numerical simulations with higher crack densities will be produced.

Extensions of this work fall into two categories: (i) extending the numerical methodologies introduced in this thesis to more generic loading and material conditions, and (ii) employing the current methodologies to understand complex geomechanical processes. The suggested extensions into the numerical methodology include:

- **The domain integral to compute higher order parameters:**

  The main focus of the present research is the computation of SIFs as the dominant influential parameters near the crack front. Numerical and experimental results have recently demonstrated that higher-order terms of the crack tip asymptotic field, in particular the T-stress, can also influence the stress distribution near the crack tip, and consequently the onset of fracture growth [Smith et al., 2001; Ayatollahi et al., 2006; Berto and Lazzarin, 2010]. Therefore, the accurate computation of higher order parameters is also of great importance in analyzing the growth of cracked bodies. The domain integral method presented in this thesis can be extended to compute the T-stress in 3D cracked bodies based on the original works of Kfouri [1986] and Toshio and Parks [1992] that describe contour and domain integral formulations for evaluating the T-stress.

- **The domain integral to include body forces and thermal strains:**

  The formulation of the domain integral presented in this thesis includes the surface traction contribution only, and excludes the contributions of body forces and thermal strains which require extra terms in the integral formulation [Shih et al., 1986]. An extension to the proposed disk-shaped domain integral method therefore should include those contributions as extra integral terms in order to demonstrate the applicability of this approach for more general loading conditions such as the ones in thermo-hydro-mechanical coupled systems.

- **The SIF computation of sharp V-notches:**

  The proposed SIF estimation methodologies are also applicable to determine the notch stress intensity factors of sharp isotropic and bi-material V-notches. This requires the evaluation of energy integrals at the notch tip using disk-shaped domains and virtual triangular elements. This allows to efficiently use unstructured meshes to analyze V-notched structures.

- **The SIF computation and contact treatment of interfacial cracks:**

  Interfacial cracks are present in many geological and engineering applications, and therefore the accurate crack growth modeling of those cracks is of great importance. The contact treatment and SIF computation methodologies developed in this thesis can be extended to bi-material media to study the behavior of interfacial cracks.

- **The SIF computation and contact treatment of anisotropic media:**

  The proposed methodologies can be extended to compute the SIFs for an anisotropic medium. The contact treatment, however, requires no extension, and is expected to perform equally well in an anisotropic medium.

- **The contact treatment for two-dimensional fractured media:**

  Three-dimensional numerical simulations on contact treatment and fracture growth demand significant computational cost. On the other hand, some geological fractured media can be modeled with great accuracy as two-dimensional problems. A similar contact treatment methodology can be proposed for analysing the deformation behavior of two-dimensional fractured media.

The suggested extensions in understanding geomechanical processes include:

- **Simulating crack growth under tension and compression:**

  The procedure developed in this thesis can be employed to simulate crack growth under combined tensile and compressive loading conditions. Growth patterns, including the coalescence and branching mechanisms, can be studied, as well as the influence of crack field interactions on ensuing crack paths. One can also study the influence of SIF variation near the corners on the crack growth pattern. Fault activation and rupture are interesting examples of the introduced numerical methodology in geomechanical applications.

- **New constitutive laws for micro-structured materials:**

  The numerical simulations of the hysteretic behavior of fractured media showed that a micromechanical model can be used to reproduce the overall stress–strain curves of micro-structured materials. These results demonstrate that new constitutive laws for rocks and similar materials can be developed based on their micro-mechanical parameters. These stress-dependent constitutive laws can be of great interest when analyzing rock bodies subjected to complex tri-axial stresses.

References

3DEC (1994). 3DEC Manual. *ITASCA Consulting Group. Minneapolis, USA*.

Abaqus (2012). ABAQUS User's Manual, Version 6.12 Documentation. *Dassault Systemes Simulia Corp. Providence, RI, USA*.

Agwai, A., Guven, I., and Madenci, E. (2011). Predicting crack propagation with peridynamics: A comparative study. *International Journal of Fracture*, 171(1):65–78.

Akin, J. E. (1976). The generation of elements with singularities. *International Journal for Numerical Methods in Engineering*, 10:1249–1259.

Aleshin, V. and Van Den Abeele, K. (2005). Micro-potential model for stressstrain hysteresis of micro-cracked materials. *Journal of the Mechanics and Physics of Solids*, 53:795–824.

Aleshin, V. and Van Den Abeele, K. (2007a). Friction in unconforming grain contacts as a mechanism for tensorial stress-strain hysteresis. *Journal of the Mechanics and Physics of Solids*, 55:765–787.

Aleshin, V. and Van Den Abeele, K. (2007b). Microcontact-based theory for acoustics in microdamaged materials. *Journal of the Mechanics and Physics of Solids*, 55:366–390.

Aliabadi, M. (1997). Boundary element formulations in fracture mechanics. *Applied Mechanics Reviews*, 50(2):83–96.

Anderson, T. L. (2005). *Fracture Mechanics, Fundamentals and Applications*. CRC, Boca Raton.

Andersson, J. and Dverstorp, B. (1987). Conditional simulations of fluid flow in three-dimensional networks of discrete fractures. *Water Resources Research*, 23(10):1876.

Ayatollahi, M. R., Aliha, M. R. M., and Hassani, M. M. (2006). Mixed mode brittle fracture in PMMA - An experimental study using SCB specimens. *Materials Science and Engineering A*, 417:348–356.

Ayatollahi, M. R. and Nejati, M. (2011a). An over-deterministic method for calculation of coefficients of crack tip asymptotic field from finite element analysis. *Fatigue & Fracture of Engineering Materials & Structures*, 34(3):159–176.

Ayatollahi, M. R. and Nejati, M. (2011b). Determination of NSIFs and coefficients of higher order terms for sharp notches using finite element method. *International Journal of Mechanical Sciences*, 53(3):164–177.

Baghbanan, A. and Jing, L. (2007). Hydraulic properties of fractured rock masses with correlated fracture length and aperture. *International Journal of Rock Mechanics and Mining Sciences*, 44:704–719.

Baghbanan, A. and Jing, L. (2008). Stress effects on permeability in a fractured rock mass with correlated fracture length and aperture. *International Journal of Rock Mechanics and Mining Sciences*, 45:1320–1334.

Baietto, M. C., Pierres, E., and Gravouil, A. (2010). A multi-model X-FEM strategy dedicated to frictional crack growth under cyclic fretting fatigue loadings. *International Journal of Solids and Structures*, 47(10):1405–1423.

Banks-Sills, L. (1987). Quarter-point singular elements revisited. *International Journal of Fracture*, 34:63–69.

Banks-Sills, L. (1991). Application of the finite element method to linear elastic fracture mechanics. *Applied Mechanics Reviews*, 44(10):447–461.

Banks-Sills, L. (2010). Update: Application of the finite element method to linear elastic fracture mechanics. *Applied Mechanics Reviews*, 63(2):020803.

Banks-Sills, L. and Bortman, Y. (1984). Reappraisal of the quarter-point quadrilateral element in linear elastic fracture mechanics. *International Journal of Fracture*, 25:169–180.

Banks-Sills, L. and Sherman, D. (1992). On the computation of stress intensity factors for three-dimensional geometries by means of the stiffness derivative and J-integral methods. *International Journal of Fracture*, 53(1):1–20.

Barsoum, R. S. (1976). On the use of isoparametric finite elements in linear fracture mechanics. *International Journal for Numerical Methods in Engineering*, 10:25–37.

Barsoum, R. S. (1977). Triangular quarter-point elements as elastic and perfectly-plastic crack tip elements. *International Journal for Numerical Methods in Engineering*, 11:85–98.

Barton, N., Bandis, S., and Bakhtar, K. (1985). Strength, deformation and conductivity coupling of rock joints. *International Journal of Rock Mechanics and Mining Sciences and Geomechanics Abstracts*, 22(3):121–140.

Bažant, Z. P. and Estenssoro, L. F. (1979). Surface singularity and crack propagation. *International Journal of Solids and Structures*, 15:405–426.

Béchet, E., Moës, N., and Wohlmuth, B. (2009). A stable Lagrange multiplier space for stiff interface conditions within the extended finite element method. *International Journal for Numerical Methods in Engineering*, 78:931–954.

Beissel, S. R., Johnson, G. R., and Popelar, C. H. (1998). An element-failure algorithm for dynamic crack propagation in general directions. *Engineering Fracture Mechanics*, 61(3-4):407–425.

Benthem, J. P. (1977). State of stress at the vertex of a quarter-infinite crack in a half-space. *International Journal of Solids and Structures*, 13(5):479–492.

Benthem, J. P. (1980). The quarter-infinite crack in a half space; Alternative and additional solutions. *International Journal of Solids and Structures*, 16:119–130.

Benzley, S. E. (1974). Representation of singularities with isoparametric finite elements. *International Journal for Numerical Methods in Engineering*, 8:537–545.

Berto, F. and Lazzarin, P. (2010). On higher order terms in the crack tip stress field. *International Journal of Fracture*, 161:221–226.

Bird, G. E., Trevelyan, J., and Augarde, C. E. (2010). A coupled BEM/scaled boundary FEM formulation for accurate computations in linear elastic fracture mechanics. *Engineering Analysis with Boundary Elements*, 34(6):599–610.

Bonnet, E., Bour, O., Odling, N. E., Davy, P., Main, I., Cowie, P., and Berkowitz, B. (2001). Scaling of fracture systems in geological media. *Reviews of Geophysics*, 39(1999):347–383.

Borden, M. J., Verhoosel, C. V., Scott, M. A., Hughes, T. J. R., and Landis, C. M. (2012). A phase-field description of dynamic brittle fracture. *Computer Methods in Applied Mechanics and Engineering*, 217-220:77–95.

Bremberg, D. and Dhondt, G. (2008). Automatic crack-insertion for arbitrary crack growth. *Engineering Fracture Mechanics*, 75:404–416.

Bremberg, D. and Dhondt, G. (2009). Automatic 3-D crack propagation calculations: a pure hexahedral element approach versus a combined element approach. *International Journal of Fracture*, 157(1-2):109–118.

Bremberg, D. and Faleskog, J. (2015). A numerical procedure for interaction integrals developed for curved cracks of general shape in 3-D. *International Journal of Solids and Structures*, 62:144–157.

Budiansky, B. and Rice, J. R. (1973). Conservation laws and energy-release rates. *Journal of Applied Mechanics*, 40:201–203.

Bui, H. D. (1983). Associated path independent J-integrals for separating mixed modes. *Journal of the Mechanics and Physics of Solids*, 31(6):439–448.

Byskov, E. (1970). The calculation of stress intensity factors using the finite element method with cracked elements. *International Journal of Fracture Mechanics*, 6(2):159–167.

Camacho, G. T. and Ortiz, M. (1996). Computational modelling of impact damage in brittle materials. *International Journal of solids and structures*, 33(2):2899–2938.

Carmona, H. A., Wittel, F. K., Kun, F., and Herrmann, H. J. (2008). Fragmentation processes in impact of spheres. *Physical Review E - Statistical, Nonlinear, and Soft Matter Physics*, 77:1–10.

Carter, B. J., Wawrzynek, P. A., and Ingraffea, A. R. (2000). Automated 3-D crack growth simulation. *International Journal for Numerical Methods in Engineering*, 47:229–253.

Chan, S. K., Tuba, I. S., and Wilson, W. K. (1970). On the finite element method in linear fracture mechanics. *Engineering Fracture Mechanics*, M(1).

Charles, R. J. (1958). Static fatigue of glass. I. *Journal of Applied Physics*, 29(11):1549.

Chen, F. H. K. and Shield, R. T. (1977). Conservation laws in elasticity of the J-integral type. *Journal of Applied Mathematics and Physics*, 28(1):1–22.

Cherepanov, G. P. (1967). Crack propagation in continuous media. *Journal of Applied Mathematics and Mechanics*, 31:503–512.

Cherepanov, G. P. (1979). *Mechanics of brittle fracture*. McGraw-Hill, New York.

Chidgzey, S. R., Trevelyan, J., and Deeks, A. J. (2008). Coupling of the boundary element method and the scaled boundary finite element method for computations in fracture mechanics. *Computers and Structures*, 86(11-12):1198–1203.

Cundall, P. A. (1988). Formulation of a three-dimensional distinct element model–Part I. A scheme to detect and represent contacts in a system composed of many polyhedral blocks. *International Journal of Rock Mechanics and Mining Sciences and Geomechanics Abstracts*, 25(3):107–116.

Daimon, R. and Okada, H. (2014). Mixed-mode stress intensity factor evaluation by interaction integral method for quadratic tetrahedral finite element with correction terms. *Engineering Fracture Mechanics*, 115:22–42.

Dally, J. W. and Riley, W. F. (1991). *Experimental stress analysis*. McGraw Hill, Singapore.

David, E. C., Brantut, N., Schubnel, A., and Zimmerman, R. W. (2012). Sliding crack model for nonlinearity and hysteresis in the uniaxial stress-strain curve of rock. *International Journal of Rock Mechanics and Mining Sciences*, 52:9–17.

De Dreuzy, J. R., Méheust, Y., and Pichot, G. (2012). Influence of fracture scale heterogeneity on the flow properties of three-dimensional discrete fracture networks (DFN). *Journal of Geophysical Research: Solid Earth*, 117:1–21.

DeLorenzi, H. G. (1982). On the energy release rate and the J-integral for 3-D crack configurations. *International Journal of Fracture*, 19:183–193.

Dershowitz, W. S. and Einstein, H. H. (1988). Characterizing rock joint geometry with joint system models. *Rock Mechanics and Rock Engineering*, 21:21–51.

Dolbow, J., Moës, N., and Belytschko, T. (2001). An extended finite element method for modeling crack growth with frictional contact. *Computer Methods in Applied Mechanics and Engineering*, 190(51-52):6825–6846.

Einstein, H. H. and Dershowitz, W. S. (1990). Tensile and shear fracturing in predominantly compressive stress fields–a review. *Engineering Geology*, 29:149–172.

Elguedj, T., Gravouil, A., and Combescure, A. (2007). A mixed augmented Lagrangian-extended finite element method for modelling elasticplastic fatigue crack growth with unilateral contact. *International Journal for Numerical Methods in Engineering*, 71:1569–1597.

Erdogan, F. and Sih, G. C. (1963). On the crack extension in plates under plane loading and transverse shear. *Journal of Basic Engineering*, 85(4):519.

Eshelby, J. D. (1970). *Energy relations and the energy-momentum tensor in continuum mechanics. In: Kanninen, M.F., Adler, W.F., Rosenfield, A.R. and Jaffee, R.I. (eds.), Inelastic Behavior of Solids.* McGraw-Hill, New York.

Fan, R. and Fish, J. (2008). The rs-method for material failure simulations. *International Journal for Numerical Methods in Engineering*, 73:1607–1623.

Fischer, K. A. and Wriggers, P. (2005). Frictionless 2D contact formulations for finite deformations based on the mortar method. *Computational Mechanics*, 36:226–244.

Fischer, K. A. and Wriggers, P. (2006). Mortar based frictional contact formulation for higher order interpolations using the moving friction cone. *Computer Methods in Applied Mechanics and Engineering*, 195:5020–5036.

Freese, C. E. and Tracey, D. M. (1976). The natural isoparametric triangle versus collapsed quadrilateral for elastic crack analysis. *International Journal of Fracture*, 12(3):767–770.

Giannakopoulos, A. (1989). The return mapping method for the integration of friction constitutive relations. *Computers & Structures*, 32:157–167.

Gosz, M., Dolbow, J., and Moran, B. (1998). Domain integral formulation for stress intensity factor computation along curved three-dimensional interface cracks. *International Journal of Solids and Structures*, 35(15):1763–1783.

Gosz, M. and Moran, B. (2002). An interaction energy integral method for computation of mixed-mode stress intensity factors along non-planar crack fronts in three dimensions. *Engineering Fracture Mechanics*, 69(3):299–319.

Gudmundsson, A. (1987). Geometry, formation and development of tectonic fractures on the Reykjanes Peninsula, southwest Iceland. *Tectonophysics*, 139:295–308.

Ha, Y. D. and Bobaru, F. (2010). Studies of dynamic crack propagation and crack branching with peridynamics. *International Journal of Fracture*, 162(1-2):229–244.

Harding, S., Kotousov, A., Lazzarin, P., and Berto, F. (2010). Transverse singular effects in V-shaped notches stressed in mode II. *International Journal of Fracture*, 164(1):1–14.

Hartmann, S. and Ramm, E. (2008). A mortar based contact formulation for non-linear dynamics using dual Lagrange multipliers. *Finite Elements in Analysis and Design*, 44:245–258.

He, Z., Kotousov, A., and Berto, F. (2015). Effect of vertex singularities on stress intensities near plate free surfaces. *Fatigue & Fracture of Engineering Materials & Structures*, 38:860–869.

Henshell, R. D. and Shaw, K. G. (1975). Crack tip finite elements are unnecessary. *International Journal for Numerical Methods in Engineering*, 9:495–507.

Hibbitt, H. D. (1977). Some properties of singular isoparametric elements. *International Journal for Numerical Methods in Engineering*, 11:180–184.

Horii, H. and Nemat-Nasser, S. (1983). Overall moduli of solids with microcracks: Load-induced anisotropy. *Journal of the Mechanics and Physics of Solids*, 31(2):155–171.

Huber, O., Nickel, J., and Kuhn, G. (1993). On the decomposition of the J-integral for 3D crack problems. *International Journal of Fracture*, 64(4):339–348.

Huseby, O., Thovert, J., Led, B., and Adler, P. M. (2000). Three-dimensional characterization of a fractured granite and transport properties. *Journal of Geophysical Research*, 105:21387–21401.

Huseby, O., Thovert, J. F., and Adler, P.M. (1999). Geometry and topology of fracture systems. *Journal of Physics A: Mathematical and General*, 30:1415–1444.

Hussain, M. A., Coffin, L. F., and Zaleski, K. A. (1981). Three dimensional singular element. *Computers & Structures*, 13(4):595–599.

Ibrahimbegovic, A. (2009). *Nonlinear Solid Mechanics*. Springer-Verlag, Dordrecht.

Ingraffea, A. R. and Manu, C. (1980). Stress intensity factor computation in three dimensions with quarter-point elements. *International Journal for Numerical Methods in Engineering*, 15:1427–1445.

Irwin, G. R. (1956). Onset of fast crack propagation in high steel and aluminium alloys. *Sagamore Research Conference Proceedings*, 2:289–305.

Jaeger, J. C., Cook, N. G. W., and Zimmerman, R. W. (2007). *Fundamentals of Rock Mechanics*. Wiley-Blackwell, Oxford, 4th edition.

Jafari, A. and Babadagli, T. (2011). Effective fracture network permeability of geothermal reservoirs. *Geothermics*, 40(1):25–38.

Jayaswal, K. and Grosse, I. R. (1993). Finite element error estimation for crack tip singular elements. *Finite Elements in Analysis and Design*, 14(1):17–35.

Jing, L. (2003). A review of techniques, advances and outstanding issues in numerical modelling for rock mechanics and rock engineering. *International Journal of Rock Mechanics and Mining Sciences*, 40(4):283–353.

Jing, L., Ma, Y., and Fang, Z. (2001). Modeling of fluid flow and solid deformation for fractured rocks with discontinuous deformation analysis (DDA) method. *International Journal of Rock Mechanics and Mining Sciences*, 38:343–355.

Kachanov, M., Shafiro, B., and Tsukrov, I. (2003). *Handbook of elasticity solutions*. Kluwer Academic Publishers, Dordrecht.

Kachanov, M. L. (1982a). A microcrack model of rock inelasticity part I: Frictional sliding on microcracks. *Mechanics of Materials*, 1:29–41.

Kachanov, M. L. (1982b). A microcrack model of rock inelasticity part II: Propagation of microcracks. *Mechanics of Materials*, 1:29–41.

Kassir, M. K. and Sih, G. C. (1975). *Mechanics of fracture 2: three-dimensional crack problems*. Noordhoff International Publishing, Leyden.

Kfouri, A. P. (1986). Some evaluations of the elastic T-term using Eshelby's method. *International Journal of Fracture*, 30:301–315.

Khanal, M., Schubert, W., and Tomas, J. (2004). Ball impact and crack propagation - simulations of particle compound material. *Granular Matter*, 5:177–184.

Khanal, M., Schubert, W., and Tomas, J. (2008). Compression and impact loading experiments of high strength spherical composites. *International Journal of Mineral Processing*, 86:104–113.

Khoei, A. R. and Nikbakht, M. (2007). An enriched finite element algorithm for numerical computation of contact friction problems. *International Journal of Mechanical Sciences*, 49(2):183–199.

Kim, Y. J., Kim, H., and Im, S. (2001). Mode decomposition of three-dimensional mixed-mode cracks via two-state integrals. *International Journal of Solids and Structures*, 38:6405–6426.

Klinsmann, M., Rosato, D., Kamlah, M., and McMeeking, R. M. (2015). An assessment of the phase field formulation for crack growth. *Computer Methods in Applied Mechanics and Engineering*, 294:313–330.

Koers, R. W. J. (1989). Use of modified standard 20-node isoparametric brick elements for representing stress/strain fields at a crack tip for elastic and perfectly plastic material. *International Journal of Fracture*, 40(2):79–110.

Kotousov, A., Lazzarin, P., Berto, F., and Harding, S. (2010). Effect of the thickness on elastic deformation and quasi-brittle fracture of plate components. *Engineering Fracture Mechanics*, 77(11):1665–1681.

Kotousov, A., Lazzarin, P., Berto, F., and Pook, L. P. (2013). Three-dimensional stress states at crack tip induced by shear and anti-plane loading. *Engineering Fracture Mechanics*, 108:65–74.

Kuna, F. and Herrmann, H. J. (1996). A study of fragmentation processes using a discrete element method. *Computer Methods in Applied Mechanics and Engineering*, 138:3–18.

Kuna, M. (2013). *Finite Elements in Fracture Mechanics: Theory - Numerics - Applications*. Springer, Dordrecht.

Lang, P. S., Paluszny, A., and Zimmerman, R. W. (2014). Permeability tensor of three-dimensional fractured porous rock and a comparison to trace map predictions. *Journal of Geophysical Research: Solid Earth*, 119:6288–6307.

Latham, J. P., Xiang, J., Belayneh, M., Nick, H. M., Tsang, C. F., and Blunt, M. J. (2013). Modelling stress-dependent permeability in fractured rock including effects of propagating and bending fractures. *International Journal of Rock Mechanics and Mining Sciences*, 57:100–112.

Laursen, T. A. and Simo, J. C. (1993). Algorithmic symmetrization of coulomb frictional problems using augmented lagrangians. *Computer Methods in Applied Mechanics and Engineering*, 108(2):133–146.

Lawn, B. R. and Marshall, D. B. (1998). Nonlinear stress-strain curves for solids containing closed cracks with friction. *Journal of the Mechanics and Physics of Solids*, 46(1):85–113.

Leung, C. T. O. and Zimmerman, R. W. (2012). Estimating the hydraulic conductivity of two-dimensional fracture networks using network geometric properties. *Transport in Porous Media*, 93:777–797.

Li, F. Z., Shih, C. F., and Needleman, A. (1985). A comparison of methods for calculating energy release rates. *Engineering Fracture Mechanics*, 21(2):405–421.

Li, X., Shephard, M. S., and Beall, M. W. (2005). 3D anisotropic mesh adaptation by mesh modification. *Computer Methods in Applied Mechanics and Engineering*, 194(48-49):4915–4950.

Lim, I. L., Johnston, I. W., and Choi, S. K. (1993). Application of singular quadratic distorted isoparametric elements in linear fracture mechanics. *International Journal for Numerical Methods in Engineering*, 36:2473–2499.

Lisjak, A. and Grasselli, G. (2014). A review of discrete modeling techniques for fracturing processes in discontinuous rock masses. *Journal of Rock Mechanics and Geotechnical Engineering*, 6(4):301–314.

Liu, F. and Borja, R. I. (2008). A contact algorithm for frictional crack propagation with the extended finite element method. *International Journal for Numerical Methods in Engineering*, 76:1489–1512.

Liu, F. and Borja, R. I. (2010). Stabilized low-order finite elements for frictional contact with the extended finite element method. *Computer Methods in Applied Mechanics and Engineering*, 199(37-40):2456–2471.

Long, J. C. S., Remer, J. S., Wilson, C. R., and Witherspoon, P. A. (1982). Porous media equivalents for networks of discontinuous fractures. *Water Resources Research*, 18(3):645.

Lynn, P. P. and Ingraffea, A. R. (1978). Transition elements to be used with quarter-point crack-tip elements. *International Journal for Numerical Methods in Engineering*, 12:1031–1036.

Malinouskaya, I., Thovert, J. F., Mourzenko, V. V., Adler, P. M., Shekhar, R., Agar, S., Rosero, E., and Tsenn, M. (2014). Fracture analysis in the Amellago outcrop and permeability predictions. *Petroleum Geoscience*, 20:93–107.

Manu, C. (1983). Quarter-point elements for curved crack fronts. *Computers & Structures*, 17(2):227–231.

Matthäi, S. K., Geiger, S., and Roberts, S. G. (2001). *The complex systems platform CSP3D3.0: Users Guide*. Technical report, ETH Zurich Research Reports.

McNeill, S. R., Peters, W. H., and Sutton, M. A. (1987). Estimation of stress intensity factor by digital image correlation. *Engineering Fracture Mechanics*, 28(1):101–112.

Mi, Y. and Aliabadi, M. H. (1992). Dual boundary element method for three-dimensional fracture mechanics analysis. *Engineering Analysis with Boundary Elements*, 10(2):161–171.

Min, K. B., Rutqvist, J., Tsang, C. F., and Jing, L. (2004). Stress-dependent permeability of fractured rock masses: A numerical study. *International Journal of Rock Mechanics and Mining Sciences*, 41:1191–1210.

Moës, N., Dolbow, J., and Belytschko, T. (1999). A finite element method for crack growth without remeshing. *International Journal for Numerical Methods in Engineering*, 46(1):131–150.

Moran, B. and Shih, C. F. (1987a). A general treatment of crack tip contour integrals. *International Journal of Fracture*, 35(4):295–310.

Moran, B. and Shih, C. F. (1987b). Crack tip and associated domain integrals from momentum and energy balance. *Engineering Fracture Mechanics*, 27(6):615–642.

Munjiza, A., Owen, D. R. J., and Bicanic, N. (1995). A combined finite-discrete element method in transient dynamics of fracturing solids. *Engineering Computations*, 12:145–174.

Murti, V. and Valliappan, S. (1986). A universal optimum quarter point element. *Engineering Fracture Mechanics*, 25(2):237–258.

Nahta, R. and Moran, B. (1993). Domain integrals for axisymmetric interface crack problems. *International Journal of Solids and Structures*, 30(15):2027–2040.

Nakamura, T. and Parks, D. M. (1988). Three-dimensional stress field near the crack front of a thin elastic plate. *Journal of Applied Mechanics*, 55:805–813.

Nakamura, T. and Parks, D. M. (1989). Antisymmetrical 3-D stress field near the crack front of a thin elastic plate. *International Journal of Solids and Structures*, 25(12):1411–1426.

Needleman, A. (1987). A continuum model for void nucleation by inclusion debonding. *Journal of Applied Mechanics*, 54(3):525.

Nejati, M., Paluszny, A., and Zimmerman, R. W. (2013). Theoretical and numerical modeling of rock hysteresis based on sliding of microcracks. *47th US Rock Mechanics/Geomechanics Symposium*, pages 573–581.

Nejati, M., Paluszny, A., and Zimmerman, R. W. (2015a). A disk-shaped domain integral method for the computation of stress intensity factors using tetrahedral meshes. *International Journal of Solids and Structures*, 69-70:230–251.

Nejati, M., Paluszny, A., and Zimmerman, R. W. (2015b). A finite element framework for modeling internal frictional contact in three-dimensional fractured media using unstructured tetrahedral meshes. *Computer Methods in Applied Mechanics and Engineering*, submitted.

Nejati, M., Paluszny, A., and Zimmerman, R. W. (2015c). On the use of quarter-point tetrahedral finite elements in linear elastic fracture mechanics. *Engineering Fracture Mechanics*, 144:194–221.

Nick, H. M., Paluszny, A., Blunt, M. J., and Matthäi, S. K. (2011). Role of geomechanically grown fractures on dispersive transport in heterogeneous geological formations. *Physical Review E - Statistical, Nonlinear, and Soft Matter Physics*, 84:1–9.

Nikishkov, G. P. and Atluri, S. N. (1987a). An equivalent domain integral method for computing crack-tip integral parameters in non-elastic, thermo-mechanical fracture. *Engineering Fracture Mechanics*, 26(6):851–867.

Nikishkov, G. P. and Atluri, S. N. (1987b). Calculation of fracture mechanics parameters for an arbitrary three-dimensional crack, by the 'equivalent domain integral' method. *International Journal for Numerical Methods in Engineering*, 24(9):1801–1821.

Nuismer, R. J. (1975). An energy release rate criterion for mixed mode fracture. *International Journal of Fracture*, 11(2):245–250.

Okada, H., Kawai, H., and Araki, K. (2008). A virtual crack closure-integral method (VCCM) to compute the energy release rates and stress intensity factors based on quadratic tetrahedral finite elements. *Engineering Fracture Mechanics*, 75(15):4466–4485.

Olsson, R. and Barton, N. (2001). An improved model for hydromechanical coupling during shearing of rock joints. *International Journal of Rock Mechanics and Mining Sciences*, 38:317–329.

Ooi, E. T. and Yang, Z. J. (2011). Modelling dynamic crack propagation using the scaled boundary finite element method. *International Journal for Numerical Methods in Engineering*, 88:329–349.

Ortiz, M. (1988). Microcrack coalescence and macroscopic crack growth initiation in brittle solids. *International Journal of Solids and Structures*, 24(3):231–250.

Ortiz, M. and Pandolfi, A. (1999). Finite-deformation irreversible cohesive elements for three-dimensional crack-propagation analysis. *International Journal for Numerical Methods in Engineering*, 44:1267–1282.

Osher, S. and Sethian, J. A. (1988). Fronts propagating with curvature dependent speed: Algorithms based on Hamilton-Jacobi formulations. *Journal of Computational Physics*, 79:12–49.

Pain, C. C., Umpleby, A. P., de Oliveira, C. R. E., and Goddard, A. J. H. (2001). Tetrahedral mesh optimisation and adaptivity for steady-state and transient finite element calculations. *Computer Methods in Applied Mechanics and Engineering*, 190(29-30):3771–3796.

Painter, S. and Cvetkovic, V. (2005). Upscaling discrete fracture network simulations: An alternative to continuum transport models. *Water Resources Research*, 41:1–10.

Paluszny, A. and Matthäi, S. K. (2009). Numerical modeling of discrete multi-crack growth applied to pattern formation in geological brittle media. *International Journal of Solids and Structures*, 46:3383–3397.

Paluszny, A., Tang, X. H., and Zimmerman, R. W. (2013). Fracture and impulse based finite-discrete element modeling of fragmentation. *Computational Mechanics*, 52(5):1071–1084.

Paluszny, A. and Zimmerman, R. W. (2011). Numerical simulation of multiple 3D fracture propagation using arbitrary meshes. *Computer Methods in Applied Mechanics and Engineering*, 200:953–966.

Paluszny, A. and Zimmerman, R. W. (2013). Numerical fracture growth modeling using smooth surface geometric deformation. *Engineering Fracture Mechanics*, 108:19–36.

Parks, D. M. (1974). A stiffness derivative finite element technique for determination of crack tip stress intensity factors. *International Journal of Fracture*, 10(4):487–502.

Peake, M. J., Trevelyan, J., and Coates, G. (2013). Extended isogeometric boundary element method (XIBEM) for two-dimensional Helmholtz problems. *Computer Methods in Applied Mechanics and Engineering*, 259:93–102.

Peano, A. and Pasini, A. (1982). A warning against misuse of quarter-point elements. *International Journal for Numerical Methods in Engineering*, 13:314–320.

Pierrès, E., Baietto, M. C., and Gravouil, A. (2010). A two-scale extended finite element method for modelling 3D crack growth with interfacial contact. *Computer Methods in Applied Mechanics and Engineering*, 199(17-20):1165–1177.

Pook, L. P., Berto, F., Campagnolo, A., and Lazzarin, P. (2014). Coupled fracture mode of a cracked disc under anti-plane loading. *Engineering Fracture Mechanics*, 128:22–36.

Portela, A., Aliabadi, M. H., and Rooke, D. P. (1993). Dual boundary element incremental analysis of crack propagation. *Computers & Structures*, 46(2):237–247.

Puso, M. A. and Laursen, T. A. (2004). A mortar segment-to-segment contact method for large deformation solid mechanics. *Computer Methods in Applied Mechanics and Engineering*, 193:601–629.

Pyrak-Nolte, L. J. and Morris, J. P. (2000). Single fractures under normal stress: The relation between fracture specific stiffness and fluid flow. *International Journal of Rock Mechanics and Mining Sciences*, 37:245–262.

Rabczuk, T., Bordas, S., and Zi, G. (2010). On three-dimensional modelling of crack growth using partition of unity methods. *Computers and Structures*, 88(23-24):1391–1411.

Rabold, F. and Kuna, M. (2014). Automated finite element simulation of fatigue crack growth in three-dimensional structures with the software system ProCrack. *Procedia Materials Science*, 3:1099–1104.

Rabold, F., Kuna, M., and Leibelt, T. (2013). PROCRACK: A software for simulating three-dimensional fatigue crack growth. *Lecture Notes in Applied and Computational Mechanics*, 66:355–374.

Rajaram, H., Socrate, S., and Parks, D. M. (2000). Application of domain integral methods using tetrahedral elements to the determination of stress intensity factors. *Engineering Fracture Mechanics*, 66(5):455–482.

Raju, I. S. and Shivakumar, K. N. (1990). An equivalent domain integral method in the two-dimensional analysis of mixed mode crack problems. *Engineering Fracture Mechanics*, 37(4):707–725.

Reeves, D. M., Parashar, R., Pohll, G., Carroll, R., Badger, T., and Willoughby, K. (2013). The use of discrete fracture network simulations in the design of horizontal hillslope drainage networks in fractured rock. *Engineering Geology*, 163:132–143.

Renshaw, C. E. and Pollard, D. D. (1994). Numerical simulation of fracture set formation: A fracture mechanics model consistent with experimental observations. *Journal of Geophysical Research*, 99:9359–9372.

Ribeaucourt, R., Baietto-Dubourg, M. C., and Gravouil, A. (2007). A new fatigue frictional contact crack propagation model with the coupled X-FEM/LATIN method. *Computer Methods in Applied Mechanics and Engineering*, 196(33-34):3230–3247.

Rice, J. R. (1968). A path independent integral and the approximate analysis of strain concentration by notches and cracks. *Journal of Applied Mechanics*, 35:379–386.

Rigby, R. H. and Aliabadi, M. H. (1998). Decomposition of the mixed-mode J-integral-revisited. *International Journal of Solids and Structures*, 35(17):2073–2099.

Rybicki, E. F. and Kanninen, M. F. (1977). A finite element calculation of stress intensity factors by a modified crack closure integral. *Engineering Fracture Mechanics*, 9:931–938.

Saouma, V. E. and Schwemmer, D. (1984). Numerical evaluation of the quarter-point crack tip element. *International Journal for Numerical Methods in Engineering*, 20:1629–1641.

Schöllmann, M., Fulland, M., and Richard, H. A. (2003). Development of a new software for adaptive crack growth simulations in 3D structures. *Engineering Fracture Mechanics*, 70:249–268.

Schöllmann, M., Richard, H. A., Kullmer, G., and Fulland, M. (2002). A new criterion for the prediction of crack development in multiaxially loaded structures. *International Journal of Fracture*, 117(2):129–141.

Segall, P. and Pollard, D. D. (1983). Nucleation and growth of strike slip faults in granite. *Journal of Geophysical Research*, 88(2):555.

Segedin, C. M. (1951). Note on a penny-shaped crack under shear. *Mathematical Proceedings of the Cambridge Philosophical Society*, 47(2):396–400.

Shephard, M. S., Weidner, T. J., Yehia, N. A. B., and Burd, G. S. (1985). Automatic crack propagation tracking. *Computers & Structures*, 20:211–223.

Shi, G. (1988). *Discontinuous deformation analysis–a new numerical model for the statics, dynamics of block systems*. PhD thesis, University of California, Berkeley, USA.

Shih, C. F., Lorenzi, H. G., and German, M. D. (1976). Crack extension modeling with singular quadratic isoparametric elements. *International Journal of Fracture*, 12(3):647–651.

Shih, C. F., Moran, B., and Nakamura, T. (1986). Energy release rate along a three-dimensional crack front in a thermally stressed body. *International Journal of Fracture*, 30:79–102.

Shivakumar, K. N. and Raju, I. S. (1992). An equivalent domain integral method for three-dimensional mixed-mode fracture problems. *Engineering Fracture Mechanics*, 42(6):935–959.

Shivakumar, K. N., Tan, P. W., and Newman Jr., J. C. (1988). A virtual crack-closure technique for calculating stress intensity factors for cracked three dimensional bodies. *International Journal of Fracture*, 36:43–50.

Shockey, D. A., Curran, D. R., Seaman, L., Rosenberg, J. T., and Petersen, C. F. (1974). Fragmentation of rock under dynamic loads. *International Journal of Rock Mechanics and Mining Sciences and Geomechanics Abstracts*, 11:303–317.

Sih, G. C. (1974). Strain-energy-density factor applied to mixed mode crack problems. *International Journal of Fracture*, 10(3):305–321.

Simo, J. C. and Laursen, T. A. (1992). An augmented lagrangian treatment of contact problems involving friction. *Computers & Structures*, 42:97–116.

Simpson, R. and Trevelyan, J. (2011). A partition of unity enriched dual boundary element method for accurate computations in fracture mechanics. *Computer Methods in Applied Mechanics and Engineering*, 200(1-4):1–10.

Smith, D. J., Ayatollahi, M. R., and Pavier, M. J. (2001). The role of T-stress in brittle fracture for linear elastic materials under mixed-mode loading. *Fatigue & Fracture of Engineering Materials & Structures*, 24:137–150.

Stüben, K. (2001). A review of algebraic multigrid. *Journal of Computational and Applied Mathematics*, 128:281–309.

Sukumar, N., Moës, N., Moran, B., and Belytschko, T. (2000). Extended finite element method for three-dimensional crack modelling. *International Journal for Numerical Methods in Engineering*, 48(11):1549–1570.

Toshio, N. and Parks, D. M. (1992). Determination of elastic T-stress along three-dimensional crack fronts using an interaction integral. *International Journal of Solids and Structures*, 29(13):1597–1611.

Tracey, D. M. (1971). Finite elements for determination of crack tip elastic stress intensity factors. *Engineering Fracture Mechanics*, 3(3):255–265.

Tracey, D. M. (1974). Finite elements for three-dimensional elastic crack analysis. *Nuclear Engineering and Design*, 26:282–290.

Trollé, B., Gravouil, A., Baietto, M.-C., and Nguyen-Tajan, T. M. L. (2012). Optimization of a stabilized X-FEM formulation for frictional cracks. *Finite Elements in Analysis and Design*, 59:18–27.

Tur, M., Fuenmayor, F. J., and Wriggers, P. (2009). A mortar-based frictional contact formulation for large deformations using Lagrange multipliers. *Computer Methods in Applied Mechanics and Engineering*, 198:2860–2873.

UDEC (1992). UDEC Manual. *ITASCA Consulting Group. Minneapolis, USA*.

Červenka, J. and Saouma, V. E. (1997). Numerical evaluation of 3-D SIF for arbitrary finite element meshes. *Engineering Fracture Mechanics*, 57(5):541–563.

Wait, R. (1978). A note on quarter-point triangular elements. *International Journal for Numerical Methods in Engineering*, 12:1333–1336.

Walsh, J. B. (1965). The effect of cracks on the uniaxial elastic compression pressure. *Journal of Geophysical Research*, 70:399–411.

Walters, M. C., Paulino, G. H., and Dodds, R. H. (2005). Interaction integral procedures for 3-D curved cracks including surface tractions. *Engineering Fracture Mechanics*, 72(11):1635–1663.

Wang, Y. and Tonon, F. (2011). Dynamic validation of a discrete element code in modeling rock fragmentation. *International Journal of Rock Mechanics and Mining Sciences*, 48(4):535–545.

Williams, M. L. (1957). On the stress distribution at the base of a stationary crack. *Journal of Applied Mechanics*, 24:109–114.

Wriggers, P. (2006). *Computational Contact Mechanics*. Springer-Verlag, Berlin.

Wriggers, P. and Zavarise, G. (1993). Application of augmented Lagrangian techniques for non-linear constitutive laws in contact interfaces. *Communications in Numerical Methods in Engineering*, 9(10):815–824.

Yang, B., Laursen, T. A., and Meng, X. (2005). Two dimensional mortar contact methods for large deformation frictional sliding. *International Journal for Numerical Methods in Engineering*, 62:1183–1225.

Yang, Z. (2006). Fully automatic modelling of mixed-mode crack propagation using scaled boundary finite element method. *Engineering Fracture Mechanics*, 73(12):1711–1731.

Yastrebov, V. A. (2013). *Numerical Methods in Contact Mechanics*. ISTE Ltd, London.

Yau, J. F., Wang, S. S., and Corten, H. T. (1980). A mixed-mode crack analysis of isotropic solids using conservation laws of elasticity. *Journal of Applied Mechanics*, 47:335–341.

Yeo, I. W., de Freitas, M. H., and Zimmerman, R. W. (1998). Effect of shear displacement on the aperture and permeability of a rock fracture. *International Journal of Rock Mechanics and Mining Sciences*, 35(8):1051–1070.

Zavarise, G. and De Lorenzis, L. (2009). The node-to-segment algorithm for 2D frictionless contact: Classical formulation and special cases. *Computer Methods in Applied Mechanics and Engineering*, 198(41-44):3428–3451.

Zavarise, G., Wriggers, P., and Schrefler, B. A. (1995). On augmented Lagrangian algorithms for thermomechanical contact problems with friction. *International Journal for Numerical Methods in Engineering*, 38(December 1993):2929–2949.

Zhang, X. and Sanderson, D. J. (1998). Numerical study of critical behaviour of deformation and permeability of fractured rock masses. *Marine and Petroleum Geology*, 15:535–548.

Zienkiewicz, O. C. and Taylor, R. L. (1989). *The Finite Element Method: Basic Formulation and Linear Problems*, volume 1. McGraw-Hill, Maidenhead, UK.

Appendix:

Stress intensity factors for an embedded penny-shaped/elliptical crack in an infinite body under uniaxial tension or compression

Analytical solutions for the SIFs of penny-shaped and elliptical cracks embedded in infinite solids subjected to uniform tension or shear have been derived in Kassir and Sih [1975]. Consider an inclined penny-shaped/elliptical crack embedded in a solid under uniaxial tension σ, as shown in Fig. 4.8b. The crack plane is perpendicular to the X_1X_2 plane, and makes an angle β with the applied load direction, which is oriented along the X_2 axis. The normal and shear stress components on the crack face are $\sigma_{zz} = \sigma \sin^2 \beta$ and $\sigma_{zx} = \sigma \sin \beta \cos \beta$. The SIFs of the penny-shaped crack are therefore given by

$$\begin{aligned} K_{\mathrm{I}} &= 2\sigma\sqrt{a/\pi}\sin^2\beta \\ K_{\mathrm{II}} &= \frac{2\sigma\sqrt{a/\pi}}{2-\nu}\sin 2\beta\cos\phi \\ K_{\mathrm{III}} &= \frac{2(1-\nu)\sigma\sqrt{a/\pi}}{2-\nu}\sin 2\beta\sin\phi \end{aligned} \tag{A.1}$$

where a and ν are the crack radius and Poisson's ratio, respectively, and ϕ is the polar angle, as shown in Fig. A.1a. It should be noted that incorrect solutions for the SIFs of penny-shaped cracks were reported by Cherepanov [1979]. These solutions, which do not contain Poisson's ratio, were incorrectly employed to validate the numerical results by Nikishkov and Atluri [1987b]. The SIFs of the elliptical crack are given by

$$\begin{aligned} K_{\mathrm{I}}(\omega) &= \frac{\sigma\sqrt{\pi a}}{E(k)}\sin^2\beta\,\Pi(\omega) \\ K_{\mathrm{II}}(\omega) &= \frac{\Psi k'\sigma\sqrt{\pi a}}{2\Pi(\omega)}\sin 2\beta\cos\omega \\ K_{\mathrm{III}}(\omega) &= \frac{\Psi(1-\nu)\sigma\sqrt{\pi a}}{2\Pi(\omega)}\sin 2\beta\sin\omega \end{aligned} \tag{A.2}$$

where

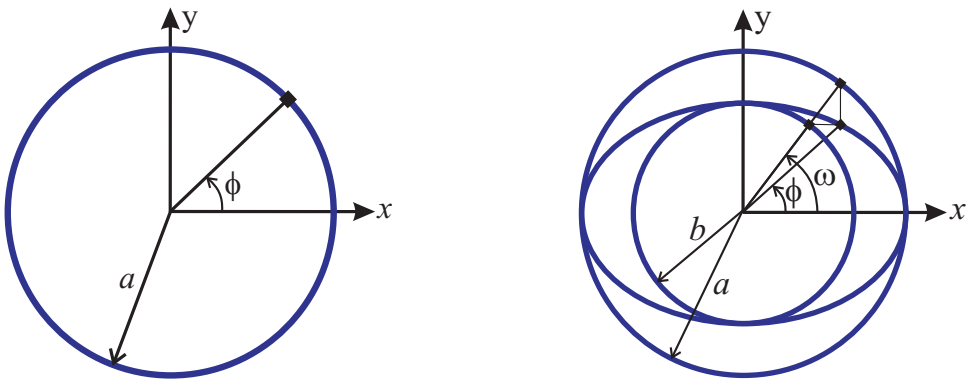

(a) (b)

Figure A.1: Configurations of (a) penny-shaped and (b) elliptical cracks.

$$\begin{aligned}\Psi &= \frac{k^2 k'}{\big(k^2-\nu\big)E(k)+\nu k'^2 K(k)}\\ \Pi(\omega) &= \Big(k'^2\sin^2\omega + k'^4\cos^2\omega\Big)^{1/4}\end{aligned} \tag{A.3}$$

In these formulas, $k' = b/a$, $k^2 = 1-k'^2$, a and b are the lengths of semi-major and semi-minor axes of the ellipse ($a > b$), and $K(k)$ and $E(k)$ are the complete first and second elliptic integrals, given by

$$\begin{aligned}K(k) &= \int_0^{\pi/2} \frac{1}{\sqrt{1-k^2\sin^2 t}}\,\mathrm{d}t\\ E(k) &= \int_0^{\pi/2} \sqrt{1-k^2\sin^2 t}\,\mathrm{d}t\end{aligned} \tag{A.4}$$

Angle ω parameterizes the points of the ellipse by the equations $x = a\cos\omega, y = b\sin\omega$, and is related to the polar angle ϕ by $k'\tan\omega = \tan\phi$ (see Fig. A.1b). Rewriting Eq. (A.4) in terms of the polar angle ϕ gives [Kachanov et al., 2003]:

$$\begin{aligned}K_{\mathrm{I}}(\phi) &= \frac{k'\sigma\sqrt{\pi a}}{E(k)}\,\frac{\Pi_1(\phi)}{\Pi_2(\phi)}\sin^2\beta\\ K_{\mathrm{II}}(\phi) &= \frac{\Psi k'^2\sigma\sqrt{\pi a}}{2\Pi_1(\phi)\Pi_2(\phi)}\sin 2\beta\cos\phi\\ K_{\mathrm{III}}(\phi) &= \frac{\Psi(1-\nu)\sigma\sqrt{\pi a}}{2\Pi_1(\phi)\Pi_2(\phi)}\sin 2\beta\sin\phi\end{aligned} \tag{A.5}$$

where

$$\begin{aligned}\Pi_1(\phi) &= \Big(\sin^2\phi + k'^4\cos^2\phi\Big)^{1/4}\\ \Pi_2(\phi) &= \Big(k'^2\sin^2\phi + k'^4\cos^2\phi\Big)^{1/4}\end{aligned} \tag{A.6}$$

Now consider an inclined penny-shaped/elliptical crack embedded in a solid under uniaxial compression σ, as shown in Fig. (5.5a). Here, all compressive stresses and pressures are considered to be positive. The crack plane is perpendicular to the X_1X_2 plane, and makes an angle β with the applied load direction, which is oriented along the X_2 axis. Also consider a fluid pressure p_0 is first applied over the crack surfaces, which results in the opening of the crack surfaces and inducing initial aperture. Then, the fluid pressure is removed, although the inducing aperture is still present, and the external compressive stress is applied to the cube, where as a result, the crack surfaces might go into contact. The induced normal and shear stress components on the contacting crack surfaces are $\sigma_{zz} = (\sigma\sin^2\beta - p_0)$ and $\sigma_{zx} = \sigma\sin\beta\cos\beta$. The frictional stress is therefore evaluated using Coloumb constitutive

law as $\tau_{\mathrm{f}} = \mu(\sigma \sin^2\beta - p_0) + \tau_c$. In the stick condition no crack deformation happens after the crack closure, and only the applied shear and normal stress before the crack closure contributes to the crack deformation. In slip condition, however, in addition to the normal and shear deformations happening while the crack is closing, crack deformation also occurs due to effective shear stress over the crack surface when it is slipping. According to the analytical solution of a penny-shaped crack under uniform shear given by Segedin [1951], the relative displacement of the crack surfaces is in the direction of applied shear stress only. On the other hand, the direction of the frictional traction is opposite to the direction of the induced shear stress over the crack surface. The effective shear stress is therefore obtained as $\tau_{\mathrm{ef}} = \sigma_{zx} - \tau_{\mathrm{f}}$, where τ_{f} is in the same direction as σ_{zx}. The total crack deformation is then obtained by superimposing the deformations induced before and after the crack closure, giving the SIFs of the penny-shaped crack in stick and slip conditions respectively by

$$\begin{aligned} K_{\mathrm{I}} &= \sigma\alpha_1\sqrt{a/\pi} \\ K_{\mathrm{II}} &= \sigma\alpha_1\frac{2\sqrt{a/\pi}}{2-\nu}\cos\phi \\ K_{\mathrm{III}} &= \sigma\alpha_1\frac{2(1-\nu)\sqrt{a/\pi}}{2-\nu}\sin\phi \end{aligned} \tag{A.7}$$

$$\begin{aligned} K_{\mathrm{I}} &= \sigma\alpha_1\sqrt{a/\pi} \\ K_{\mathrm{II}} &= \sigma\alpha_2\frac{2\sqrt{a/\pi}}{2-\nu}\cos\phi \\ K_{\mathrm{III}} &= \sigma\alpha_2\frac{2(1-\nu)\sqrt{a/\pi}}{2-\nu}\sin\phi \end{aligned} \tag{A.8}$$

where

$$\begin{aligned} \alpha_1 &= -2p_0/\sigma \\ \alpha_2 &= 2\Big[\mu\big(\sin^2\beta - p_0/\sigma\big) + \tau_c/\sigma\Big] - \sin 2\beta - 2(1-\cot\beta)p_0/\sigma \end{aligned} \tag{A.9}$$

The first two terms in α_2 are associated with the crack deformation during crack sliding, while the last term is due to the crack deformation during crack closure. The SIFs of the elliptical crack in stick and slip conditions are also respectively given by

$$
\begin{aligned}
K_{\mathrm{I}}(\omega) &= \sigma\alpha_1 \frac{\sqrt{\pi a}}{2E(k)}\,\Pi(\omega) \\
K_{\mathrm{II}}(\omega) &= \sigma\alpha_1 \frac{\Psi k'\sqrt{\pi a}}{2\Pi(\omega)}\cos\omega \\
K_{\mathrm{III}}(\omega) &= \sigma\alpha_1 \frac{\Psi(1-\nu)\sqrt{\pi a}}{2\Pi(\omega)}\sin\omega
\end{aligned}
\tag{A.10}
$$

$$
\begin{aligned}
K_{\mathrm{I}}(\omega) &= \sigma\alpha_1 \frac{\sqrt{\pi a}}{2E(k)}\,\Pi(\omega) \\
K_{\mathrm{II}}(\omega) &= \sigma\alpha_2 \frac{\Psi k'\sqrt{\pi a}}{2\Pi(\omega)}\cos\omega \\
K_{\mathrm{III}}(\omega) &= \sigma\alpha_2 \frac{\Psi(1-\nu)\sqrt{\pi a}}{2\Pi(\omega)}\sin\omega
\end{aligned}
\tag{A.11}
$$